From Solid State Chemistry to Heterogeneous Catalysis

Svetlana Ivanova
José A. Odriozola
Luis F. Bobadilla

From Solid State Chemistry to Heterogeneous Catalysis

From Solid State Chemistry to Heterogeneous Catalysis

By

Svetlana Ivanova, José A. Odriozola and Luis F. Bobadilla

Cambridge Scholars Publishing

From Solid State Chemistry to Heterogeneous Catalysis

By Svetlana Ivanova, José A. Odriozola and Luis F. Bobadilla

This book first published 2021

Cambridge Scholars Publishing

Lady Stephenson Library, Newcastle upon Tyne, NE6 2PA, UK

British Library Cataloguing in Publication Data
A catalogue record for this book is available from the British Library

ISBN (10): 1-5275-7210-2
ISBN (13): 978-1-5275-7210-2

TABLE OF CONTENTS

PREFACE

The development of heterogeneous catalysis as a scientific discipline with a well-established theoretical basis has been mostly possible thanks to the contribution of solid state chemistry and modern surface science. From a fundamental point of view, solid state chemistry is the starting point for designing a solid with optimal composition, structure and surface properties for practical applications including heterogeneous catalytic processes.

While some excellent books gathering general aspects of heterogeneous catalysis based on first principles are already available, this textbook provides fundamental insights into solid state chemistry in order to expand the horizons of heterogeneous catalysis as a central discipline laying at the frontier of chemistry, physics, engineering and materials science. Hence, we have covered an ample range of solid state concepts such as symmetry and diffraction techniques for structure elucidation and solids bonding as well as defects' formation and their implications in heterogeneous catalysis. Moreover, the last chapter emphasizes the importance of heterogeneous catalysis as a surface phenomenon and how solid surfaces are reconstructed during the chemical reaction.

This textbook is based on our own experience of many years delivering university lectures of key modules in inorganic chemistry, solid state chemistry, materials science and industrial and environmental catalysis for chemistry and engineering students. The genesis of this book is the lack of a comprehensive and contemporary academic textbook which unifies all the key aspects of solid state chemistry and their direct implications in surface chemistry and heterogeneous catalysis, including the most recent developments. At the end of the book, we have included a useful list of questions for every chapter as a handy tool to test the learning outcomes.

We gratefully appreciate the constructive suggestions provided by our colleagues in the research group “Surface Chemistry and Catalysis” at the Institute of Materials Science (CSIC-US) and the Inorganic Chemistry Department at University of Sevilla.

Sevilla, May 2021

The authors,
José A. Odriozola
Svetlana Ivanova
Luis F. Bobadilla

CHAPTER 1

SYMMETRY AND BASIC CONCEPTS

"The chief forms of beauty are order and symmetry and definiteness…"
Aristotle

Personal archive; Mosque–Cathedral of Córdoba, Spain; Notre Dame du Paris; houses in Ghent, Belgium

The word *symmetry* derives from the Greek *sun* ('with') and *metron* ('measure'), and usually relates to proportionality and beauty in their philosophical aspect. Beauty and symmetry are strictly related; humans and some other species find symmetrical patterns much more attractive than asymmetric patterns and their preference arises from the primary needs of

visualization and orientation, independently of biological signals. A sensory bias for symmetry exists and reflects the natural patterns of order and beauty which are repeated continuously in manufactured decorative and artistic patterns.

Before introducing the concepts of symmetry in solid state chemistry, it is worth briefly recalling and redefining crystal systems and Bravais lattices, together with some symmetry elements and related operations.

Crystal systems and Bravais lattices

In 1850, August Bravais defined his concept of crystalline lattices, *i.e.* group of parallelepipeds that fill up space, in pioneering work on the basis of geometrical and mathematical principles. This work, confirmed 60 years later using X-ray diffraction, provides the basis for classification of crystal systems and lattice unit cells. It is useful, in order to discuss the origin of the crystal systems and Bravais lattices, to first imagine an empty space structured by a set of vectors connecting an infinite array of discrete equivalent points (*Figure 1*).

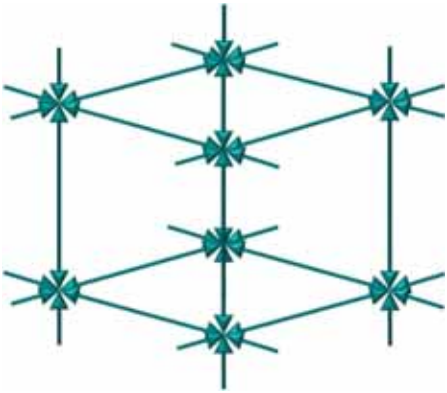

Figure 1. Definition of Bravais point array by position vectors.

The use of translation vectors fills up the space and an infinite number of equivalent points form a network. The application of the symmetry elements (translation included) over such a set of points produces crystal systems and Bravais lattices. Therefore, the set of points is defined by a position vector $\vec{R}$

$$\vec{R} = u\vec{a} + v\vec{b} + w\vec{c}$$

where $\vec{a}, \vec{b}$ and $\vec{c}$ are mutually non coplanar vectors and *u*, *v* and *w* any positive, negative (zero included) integer values.

Although the lattice is sufficiently defined by the three position vectors, in practice six parameters called ***lattice parameters*** are used, the magnitude of the vectors ***a***, ***b*** and ***c*** (lattice lengths) and the angles between them $\boldsymbol{\alpha}$ (between ***b*** and ***c***), $\boldsymbol{\beta}$ (between ***a*** and ***c***) and $\boldsymbol{\gamma}$ (between ***a*** and ***b***).

Logically the most symmetrical situation occurs when all vectors present the same length and are mutually perpendicular. The cubic system is then generated with volume $\vec{a} \cdot (\vec{b} \times \vec{c})$. If this volume encloses only one lattice point the generated Bravais lattice is designated as **primitive**, **P** (*Figure 6*). Every vertex of the cubic **P** lattice is occupied by an equivalent point (represented by a sphere) and exactly 1/8 of this sphere lies within the limits of the cell resulting in one single point per lattice (8 vertex * 1/8 of a point = 1). For commodity, the point is placed at the origin and generates all other points by translation, the sum of the position and translation vectors.

A new Bravais lattice is created after adding a second point in the center of the cube: known as a cubic **I** lattice (**I** stands for *inner*). All points have eight-fold coordination and the resulting lattice is called **conventional**, as two points are necessary to describe the lattice. The coordinates of the points are (0,0,0) and (½, ½, ½). The added point belongs entirely to the cell (8 vertex * 1/8 + 1 = 2 points). This conventional cell usually contains a primitive cell but the conventional lattice parameters and the primitive cell parameters differ (*Figure 2*)

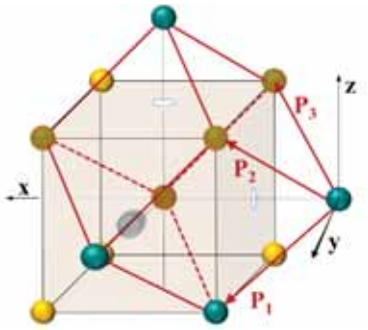

Figure 2. Conventional cubic **I** lattice and corresponding primitive (colors changed for clarity). P_1, P_2 and P_3 the new primitive vectors

We can add three more points to the (0, 0, 0) point to create new conventional **F** cubic lattice (**F** for *face-centered*), where every point has 12 neighbors and all additional points occupy the center of the cube faces. The new point coordinates are (½, 0, 0), (0, ½, 0) and (0, 0, ½,). Each added point counts as a half point for each cell as it is shared by two adjacent cells. A total of four points results from the 8 vertex * 1/8 points and 6 face centered * 1/2. Again, the resulting cell is conventional containing a new primitive cell (*Figure 3*).

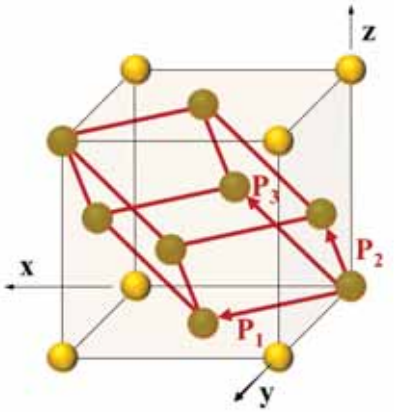

Figure 3. Conventional cubic **F** lattice and corresponding primitive. P_1, P_2 and P_3 the new primitive vectors

Problem I *Can we generate a new Bravais lattice adding points at the centers of the cube and on all faces?*

*No, the coordination of the **I**-centered atom is different from the **F**-centered one. By definition, the Bravais lattice only consists of equivalent points, which is not the case here. The resulting lattice is therefore not a Bravais lattice.*

After considering all possible combinations for the cubic Bravais lattices, the next logical step is to decrease the symmetry. If we maintain the mutually perpendicular vectors, but we change the length of one of them - *c*, for example, we can generate the tetragonal structure with $a=b\neq c$ and $\alpha=\beta=\gamma=90^{o}$. The symmetry change can be presented as stretching or compressing the cube along the *c* axis. The cubic **P** generates the tetragonal **P** lattice and the tetragonal **I** lattice arises from the cubic **I**. What happens when we stretch the cubic F lattice? It appears to be identical to a tetragonal **I** (*Figure 4*).

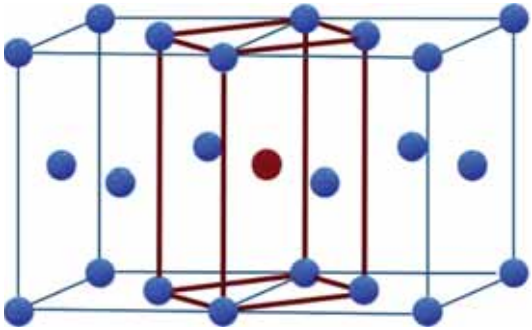

Figure 4. Tetragonal **I** creation after stretching the cubic **F** lattice

If we continue to lower the symmetry maintaining the orthogonality of the vectors and changing their lengths ($a \neq b \neq c$ and $\alpha = \beta = \gamma = 90^{o}$), the result is an orthorhombic lattice. The distortion of tetragonal **P** along *a* or *b* results in an orthorhombic **P** lattice. However, if we stretch the tetragonal **P** lattice along the face diagonal, a new orthorhombic lattice centered on two opposite sides results, the orthorhombic **C** lattice where the *a*-*b* plane is centered. Correspondingly, the *b*-*c* plane is centered on the **A** centered lattice and **B** orthorhombic results from the *a*-*c* plane. If the originally distorted lattice is the tetragonal **I**, the orthorhombics **I** and **F** are obtained after axial and face diagonal distortions, respectively.

All remaining Bravais lattices are generated after angle distortions. The angle alteration of the orthorhombic **P** creates the monoclinic **P** lattice; the distorted angle being defined by convention as the one on the *a*-*c* plane always designated as β. The two opposite side centered orthorhombic lattices also generate the **P** monoclinic lattice, whereas the orthorhombic **I** and **F** transform to a monoclinic **C** lattice (*Figure 5*).

Since axes *a*, *b* and *c* are arbitrarily labeled, it is accepted that the resulting lattice is always **C**-centered and the same applies to the orthorhombic lattices.

The last-mentioned symmetry decrease generates the triclinic **P** lattice, the one with the lowest symmetry.

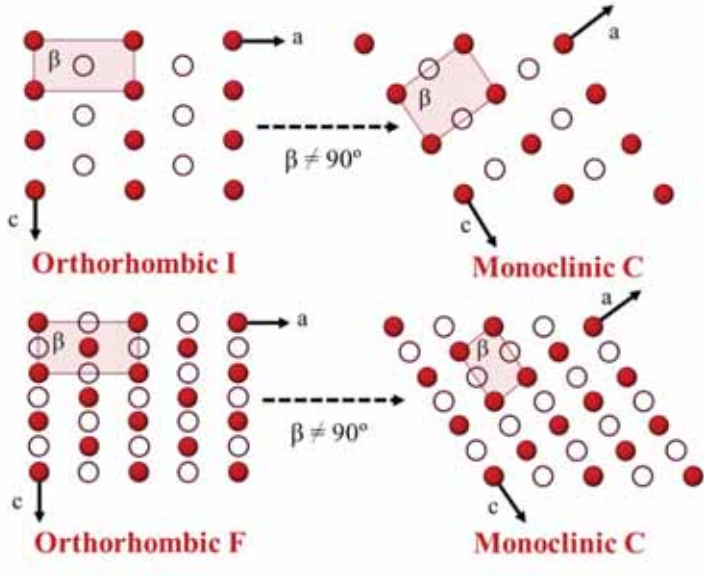

Figure 5. 2-D projection of the monoclinic lattices generated from the orthorhombic lattices. Empty symbols represent points at a ½ distance.

The final two Bravais lattices are the hexagonal **P** and trigonal **P** lattice, related closely to the first one and created by stretching the cube along its diagonal with a=b=c and $\alpha=\beta=\gamma\neq90^{o}$. A trigonal **P** lattice with a=b≠ c and $\gamma=120^{o}$ is a 1/3 part of the hexagonal P lattice. All 14 Bravais lattices are summarized in *Figure 6*.

Figure 6. The 14 Bravais lattices.

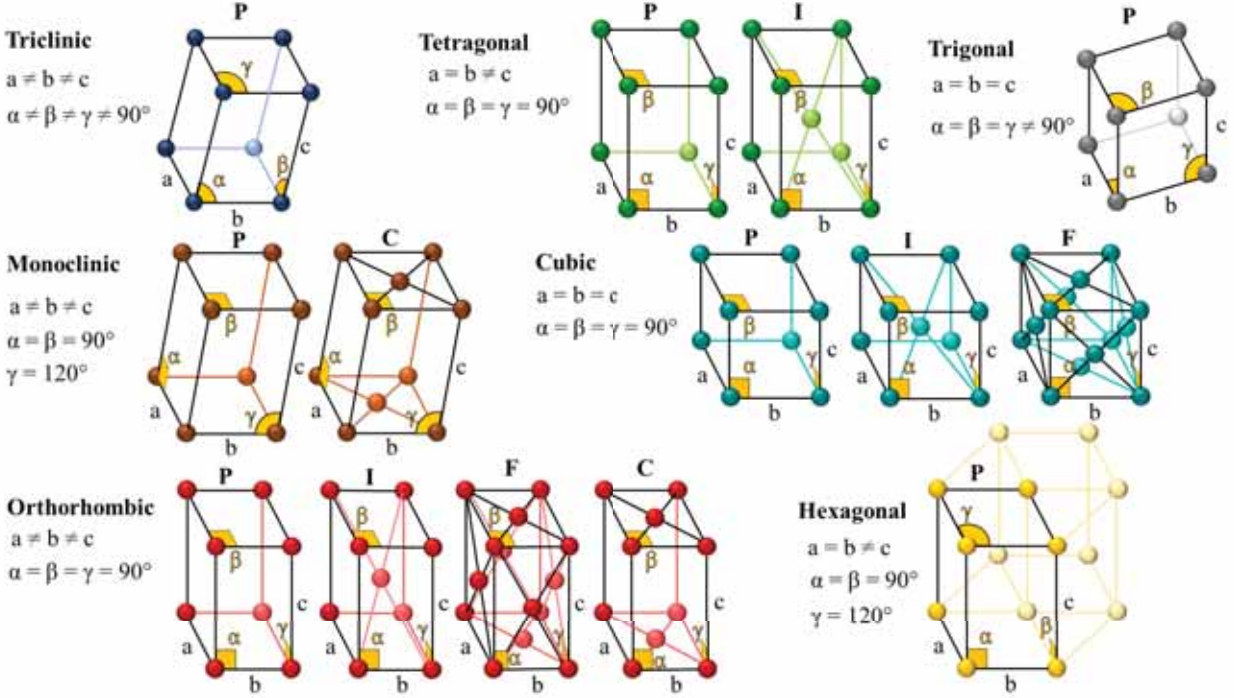

One half of the Bravais cells are primitive and the other half are conventional. We can define another special type of primitive cell: the Wigner-Seiz lattice. It is defined as a space around a point as close to that point as to any other lattice point. In real space it is a purely mathematical concept, constructed by drawing lines from a chosen point to all its nearest neighbors and then drawing a bisecting plane perpendicular to each of these planes. The 3 D construction results in a polyhedron which contains the original point (*Figure 7*).

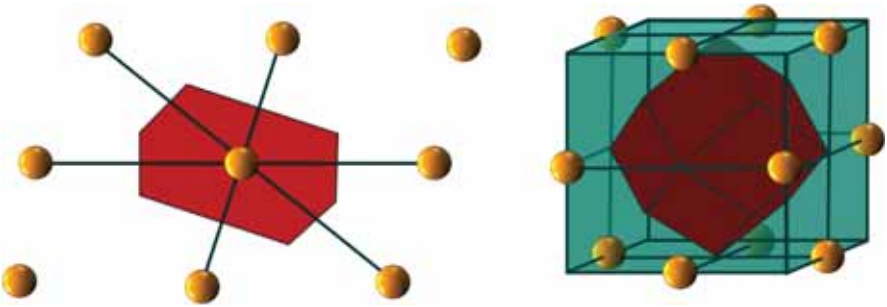

Figure 7. 2D construction of the Wigner-Seitz cell and 3D representation of the cell corresponding to the Cubic F Bravais cell.

In real space, the Wigner-Seitz cell remains a mathematical concept; however, in the reciprocal space the first Brillouin zone is defined as the Wigner-Seitz cell of the reciprocal space. The Brillouin zone allows us to understand the electronic energy bands and resulting electronic properties of the solids.

Symmetry elements

Rotational axis

An **axis of rotation**, as the name indicates, relates to the operation of rotation. An object presents an axis of rotation when a simple turn, by an angle of $2\pi/n$, results in an equivalent configuration. The n refers to the number of rotations after which the initial position is recovered. As an example, the initial position in a rectangle is obtained after four rotations at 90º, n being equal to 4, indicating a four-fold axis of rotation (*Figure 8*).

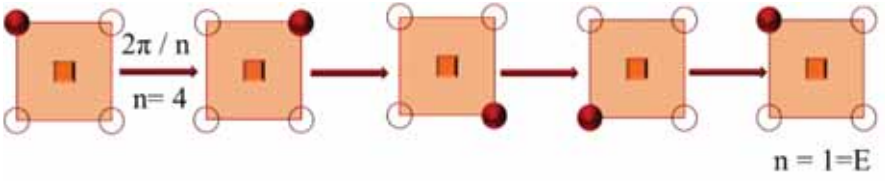

Figure 8. 4-fold rotation axis operations

n=1 corresponds to the identity operation (E) where the object remains unchanged. All objects present identity element E. By definition any type of ***n*** is possible, but only 2, 3, 4, 5 and 6 are found in 3-D space (although 5 is a very special case usually omitted).

One structure can contain multiple axes of rotation, the cube for example presents four, three and two-fold axes (*Figure 8*). However, the structures are classified by their highest order rotation axis, called the **principal axis of rotation**. All axes are represented graphically by a regular polygon, indicating an axis perpendicular to its base and with the same number of sides as the order of the axis (*Table 1*).

Table 1. Direct, inverse and helicoidal (screw) axis labeling

	Direct axes				Inverse axes				Helicoidal axes									
Axes perpendicular to the plane of projection	2	3	4	6	$\bar{2}$	$\bar{3}$	$\bar{4}$	$\bar{6}$	2_1	3_1	3_2	4_1	4_2	4_3	6_1	6_2	6_3	6_4	6_5
Axes parallel to the plane of projection																			

Two types of nomenclatures are usually employed to indicate the symmetry of the objects, i.e. Schönflies symbols for molecular symmetry operations and Hermann-Mauguin equivalents when considering solid classification. Both symbols reflect the highest symmetry elements (or a combination of a few elements generating the point and space groups' classification). Thus, for an object with a 4-fold axis of rotation, the Schönflies symbol is C_4, and the equivalent in the Hermann-Mauguin nomenclature is 4 (see Annex I for more equivalents).

As an example, three successive rotations at a rotation angle of $2\pi/4=90^{o}$ on the 4-fold axis will generate three equivalent points and the fourth one will coincide with the identity operation. Two successive operations (notated C_4^2 for molecules and 4 for solids) will rotate the molecule/lattice at 180º.

Finding the rotation axes for more complicated structures can be more complex and a basic approach is usually applied. In the case of a lattice, the highest order axis is first identified, and then all other elements, using for that purpose a bare polyhedron (a geometrical figure without counting atoms or considering their chemical nature). The rotation axes of a cube are presented in *Figure 9*.

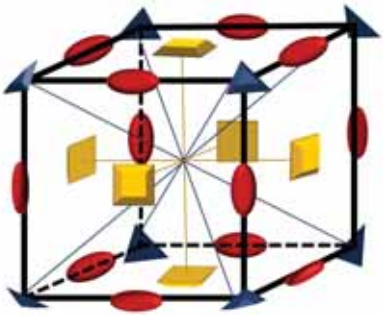

Figure 9. Rotational axes of a cube.

Mirror planes

The **mirror planes** introduce the operation of reflection. An object presents a mirror plane when a reflection on this plane results in an equivalent specular image. To specify the plane, the σ symbol is used for molecule and **m** for solids. This operation converts the right-hand object into a left-hand one and each object moves across the plane perpendicularly to a new position as far from the plane as the original one. A position with coordinates (x,y,z) is converted into (x, y, $\bar{z}$) when the reflection occurs in *x*-*z* plane. The use of the bar symbol over z instead of –z indicates that the position of this point is at coordinate (1-z) and enters within the defined cell.

Problem II. *Find the rotation axes of an octahedron.*

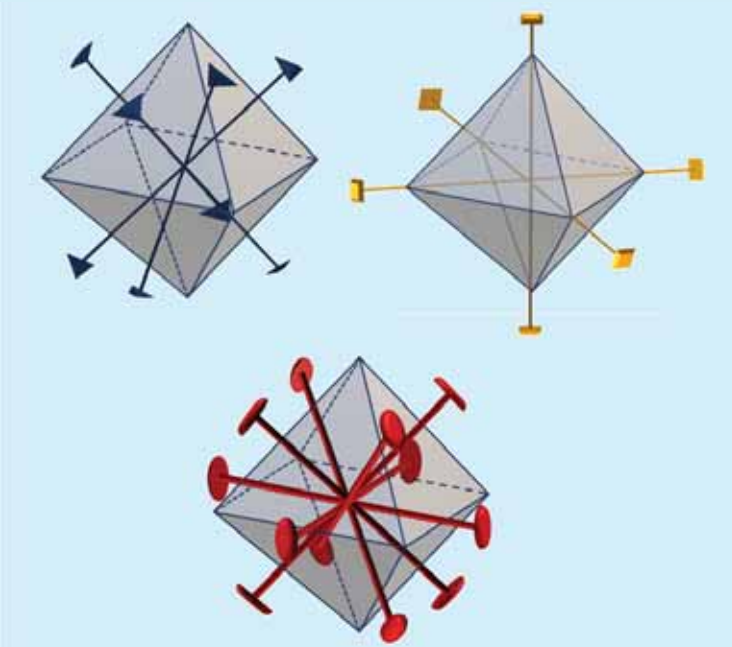

A way to reduce the complexity of the symmetry operations is to associate the rotation features with geometrical elements. Thus, if we consider the vertices (6 in total) and axes passing through two opposite vertices, it is evident that the octahedron contains three 4-fold rotation axes and three coincident 2-fold axes. Now, if we switch to the faces, we have 8 equilateral triangular faces, and a set of four 3-fold axes appears (with the axis crossing the mid-points of a pair of triangular faces on the opposite sides of the octahedron). With the edges now left (12 in total), six C_2 axes are crossing every pair of opposite edges. These axes are perpendicular to C_2, coincident with the highest order axis, and adopt a prime symbol (C_2'). There are two possible directions of rotation for the sets of C_3 and C_4 axes: clockwise and anticlockwise, which doubles the sets, and the rotational symmetry operations for an octahedron are: **E, 8C_3, 6C_4, 3C_2, 6C_2'** a set of 24 operations.

Problem III. *Compare the rotational axes of cube and octahedron.*

Problem IV. *Find all equivalent positions upon reflection for the polyhedron indicated in the figure and starting point 1.*

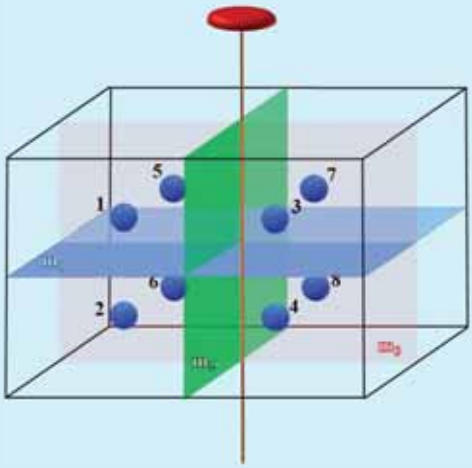

For an orthogonal parallelepiped with three perpendicular mirrors, we can generate multiple positions from the initial position **1**. The reflection in plane m_1 generates point **2**, and the operation through m_2 produces **3** and **4** from the positions **1** and **2**, respectively. The last operation m_3 generates **5**, **6**, **7** and **8** from **1**, **2**, **3** and **4**. There are eight equivalent positions of point **1**. However, if the initial point is situated on one of the planes, only four positions are generated and if it is placed at the intersection of them all, only one position is available.

For every set of symmetry operations, the number of all resulting equivalent positions depends on the position of the starting point.

We can apply another operator to pass from one equivalent position to another. Positions **1** and **2** generate positions **7** and **8** in the presence of a 2-fold axis in the plane m_2. The same operation will generate **5** and **6** from **3** and **4**.

Symmetry center

Problem V. *Which point is generated from position 1 in the presence of the center of symmetry of the octahedron.*

The squares, rectangles, parallelepipeds (orthogonal or not) and octahedra present a center of symmetry unlike the triangles and the tetrahedra.

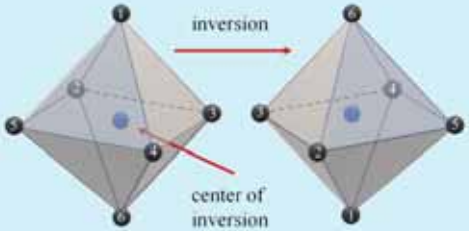

A more complex symmetry operation is **inversion**, a new position is generated through a center at an opposite position to the starting point, as far from the center as the original point. This operation is designated with ***i*** for molecules and with a bar over a symbol ($\bar{1}$), indicating the presence of the center of symmetry for the solids. Similar to the mirror plane operation, the positions generated with the inversion operator are of different chirality. The presence of a symmetry center in the origin inverts the (x,y,z) point to ($-x$,$-y$,$-z$).

All equivalent positions of a point with coordinates (x,y,z) generated after proper symmetry operations such as rotation, reflection and inversion through a center of symmetry are summarized in *Figure 10*.

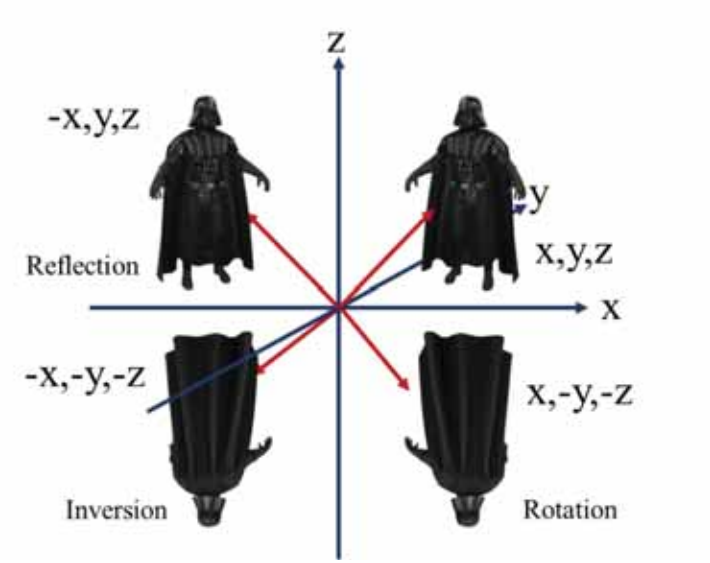

Figure 10. Equivalent positions generated after proper symmetry operations over a given (*x*,*y*,*z*) point.

Rotoinversion

The improper rotation (rotoinversion), labelled *Sn* for molecules and $\bar{n}$ for solids, is a combination of two operations, rotation at 2π/n and inversion through a center of inversion (*Figure 11*).

The rotoinversion of a point (*x*,*y*,*z*) along the $\bar{2}$ axis transforms its position at a given (x,y,$\bar{z}$) point via temporary positions ($\bar{x}$,$\bar{y}$,$\bar{z}$) or ($\bar{x}$,$\bar{y}$,z), as a function of the primary operation, inversion or rotation, respectively. The geometrical symbol for the improper axis is the same as for the proper one, but with a white/black circle inside (*Table 1* inverse axis symbols).

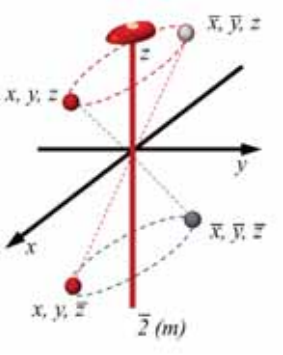

Figure 11. Operation of rotoinversion.

If we consider a tetrahedron (T_d), usually not presenting 4-fold axis or symmetry center, its four vertices are related through the $\bar{4}$ axis. Each axis crosses two opposite T_d edges and, if we draw the tetrahedra within a cube (*Figure 12*), it will be located along the perpendiculars to the opposite faces of the cube diagonals. The first rotation at 90º and inversion generates a similar tetrahedron, but with different relative position of its vertex (in a different color for clarity). The first $\bar{4}$ (z) and second $[\bar{4}\ (z)]^2$ operations are related to the third $[\bar{4}\ (z)]^3$ and fourth $[\bar{4}\ (z)]^4$ by a 2-fold axis with the same orientation as the $\bar{4}$ axis.

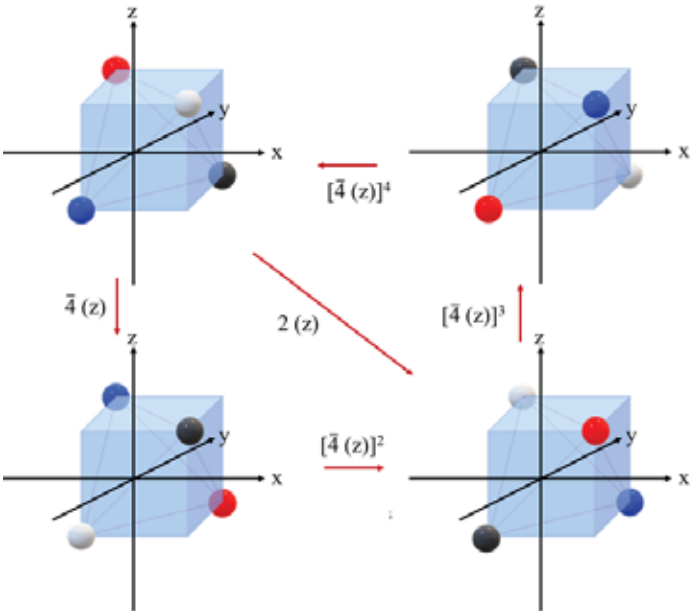

Figure 12. $\bar{4}$ axis operation in tetrahedron.

All symmetry elements discussed so far are point symmetry elements and every molecule or polyhedron of finite size possesses a set of symmetry operations that upon combination could describe the whole molecule or a finite part of a solid. Such a set of symmetry elements is known as a **point group** and the symbols that describe it correspond to the principal elements of symmetry for finite objects. To label the point groups, first we have to find the principal axis of rotation and afterwards all perpendicular mirror planes to that axis, if any. The mirror planes (*m*) perpendicular to the principal axis that is established are indicated by a bar symbol / (**4/m**, for example).

Problem VI. *Use cube symmetry elements to deduce the symmetry elements, their corresponding Hermann-Mauguin symbols and point groups.*

Thus, a cube presents three mutually perpendicular 4-fold axes and two perpendicular mirror planes (4/m), four 3-fold axes situated on cube diagonals (3), and six 2-fold axes perpendicular to the opposite edges and the corresponding perpendicular mirror planes situated along the face diagonals (2/m).

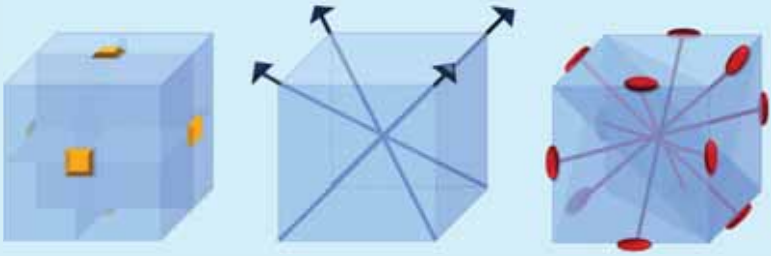

The symbols of the cube's point group should be 4/m32/m which we can simplify, by only considering the mirror planes, as all their intersections are defined by one axis. So, the point group notation for a cube becomes *m*3*m*

Problem VII. *Repeat the operation for a tetrahedron.*

A new question arises: *how many point groups are possible?* Usually, the number of point groups originated by all possible combinations of

symmetry operations is very large. However, only the point groups compatible with the lattice translation vectors (Bravais lattice vectors) count for crystals. Thus, the number of groups, known as **crystallographic point groups**, is limited to **32**.

Point groups

A simple rotation through an angle, with the condition $n\alpha=2\pi$, where *n* is an integer number equal to 1, 2, 3, 4 and 6, will generate 5 corresponding singular point groups (*Figure 13*). This figure represents the point groups' 2D projection where all equivalent positions obtained after applying the symmetry operators are indicated.

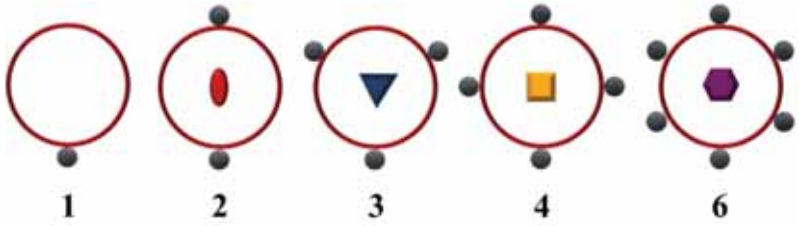

Figure 13. 2-D projection of simple rotational point groups.

Upon combination of those proper rotations, only the groups formed upon the condition that any effect produced by a combination of two operations is equal to a third one (A•B=C) are defined as point groups.

Problem VIII. *Consider a cube and three symmetry operations:* ***A*** *3-fold axis rotation around the body diagonal;* ***B*** *3-fold axis rotation around the other body diagonal; and,* ***C*** *2-fold axis on any line passing through the centers of the cube's faces. Determine the compatibility of the rotation operations with the condition A•B=C.*

If compatibility is to be tested, we have to be sure that A, B and C comply with the group properties: i) the successive application of two operators originates another which is a part of the same group A•B=C; ii) the composition of any two operators is associative (A•B)C =A(B•C); iii) an identity operator exists and A•E= E•A=A; and, iv) every operator presents an inverse one and their combination results in the identity operator $A \bullet A^{-1} = A^{-1} \bullet A = E$.

It is clear that the application of A and B has the same effect as C.

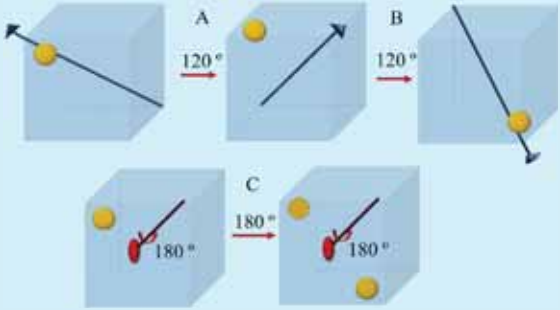

An alternative way to determine the compatibility of the rotation is to use the Euler equations relating the angles of rotation (α, β ,γ) with the angles between the rotation axes (A, B, C).

$$\cos(A \wedge B) = \frac{\cos(\gamma/2) + \cos(\alpha/2)\cos(\beta/2)}{\sin(\alpha/2)\sin(\beta/2)}$$

$$\cos(A \wedge C) = \frac{\cos(\beta/2) + \cos(\alpha/2)\cos(\gamma/2)}{\sin(\alpha/2)\sin(\gamma/2)}$$

$$\cos(B \Lambda C) = \frac{\cos(\alpha/2) + \cos(\beta/2)\cos(\gamma/2)}{\sin(\beta/2)\sin(\gamma/2)}$$

If the substitution of rotation angles results in acceptable values of intra-rotational angles the group meets the condition A•B=C

Such groups are summarized in *Table 2* and *Figure 14*.

Table 2. Compatibility of the rotational combinations.

A	B	C	ABC	A∧B	A∧C	B∧C
2	2	2	222	90º	90º	90º
3	2	2	32	90º	90º	60º
4	2	2	422	90º	90º	45º
6	2	2	622	90º	90º	30º
4	3	2	432	54º44’	45º	35º16’
2	3	3	23	54º44’	54º44’	70º32’

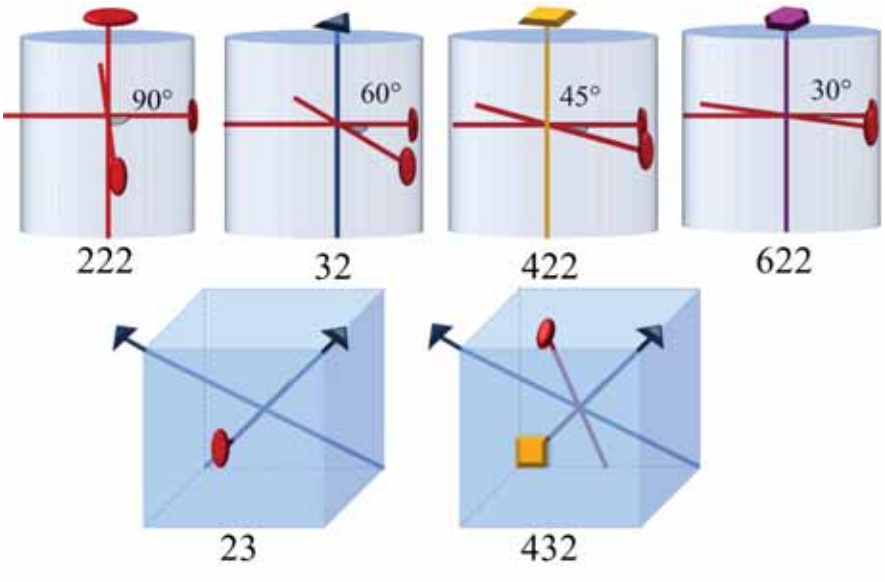

Figure 14. Point groups originated following rotational combinations.

The point groups resulting from the combination of rotational axes are named over the participants starting with the principal axis; two digits are sufficient to indicate the point group. However, in some cases a third one appears for additional clarification of the crystal system.

The presence of rotoinversion generates another 5-point groups where only one pattern is produced and cannot be generated by another simple operation or combination of more symmetry elements. The 2-D projection must indicate all equivalent positions, but in this case negative coordinates and specular images appear. The symbols ’ and – are therefore used whenever the equivalent position is chiral and with negative *z* coordinates. The presence of mirror planes in the plane of the paper are indicated with crossed black lines in the right corner of the sketch (*Figure 15*).

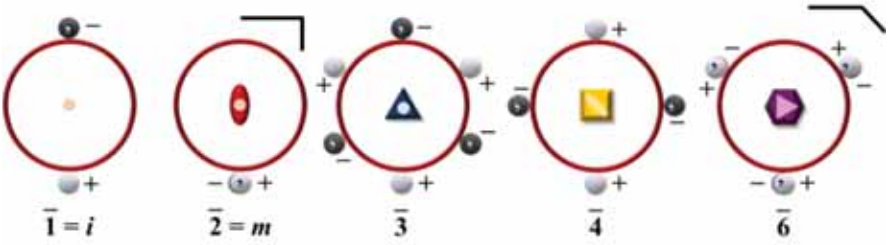

Figure 15. 2D projections of the inverted axis point groups

The inversion 2-fold axis, $\bar{2}$, is always written as *m* (mirror plane). The $\bar{6}$ group can also be denoted 3/m, as the same result is obtained after successive 3-fold axis rotation and reflection through a mirror plane perpendicular to that axis.

Operations producing left-handed objects can be combined to produce right-handed objects. There are 16 groups that contain improper axes deriving from groups with the proper rotation axis, *n*. The improper axis, $\bar{n}$, either substitutes the proper one or is parallel to it. The combination of both is indicated as a fraction, n/$\bar{n}$. Simplifying the labeling, we use n/m (instead of n/$\bar{n}$) when *n* is an even number and $\bar{n}$ implies a mirror plane. For *n* odd numbers the *n*/$\bar{n}$ is denoted as $\bar{n}$. Nevertheless, $\bar{2}$ is always *m*, and a group such as $\bar{2}\bar{2}2$ converts into *mm*2. Some examples are shown in *Figure 16* and all 16 groups are summarized in *Table 3*.

Table 3. 16 point groups generated by a combination of proper/improper rotation axes and mirror planes.

2/m	**2mm**		
mmm			
4/m	**$\bar{4}$2m**	**4mm**	**4/mmm**
3m	**$\bar{3}$m**		
6/m	**6mm**	**$\bar{6}$m2**	**6/mmm**
m3	**$\bar{4}$3m**	**m3m**	

The red colored groups correspond to a combination of an even order principal axis and inversion center (center of symmetry), the groups in blue correspond to an axis and a plane that contains the axis, and all the others correspond to three axes and a center of symmetry.

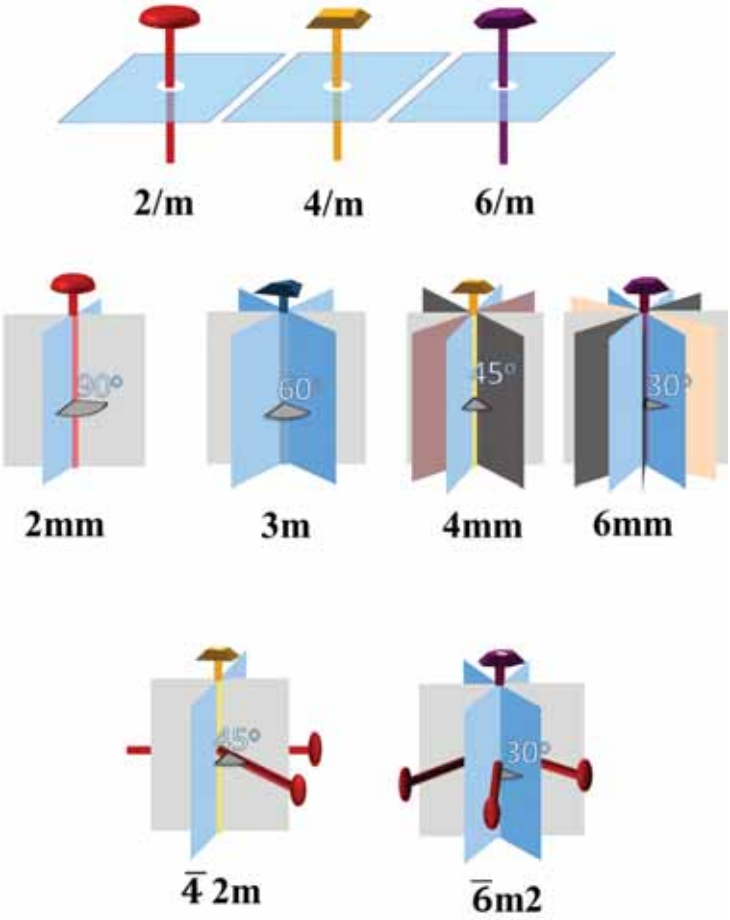

Figure 16. Examples of rotational axis and combinations of mirror plane point groups.

The 2-D projections of the groups include all equivalent positions and symmetry elements. Some examples are listed in *Figure 17*. The bold lines correspond to a mirror plane perpendicular to the plane of projection and the arrow a 2-fold axis perpendicular to the principal one.

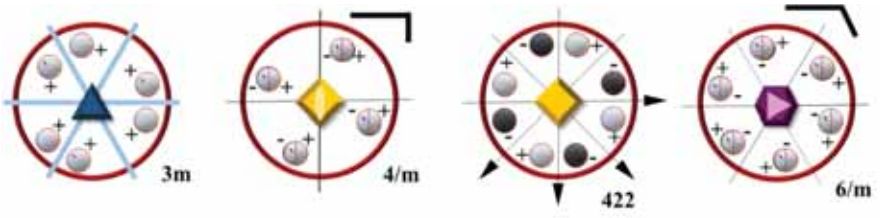

Figure 17. 2-D projection of selected point groups.

The crystallographic point groups are classified by their principal axis followed by all other elements of symmetry. *Table 4* shows the distribution of the 32 point groups and their corresponding crystalline systems.

Table 4. Summary of the 32 point groups for solids

Crystalline system	Characteristic symmetry element	Point groups
Cubic	3-fold axis	*m*3*m*, 23, *m*3, $\bar{4}$3*m*, 432
Tetragonal	4-fold or axis on *z*	4/*mmm*, $\bar{4}$2*m*, 4*mm*, 4/*m*, 422, 4, $\bar{4}$
Orthorhombic	Three elements (2-fold axes and an *m* perpendicular to each other)	*mmm*, *mm*2, 222
Monoclinic	2-fold axis on *y* (or a perpendicular *m* plane)	2/*m*, *m*, *2*
Triclinic	none	1, $\bar{1}$
Hexagonal	6-fold axis on *z*	6/ *mmm*, $\bar{6}$2*m*, 6*mm*, 6/*m*, 622, 6, $\bar{6}$
Rhombohedral	3-fold axis (or *3*)	$\bar{3}$*m*, 3*m*, 32, $\bar{3}$*3*, 3

Detailed observation of *Table 4* allows us to specify some general hints on the interpretation of point groups and their relation to the seven crystal systems. A 3 in the second position always signifies that this point group belongs to the cubic system, specifying the 3-fold axis along the cube diagonals. A 4 in the first position and the absence of 3 in the second one indicates that the point group belongs to the tetragonal system. A 6 in the first position points to a hexagonal system and a 3 in the first position to the rhombohedral system. Only two groups fit into the triclinic system, 1 and $\bar{1}$. As for the orthorhombic system, three mutually perpendicular elements are always present, whereas for the monoclinic system, two elements appear in the best case, 2-fold axis and perpendicular mirror plane.

A chart similar to that used for molecular symmetry determination can be employed to relate crystal systems with their symmetry elements and point groups (*Scheme 1*).

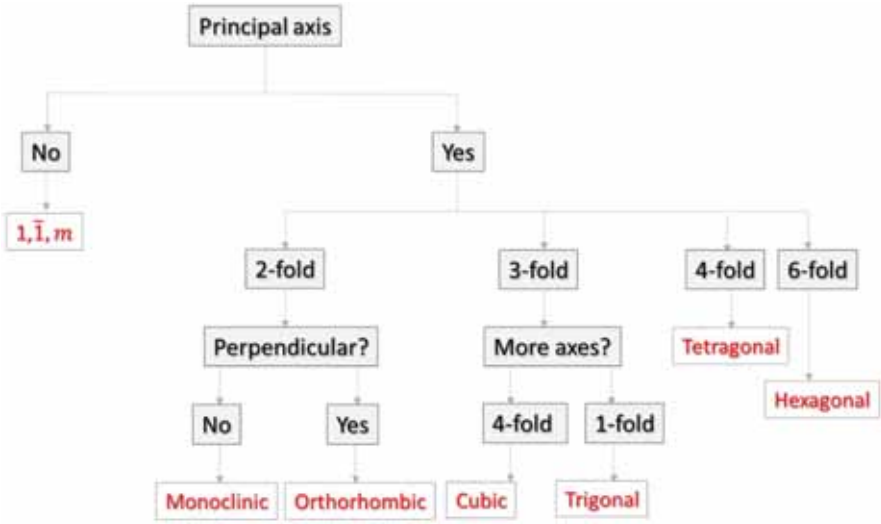

Scheme 1. Point group classification chart

Point groups represent the compatibility of the symmetry elements and their relation to the unit cells.

Describing solids, however, involves defining the infinity of the crystal, and to do so we need extra symmetry operations comprising translation. The operation of translation corresponds to position shift over the space

directions. Therefore, the crystal can be defined as a periodical repetition (translation in 3-D) of a motif, including unit cell and all atoms positioned within it. The atoms are not necessary symmetrically ordered, but they form a set with all symmetry elements of a point group. Therefore, to repeat this motif and to determine a crystals' periodic structure, two more symmetry elements must be defined: screw (helicoidal) axis and glide planes.

Screw axis

The **screw axis** combines two successive operations; clockwise rotation at $2\pi/n$ degrees around the axis and translation of the n/X fraction of the parameter parallel to the axis under consideration, X. These operations are denoted as X_n (n<X). So, for the 2_1 axis parallel to z, the rotation is 180º ($2\pi/2$ degree angle) with a translation of c/2. The next action reproduces the initial position in the upper unit cell (*Figure 18*).

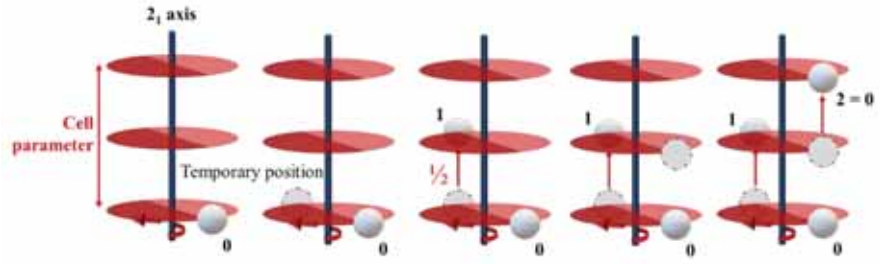

Figure 18. 2_1 screw axis operation (rotation at 180º and translation of ½ of parameter)

Problem IX. *Study the case of 3_1 and 3_2 screw axis parallel to z.*
The 3_1 operation includes a first clockwise rotation at 120º and a translation parameter of 1/3 of the parameter parallel to the axis - c. The second and third rotation are again at 120º with parameters 2/3 c and 3/3 c. For the 3_2 axis, the first rotation is the same at 120º, but with parameter 2/3 c, the second with parameter 4/3 c and the last with parameter 6/3 c. The second and third rotation and translation are outside the cell, but present equivalent points in the original cell. We can see that 3_1 and 3_2 are chiral one to another and that they differ in the direction of rotation.

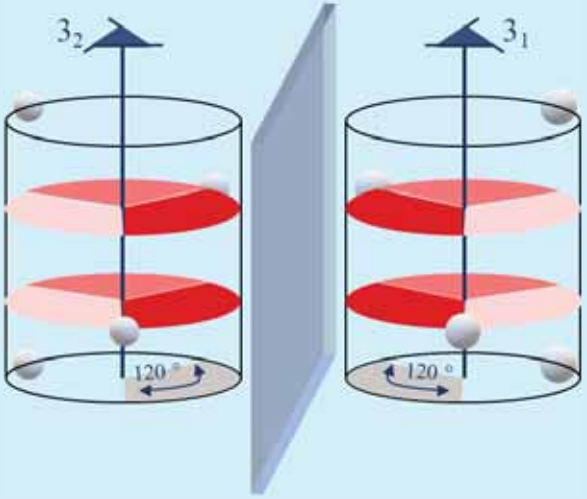

Glide plane

The second element, glide plane (g), combines reflection and translation in directions (one or two) parallel to the mirror plane. Glide plane notation includes parameter ***a***, if the direction of translation is parallel to *a*, ***b*** if parallel to *b*, and ***c*** if parallel to *c*. If the translation occurs along two parallel axes after the mirror operation, the translation parameter appears as a modulus of half the sum of the involved parameters and the glide plane is denoted as ***n***. Two successive translations, first parallel to the mirror plane and second in a direction perpendicular to that plane, both with a modulus of ¼ of the parameters, form the ***d*** plane (*Figure 19*).

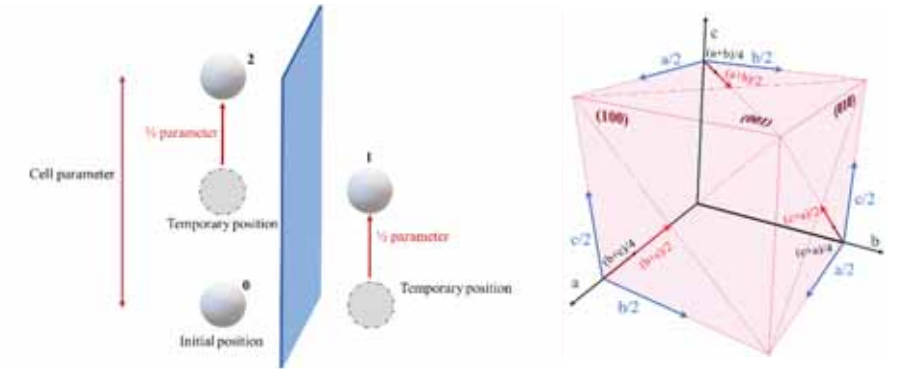

Figure 19. Glide planes: operation and directions.

But how are the equivalent points situated after a glide plane operation?

If the glide plane is an ***n***-type the projection occurs along the face diagonal (½ (a+b)). For an ***n*** operation perpendicular to plane x, a point with coordinates x,y,z converts into (-x, y+½, z+½) (*Figure 20*)

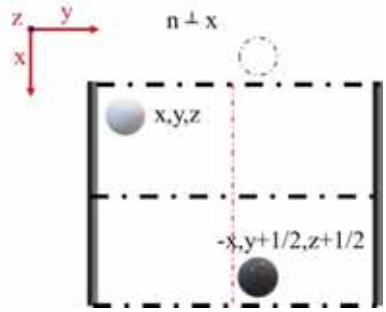

Figure 20. ***n***-glide plane operation

Problem X. *Situate the equivalent point of x,y,z after a glide operation on the a plane perpendicular to* ***y*** *and crossing the origin.*

After situating the plane perpendicular to y and crossing the origin (indicated with dashed lines in 2D projection chart), the glide plane operation includes reflection to coordinates x, -y, z and translation to a ½ of the parameter parallel to the plane (x+½, -y, z).

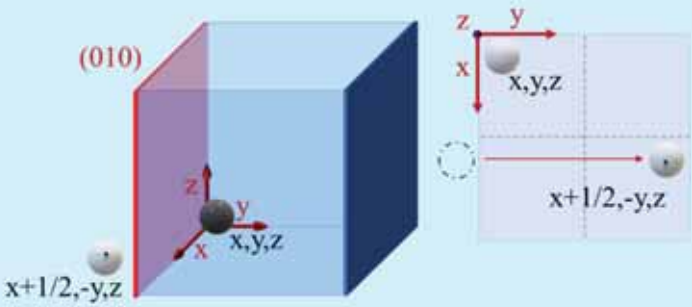

This point is situated outside the original cell (temporary position in dashed circle), but has an equivalent point within the cell (indicated in cell' 2D projection considering the x-y as plane of projection). Note the appearance of the comma sign after the glide operation indicating a left-hand replica.

Problem XI. *Now situate, using the 2D projection plot, the point that results from the glide plane operation on a plane perpendicular to* ***z*** *and crossing the origin.*

Screw axis and glide operations are compared in *Figure 21*.

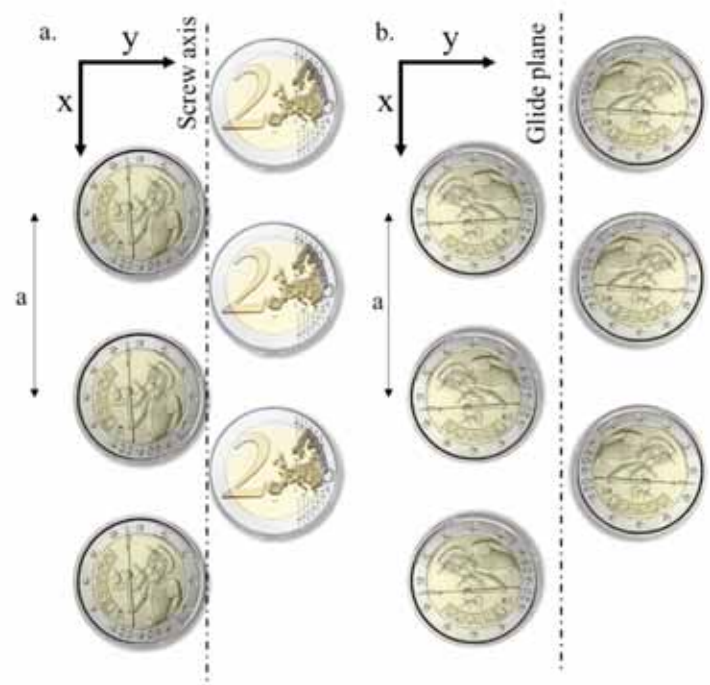

Figure 21. Arrangement of elements after screw axis and glide plane operations.

The introduction of translational elements (screw axis or glide plane) and Bravais lattice type to the 32 point groups generates the 230 **space groups**. *So, how are the space groups derived?*

First, we must choose a point group and then combine it with the possible Bravais lattices for that crystalline system. For example, if we take the 2/*m* group, belonging to the monoclinic systems (monoclinic P and C), two space groups arise, P *2/m* and C *2/m*. And if we consider that the principal axis might convert into a screw axis of the same order and the mirror plane might become a glide plane, four more space groups are generated: P $2_1/m$, P$2/c$, P$2_1/c$, C$2/c$. If we apply the same argument to all monoclinic groups (2 and *m*), 7 more space groups are generated (P2, C2, P2_1, P*m*, C*m*, P*c* and C*c)*, giving us a total of 13 space groups for the monoclinic system (*Scheme 2*).

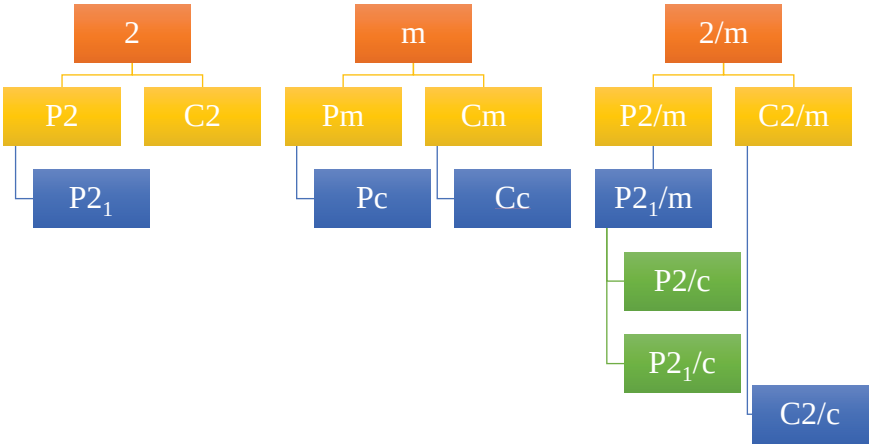

Scheme 2. Monoclinic system space groups

The group P$2_1/c$ is formed from combination of 2_1 screw axis parallel to *b*, and a glide plane *c* (*Figure 22*).

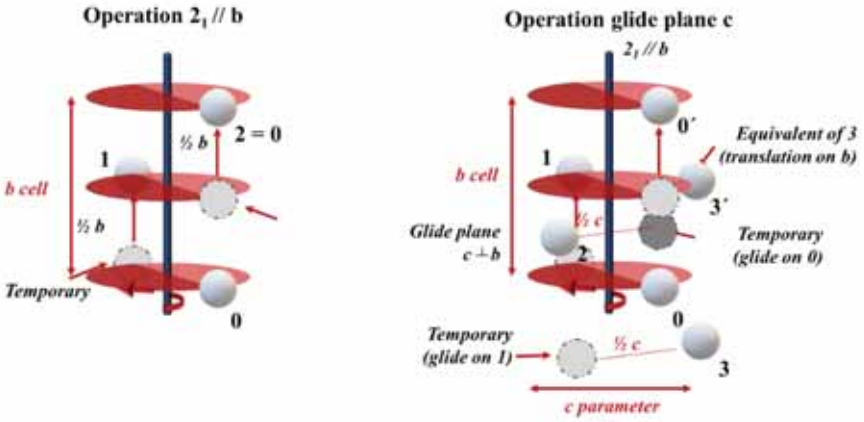

Figure 22. Equivalent position generation for the P$2_1/c$ group.

The 2_1 operation over point 1 generates point 2 after clockwise rotation at 120º and translation at ½ b parameter. The application of a glide plane, *c*, perpendicular to *b* (mirror operation and ½ c translation), produces points 3 and 4 from 1 and 2, respectively. Point 4 is outside the cell but its equivalent, point 4', is situated within the original cell.

The cell symmetry illustration including the relative orientation of all its elements and general atomic positions are defined by convention, in accordance with the International Union of Crystallography, and represented in 2D projections.

For the P 2_1/c group, a polygon representing the monoclinic system is drawn including some specified positions (*Figure 23*). The initial position 1 with coordinates (x,y,z), following operation 2_1 (axis parallel to b, translation ½ of b), generates point 2 with coordinates (-x, ½+y, ½-z). The glide operation on 1 generates point 3, and point 4 is originated by 2 after the same operation. The presence of a glide plane at ¼ height (indicated in Figure 21 a) converts the coordinates of point 3 in (x, ½-y, ½+z) and those of point 4 into (-x, -y, -z). Therefore, the combination of both operations generates 4 equivalent positions. *But how are the positions 1, 4 and 2, 3 related?* They can be correlated by placing inversion (symmetry) centers. Using only the inversion center, all the general positions are generated.

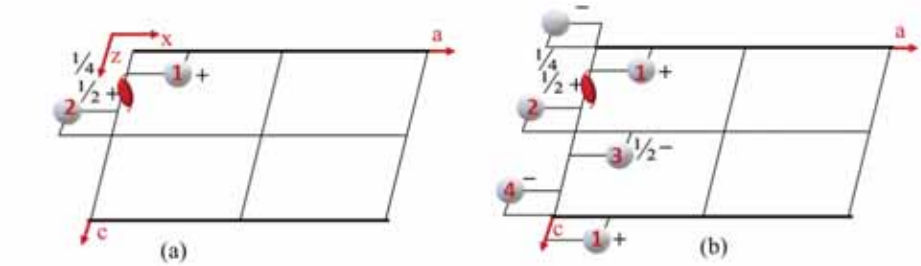

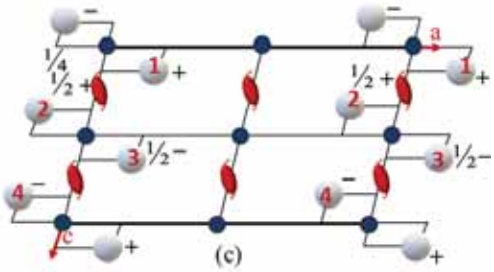

Figure 23. *P* $2_1/c$ group symmetry illustration: a) operation 2_1; b) operation glide plane; and c) symmetry center element

Every one of the 230 space groups is represented in the *International tables for crystallography*, containing all necessary information on atoms positions, symmetry elements, point group and crystal system to which the group belongs (*Figure 24*).

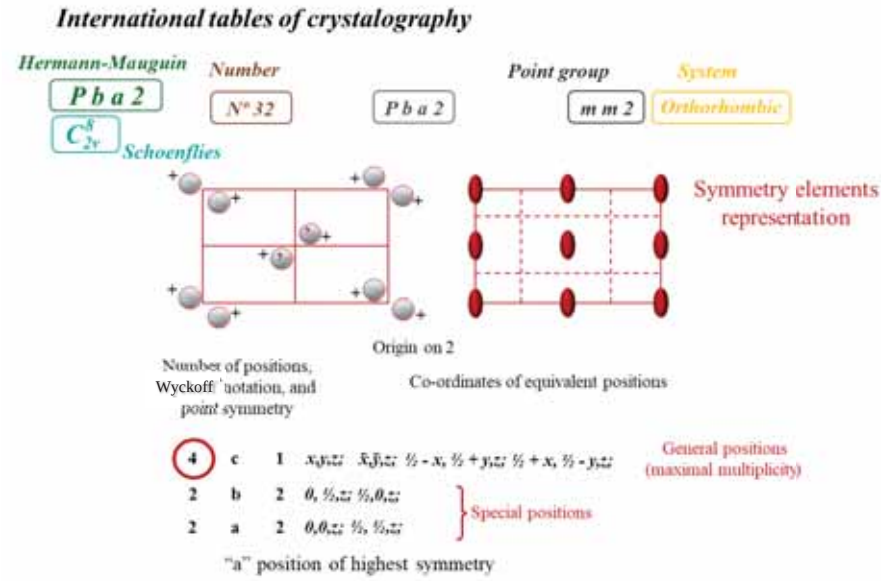

Figure 24. A crystallographic table (as in the *International tables for crystallography*).

The first line of information includes the Hermann Mauguin symbols designating the space group (short and extended version, in our example the same), the corresponding point group, and the crystalline system. The assigned group number and Schönflies correspondence also appear, as does the information, if multiple choices exist, on the origin of the cell. The origin is also indicated under the diagrams, taking into account some basic rules; if a center of symmetry exists, the origin coincides with it, otherwise the origin is placed on the point of maximal symmetry, principal axis, screw axis, glide plane or their intersections. The 2D diagrams indicate the general position and, in a separate graph, the symmetry elements (polygons in the central part of the table). The monoclinic systems are generally represented on the *a*-*c* plane, whereas the orthorhombic and cubic ones are represented on the *a*-*b* plane (although due to the complexity of the cubic systems only representations of the symmetry elements are shown).

The tables include all general and special position coordinates. The general (equivalent) positions are the positions of maximal multiplicity mismatching the symmetry positions. The special positions are those coinciding with symmetry elements, and normally contain a restrictive coordinate (zeros, fractions or duplicates).

The last element that appears in the tables is the Wyckoff notation or the position code, where ***a*** designates the position for minor height.

The information included in the *International tables of crystallography* allows the construction of the entire crystal structure, as we will see in the following chapter.

Books Used and References

Structure and bonding in crystalline materials, Gregory Rohrer, Cambridge University Press, Cambridge UK 2004.

Inorganic chemistry, 4th edition, James E. Huheey, Ellen A. Keiter, Richard L. Keiter, Harper Collins College Publishers, USA 1993.

Cristaloquímica de materiales de la estructura a las propiedades de los sólidos inorgánicos, 1st ed., Carlos Pico Marín, Maria Luisa Lopez Garcia, Maria Luisa Veiga Blanco, Editorial Sintesis, Spain, 2008.

Crystal chemistry from basic tools to materials creation Gérard Férey, World Scientific, Singapore, 2017.

Symmetry and Structure: Readable Group Theory for Chemists, 2nd edition, S. F.A. Kettle, 1995 John Wiley & Sons, Ltd, UK.

Solid state chemistry and its application 2nd edition, Anthony R. West, 2014 John Wiley & Sons, Ltd, UK.

Inorganic Chemistry, 5th Edition, Gary L. Miessler, Paul J. Ficher, Donald A. Tarr, 2014 Pearson Education.

S. F.A. Kettle and L. J. Norrby, J. Chem Educ., 70, 1993, 959-963.

J. P. Fackler, Jr., J. Chem Educ., 55, 1978, 79-83.

CHAPTER 2

ARRANGEMENT OF ATOMS IN SOLIDS. CRYSTAL STRUCTURES

"Crystals reveal their hidden structure
only when broken"
Sigmund Freud

Some 70% of all known chemical compounds are solids generally classified by the order of their building units. Regular repeating orders with specific patterns in the three spatial dimensions are typical of all crystalline solids, whereas the absence of any such order is characteristic of non-crystalline or amorphous materials.

Referring to a specific pattern, we often imagine a cell, translated through all 3D space vectors, completely filling the space without creating voids or overlaps. This cell could be primitive, when only one lattice point describes it, or conventional with 2 or more lattice points. *However, how can the crystal structure be defined? And what is the difference between the Bravais lattice and a crystal structure?* A structure is obtained when we locate a basis at each Bravais lattice point. The basis is the identification of the structure's chemical composition; it is formed by one or more atoms corresponding to crystal stoichiometry. The lattice may contain one or more formula units. So, the structure consists of one of the Bravais lattices plus a set of atoms at each lattice point.

The best way to describe a structure is to specify its formula unit, crystalline system, cell parameters and space group, and the coordinates of all independent sites and their occupational elements. Using all those details (present in the crystallographic tables), we can generate the structure either through the corresponding 2-D projection or by using the polyhedral model.

Structure generation from symmetry elements

Let us take as an example the structure of titanium dioxide anatase (*Table 1*). The space group $I4_1/amd$ indicates that the structure is tetragonal with $a=b\neq c$ and $\alpha=\beta=\gamma=90^o$. The Bravais lattice is **I**-tetragonal and the basis is a multiple integer of the formula unit, four units per lattice (the latter information is also useful for density calculation of compounds). The basis consists of Ti and O atoms with positions indicated in the table. Only half of the positions are generated by the points present in the table, the other half originate from the *+I* operation, where (½, ½, ½) is added to each coordinate listed in the table.

Table 1. TiO_2 anatase structure.

Formula unit TiO_2 anatase	**Space group $I4_1/amd$ (n.141)**
Cell dimensions	a=3.785 Å and c= 9.514 Å
Cell content	4 formula units
Atomic positions	Ti in (4a)
	(0, 0, 0); (0, ½, ¼); *+I*
	O in (8e) (0, 0, *z*); (0, 0, $\bar{z}$) (0, ½, *z*+¼); (0, ½, ¼ - *z*); *+I* *z=0.2*

Using the table, we can generate the coordinates of the 12 points, where $\bar{z}$ is equal to 1-*z*, and all points with coordinates superior to 1 or inferior to 0 are replaced by their equivalent positions within the projected cell (adding or removing 1). Taking into account that the projection describes a tetragonal cell, the *a*-*c* plane is chosen and the origin is placed in the upper left-hand corner indicated by the axis insertion. *Figure 1* shows the projection generated by the 12 points calculated according to the table and using different symbols for Ti (blue circle) and O (red circle).

Ti	0	0	0
	0.5	0.5	0.5
	0	0,5	0.25
	0.5	1	0.75
O	0	0	0.2
	0.5	0.5	0.7
	0	0	0.8
	0.5	0.5	0.3
	0	0.5	0.45
	0.5	1	0.95
	0	0,5	0.05
	0.5	1	0.55

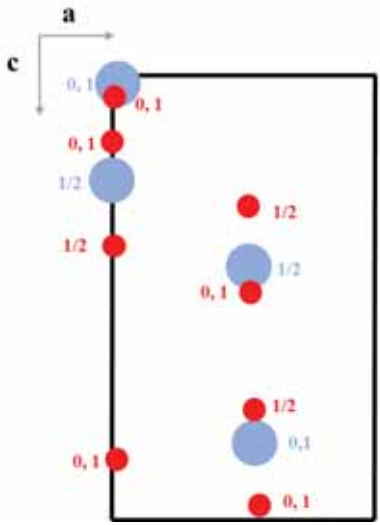

Figure 1. Point coordinates and 2-D projection of the anatase structure.

Nevertheless, in order to complete the projection, we must include all points originated by the translation and the coordinates of the repeating points (*Figure 2*).

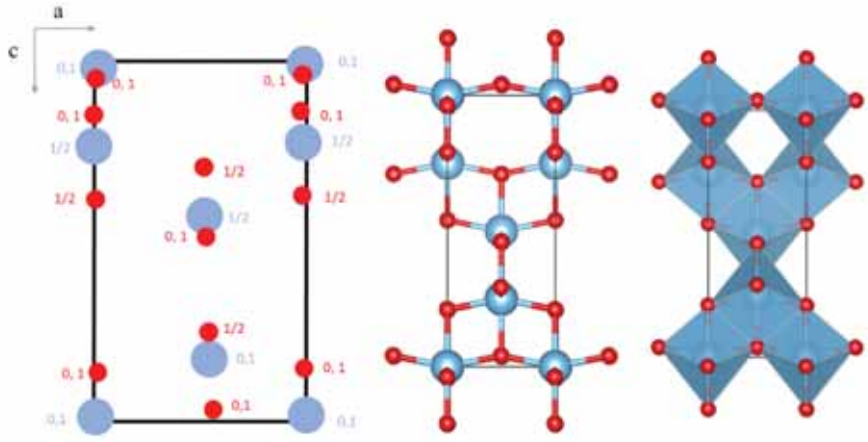

Figure 2. Anatase structure full 2-D projection and generated structures (using Vesta software).

After translation, the (0,0,0) coordinate atom **Ti** appears at every vertex and the presence of oxygen multiplies. The translation operation allows the projection to be terminated and the coordination of every atom found in the structure to be determined, *i.e.* Ti has 6 oxygen neighbors (*Figure 2*).

Any change of the projection plane modifies the models, in such a way that the generated distribution is completely different (*Figure 3*).

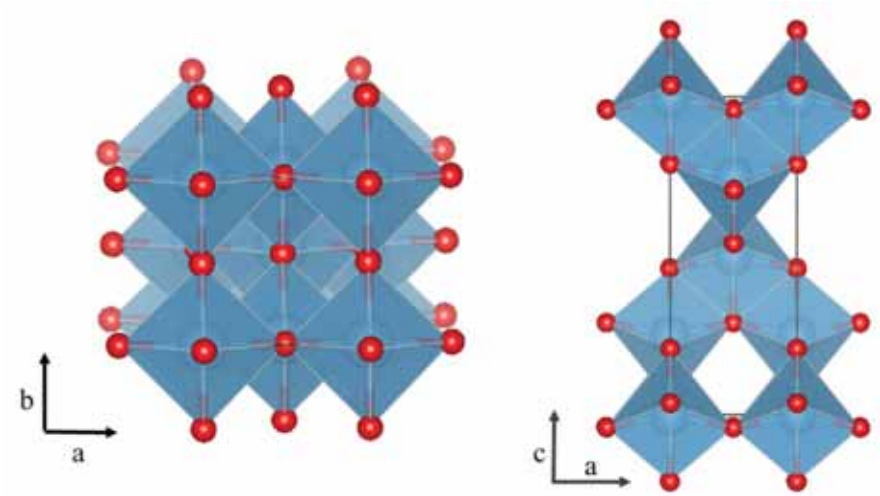

Figure 3. Anatase structure generation in the *a*-*b* and *a*-*c* plane.

The 2D projection is suitable for calculating the bond distances, angles or spacings in the lattice. The bond distance calculation is based on an estimation of the length L of any vector $\vec{R}$ with components *xa*, *yb* and *zc*, where *a*, *b* and *c* are the lattice parameters. The length L is the square root of the scalar product of the vectors

$$L = (\vec{R} \cdot \vec{R})^{1/2}$$

The scalar product of both vectors can be resolved using a matrix multiplication

$$L^2 = [x \quad y \quad z] \begin{bmatrix} \vec{a}.\vec{a} & \vec{a}.\vec{b} & \vec{a}.\vec{c} \\ \vec{b}.\vec{a} & \vec{b}.\vec{b} & \vec{b}.\vec{c} \\ \vec{a}.\vec{c} & \vec{b}.\vec{c} & c.\vec{c} \end{bmatrix} \begin{bmatrix} x \\ y \\ z \end{bmatrix}$$

And referring to the unit cell parameters

$$L^2 = [x \quad y \quad z]\begin{bmatrix} a^2 & abcos\gamma & accos\beta \\ bacos\gamma & b^2 & bccos\alpha \\ cacos\beta & cbcos\alpha & c^2 \end{bmatrix}\begin{bmatrix} x \\ y \\ z \end{bmatrix} = [x \quad y \quad z][\Gamma]\begin{bmatrix} x \\ y \\ z \end{bmatrix}$$

where, Γ is the 3x3 matrix known as a metric tensor.

The distance between two points with coordinates (x_1,y_1,z_1) and (x_2,y_2,z_2) is

$$L^2 = [\Delta x \quad \Delta y \quad \Delta z][\Gamma]\begin{bmatrix} \Delta x \\ \Delta y \\ \Delta z \end{bmatrix}$$

where, $\Delta x=(x_2-x_1)$, $\Delta y=(y_2-y_1)$, and $\Delta z=(z_2-z_1)$.

The metric tensor is reduced in every crystal system depending on the α, β and γ angles, as shown in **Appendix II**.

For all orthogonal systems, the cosine of any angle is equal to zero and the metric tensor becomes a diagonal matrix. Returning to the example of the TiO_2 anatase structure, we can calculate the Ti-O bond distance. The bond length, for Ti at coordinates (0,0,0) and O at (0, 0, 0.2) with α=β=γ=90º, is as follows:

$$L^2 = [0 \quad 0 \quad 0.2]\begin{bmatrix} a^2 & 0 & 0 \\ 0 & b^2 & 0 \\ 0 & 0 & c^2 \end{bmatrix}\begin{bmatrix} 0 \\ 0 \\ 0.2 \end{bmatrix} = (0.2)^2c^2 \text{ and } L=1.902 \text{ Å}$$

We can also calculate the angle, θ, between two vectors $\overrightarrow{R_1}, \overrightarrow{R_2}$ defined by their scalar product and their lengths, R_1 and R_2.

$$cos\theta = \frac{\overrightarrow{R_1} \cdot \overrightarrow{R_2}}{R_1 R_2}$$

For vectors with directions (x,y, z) and (x_1, y_1, z_1), the bond angle between them is equal to

$$cos\theta = \frac{[x_1, y_1, z_1]\begin{bmatrix} x \\ y \\ z \end{bmatrix}}{|x_1, y_1, z_1||x, y, z|} = \frac{(x_1)(x) + (y_1)(y) + (z_1)(z)}{\sqrt{x_1^2 + y_1^2 + z_1^2}\sqrt{x^2 + y^2 + z^2}}$$

The volume of the cell is given by $\vec{a}.(\vec{b} * \vec{c})$

$$V=\vec{a}.(\vec{b} * \vec{c}) = abc\sqrt{1 - cos^2\alpha - cos^2\beta - cos^2\gamma + 2cos\alpha cos\beta cos\gamma}$$

Problem I *Using the next table, please generate the projection of TiO_2 rutile structure and compare it to the titanium anatase structure. Calculate the bond distance, Ti-O, and the bond angle.*

Formula unit TiO_2 rutile	**Space group $P4_2/mnm$ (n.136)**
Cell dimensions	a=4.5837 Å and c= 2.9581 Å
Cell content	2 formula units
Atomic positions	Ti in (2a)
	(0,0,0); *+I*
	O in (4f) (*x,x,0*); *+I* *x=0.3053*

Nevertheless, sometimes the 2D projection of the structure is not helpful for understanding the atom/ion arrangements and the ball and sticks or polyhedral model must be used. The former represents the atoms/ions as spheres connected by sticks (bonds), and the latter represents the structure on the basis of coordinated polyhedra with the electropositive atom occupying its centre, and with the highest electronegativity atoms at the vertices. Tetrahedron, octahedron, square pyramid, trigonal prism and cube are the most common polyhedra. This model, proposed by Pauling, is the most widely used one at present for describing crystal structures, as it represents their complexity fairly well and facilitates the visualization of the interstitial positions and their coordination, connectivity, and location. The atom/ion (M) in the centre of the polyhedron indicates the coordination, whereas the number of bonds of the electronegative element (X) specifies the connectivity. For a tetrahedron, MX_4, the coordination of M is 4-fold and X can share 0 (isolated tetrahedron), 1, 2, 3, or 4 vertices. When the tetrahedron shares one vertex, only 3 X atoms counts unity for the polyhedron while the shared atom counts for one half, and the resulting tetrahedron is $MX_{3.5}$. If X is shared by two tetrahedra, a dimer structure,

M_2X_7, is formed. Applying the same methodology to the double shared tetrahedron, we obtain the M_2X_6 structure. Of course, more than one X can be shared, resulting in MX_3, $MX_{2.5}$ (M_2X_5), or MX_2 (*Figure 4*).

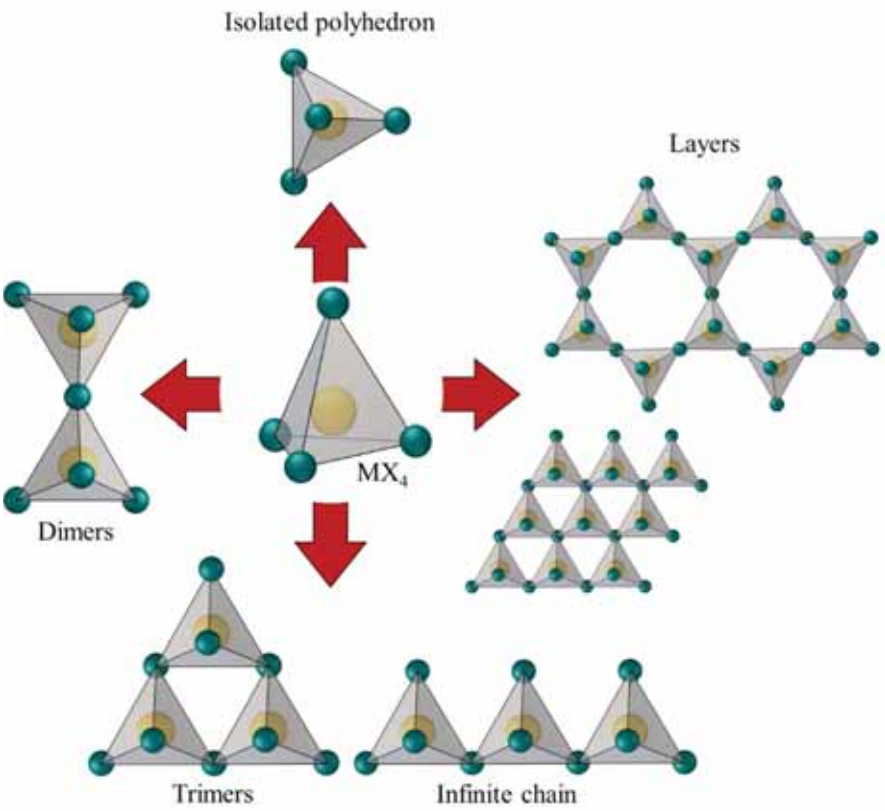

Figure 4. Examples of vertex-sharing tetrahedral organization.

This kind of formula (M_2X_5 for example) is only structural, not chemical. When the Ms are cations and the Xs are anions, as in O_2^-, an electrical neutrality must be achieved. In M_2X_5, 2M has to compensate 10 negative oxygen charges. The virtual coordination for M in this case will be 5-fold M and 5-fold M; 4-fold and 6-fold; 3-fold and 7-fold; or 2-fold and 8-fold. However, as we stipulate a structural formula corresponding to tetrahedra, none of the combinations are possible and the remaining negative charges of $M_2X_5^-$ and $M_2X_5^{2-}$ must be compensated by the introduction of mono or

bivalent cations A^{+}, A^{2+}, or A_2^{+}. So, the chemical composition of this solid will vary until the elements fulfill all the basic requirements.

The variability of the structures is even more important when the polyhedron is an octahedron. In *Figure 5*, some frequent octahedral organizations are presented.

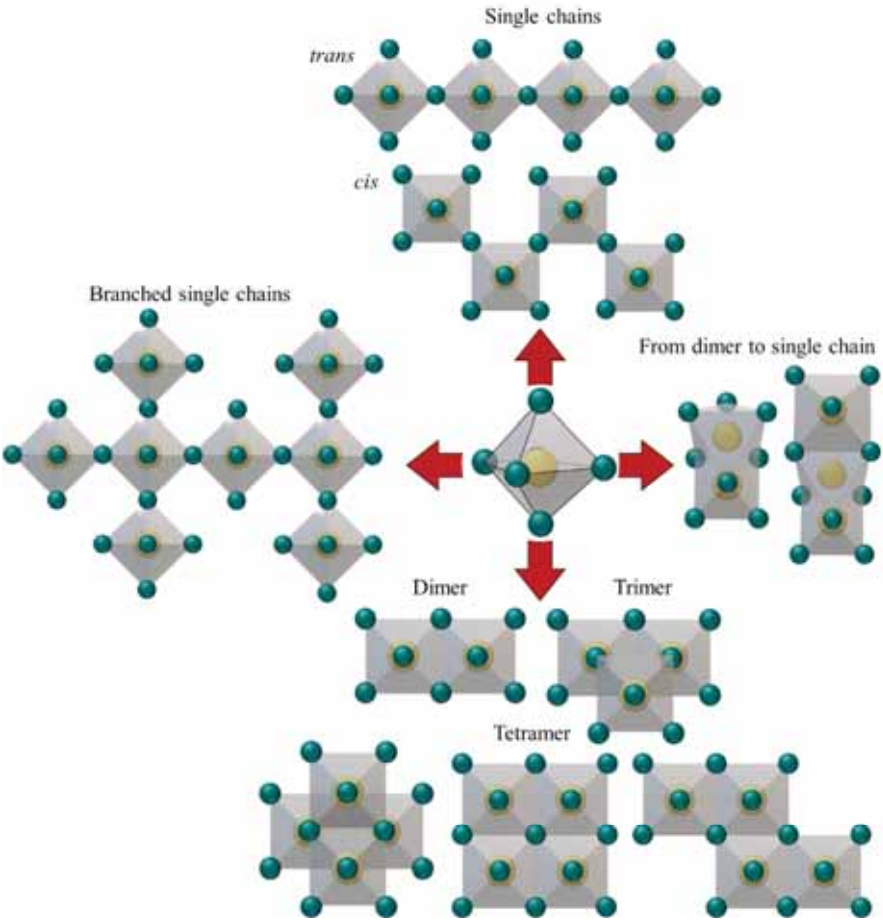

Figure 5. Examples of octahedral organization in structures.

If we go back to the initial TiO_2 anatase structure, Ti^{4+} occupies octahedral sites surrounded by 6 O^{2-}, organized in alternating layers of vertex-sharing and edge-sharing octahedra (*Figure 6*).

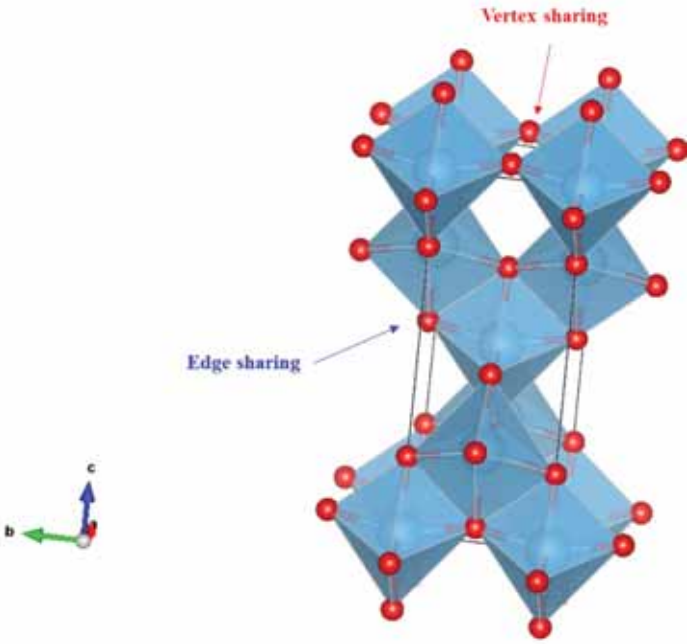

Figure 6. TiO_2 anatase structure organization, layers of edge-sharing and vertex-sharing octahedra.

Prototype structures

There is an alternative way to describe the crystalline structure, i.e. placing the atoms in a prototype close packed structures or in well-defined interstitial sites. Thus, the structures are organized by a pattern of site occupancy with a defined coordination number and type of packing.

The structures are built up from successive layers of atoms (represented by spheres), classified by two types; close-packed layer when an atom contacts with at least six neighbors, and loosely packed layers with four neighboring atoms (*Figure 7*).

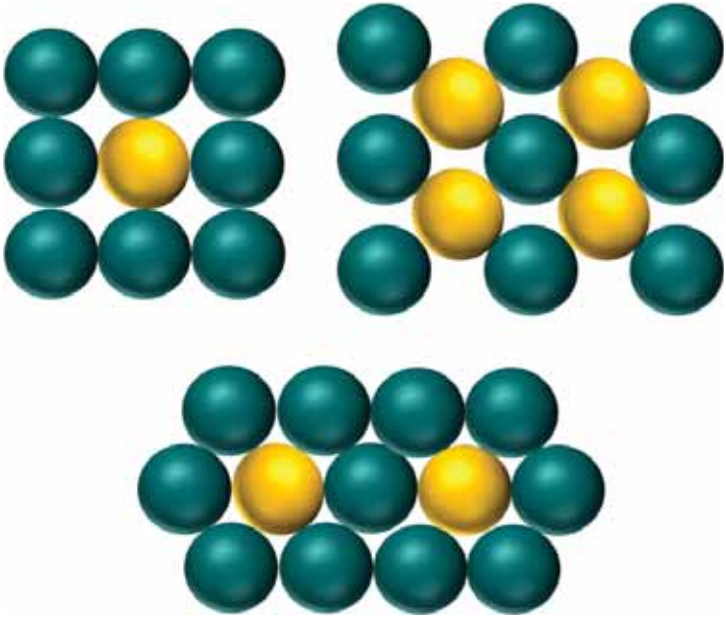

Figure 7. Examples of close and loose packed layers.

All three-dimensional structures arise from the superposition of two or more layers. Some structures are organized by the superposition of close-packed layers in different sequences. If the 2nd close packed layer is positioned exactly over the first layer (A), the *AAAA* stacking order is obtained, resulting in a simple hexagonal structure. However, if the 1st layer, (A), accommodates a 2nd layer, (B) within its voids, and there is a 3rd layer, (A), repeating the 1st layer, the result is *ABABAB* stacking, giving rise to a compact hexagonal structure. When the 3rd layer occupies the voids within the 2nd layer, the result is *ABCABCABC* stacking, and the consequent structure is a face-centered cubic (*fcc*).

Two more structures originate from the assemblage of loosely packed layers: the body-centered cubic structure (*bcc*) with *ABABAB* and the simple cubic structure with an *AAAA* stacking sequence (*Figure 8*).

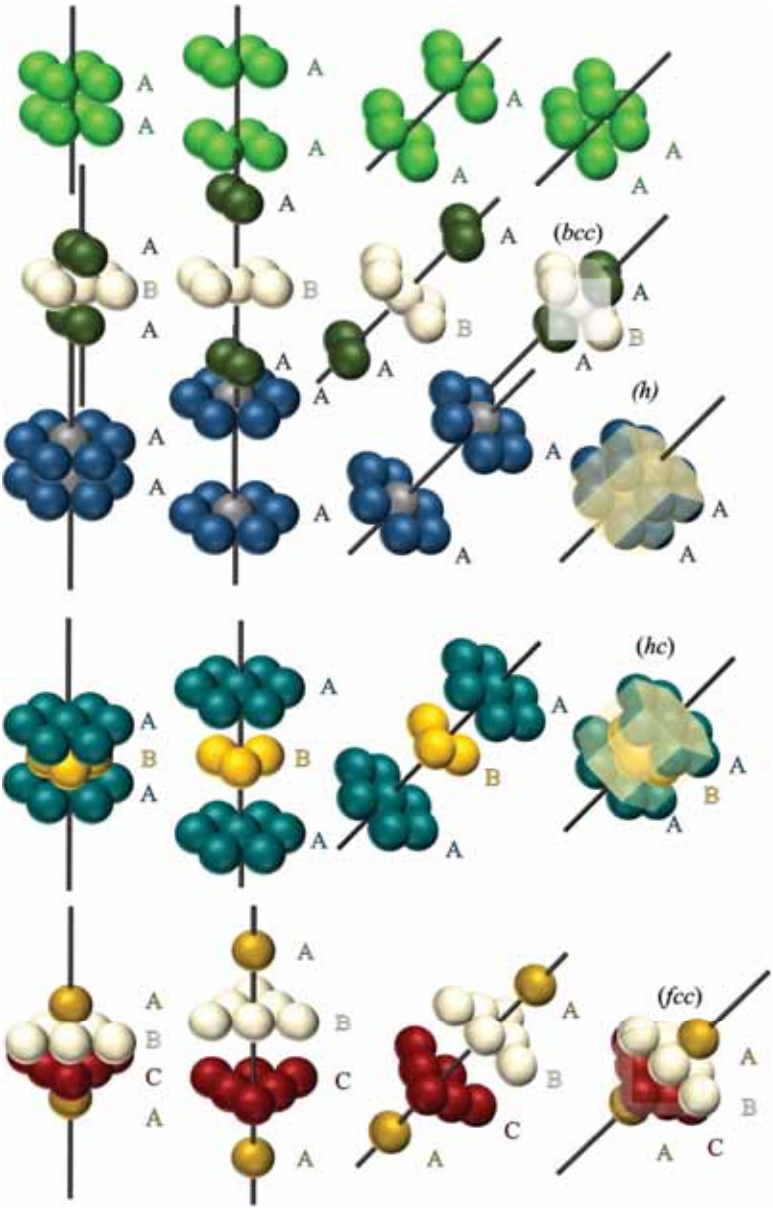
A
A
A

The coordination of the atoms in the structure increases from a simple cubic to an *fcc* arrangement, also affecting the structure packing factor (PF) (*Table 2*), expressed as the fraction of atoms (considered as spheres) occupying the cell.

$$PF\% = \frac{V_{atoms/ions}}{V_{unit\ cell}} = \frac{\#_{atoms} * \frac{4}{3}\pi r_{atom}^3}{V_{unit\ cell}} * 100$$

Table 2. Examples of unit cells with their corresponding coordination numbers and packing factors.

Cell	Coordination number	Packing factor, %
Simple cubic	6	52
Simple Hexagonal	8	60
Body-centered cubic (bcc)	8	68
Body-centered tetragonal	10	69
Face-centered tetragonal	11	72
Face-centered cubic	12	74

In general, close-packed stacking enfolds some empty space between layers, defined as interstitial sites. The type of interstitial site depends on the structure and on the voids available in it. We assume it is a cubic hole whenever eight atoms (spheres) surround a void, while octahedral and tetrahedral sites are created with 6 and 4 atoms (*Figure 9*).

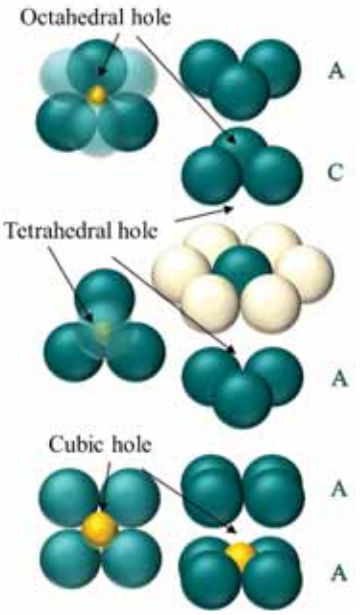

Figure 9. Most frequent interstitial sites.

Some simple calculations will enable us to determine the lattice parameter/atomic (ionic) radius relationship, (a/R): the maximal radius of inserted interstitial atoms and the number of atoms that belong to the structure.

Problem II *Discuss the a/R ratio and packing factor of the fcc structure.*

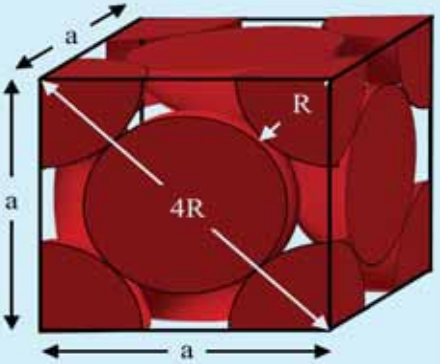

In an *fcc* structure, the atoms are in contact along the face diagonal, and the a/R relation is easily deduced using Pythagoras' theorem in the half face right triangle where $(4R)^2 = a^2 + a^2$, and $a = 2R\sqrt{2}$.

The packing factor is also easy to calculate assuming 4 atoms of radius R belonging to the cell [include the fraction corresponding to the atoms occupying cube vertices, each 1/8, and the fraction corresponding to the atoms in the face centers, each ½; (8* 1/8 +6* ½ =4)]. The packing factor is calculated as the fraction unit cell volume occupied by the atoms

$$PF\% = \frac{4*\frac{4}{3}\pi R^3}{(2R\sqrt{2})^3}*100 = 74\%.$$

In the *fcc* structure, two type of interstices exist, octahedral and tetrahedral. To evaluate the ***r*** of the atom that can be introduced, it must first be in position. The *fcc* structure presents 4 octahedral (O_h) and 8 tetrahedral (T_d) holes. The O_h holes are positioned, one in the center of the cube and 12 more (1/4 fraction to the cube) in the middle of every edge, whereas the tetrahedral sites are formed between 3 face-centered atoms and one of the vertices of the cube, which total 8 in all (*Figure 10*).

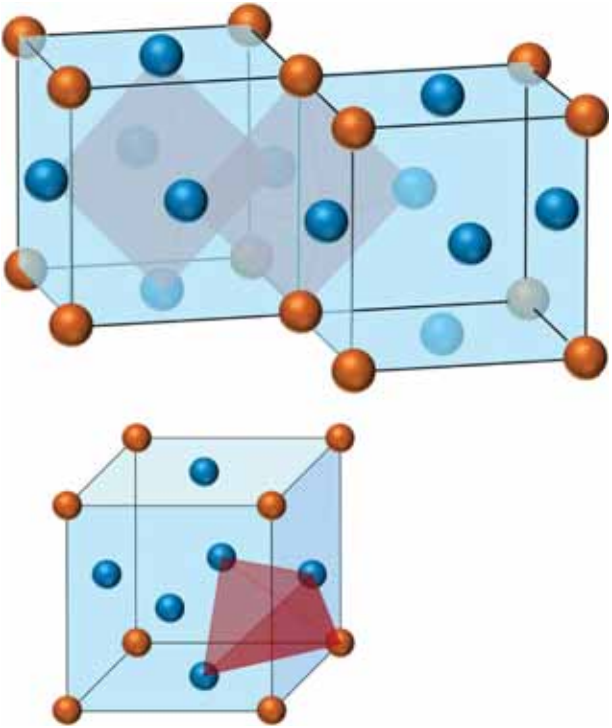

Figure 10. Positions of the octahedral and tetrahedral interstices in an *fcc* lattice.

Problem III. *Determine the r/R ratio (r radius of the inserted atom and R radius of the packing atom) for the octahedral and tetrahedral holes in fcc structures*

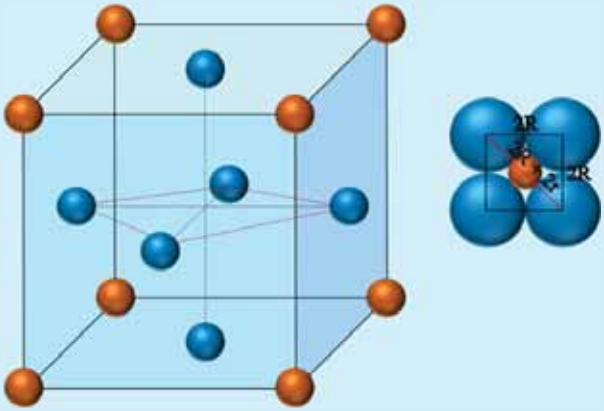

After geometric consideration of the inner cube octahedron and its edges using Pythagoras' theorem $[(2R+2r)^2= (2R)^2 + (2R)^2]$ the **r/R** ratio is found to be **0.414**, **r** being the inserted atom/ion with a lower radius than that of the packing atom/ion R. If r is larger than that value, the spheres of radius, R, are no longer in contact, while for lower values the inserted interstice possess some degree of freedom.

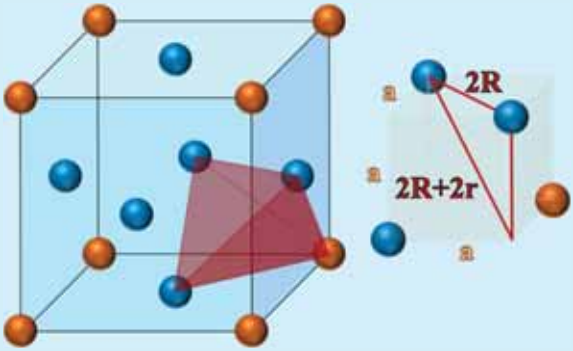

In the tetrahedral hole, the same considerations lead us to apply Pythagoras' theorem twice: once to determine the **a/R** relationship from the upper face of the right triangle, giving $a^2=2R^2$, and then to substitute that value into the red triangle relation, to determine the **r/R** ratio (**r/R = 0.225**).

Problem IV. *Do the same for simple cubic structure and compare the size of the resulting interstices.*

The adatom/ion occupies the interstice in which the repulsions between species of the same charge diminish. The O_h hole could accommodate ions that are larger than the available empty space, provided that the cubic hole dimensions are not attained: a premise that allows us to specify a range of r/R relations at which the structure will remain stable.

$0.225 < (r/R) < 0.414$	Tetrahedral sites
$0.414 < (r/R) < 0.732$	Octahedral sites
$0.732 < (r/R)$	Cubic sites

These relations are useful for predicting the occupation of the interstitial sites in multiple ion structures.

Problem V. *In the ilmenite structure ($FeTiO_3$), the O^{2-} layers are distributed in a distorted hexagonal-like arrangement. Using the ionic radius, predict the occupation of the interstitial sites for Fe^{2+} and Ti^{4+}.*

Ionic radius: O^{2-} 0.140 nm, Fe^{2+} 0.077 nm, Ti^{4+} 0.061 nm, Ca^{2+} 0.1nm

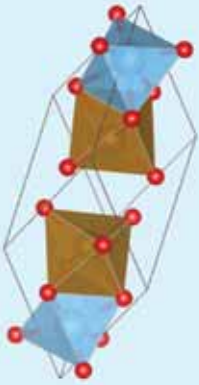

The r/R relation for Fe^{2+}/O^{2-} and Ti^{4+}/O^{2-} are 0.55 and 0.435, respectively, indicating that both cations will occupy the octahedral holes, which are more distorted in the case of Fe^{2+}.

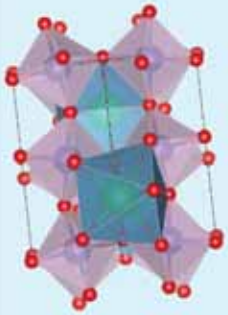

The Ca^{2+}/O^{2-} ratio of $CaTiO_3$ may be expected to increase to 0.72, and the Ca^{2+} participates in eight bonds forming a distorted cube.

The crystal structures can be classified by taking into account packing, composition and filled interstitial sites. An eutactic arrangement is a set of atoms that occupy the close packed positions without entering into contact. The structure is called a superlattice structure when more than one atom

occupies a single eutactic site in a periodic arrangement. In contrast, the interstitial sites may be fully or partially occupied, or empty. The distribution between the packing and interstitial atoms is arbitrary, although electronegative atoms will occupy the close packed positions with greater frequency.

There are many ways to classify solids, nevertheless in this book we will use the classification according to the formula unit MX (M-metal, X anion), starting with the highest ratio and continuing in decreasing order.

M_2X type (M/X =2)

A representative example of this type of structure is Li_2O (*Figure 11*).

Formula unit Li_2O	**Space group $Fm\bar{3}m$ (n.225)**
Cell dimensions	a=4.873 Å
Cell content	4 formula units
Atomic positions	Li in (8c)
	(¼, ¼, ¼), (¼, ¼, ¾); + ***F***
	O in (4a)
	(0, 0, 0); +***F***

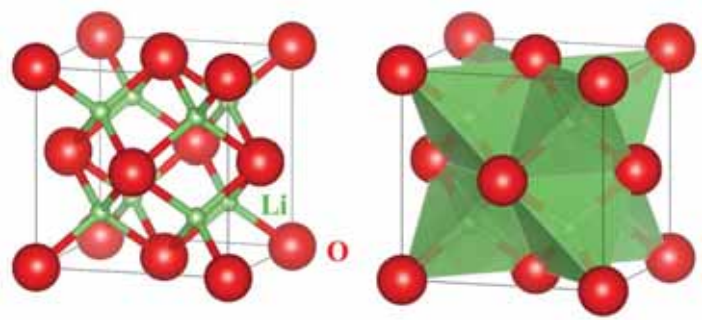

Figure 11. Li_2O structure.

The ion arrangement in this *antifluorite* structure is similar to that of the CaF_2 *fluorite* structure with inverted cation and anion positions. Li^+ occupies the tetrahedral sites and oxide ions form the close packing. Every cation is surrounded by four oxide ions, whereas the oxide ions are neigboring with 8 Li^+ in a 4:8 coordination.

MX type (M/X =1)

Examples of such structures are CsCl, NaCl, NiAs and ZnS.

Formula unit CsCl	**Space group P*m*$\bar{3}$*m* (n.221)**
Cell dimensions	a=4.123 Å
Cell content	1 formula units
Atomic positions	Cs in (1a)
	(0,0,0)
	Cl in (1b)
	(½, ½, ½),

The CsCl cell is formed by two interpenetrating primitive Cs and Cl cells (extended view *Figure 12*) and is equally represented by positioning Cs or Cl in the cubic site. Every cation is surrounded by eight anions and *vice versa* and every ion has a coordination number of 8. This structure type is also found for CsBr, CsI, TlCl, TlI, and NH_4Cl.

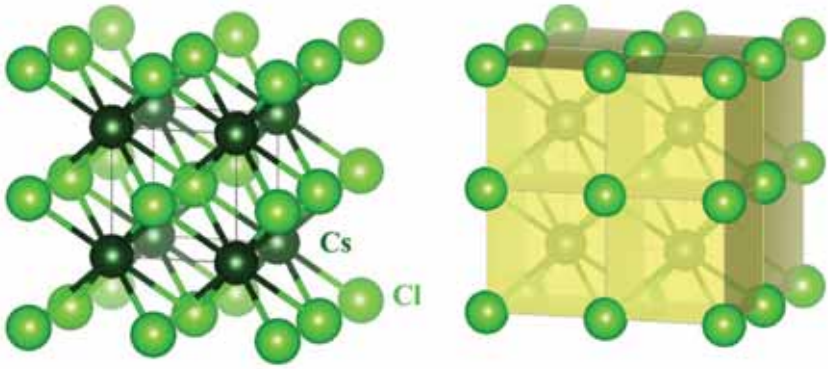

Figure 12. CsCl structure.

The NaCl type structure (also known as rock salt structure) is arranged in *fcc* packing, in such a way that Cl^- and Na^+ occupy all the octahedral sites. As with CsCl, this structure can be described as two interpenetrating *fcc* structures, one of Na^+ and other of Cl^-. Sodium cations are surrounded by six Cl^- neighbors and *vice versa*, giving a coordination of 6:6.

Formula unit NaCl	**Space group P*m*$\bar{3}$*m* (n.225)**
Cell dimensions	a=5.6402 Å
Cell content	4 formula units
Atomic positions	Na in (4 a)
	(0,0,0); +F
	Cl in (1b)
	(½, ½, ½); +F

The structure can be represented as [$NaCl_6$] octahedra sharing edges (*Figure 13*).

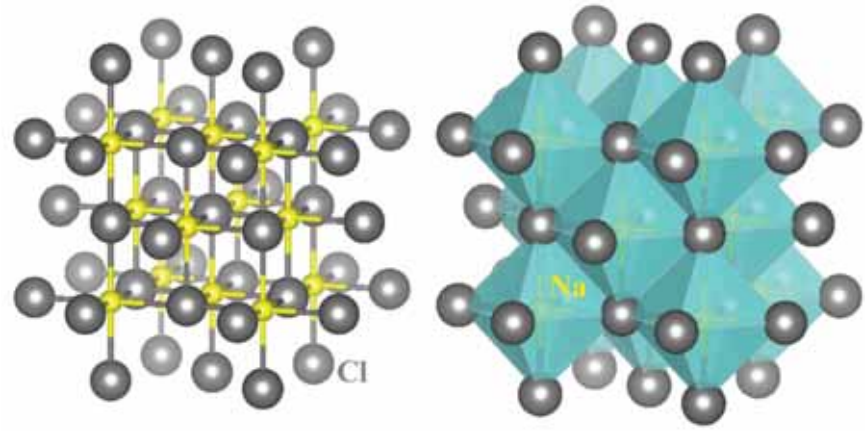

Figure 13. NaCl structure.

The rock salt structure is adopted in an important number of compounds, it is found in most alkali halides, all alkali hydrides, monoxides and sulfides of the alkali earth metals (Ca, Mg, Sr, Ca) etc.

NiAs structure is equivalent to NaCl structure but in compact hexagonal environment.

Formula unit NiAs	**Space group $P6_3mc$ (n.186)**
Cell dimensions	a=3.6 Å, c=5.01 Å
Cell content	2 formula units
Atomic positions	As in (2 a)
	(0,0,0); (0,0, ½)
	Ni in (2 b)
	$\pm(1/3\ 2/3\ 1/4)$

Ni occupies octahedral sites while As packs the hexagonal structure. On that base, the structure can be represented as columns of Ni octahedra edge-sharing in directions *a* and *b* and face-sharing in direction *c*. The As is positioned in a trigonal prismatic environment formed by six Ni atoms (*Figure 14*).

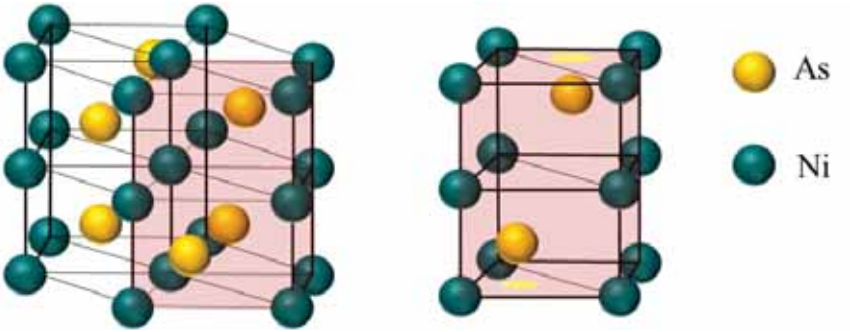

Figure 14. NiAs structure.

ZnS crystallizes in two different structures: compact hexagonal and cubic. Both structures are known as polymorphs, equivalent in stoichiometry, but different in structural arrangements. In the hexagonal structure, known as *wurtzite* (*Figure 15*), the Zn^{2+} occupies half of the interstitials in a hexagonal graphite type network.

Formula unit ZnS wurtzite	**Space group P6$_3$*mc* (n.186)**
Cell dimensions	a=3.81 Å, c=6.23 Å
Cell content	2 formula units
Atomic positions	Zn in (2b)
	$(1/3\ 2/3\ z)\ (1/3\ 2/3\ z+1/2)$ with z=0
	S in (2 b)
	$(1/3\ 2/3\ z)(1/3\ 2/3\ z+1/2)$ with z=3/8

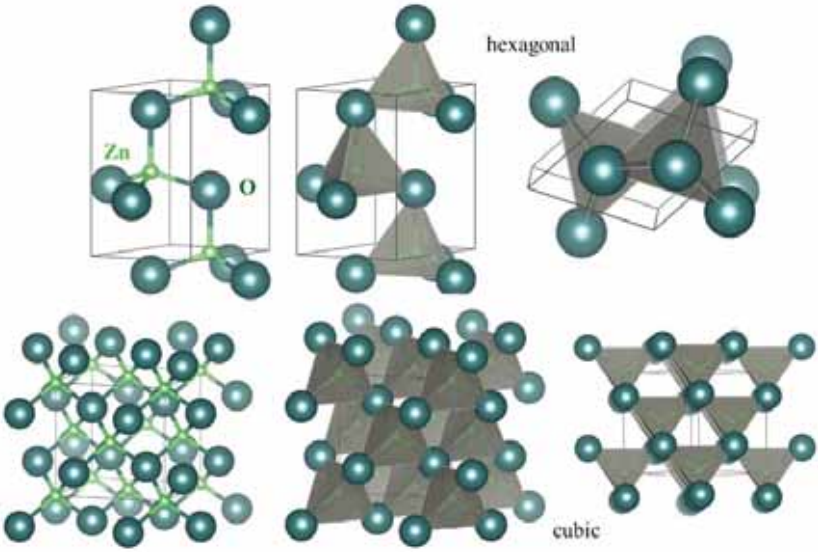

Figure 15. ZnS hexagonal and cubic structures.

The cubic variety (ZnS blende) is represented as *fcc* of S^{2-} with half of the tetrahedral sites occupied by Zn^{2+} in an ordered manner.

Formula unit ZnS blende	**Space group F$\bar{4}$3m (n.186)**
Cell dimensions	a=4.873 Å,
Cell content	4 formula units
Atomic positions	Zn in (4c)
	(¼, ¼, ¼); ***+F***
	S in (4a)
	(0,0,0); ***+F***

For both structures the 3-D network is formed by layers of Zn^{2+} tetrahedra sharing vertices. Both structures differ in the sequence of stacking, three different layers are present for the cubic structure (*Figure 15*) whereas only two are present for wurtzite.

Problem V. *Calculate the bond distances, Zn-S, for both structures and comment on both values.*

M_2X_3 type (M/X = 0.66)

This group is represented by the mineral corundum, α-Al_2O_3.

Formula unit Al_2O_3 corundum	**Space group R$\bar{3}$c (n.167)**
Cell dimensions	a=4.7617 Å, c=12.9947
Cell content	6 formula units
Atomic positions	Al in (12c)
	(x, 0, z), (0, 0 ½ -z) ± ($^2/_3$ $^1/_3$ $^1/_3$)
	O in (18 e)
	(x, 0, ¼) (-x, -x ¼) ± ($^2/_3$ $^1/_3$ $^1/_3$)

The O^{2-} ions are arranged in hexagonal packing where only 2/3 of the octahedral sites are occupied by Al^{3+}. The structure is arranged in zigzag chains of edge-sharing octahedra connecting to the other chains through the vertices. This type of connection generates vacant positions distributed diagonally throughout the structure (*Figure 16*).

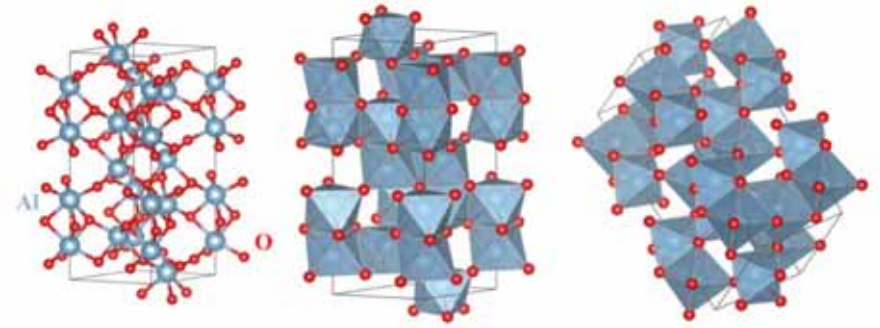

Figure 16. α-Al_2O_3 corundum structure.

This structure is taken as reference for other compounds, such as ilmenite $FeTiO_3$ or $LiNbO_3$, where aliovalent substitution of Al^{3+} ions by Fe^{2+}/Ti^{4+} or Li^{+}/Nb^{5+} occurs. The Fe^{2+}/Ti^{4+} cations are distributed in two different zigzag chains, whereas Li^{+}/Nb^{5+} coexist in the same chain together with the associated vacant positions, *Figure 17*.

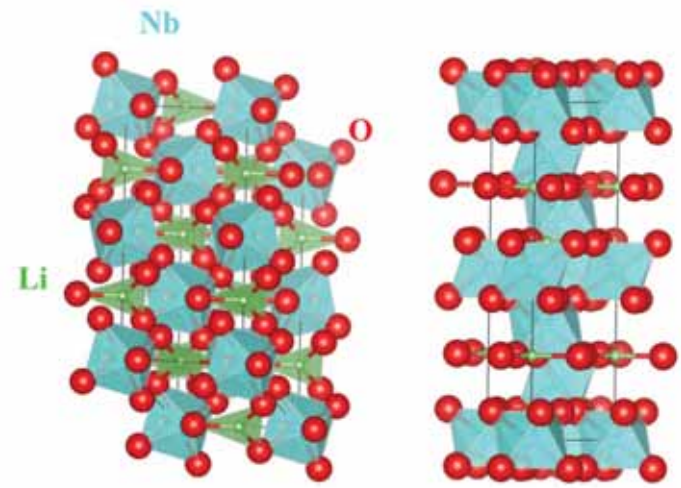

Figure 17. $LiNbO_3$ structure.

MX_2 type (M/X = 0.5)

The TiO_2 and CaF_2 structures belong to this group.

Formula unit CaF_2	**Space group $Fm\bar{3}m$ (n.225)**
Cell dimensions	a=5.4626 Å
Cell content	4 formula units
Atomic positions	Ca in (4a)
	(0,0,0); ***+F***
	F in (8c)
	(¼, ¼, ¼), (¼, ¼, ¾); ***+ F***

The CaF_2 *fluorite* structure is the inverse of Li_2O described above. Ca^{2+} packs the *fcc* structure, while F^- occupies all the tetrahedral sites. F^- and Ca^{2+} coordination is 4 and 8, respectively (*Figure 18*). Instead of tetrahedra, the polyhedral representation suggests that all Ca^{2+} sites occupy cubic interstices.

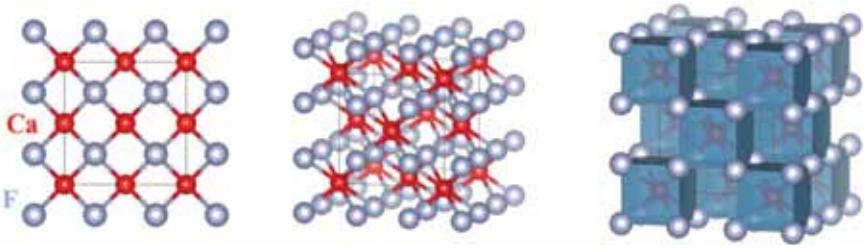

Figure 18. CaF_2 structure.

Other **MX_2** type structures are CdI_2 and $CdCl_2$, both originated from anions in close packing with half of the octahedral sites occupied by cations. The octahedral sites are occupied alternatively one at every two layers forming a lamellar structure with global coordination 6:3 (*Figure 19*).

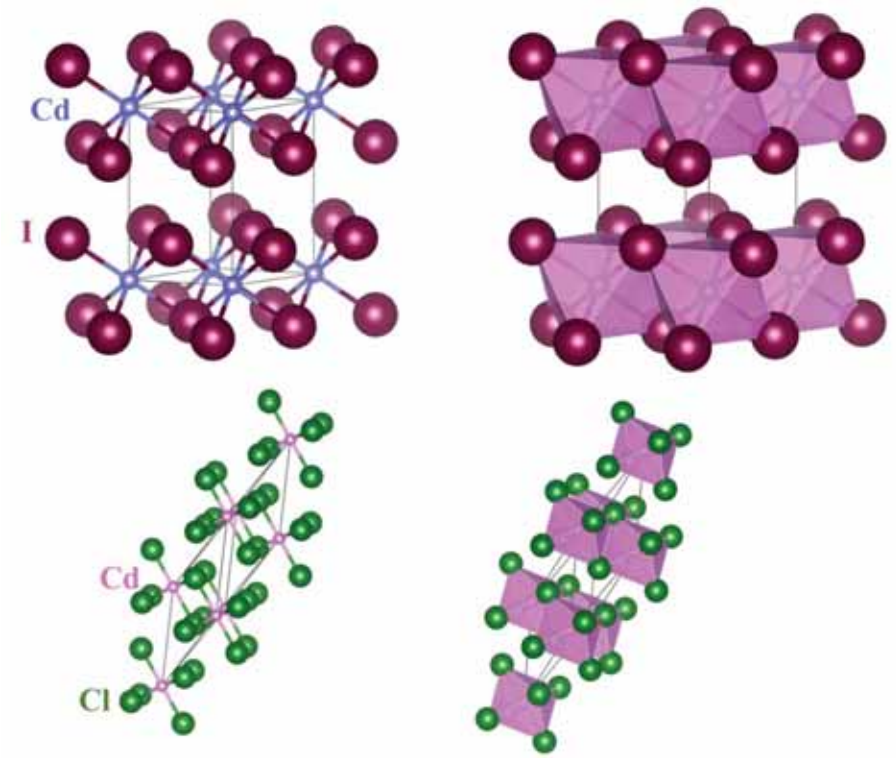

Figure 19. CdI_2 and $CdCl_2$ structures.

M_3X_4 and AM_2X_4 type ($0.75 \geq M/X \leq 0.5$) with A≠M

This is the group of the **spinels** (named after the mineral spinel - $MgAl_2O_4$) with the general formula AM_2X_4, where A corresponds generally to bivalent A^{2+} and M to trivalent M^{3+} ions.

Formula unit $MgAl_2O_4$	**Space group F$d\bar{3}m$ (n.227)**
Cell dimensions	a=8.0800 Å
Cell content	8 formula units
Atomic positions	Mg in (8a)
	*(0,0,0); (¼, ¼, ¼); +**F***
	Al in (16d) *(⅝ ⅝ ⅝)(⅝ ⅞ ⅞) (⅞ ⅝ ⅞)(⅞ ⅞ ⅝); + **F***
	O in (32e) *± (x,x,x) (¼ x, ¼ x, -x) (¼ -x, ¼ x, -x) (¼ -x, ¼ -x, x); +**F*** *x*=⅜

Although a very complex structure, it can be described as *fcc* packing of O^{2-} with A^{2+} occupying the tetrahedral and M^{3+} the octahedral sites (*Figure 20*).

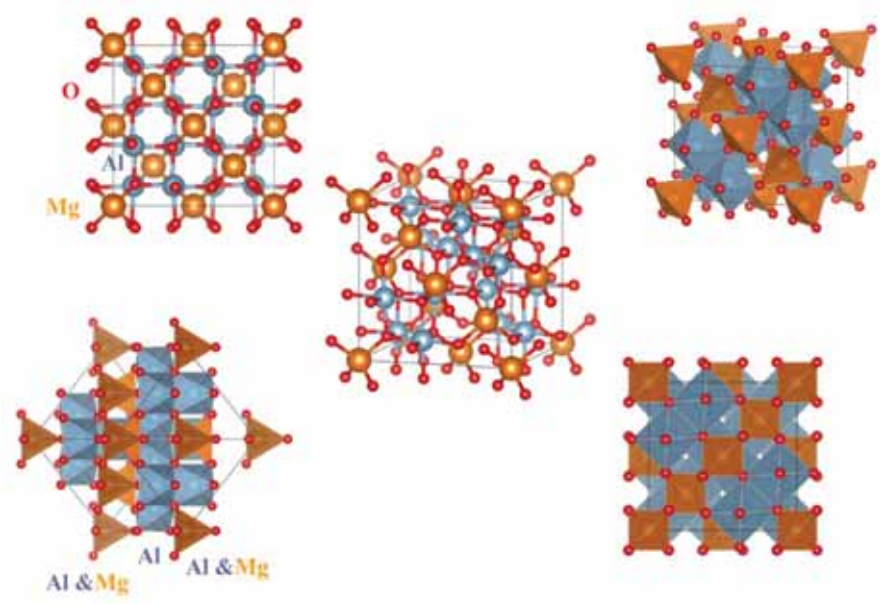

Figure 20. $MgAl_2O_4$ spinel structure.

The AlO subnetwork can be described as an entwined and intersecting structure of linear chains of edge-sharing Al^{3+} octahedra. The tetrahedral Mg^{2+} ions share their vertices with $[AlO_6]$ layers. Two types of layers are formed, one built only of Al^{3+} and the second of mixed Mg^{2+} and Al^{3+} where an octahedron is surrounded by 6 tetrahedra alternatively directed up and down, and each tetrahedra has only three octahedral neighbors. The polyhedral connection occurs via vertex-sharing.

Fe_3O_4 is also within this group with the formula of $Fe^{2+}Fe^{3+}{}_2O_4$. However, for there to be any similarity with the $MgAl_2O_4$ structure, Fe^{3+} and Fe^{2+} must, respectively, occupy the octahedral and tetrahedral sites. Nevertheless, one half of the former is positioned in the tetrahedral sites and the other half, together with Fe^{2+}, in the octahedral sites (*Figure 21*). This spinel is called ***inverse*** spinel to differentiate its structure from that of the ***direct*** spinel $MgAl_2O_4$. The difference in the distribution arises from the differences of cation size.

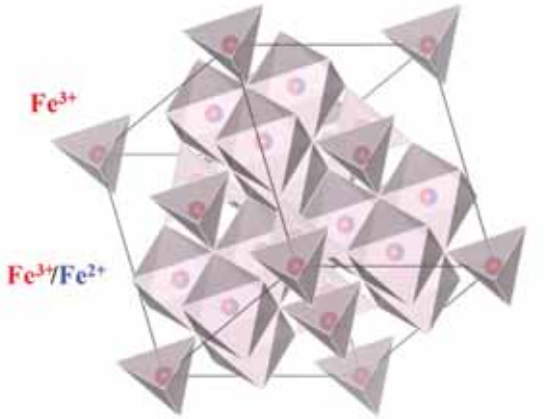

Figure 21. Fe_3O_4 structure.

MX_3 and AMX_3 type (M/X = 0.33)

ReO_3 is representative of this group and presents a very simple structure.

Formula unit ReO_3	**Space group $Pm\bar{3}m$ (n.221)**
Cell dimensions	a=4.013 Å
Cell content	1 formula units
Atomic positions	Re in (1a)
	(0, 0, 0)
	O in (3d)
	(½, 0, 0), (0, ½, 0), (0, 0, ½)

The Re octahedra are positioned on the vertices of a primitive cubic lattice. The 3-D structure originates through vertex-sharing to form a cuboctahedral interstice (*Figure 22*). The possibility of filling this interstice with other cations originates another very important family of compounds, perovskites, with the general formula **AMX_3** (*Figure 22*). The M coordination remains 6-fold, but there are 12 closest neighbors of the A site.

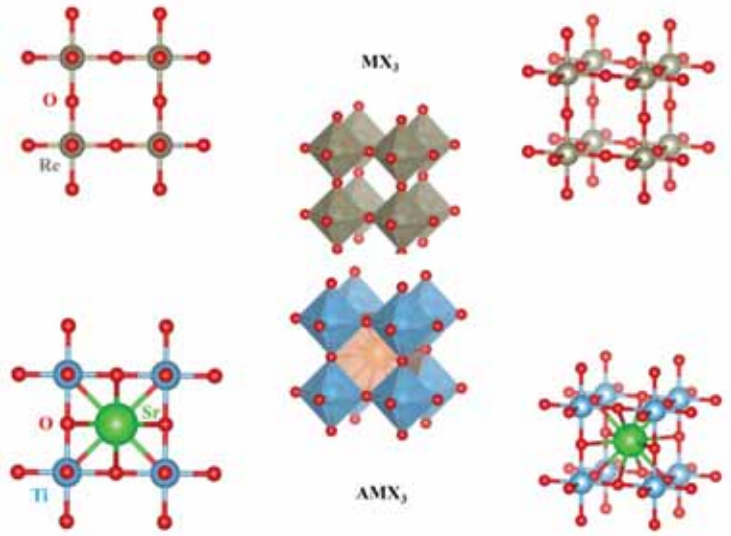

Figure 22. ReO_3 and $SrTiO_3$ structures.

Formula unit $SrTiO_3$ perovskite	**Space group $Pm\bar{3}m$ (n.221)**
Cell dimensions	a=4.013 Å
Cell content	1 formula units
Atomic positions	Ti in (1a)
	(0, 0, 0)
	Sr in (1b)
	(½, ½, ½)
	O in (3d)
	(½, 0, 0), (0, ½, 0), (0, 0, ½)

Despite its structural simplicity, the perovskite family (AMX_3, with X from the chalcogenide or halide families) offers important variety in compositions and properties. Both the A and the M sites accept different combinations of cations of distinct oxidation states, with M oscillating between +2 and +6 always maintaining the electroneutrality. The A site can even remain vacant, like in ReO_3. The X sites also accept the presence of some vacant sites. Nevertheless, not all combinations are possible and they must obey some geometrical requisites. The perovskite structure remains stable under some conditions of cationic size determined by the so-called tolerance factor, ***t***, where:

$$t = \frac{r_A + r_x}{\sqrt{2}(r_M + r_x)}$$

with $0.8 \leq t \leq 1$. When ***t*** is in the range of 0.85 – 0.9, the structure undergoes important modifications. A cations are smaller, and the MX_6 octahedra tilt toward the A site, while the M- X- M bond becomes a zigzag bond, and the size of the A site is reduced. The tilting of the octahedra causes structure distortion to tetragonal, orthorhombic, and even monoclinic symmetry (*Figure 23*). More detailed explication can be found in *Crystal chemistry from basic tools to materials creation* by Gérard Férey. This structure of "breathing" is very important and influences various properties. For example, the Ti is displaced in the $BaTiO_3$ structure from its normal position leading to a polarization of the Ti-O-Ti bond and the ferroelectric properties of this compound.

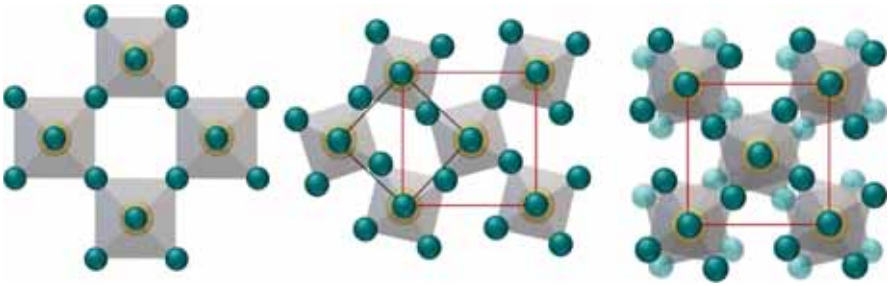

Figure 23. Octahedra tilting for the perovskite structure

Another important group entering the MX_3 type is the pyrochlore structure, an example being the cubic form of FeF_3.

Formula unit FeF_3 pyrochlore	**Space group F$d\bar{3}m$ (n.227)**
Cell dimensions	a=8.08 Å
Cell content	16 formula units
Atomic positions	Fe in (16c)
	(0, 0, 0), (¾, ¼, ½) (¼, ½, ¾) (½, ¾, ¼); +*F*
	F in (*48f*)
	± (x, 1/8, 1/8); **+ *F***; + *additional position from the crystallographic table*

The structure is organized in layers of vertex-sharing Fe octahedra. Two different layers are formed, one denser (*Figure 24* red framed layer) and other lighter enclosing individually connecting octahedra. The denser layer corresponds to a hexagonal packing of vertex-sharing octahedra, similar to the distribution found in Magneli bronzes.

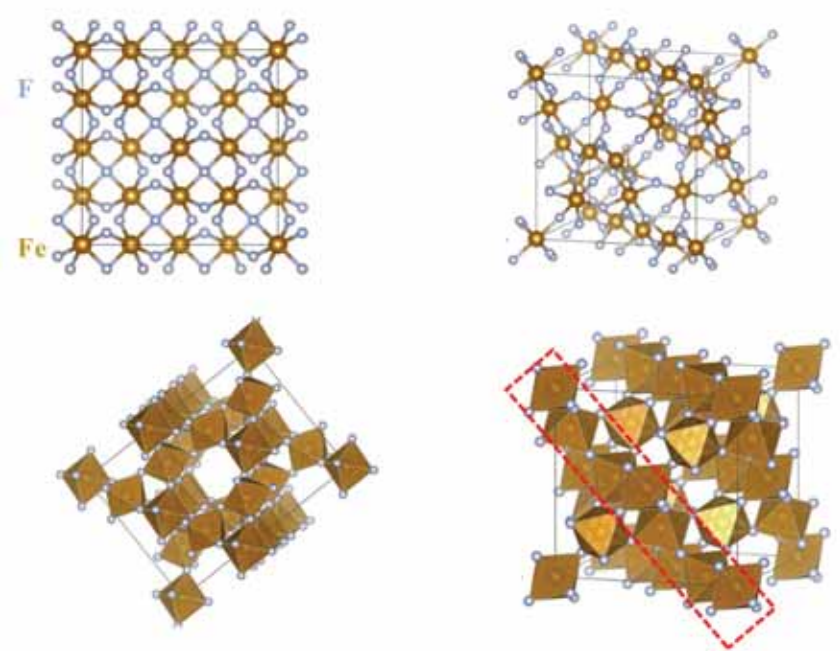

Figure 24. FeF_3 pyrochlore structure.

We can generate the structure, regardless of its complexity, by following some consecutive steps:

i) Draw the structure's projection on a selected plane or along a certain direction.
ii) Determine the coordination of atoms/ions, bond lengths, and angles.
iii) Determine the coordination number and polyhedral organization of the structure.
iv) Generate the final structure, regardless of whether the prototype structures are considered.

Books Used and References

Crystal chemistry from basic tools to materials creation, Gérard Férey, World Scientific, Singapore, 2017

Structure and bonding in crystalline materials, Gregory Rohrer, Cambridge University Press, Cambridge UK 2004.

Solid state chemistry and its application 2nd edition, Anthony R. West, 2014 John Wiley & Sons, Ltd, UK.

All structures are generated with Vesta software using the CIF from http://www.crystallography.net/cod/index.php and the references listed below in the same order as they appear in this chapter:

TiO_2 anatase: M. Rezaee, K. Mousavi, M. Seyyed; K. H. Liu, The role of brookite in mechanical activation of anatase-to-rutile transformation of nanocrystalline TiO_2: An XRD and Raman spectroscopy investigation, *CrystEngComm,* 2011, 13, 5055.

TiO_2 rutile: E. P. Meagher, G. A. Lager, Polyhedral thermal expansion in the TiO_2 polymorphs: Refinement of the crystal structure of rutile and brookite at high temperature Sample at 300 degrees C, *The Canadian Mineralogist*, 1979, 17, 77-85

$FeTiO_3$: T. F. W. Barth, E. Posnjak, The Crystal Structure of Ilmenite, *Zeitschrift fuer Kristallographie, Kristallgeometrie, Kristallphysik, Kristallchemie* (-144,1977), 1934, 88, 265-270.

$CaTiO_3$: A. Beran, E. Libowitzky, T. Armbruster, A single-crystal infrared spectroscopic and X-ray diffraction study of untwinned San Benito perovskite containing O H groups, *Canadian Mineralogist*, 1996, 34, 803-809

Li_2O: T. W. D. Farley, W. Hayes, S. Hull, M. T. Hutchings, M. Vrtis, Investigation of thermally induced Li^+ ion disorder in Li_2O using neutron diffraction, *Journal of Physics: Condensed Matter*, 1991, 3, 4761-4781

CsCl: R. W. G. Wyckoff, Second edition. Interscience Publishers, New York, New York, Crystal Structures, 1963, 1, 85-237

NaCl: K. Wang, R. R. Reeber, Thermal expansion of alkali halides at high pressure: NaCl as an example Sample: T = 50 K, Molar volume = 26.35 cc/mol, *Physics and Chemistry of Minerals*, 1996, 23, 354-360

NiAs: N. Alsen, Roentgenographische Untersuchungen der Kristallstrukturen von Magnetkies, Breithauptit, Pentlandit, Millerit und verwandten Verbindungen, *Geologiska Foereningens i Stockholm Foerhandlingar*, 1925, 47, 19-73.

ZnS: G. Aminoff, Untersuchungen ueber die kristallstrukturen von wurtzit und rotnickelkies, *Zeitschrift fur Kristallographie*, 1923, 58, 203-219; E. A. Jumpertz, Electron-density distribution in zinc blende, *Zeitschrift für Elektrochemie und angewandte physikalische Chemie*, 1955, 59, 419-425

Al_2O_3: V. G. Tsirelson, M. Y. Antipin, R. G. Gerr, R. P. Ozerov, Y. T. Struchkov, Ruby structure peculiarities derived from X-ray data. Localization of chromium atoms and electron deformation density, *Physica Status Solidi, Sectio A: Applied Research*, 1985, 87, 425-433.

$LiNbO_3$: A.V. Postnikov, V. Caciuc, G. Borstel, Structure optimization and frozen phonons in $LiNbO_3$, *Journal of Physics and Chemistry of Solids*, 2000, 61, 295-299.

CaF_2: S. Speziale, T. S. Duffy, Single-crystal elastic constants of fluorite (CaF_2) to 9.3 GPa Sample: P = 0 GPa, *Physics and Chemistry of Minerals*, 2002, 29, 465-472.

CdI_2: Y.M. de Haan, Structure refinements, thermal motion and Madelung constants of cadmium iodide- and cadmium hydroxide-type layer structures, National *Bureau of Standards (U.S.), Special Publication*, 1969, 1969, 233-236

$CdCl_2$: L. Pauling, J. L. Hoard, The crystal structure of cadmium chloride, *Zeitschrift fuer Kristallographie, Kristallgeometrie, Kristallphysik, Kristallchemie* (144,1977), 1930, 74, 546-551.

$MgAl_2O_4$: T. Yamanaka, Thermal movement of atoms in the spinel structure. *Kobutsugaku Zasshi, Journal of the Mineralogical Society of Japan)*, 1983, 16, 221-231

Fe_3O_4: V. Montoro, Miscibilita fra gli ossidi salini di ferro e di manganese, *Gazzetta Chimica Italiana*, 1938, 68, 728-733.

ReO_3: K. Meisel, Rheniumtrioxyd III. Mitteilung: Ueber die Kristallstruktur des Rhenium trioxyds, *Zeitschrift fuer Anorganische und Allgemeine Chemie*, 1932, 207, 121-128.

$SrTiO_3$: N. B. Mahmood, E. K. Al-Shakarchi, B. Elouadi, Three Techniques Used to Produce $BaTiO_3$ Fine Powder, *Journal of Modern Physics*, 2011, 2, 1420-1428.

FeF_3: R. De Pape, G. Ferey, A new form of FeF_3 with the pyrochlore structure: Soft chemistry, crystal structure, thermal transitions and structural correlations with the other forms of FeF_3, *Materials Research Bulletin*, 1986, 21, 971-978

CHAPTER 3

BONDING IN SOLIDS

Any fool can know. The point is to understand
Albert Einstein (1879-1955)

Introduction

Almost all substances will, once sufficiently cooled, form a solid phase. In most cases, they will form one or more crystalline phases that, in the simplest possible way, may be described as atoms, molecules, or ions arranged in a regular repeating 3D array. The understanding of bonding between the elements in the solid is mandatory, in order to gather knowledge on the properties of these arrangements of atoms and how their properties are modified by changes within their structure. The whole spectrum of bond types may be found in solids and frequently more than one type may account for bond description. However, we may distinguish between solids with all the bonds of the same nature and solids without all the bonds of the same nature; *e.g.*, both ionic and covalent bonding may, for example, be identified in Li_2SO_4 where lithium (Li^+) cations and sulphate ($SO_4^=$) anions are linked together through ionic bonding, whereas sulphur and oxygen are covalently bonded. We may add graphite to this category of compounds that combines covalent and van der Waals forces or CdI_2, which is ionic/covalent/van der Waals. However, it must be noted that there is no such thing as pure ionic or pure covalent bonding. For instance, bonding in Gallium Arsenide (GaAs) can be considered partially covalent and partially ionic. The extent of the ionic character of the bond is called ionicity and depends on the electronegativity difference of the constituent elements. The greater the difference, the greater the ionic character of the bond. In that sense, covalent and ionic bonding are two extreme cases of the same type of phenomenon.

Solid compounds containing transitional metals may result in greater bonding complexities. Let us consider TiC, TiN, and TiO cases. *Ab initio* calculations have shown us that the electron densities around the non-metal atoms increase as the non-metal electronegativity (C < N < O) increases and

that they are spherically symmetrical. However, the electron density around titanium is a long way off the spherical symmetry that indicates directionality. The bonding may be described by the interaction of the *2p* orbitals of the non-metal atom and the t_{2g} orbitals of Ti, π character. In this bond, the electron densities around the Ti atom decrease from TiC to TiO, while those around the non-metal atoms increase, demonstrating a trend in the *ionicity* from TiC to TiO. On the other hand, a reversed tendency is observed for the bonds between the non-metal *2p* orbitals and the Ti e_{2g} orbitals, σ character, which indicates a decrease in the covalent bonding from TiC to TiO. In addition, *d-d* bonds, σ character, are observed. Charge density calculations clearly establish the contribution of covalent, ionic, and metallic bonding in these three Ti compounds. Schematic bonding types between Ti *d* orbitals and non-metal *p* orbitals are shown in *Figure 1*.

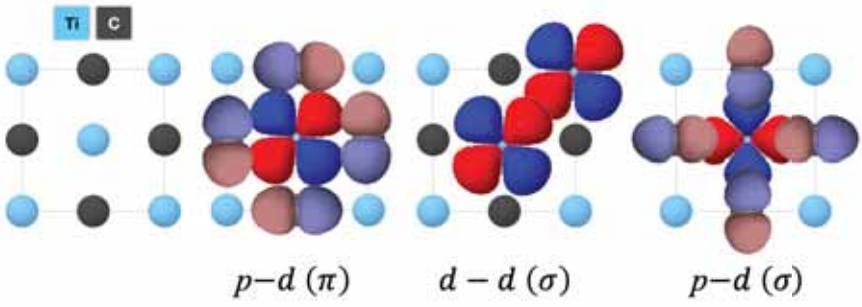

Figure 1. Bonding types in TiX solids (X = C, N, O) showing Ti *d* and non-metal *p* orbitals in the (100) plane of a rock-salt structure.

Classification of solids

Many of the characteristic properties of solids are a function of their electronic properties. A bond-based classification is useful to understand structure-property relations in solids. Four types of solids are readily defined in terms of bonding: ionic, covalent, metallic, and molecular bonds, with examples given in *Table 2*. However, the reader must be aware that real solids may exhibit features of more than one type of bonding.

Table 2. Classes of simple solids

Class	Units	Characteristics	Example
Molecular	Molecules, atoms or molecules held together by hydrogen bonding	Soft, low melting, low sublimation energy and insulating	Xe N_2 benzene (C_6H_6) $HgCl_2$ SiC H_2O (ice) HF
Ionic	Positive and negative ions	Brittle, insulating and fairly high melting point	NaCl MgO CaF_2 LiF
Covalent	Atoms (bonded to one another)	Hard, high melting point and non-conducting (when pure)	C(diamond) P SiO_2 GaAs
Metallic	Positive ions embedded in an electron 'gas'	High conductivity	Na Fe Cu

Molecular solids

These solids may be composed of atoms and molecules, with no permanent dipole moment (Xe, CO_2, CH_4, C_6H_6), that condense forming crystals held together by relatively weak van-der-Waals' forces. Electron motion in each molecule causes fluctuating dipoles that interact within the molecular groups, known as London dispersion forces. This dispersion energy can be expressed as:

$$E_{disp} = -\frac{3}{16\pi\varepsilon_0} \cdot \frac{h\omega_0\alpha^2}{d^6}$$

where, α is the electronic polarizability, and $h\omega_0$ is an average of electronic excitation energy. A close look at this expression reveals that these non-directional forces rapidly decrease with the distance and the main structural driving force is therefore the closest possible packing of the molecules. The $HgCl_2$ unit cell and a projection in the [100] direction is shown in *Figure 2*.

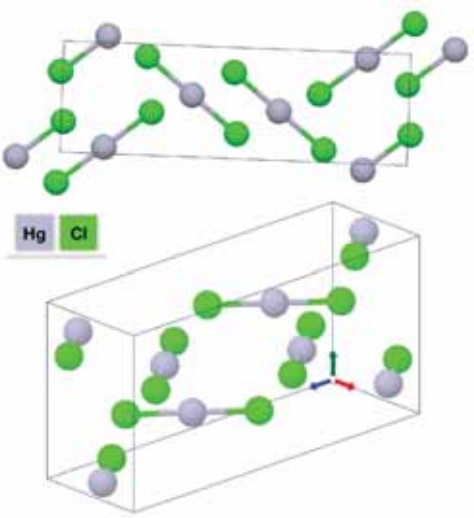

Figure 2. Molecular lattices, $HgCl_2$ view in the [100] direction and 3D view of the primitive cell.

As this molecule is far from presenting spherical symmetry, the close packing is not so obvious. The projection shows the molecules aligned along two different orientations that permit the closest possible packing, avoiding the repulsive interactions of the chlorine atoms. The closest packing, for atoms or molecules with a spherical symmetry, *e.g.*, Ar, as in metals, is evident, as shown in *Figure 3*.

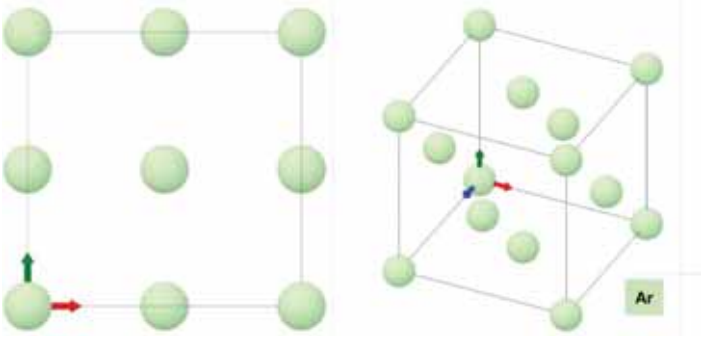

Figure 3. Molecular lattices, Ar view in the [100] direction and 3D view of the conventional cell.

Polar molecules show some directionality on packing as a result of the electrostatic interaction between their opposite charged ends. Hydrogen bonding may be an extreme case of these interacting dipoles.

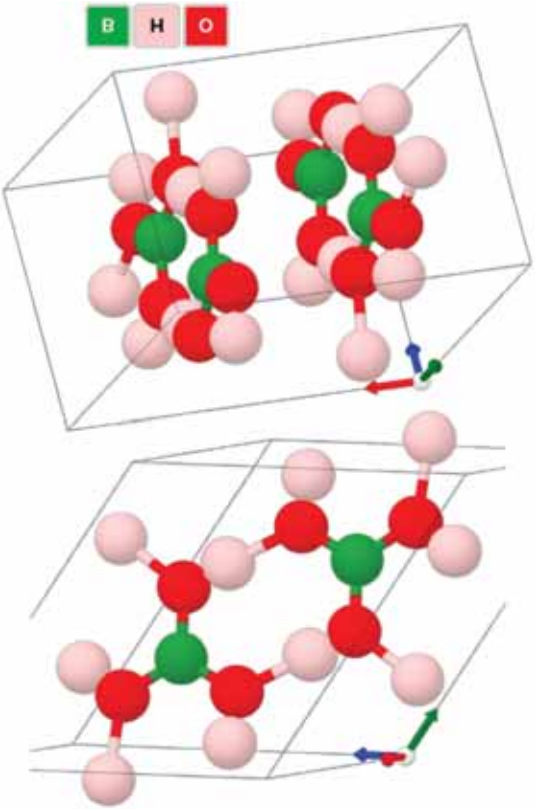

Figure 4. Molecular lattices, Structure of the triclinic polymorph of $B(OH)_3$ showing the H-bonded ring-like features.

The electronegativity difference between hydrogen and most electronegative elements such as fluorine or oxygen, among others, is because the bonding electrons are unevenly displaced and the hydrogen atoms acquire positive charges. In addition to the electrostatic character of the bond, the X-H orbital of an antibonding character may accept charge from the lone pair of a neighbouring molecule and stabilize it, thus providing a strong directional character to the bond. *Figure 4* exemplifies the structure of H-bonded solids. The 2D structure of boric acid, H_3BO_3, that crystallizes in the triclinic $P\bar{1}$

space group, consists of two H_3BO_3 sheets oriented in the [100] direction. In these sheets, boron atoms are bonded in a trigonal planar geometry to three oxygen atoms and hydrogen atoms are bonded in a distorted linear geometry to two oxygen atoms one shorter (1.00 Å) and one longer (1.65 Å). In the same way as boron, oxygen is bonded in a distorted trigonal planar geometry, although it is bonded both to boron and to hydrogen. Although the d^6 dependence of the interaction energy might suggest short-range van-der-Waals' interactions restricted to the first coordination sphere of atoms and molecules, it must be noted that the correct evaluation of the properties of these solids must take into consideration interactions far away from this first coordination sphere. For instance, if long-range interactions are not considered, errors of ~3% in the calculated equilibrium distance of solid noble gases are observed, which can increase to ~30% upon estimating the cohesive energy and close to 40%, on the analysis of the mechanical properties of the solids.

Ionic solids

Ionic crystals are held together by electrostatic interactions between ions formed between electropositive and electronegative elements after electron transfer from the former to the latter. The energy of the interaction between the ions having z_1 and z_2 charges is given by Coulomb's law:

$$E_{coul} = \frac{z_1 z_2 e^2}{4\pi\varepsilon_0 d}$$

The distance dependence (d^{-1}) makes this a long-range force and, therefore, ion interactions must be computed by considering not only the first coordination sphere. The binding of an ion depends on its coulombic interaction with all successive shells of other ions. A simple way of computing the cohesive energy is the summation of the interaction energy between all possible ion pairs within the solid.

The pair potential for the ionic bond should consider the coulombic potential, the Lennard-Jones potential of the interaction of two close shell atoms and, of course, the energies required to form the ions: ionization potential (I_M) and electron affinity (E_X). For example, an M-X pair:

$$E_{pair} = I_M - E_X + \frac{z_1 z_2 e^2}{4\pi\varepsilon_0 d} + 4\varepsilon\left(\frac{\sigma^{12}}{d} - \frac{\sigma^6}{d}\right)$$

where, σ can be taken as the diameter of the hard sphere atom and ε is the depth of the energy well. The total electrostatic contribution to the energy

must be obtained, considering all interactions between all ions. As described in earlier chapters, a crystal is formed by a collection of points that constitute a Bravais lattice and a basis is formed by *n* atoms, containing n_i atoms, having a z_i charge, of the *i-th* type. The total number of atoms in the crystal is nN_L, where N_L is the total number of lattice sites. The distance between the n_i atoms in the basis is defined by the $\overrightarrow{r_{ij}}$ vectors and the distance between lattice points by the $\overrightarrow{R_k}$ vector. The distance between any two points in the crystal is defined by a combination of lattice vectors and $\overrightarrow{r_{ij}}$ vectors, *Figure 5*, All the interatomic separations can, in order to simplify the calculations, be written in terms of a dimensionless parameter, ρ, and the shorter interatomic spacing, d_0.

$$\left|\overrightarrow{R_k} + \overrightarrow{r_{ij}}\right| = \rho\left(\overrightarrow{R_k} + \overrightarrow{r_{ij}}\right)d_0$$

The sum of all the electrostatic interactions in the crystal can be expressed as:

$$E_c = N_L \frac{ke^2}{d_0}\left\{\frac{1}{2}\sum_{1=1}^{n}\left[\sum_{\substack{j=1\\ j\neq i}}^{n}\frac{z_i z_j}{\rho\left(\overrightarrow{r_{ij}}\right)} + \sum_{k=1}^{N_L-1}\left[\sum_{j=1}^{n}\frac{z_i z_j}{\rho\left(\overrightarrow{R_k} + \overrightarrow{r_{ij}}\right)}\right]\right]\right\}$$

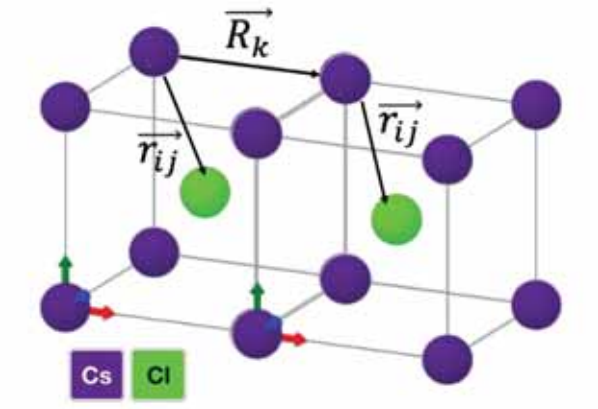

Figure 5. Position vectors. The distance between the n_i atoms at the base is defined by the $\overrightarrow{r_{ij}}$ vectors and the distance between lattice points is defined by the $\overrightarrow{R_k}$ vector.

The distance between any two points in the crystal is defined by a combination of lattice vectors and $\overrightarrow{r_{ij}}$ vectors.

This formulation, known as the Madelung constant, *A*, places a term in brackets that only depends on the structure type and the charges of the ions forming the crystal. It is therefore a constant value for each crystal structure.

The electrostatic forces favour ionic structures surrounded by ions of opposite charges and ions with the highest possible Madelung constant, which are typically those with the highest coordination number.

Covalent solids

Atoms are held together, in crystals showing no appreciable differences in electronegativities (diamond, silicon), by covalent bonds that are essentially the same as those found in small molecules. The 3D covalent structures that are generated may be considered as giant molecules bonded by overlapping atomic orbitals that share electrons, one from each atom, where the stabilization energy results in a net lowering of energy. The structure of these covalent lattices is, therefore, governed by the same criteria as those in molecules. Group IV elements have atoms with tetrahedral links to each other, as in the diamond like structure. Group V presents pyramidal tri-coordinated structures and elements of Group VI are two-coordinated, *Figure 6*.

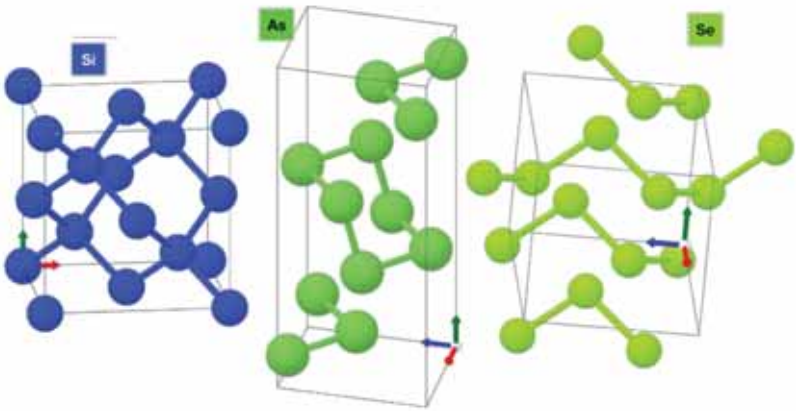

Figure 6. Covalent solids. Conventional cells of cubic, orthorhombic and trigonal polymorphs of Si As and Se, respectively.

The $Fd\bar{3}m$ silicon polymorph is a 3D arrangement of Si atoms bonded to four equivalent Si atoms at 2.37 Å by corner-sharing [$SiSi_4$] tetrahedra. As within small molecules, the coordination number decreases as the number of valence shell electrons increases, which can be seen in the orthorhombic polymorph, space group, $Cmce$, of elemental arsenic. It presents a 2D layered structure oriented in the [010] direction with As atoms bonded, in a distorted trigonal non-coplanar geometry, to three As atoms at 2.51 Å. The six valence electrons of Group VI elements may result in two-coordinated Se atoms, as within α-Se that crystallizes in the trigonal $P3_121$ space group. This 1D structure consists of Se ribbons oriented in the [001] direction with selenium atoms bonds between two equivalent Se atoms at 2.40 Å in a water-like geometry. These examples exemplify the directional character of covalent bonds in giant molecules that, as in small molecules, tends to achieve close shell electron configurations by sharing electrons. Binary AB compounds accounting for eight valence shell electrons, as in C-C bonds, formed by elements of groups IIIA and VA or IIA and VIA (the so-called III-V and II-VI compounds) may also present diamond-like structures, in the same way as some I-VII compounds such as copper (I) halides (*Figure 7*). The AB basis of these Bravais lattices results in less symmetric structures, such as $F\bar{4}3m$ space groups, formed by corner-sharing [AB_4] tetrahedra. Moreover, the electronegativity difference in these binary compounds results in bonds that are not entirely covalent.

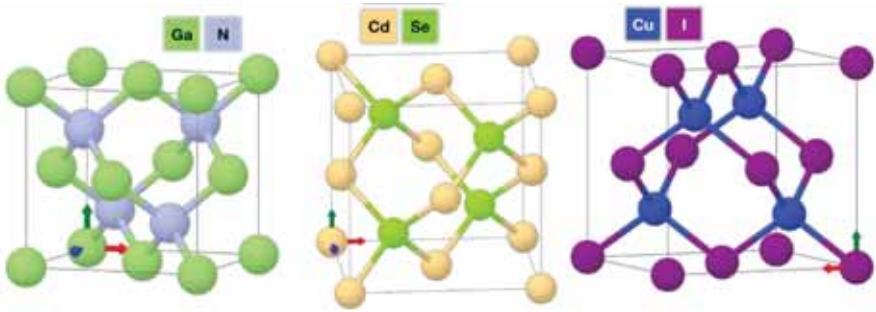

Figure 7. Covalent AB solids. Conventional cells of diamond like structures of III-V (GaN), II-VI (CdSe) and I-VII (CuI).

Different approaches have been reported for estimating the fractional ionic character or *ionicity* of the AB bonds, from the modified Pauling expression for $A_NB_{8\sim N}$ crystals, accounting for the fact that an atom forms more than one bond and the number of bonds that are formed will not always be equal to its formal valence:

$$f_i^c = 1 - \frac{N}{M} + \frac{N}{M}\left\{1 - e^{-\frac{(\chi_A - \chi_B)^2}{4}}\right\}$$

where, M is the number of nearest neighbours and χ_A and χ_B are the Pauling electronegativities of the elements A and B, and $f_i^c = 0$ for $\chi_A = \chi_B$ and $f_i^c = 1$ for $\chi_A \ll \chi_B$. This *ionicity* scale enables us to explain the structure of many binary solids. However, this scale fails to explain the polymorphism of some of these binary compounds.

Phillips proposed an *ionicity* scale based on the compounds band gap. It is assumed that the average band gap, E_g, is a combination of the ionic, E_i, and covalent, E_h, contributions, and the iconicity parameter is a function of those contributions:

$$E_g^2 = E_h^2 + E_i^2$$
$$f_1^c = \frac{E_i^2}{E_g^2}$$

The values of the covalent and ionic contributions are obtained from *d*, the bond length, and from ε_0, the static dielectric constant, respectively. Structural predictions for AB solids with tetrahedral (diamond or wurzite) and octahedral coordination (rock salt) may be established with this scale.

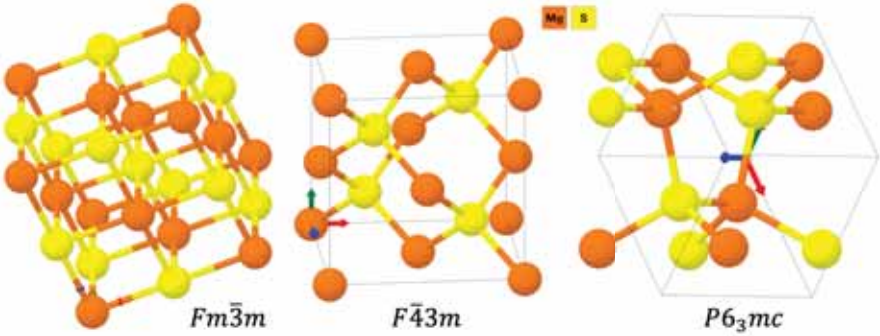

Figure 8. Structures of the rock-salt, diamond and wurzite polymorphs of MgS.

According to the model of Phillips, a tetrahedral coordination for all crystals with $f_1^c < 0.785$ is frequent, whether diamond or wurzite, while a six-fold coordination (rock-salt structure) is frequent in crystals with $f_1^c \geq 0.785$. A clear example of this approach is solid MgS with $f_1^c = 0.786$. MgS may crystallize in either rock salt, diamond or wurzite type structures, *Figure 8*,

as the borderline value of its f_1^c value might suggest to us. Note that the formation energy of the three polymorphs ranges from -1.760 eV for the most stable (rock-salt) structure to -1.744 eV for the least stable (diamond) structure, a difference of less than 2% that accounts for the borderline character of MgS.

Metallic solids

The structure of metals is characterized by close-packing with high coordination numbers, typically ranging between 8 and 12. Metals are significantly different from non-metallic solids both in structure and physical properties. High thermal and electrical conductivities are distinctive features of metals, which indicate the presence of free electrons moving within the crystal that neither account for ionic nor for covalent type bonding. The absence of electronegativity differences in pure metals and localized bonds between atoms must therefore be discarded. Working with metallic alloys, Brewer demonstrated that empty *p* and *d* orbitals of the less electronegative metals "*provide a sink for paired electrons*" of the more electronegative sort. This generalized acid-base principle of the interaction between metals explains that metals to the right of Zr stabilize the BCC structure with the d^3s configuration compared to the HCP d^2sp configuration. On the basis of this concept, it is important to remark that electrons are not free to occupy all physical space and are restricted to orbital volumes and directions. As in close-packed environments, a metal atom will interact with two or more nuclei and delocalized sharing of electrons between many atoms will occur continuously throughout the solid.

A generalized view of chemical bonding: electronic energy levels and bonds

The description of bonding, from a chemical point of view, is based on the orbital concept. In many electron systems, it is mandatory to approximate the solutions of Schrödinger's equation for the hydrogen atom. Without relativistic corrections, the Hamilton operator, $\mathcal{H}$, for a system containing many nuclei and electrons -*i.e.*, a given molecule or some crystalline material of any complexity- can be written as follows:

$$\mathcal{H} = -\sum_{i=1}^{N}\frac{h^2}{2m}\nabla_i^2 - \sum_{A=1}^{M}\frac{h^2}{2M_A}\nabla_A^2 - \frac{1}{4\pi\varepsilon_0}\left(\sum_{1=1}^{N}\sum_{A=1}^{M}\frac{z_A e^2}{r_{iA}} - \sum_{1=1}^{N}\sum_{j>1}^{N}\frac{e^2}{r_{ij}} - \sum_{A=1}^{M}\sum_{B>A}^{M}\frac{z_A z_B e^2}{R_{AB}}\right)$$

The first two terms of the operator account for the kinetic energies of the N electrons with masses m and the M nuclei with masses M_A, which are not expected to be at fixed positions. Coulombic attraction between electrons and the charged nuclei (z_A), and once separated (r_{iA}), is the third term, and the fourth and fifth terms account for electron repulsion between electrons and nuclei, respectively. By eliminating time-dependent phenomena, and fixing the positions of the nuclei (due to their lower velocities and larger masses compared to the electrons), without considering the electrostatic interaction between the nuclei, the operator can be rewritten as:

$$\mathcal{H} = -\sum_{i=1}^{N} \frac{1}{2}\nabla_i^2 - \sum_{1=1}^{N}\sum_{A=1}^{M} \frac{z_A}{r_{iA}} + \sum_{1=1}^{N}\sum_{j>1}^{N} \frac{1}{r_{ij}}$$

By using *ab initio* or "first principles" methods no further simplifications are necessary, but there are many methods that discard part of this equation or introduce experimentally available information.

We may initially ignore the electron–electron interaction, in order to understand the behavior of solids and molecules. The many-electron wave function, Ψ , solving the Hamiltonian operator may be approximated by a set of "one-electron" functions, ψ_i, called molecular orbitals (MOs). The latter is approximated as a linear combination of the basic functions of isolated atoms, which gives rise to the linear combination of atomic orbitals (LCAO).

$$\psi_i(r) = \sum_{A} \sum_{\substack{\mu=1 \\ \mu \in A}}^{n} c_{\mu i}\phi_{\mu i}(r)$$

where, the basis functions, $\phi_{\mu i}(r)$, are atomic orbitals located on the A atoms. To solve the equation, we have to find the *best* wave functions that will be characterized by the *lowest* energy, which gives rise to the variational principle.

$$E = \frac{\int \Psi^* \mathcal{H} \Psi d\tau}{\int \Psi^* \Psi d\tau} \geq E_0 \qquad \text{(equation 12)}$$

In this equation, the many electron wave function may be replaced by the linear combination of one-electron functions (atomic orbitals) and the mixing coefficients, $c_{\mu i}$, optimized to minimize the energy value. Note that

a differentiation with respect to the coefficients, $c_{\mu i}$, is equivalent to applying the variational principle.

$$E_i = \frac{\sum_A \sum_B \sum_\mu \sum_\nu c^*_{\mu i} c_{\nu i} \int \phi_\mu \mathcal{H} \phi_\nu d\tau}{\sum_A \sum_B \sum_\mu \sum_\nu c^*_{\mu i} c_{\nu i} \int \phi_\mu \phi_\nu d\tau} = \frac{\sum_A \sum_B \sum_\mu \sum_\nu c^*_{\mu i} c_{\nu i} H_{\mu\nu}}{\sum_A \sum_B \sum_\mu \sum_\nu c^*_{\mu i} c_{\nu i} S_{\mu\nu}}$$

where, $H_{\mu\nu}$ stands for $\int \phi_\mu \mathcal{H} \phi_\nu d\tau$ and $S_{\mu\nu}$ for $\int \phi_\mu \phi_\nu d\tau$.

In $\mu = \nu$, $\int \phi_\mu \mathcal{H} \phi_\mu d\tau = H_{\mu\mu}$ stands for the Coulomb integral and may be assimilated to the Valence-State Ionization Energy (VSIE) of the μ orbital, for $\mu \neq \nu$, where $H_{\mu\nu}$ is the resonance, or hopping integral. It accounts for the interaction between the orbitals μ and ν. As the orbitals are orthonormal, the overlap integral, $S_{\mu\nu} = \int \phi_\mu \phi_\nu d\tau$, is equal to 1 for $\mu = \nu$, and $0 < S_{\mu\nu} < 1$, for $\mu \neq \nu$. A parametric determination of valence-state ionization energies may be found in the referenced work of Basch *et al*.

By differentiating the energy function with respect to the different $c_{\mu i}$, the following set of secular equations is obtained:

$$\begin{gathered}
(H_{11} - E_i S_{11}) c_{1i} + (H_{12} - E_i S_{12}) c_{2i} + \cdots + (H_{1n} - E_i S_{1n}) c_{ni} = 0 \\
(H_{21} - E_i S_{21}) c_{1i} + (H_{22} - E_i S_{22}) c_{2i} + \cdots + (H_{2n} - E_i S_{2n}) c_{ni} = 0 \\
\cdots\cdots\cdots\cdots\cdots\cdots\cdots\cdots\cdots\cdots\cdots\cdots\cdots\cdots\cdots\cdots\cdots\cdots\cdots\cdots\cdots\cdots \\
(H_{n1} - E_i S_{n1}) c_{1i} + (H_{n2} - E_i S_{n2}) c_{2i} + \cdots + (H_{nn} - E_i S_{nn}) c_{ni} = 0
\end{gathered}$$

The secular determinant has to be set at zero, in order to solve this set of equations:

$$\begin{vmatrix}
H_{11} - E_i S_{11} & H_{12} - E_i S_{12} & \cdots\cdots & H_{1n} - E_i S_{1n} \\
H_{21} - E_i S_{21} & H_{22} - E_i S_{22} & \cdots\cdots & H_{2n} - E_i S_{2n} \\
\cdots\cdots & \cdots\cdots & \cdots\cdots & \cdots\cdots \\
H_{n1} - E_i S_{n1} & H_{n2} - E_i S_{n2} & \cdots\cdots & H_{nn} - E_i S_{nn}
\end{vmatrix} = 0$$

The result of these calculations is a set of n E_i values and all the mixing coefficients $c_{\mu i}$. The method leads to a general quantum-chemical solution of the Schrödinger equation without specifying the Hamiltonian operator.

It is applied here to the simplest possible molecule, H_2^+. The LCAO approach for the molecular orbitals should be:

$$\psi_i = c_1 \phi_1 + c_2 \phi_2$$

where, ϕ is the 1s atomic orbital of hydrogen, so the secular determinant is:

$$\begin{vmatrix} H_{11} - E_i & H_{12} - E_i S_{12} \\ H_{21} - E_i S_{21} & H_{22} - E_i \end{vmatrix} = 0$$

The normalization condition of the atomic orbitals sets the S_{11} and S_{22} integrals as equal to 1, and the symmetry of the H_2^+ molecule requires that $H_{11} = H_{22}$, $H_{12} = H_{21}$and $S_{12} = S_{21}$:

$$(H_{11} - E_i)^2 = (H_{12} - E_i S_{12})^2$$

The solutions to this equation are as follows:

$$E_+ = \frac{H_{11}+H_{12}}{1+S_{12}}; \qquad E_- = \frac{H_{11}-H_{12}}{1-S_{12}}$$

in which, the bonding solution, E_+, is of lower energy while the antibonding solution, E_-, is of higher energy. The composition and the shape of the molecular orbitals are calculated by using the two values that obtain the mixing coefficients, $c_{\mu i}$.

$$\psi_+ = \frac{\phi_1+\phi_2}{\sqrt{2(1+S_{12})}}; \qquad \psi_- = \frac{\phi_1-\phi_2}{\sqrt{2(1-S_{12})}}$$

The normalization constant, $\sqrt{2}$, ensures that any of these orbitals may accommodate two electrons.

As stated above, H_{11} is the energy of the 1s atomic orbital and H_{12} is the interaction energy between the two neighbouring, overlapping orbitals with an overlap integral of S_{12}. It is evident, from the solution to the secular determinant, that the E_+ and the E_- solutions are not symmetrical, as the destabilization of the antibonding molecular orbital (E_- solution) is larger than the stabilization of the bonding molecular orbital (E_+ solution), since the denominator in the bonding solution is larger than the positive overlap integral, S_{12}, *Figure 9.*

However, the overlap integral between neighbouring atomic orbitals in the popular Hückel approximation is further simplified and taken for calculations equal to zero[1], and the Coulomb and resonance integrals are parametrized as α and β, respectively. This approach results in equally stabilized and destabilized molecular orbitals, as follows:

[1] Note that neighboring atoms must overlap for bonding, zero is simply the value taken for simplifying the calculations.

$$E_+ = \alpha + \beta; \qquad E_- = \alpha - \beta$$

Figure 9 presents schematic drawings for the solutions of the H_2 problem considering the overlap integral (a) and using the Hückel approach (b).

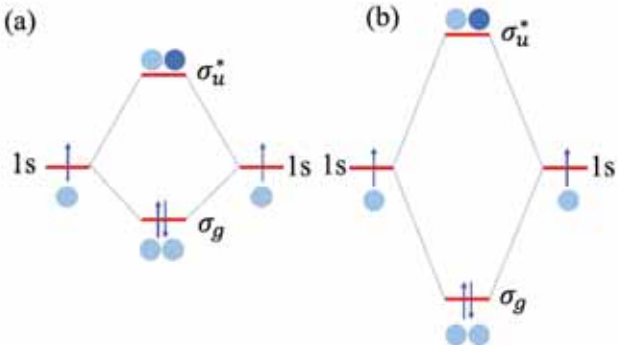

Figure 9. Schematic drawings for the solutions to the H_2 problem considering the overlap integral (a) and using the Hückel approach (b).

The low-energy solution is labelled as σ_g. Since the orbital–orbital overlap coincides with the molecular axis, the interaction is of the σ type, and the *g* (German *gerade* ≡ even) indicates that a mathematical inversion of the left atomic orbital will generate the right atomic orbital with no change in their plus/minus signs. The high-energy solution is labelled, σ_u^*, where the *u* label (German *ungerade* ≡ odd) reflects the plus/minus relationship of the left/right AOs upon inversion, and the asterisk designates an antibonding interaction. The plus/minus signs in *Figure 9* are symbolized by the colour intensity, while the sizes of the atomic orbitals are indicative of the mixing coefficients.[2]

Molecular orbitals can be built in a similar way for atoms heavier than hydrogen from the atomic orbitals of these elements. The bonding interaction depends on the degree of overlap between atomic orbitals the effective combination of which is a function of:

- Energy (should be similar);

[2] Recall that in the Hückel approach, the overlap is neglected, which is by far its main weakness, although its mathematical advantages mean that weakness is tolerated.

- Symmetry, (atomic orbitals must belong to the same symmetry class);
- Overlap extent (a function of the interatomic separation).

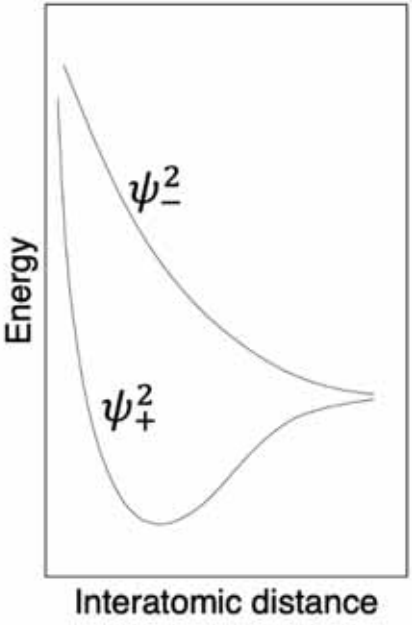

Figure 10. Variation of the energy of bonding and antibonding orbitals as a function of the interatomic distance.

Both, the magnitude of overlap, S_{12}, and resonance, $H_{12} = \beta$, integrals are closely related and are a function of the interatomic separation. The overlap integral value continuously increases as the A-B separation decreases and, therefore, the energy of the bonding orbital decreases while the antibonding orbital energy increases. However, the electrostatic repulsion between the nuclei increases as the separation decreases and the nuclei move closer, counteracting any stabilization due to the formation of the chemical bond. The balance between these two effects results in an energy minimum that determines the A-B equilibrium distance, *Figure 10*.

It is important to realize that this mathematical approach is not exclusively limited to the analysis of pure covalent bonds. If charge transfer occurs due to the difference in electronegativities between the two elements of the AB bond, *e.g.*, LiH, then the molecular orbital scheme is constructed from the

Li *2s* and the H *1s* orbitals, *Figure 11*. The energy of the H *1s* orbital is more negative than the Li *2s* orbital, has higher electronegativity, and its contribution is more important for the bonding molecular orbital. Therefore, the shared pair of electrons is more a part of hydrogen than it is of lithium, which is schematized by the relative size of atomic orbitals within the molecular orbitals.

On dealing with heavier elements, it is common to distinguish between core and valence atomic orbitals. The core orbitals are composed of the previously filled shells. As core atomic orbitals are of a smaller radius than the valence ones, the extent of the overlap in molecules is negligible, so they will have little or no influence on bonding; thus, the molecular orbital function is only built of valence shell atomic orbitals. In polyatomic molecules, the number of valence shell atomic orbitals and the geometry of the molecule requires the use of symmetry to deal with the solution to the wave function. The total number of molecular orbitals that are formed, which may be bonding, antibonding, or non-bonding, is the same as the number of valence atomic orbitals used to make them.

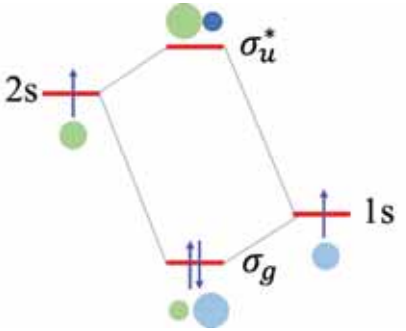

Figure 11. Sketch of the general solution of the LiH problem. The plus/minus signs are symbolized by the colour intensity, while the sizes of the atomic orbitals are indicative of the mixing coefficients

Energy levels of linear and cyclic polyenes

Let us consider open-chain conjugated molecules as examples of polyatomic molecules. The π system of ethylene is formed by the combination of *p* orbitals perpendicular to the molecular plane. A (2x2) secular determinant derived in exactly the same way as for the H_2 molecule, but using C *2p* instead of H *1s* orbitals, results in two energy levels and can

be applied to solve this system, using the Hückel approach, as schematized in *Figure 12*.

By moving to the propenyl molecule a (3x3) secular determinant is obtained

$$\begin{vmatrix} \alpha - E & \beta & 0 \\ \beta & \alpha - E & \beta \\ 0 & \beta & \alpha - E \end{vmatrix} = 0$$

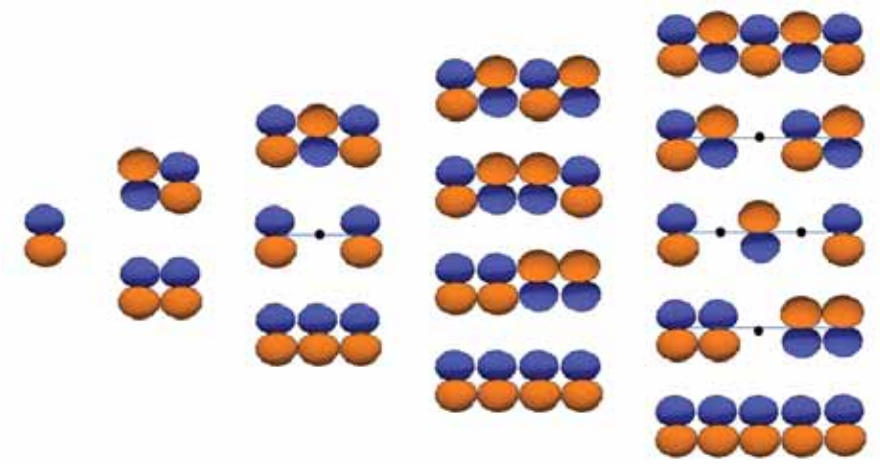

Figure 12. Carbon *2p* LCAO for developing the π system of conjugated polyenes.

Recall that in the simple Hückel approach, only the overlap between neighbouring atoms is considered. The energy solutions for this determinant are:

$$E_1 = \alpha + \beta\sqrt{2}; \qquad E_2 = \alpha; \qquad E_3 = \alpha - \beta\sqrt{2}$$

These three solutions can be generalized as:

$$E_i = \alpha + 2\beta cos\frac{i\pi}{(n+1)}; \qquad i = 1,2,3,\ldots,n$$

And, for the coefficients of the molecular orbital functions, $c_{\mu i}$.

$$c_{\mu i} = \frac{2}{(n+1)} sin\frac{i\mu\pi}{(n+1)}$$

The three wavefunctions for the propenyl molecule, are:

$$\psi_1 = \sqrt{2}\phi_1 + 2\phi_2 + \sqrt{2}\phi_3$$
$$\psi_2 = \phi_1 + \phi_3$$
$$\psi_3 = \sqrt{2}\phi_1 - 2\phi_2 + \sqrt{2}\phi_3$$

which are normalized as:

$$\psi_1 = \frac{1}{2}\left(\phi_1 + \sqrt{2}\phi_2 + \phi_3\right)$$
$$\psi_2 = \frac{1}{\sqrt{2}}\left(\phi_1 + \phi_3\right)$$
$$\psi_3 = \frac{1}{2}\left(\phi_1 - \sqrt{2}\phi_2 + \phi_3\right)$$

The number of nodes in the wavefunction increases as the energy increases, which can be seen in *Figure 12*. By increasing the number of atoms of the linear chain, the number of molecular orbitals increases and at the limit, for $n = \infty$, the energy of the molecular orbital at the bottom will be $E_i = \alpha + 2\beta$, with all the coefficients in phase, while the one at the top has the maximum number of possible nodes, $n - 1$, and $E_i = \alpha - 2\beta$.

As can be seen in *Figure 12*, the molecular orbitals that are formed extend over all atoms in the polyene chain, emphasizing the delocalized nature of molecular orbital theory. The energy difference between two consecutive molecular orbitals is for $N = \infty$:

$$E_i - E_{i+1} = \left(\alpha + 2\beta cos\frac{i\pi}{(n+1)}\right) - \left(\alpha + 2\beta cos\frac{(i+1)\pi}{(n+1)}\right)$$

$$\lim_{n\to\infty} E_i - E_{i+1} = 2\beta\left[cos\frac{i\pi}{(n+1)} - cos\frac{(i+1)\pi}{(n+1)}\right] = 0$$

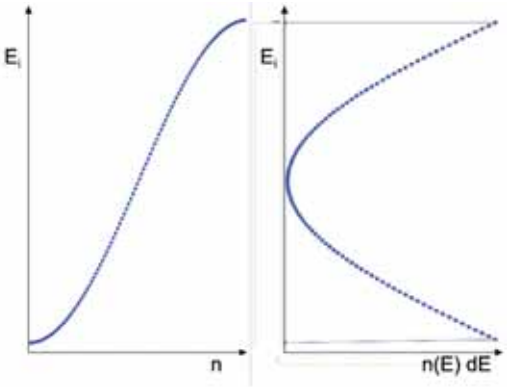

Figure 13. Energy levels for the π system of a C100 polyene molecule as a function of the number of nodes, and density of energy levels of the same system as a function of energy

Therefore, the molecular orbitals of large molecules are numerous and closely spaced in terms of their energy. *Figure 13* is a representation of the different energy levels of a hypothetical polyene molecule containing one hundred equally spaced Carbon atoms as a function of the number of nodes of the molecular orbital. Note that even through an energy continuum, the molecular orbitals are not equally spaced in energy, in such a way that the energy separation between the different molecular orbitals is smaller for the orbitals at the extremes of the sequence. Therefore, the number of molecular orbitals for a range of energy, E, to $E + \Delta E$ is higher for the lowest and highest energy levels than for the medium energy range.

Recalling the solid problem, the molecules may simply be considered giant molecules and the orbitals, called crystal orbitals, extend all over the solid. The large number of atoms in any crystal direction yields energy levels that hardly differ in energy and, for most purposes, it may be assumed that they form continuous bands of energy levels. It may be schematized in the well-known picture of boxes representing bands as a combination of atomic orbitals, *Figure 14*. As stated above, the molecular orbitals within these continuous bands are not evenly distributed over all the energies with energy regions that have a higher concentration of orbitals than others, leading to the concept of ***density of states***, *N(E)*, that may be defined as the number of energy levels, crystal orbitals, per unit volume, within the energy range E to $E + \Delta E$. Moreover, as the number of atomic orbitals increases, the number of bands increases, and these bands may or may not overlap. If there are energy regions where the bands do not overlap, an energy gap appears between the bands, such as the one shown in *Figure 14*.

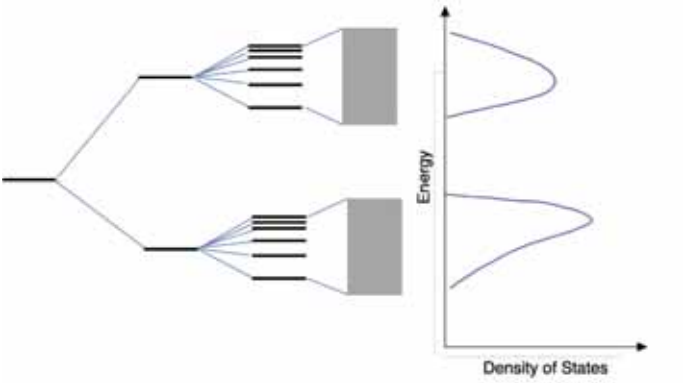

Figure 14. Schematic representation of bands for solids and their density of states

A similar approach is useful for understanding the electronic structure of the cyclic polyenes. Their energy levels can easily be solved by group theory, providing symmetry-adapted linear combinations of atomic orbitals.

Determining the energy levels for the π system of cyclic polyenes

In a cyclic molecule of symmetry C_n, the symmetry operations are:

$$C_n^1,\ C_n^2,\ C_n^3,\ \ldots..,\ C_n^n \equiv E,$$

where, n is the rotation angle defined as $\theta = \frac{2\pi}{n}$. Any of these C_n^p operations transform point A into A', *Figure 15*, according to:

$$A' = e^{i\theta p} A = \varepsilon^p A$$

where:

$$\varepsilon = e^{\frac{2\pi i}{n}}$$

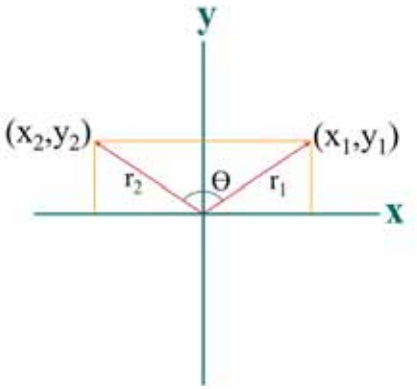

Figure 15. Rotation around a Cn, $\theta = \frac{2\pi}{n}$ axis perpendicular to XY plane

The character table of this n order group, *Table 3*, contains ***n*** irreducible representations that may be expressed as:

Table 3. Character table of group C_n

C_n	C_n^1	C_n^2	C_n^3	…..	$C_n^n \equiv E$
Γ^1	ε^1	ε^2	ε^3	…..	ε^n
Γ^2	ε^2	ε^4	ε^6	…..	ε^{2n}
Γ^3	ε^3	ε^6	ε^9	…..	ε^{3n}
…..	…..	…..	…..	…..	…..
Γ^n	ε^n	ε^{2n}	ε^{3n}	…..	ε^{n*n}

And for the C_4 group:

C_4	C_4^1	C_4^2	C_4^3	$C_4^4 \equiv E$
Γ^1	ε^1	ε^2	ε^3	ε^4
Γ^2	ε^2	ε^4	ε^6	ε^8
Γ^3	ε^3	ε^6	ε^9	ε^{12}
Γ^4	ε^4	ε^8	ε^{12}	ε^{16}

Simplifying and rearranging, the conventional character table is obtained, where Γ^4 and Γ^2 are the A and B irreducible representations, respectively, and Γ^1 and Γ^3 stand for the degenerate E representation (*Table 4*).

Table 4. Character tables[3] for group C_4

C_4	$C_4^4 \equiv E$	C_4^1	$C_4^2 \equiv C_2$	C_4^3
Γ^4	$\varepsilon^4 = 1$	$\varepsilon^4 = 1$	$\varepsilon^8 = 1$	$\varepsilon^{12} = 1$
Γ^2	$\varepsilon^8 = 1$	$\varepsilon^2 = -1$	$\varepsilon^4 = 1$	$\varepsilon^6 = -1$
Γ^1	$\varepsilon^{12} = 1$	$\varepsilon^1 = i$	$\varepsilon^2 = -1$	$\varepsilon^3 = -i$
Γ^3	$\varepsilon^{16} = 1$	$\varepsilon^3 = -i$	$\varepsilon^6 = -1$	$\varepsilon^9 = i$

C_4	E	C_4^1	C_2	C_4^3
A	1	1	1	1
B	1	-1	1	-1
E	1	i	-1	$-i$
	1	$-i$	-1	i

The point groups of cyclobutadiene or benzene are D_{4h} and D_{6h}, respectively, but the use of the corresponding cyclic subgroups, C_4 and C_6, is sufficient to determine the energy levels of these molecules. The Symmetry-Adapted Linear Combinations (SALC) of atomic orbitals are generated from the irreducible representations, according to:

$$\psi_j \propto \sum_{p=1}^{n} e^{\frac{2\pi i}{n} j(p-1)} \phi_p = \sum_{p=1}^{n} \varepsilon^{j(p-1)} \phi_p$$

The four SALCs are:

$$\begin{aligned}
\psi_4(A) &= \varepsilon^{4(1-1)}\phi_1 + \varepsilon^{4(2-1)}\phi_2 + \varepsilon^{4(3-1)}\phi_3 + \varepsilon^{4(4-1)}\phi_4 \\
&= \varepsilon^0\phi_1 + \varepsilon^4\phi_2 + \varepsilon^4\phi_3 + \varepsilon^4\phi_4 \\
\psi_2(B) &= \varepsilon^{8(1-1)}\phi_1 + \varepsilon^{2(2-1)}\phi_2 + \varepsilon^{4(3-1)}\phi_3 + \varepsilon^{6(4-1)}\phi_4 \\
&= \varepsilon^0\phi_1 + \varepsilon^2\phi_2 + \varepsilon^4\phi_3 + \varepsilon^2\phi_4 \\
\psi_1(E) &= \varepsilon^{1(1-1)}\phi_1 + \varepsilon^{1(2-1)}\phi_2 + \varepsilon^{1(3-1)}\phi_3 + \varepsilon^{1(4-1)}\phi_4 \\
&= \varepsilon^0\phi_1 + \varepsilon^1\phi_2 + \varepsilon^2\phi_3 + \varepsilon^3\phi_4 \\
\psi_3(E) &= \varepsilon^{3(1-1)}\phi_1 + \varepsilon^{3(2-1)}\phi_2 + \varepsilon^{3(3-1)}\phi_3 + \varepsilon^{3(4-1)}\phi_4 \\
&= \varepsilon^0\phi_1 + \varepsilon^3\phi_2 + \varepsilon^2\phi_3 + \varepsilon^1\phi_4
\end{aligned}$$

The two degenerate imaginary functions may be converted in two real ones by:

$$\begin{aligned}
\psi_1'(E) &= \psi_1(E) + \psi_3(E) = \phi_1 - \phi_3 \\
\psi_3'(E) &= \psi_1(E) - \psi_3(E) = -i(\phi_2 - \phi_4)
\end{aligned}$$

[3] Note that: $\varepsilon^{n*m} = \varepsilon^n * \varepsilon^m$, and therefore, $\varepsilon^4 = \varepsilon^8 = \varepsilon^{12} = 1$ and $\varepsilon^1 = \varepsilon^5 = \varepsilon^9$ or $\varepsilon^2 = \varepsilon^6$

Upon normalization, the four functions became:

$$\psi_4(A) = \frac{1}{2}(\phi_1 + \phi_2 + \phi_3 + \phi_4)$$
$$\psi_2(B) = \frac{1}{2}(\phi_1 - \phi_2 + \phi_3 - \phi_4)$$
$$\psi_1'(E) = \psi_1(E) + \psi_3(E) = \frac{1}{\sqrt{2}}(\phi_1 - \phi_3)$$
$$\psi_3'(E) = \psi_1(E) - \psi_3(E) = \frac{1}{\sqrt{2}}(\phi_2 - \phi_4)$$

The energy levels are defined by:

$$E\psi_j = \mathcal{H}\psi_j$$

$$E_j = \frac{\int \psi_j{}^* \mathcal{H} \psi_j d\tau}{\int \psi_j{}^* \psi_j d\tau} = \frac{\int \left(\sum_{p=1}^{n} \varepsilon^{j(p-1)} \phi_p\right)^* \mathcal{H} \left(\sum_{p=1}^{n} \varepsilon^{j(p-1)} \phi_p\right) d\tau}{\int \left(\sum_{p=1}^{n} \varepsilon^{j(p-1)} \phi_p\right)^* \left(\sum_{p=1}^{n} \varepsilon^{j(p-1)} \phi_p\right) d\tau}$$

In the simple Hückel method, the resonance integrals of the neighbouring orbitals are the only ones that are assigned values other than zero and all the overlap integrals, S_{ij}, for $i \neq J$ are considered equal to zero, therefore:

$$E_j = \frac{\int \left(\phi_p\right)^* \mathcal{H}\, \phi_p d\tau}{n} + \frac{\sum_{p=1}^{n} \left(\varepsilon^{j(p-1)}\right)^* \varepsilon^{j(p-2)} \int \left(\phi_p\right)^* \mathcal{H}\, \phi_{(p-1)} d\tau}{n} + \frac{\sum_{p=1}^{n} \left(\varepsilon^{j(p-1)}\right)^* \varepsilon^{jp} \int \left(\phi_p\right)^* \mathcal{H}\, \phi_{(p+1)} d\tau}{n}$$

Considering that:

$$\left(\varepsilon^{j(p-1)}\right)^* \varepsilon^{j(p-1)} = 1$$
$$\left(\varepsilon^{j(p-1)}\right)^* \varepsilon^{j(p-2)} = \varepsilon^{-j} = e^{-\frac{2\pi}{n}j} = cos\left(\frac{2\pi}{n}j\right) - i\, sin\left(\frac{2\pi}{n}j\right)$$
$$\left(\varepsilon^{j(p-1)}\right)^* \varepsilon^{jp} = \varepsilon^{+j} = e^{+\frac{2\pi}{n}j} = cos\left(\frac{2\pi}{n}j\right) + i\, sin\left(\frac{2\pi}{n}j\right)$$
$$\int \left(\phi_p\right)^* \mathcal{H}\, \phi_p d\tau = \alpha$$
$$\int \left(\phi_p\right)^* \mathcal{H}\, \phi_{(p-1)} d\tau = \int \left(\phi_{(p-1)}\right)^* \mathcal{H}\, \phi_p d\tau = \beta$$

The general expression for any cyclic molecule will be:

$$E_j = \frac{n\alpha + n\varepsilon^{-j}\beta + n\varepsilon^{+j}\beta}{n} = \alpha + (\varepsilon^{-j} + \varepsilon^{+j})\beta = \alpha + 2\beta cos\left(\frac{2\pi}{n}j\right)$$

The values of the energy levels in some polyenes are:

J	1	2	3	4	5	6
C_3H_3	$\alpha - \beta$	$\alpha - \beta$	$\alpha + 2\beta$			
C_4H_4	α	$\alpha - 2\beta$	α	$\alpha + 2\beta$		
C_5H_5	$\alpha + 0.618\beta$	$\alpha - 1.618\beta$	$\alpha - 1.618\beta$	$\alpha + 0.618\beta$	$\alpha + 2\beta$	
C_6H_6	$\alpha + \beta$	$\alpha - \beta$	$\alpha - 2\beta$	$\alpha + \beta$	$\alpha - \beta$	$\alpha + 2\beta$

This treatment may for the π system be extended to any cyclic polyene. The orbitals of medium-sized rings are shown in *Figure 16*.

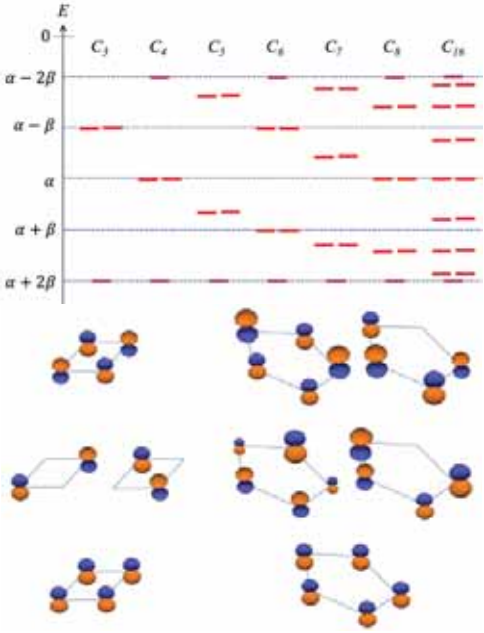

Figure 16. Top panel: Molecular orbital diagrams for the π system of cyclic polyenes; Bottom panel: Molecular orbital schemes for the π system of cyclobutadiene and cyclopendienyl structures, the relative sizes are qualitative views of the relative participation of each atomic orbital.

For any even number of members within the ring, the lowest and the highest molecular orbitals have energies equal to $\alpha + 2\beta$ and $\alpha - 2\beta$, respectively. Thus, the energy scale expands over 4 β units of energy.

The numbers of nodes increase as the molecular orbital energy increases. Moreover, note that the energy difference between states at the lowest and highest energies is smaller than these differences close to the middle of the energy sequence.

Crystal orbitals in one dimension

Up to this point, we have been able to solve elementary bonding problems related to molecules, whether of medium or large size, that are finite. When dealing with solids, the main difference is the infinite numbers of atoms that have to be considered. As stated above, we will treat *crystal orbitals* using the *LCAO* approximation and, at the forefront of our treatment, we must realize that atoms in a crystal form a regular array, all of which can be identified using the translation vector of their Bravais lattices.

A secular determinant of the order of at least *one mole x one mole* has to be used, to solve the solid-state problem, which would result in incredibly large matrices for diagonalization. However, translational symmetry, the characteristic of Bravais lattices, may make the mathematical problem straightforward by using Bloch's theorem and molecular symmetry. For simplicity, we will only consider one space coordinate.

Let us consider the atom chain represented in *Figure 17*. It is clear that the electronic structure at the extremes of that chain should differ from the electronic structure of atoms in the middle of the chain. The ends of the chain somehow represent the surface of the solid and the middle of the chain represents the bulk of the material. However, if we introduce *periodic boundary conditions*, then these differences may disappear. The *periodic boundary condition* implies that after repeating the chain an infinite number of times, N, it reverts to exactly the same value, obtained after separately moving each other by a lattice vector $\vec{a}$:

$$\psi(x + Na) = \psi(x)$$

Another way of overcoming the different nature of the ends of the monoatomic chain is to assume that the chain forms a ring with an infinite number of elements, as depicted in *Figure 17*.

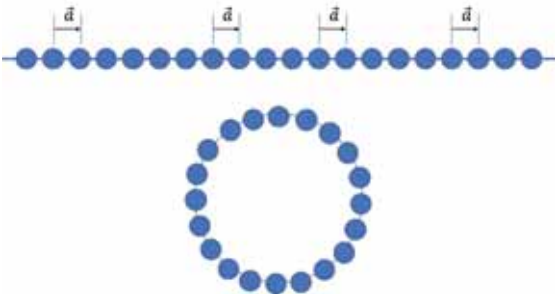

Figure 17. One dimensional monoatomic chain, the chain of N atoms is assumed to repeat infinitely. Bottom: Alternative view of the meaning of the periodic boundary condition.

Once this alternative way of approaching the infinite chain of atoms is assumed, the energy of the different levels appears trivial. Of course, this approach will not mean that the solid undergoes any curvature, as it merely represents a mathematical strategy for an easy solution to the problem.

As clearly deduced in the previous section, the energy levels for planar rings with an infinite number of atoms, *n*, are defined by:

$$E_j = \alpha + 2\beta cos\left(\frac{2\pi}{n} j\right)$$

where, *j* takes any integral values from 0, $\pm 1, \pm 2, \ldots . \pm \frac{n}{2}$ and $\frac{n}{2}$ is extremely large. By defining the wave vector k, as:

$$k = \frac{2j\pi}{na}$$

The energy becomes:

$$E_j = \alpha + 2\beta \cos ka$$

The wave vector takes values continuously from 0 to a range of $-\frac{\pi}{a} < k < \frac{\pi}{a}$. The points within $-\frac{\pi}{a}$ and $\frac{\pi}{a}$ for crystalline solids are located in the first Brillouin zone, while the edges of this first zone are located at $k = -\frac{\pi}{a}$ and $k = \frac{\pi}{a}$, and the point at $k = 0$ is at the centre of the zone. The variation in energy with k, *Figure 18*, is the dispersion of the band.

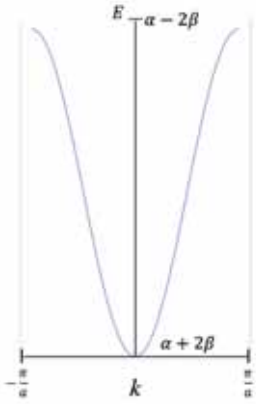

Figure 18. Dispersion energy diagram for 1D solids.

The wave functions can be expressed as in the case of cyclic polyenes:

$$\psi_j = \frac{1}{\sqrt{\sum_{p=1}^{n}\left(C_n^{(p-1)}\right)^2}} \sum_{p=1}^{n} e^{\frac{2\pi i}{n} j(p-1)} C_n^{(p-1)} \phi_p$$

And by using the k vector, the crystal orbitals of the one-dimension chain of atoms are:

$$\psi(k) = N^{-\frac{1}{2}} \sum_{p=1}^{n} e^{ik(p-1)a} \phi_p$$

The top of the band occurs at $k = \frac{\pi}{a}$ where $\cos ka = 1$ and $E = \alpha - 2\beta$ and the bottom at $k = 0$ where $\cos ka = 1$ and $E = \alpha + 2\beta$.

The inclusion of the overlap in this description slightly modifies the width and shape of the dispersion band, *Figure 19*:

$$E = \frac{\alpha + 2\beta \cos ka}{1 + 2S \cos ka} \text{ and } E = \frac{\alpha - 2\beta \cos ka}{1 - 2S \cos ka}$$

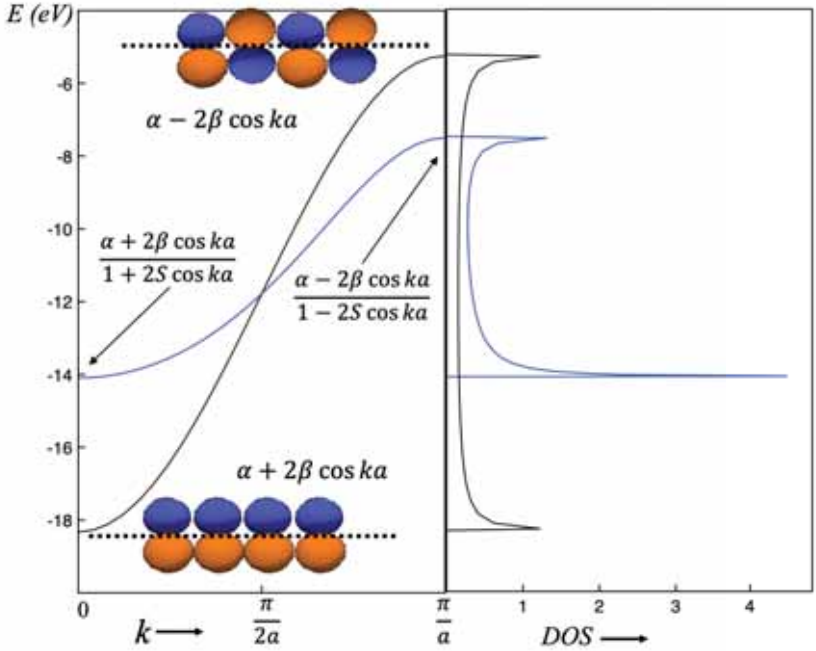

Figure 19. Left panel: Energy dispersion curves for a carbon p_π–p_π system calculated using a VSIE value of 11.787 eV for the C 2p orbital and values of β = 3.270 eV. The difference between the curves reflects whether we take into consideration the overlap for estimating the energy. The overlap integral for a C-C distance of 120 pm is estimated at S = 0.150. Right panel: density of states for both situations.

It is clear from the energy expression that the introduction of the overlap integral results in an asymmetrical dispersion curve where the top of band is destabilized and the bottom of the curve is stabilized. As a result, the number of states per unit is larger at the bottom than at the top, as can clearly be seen in *Figure 19*, where the energy dispersion curve and the Density of States (DOS) are represented for a carbon p_π–p_π system either considering the overlap integral (black line) or, in the simplified version, not considering it (blue line).

Monoatomic hydrogen chain

Let us return to the simplest possible case, in order to generate a consistent LCAO model for bonding in solids: a monoatomic equally spaced hydrogen chain. This 1D hydrogen solid has its atoms placed at lattice points labelled n = 0, 1, 2, 3, 4, 5, ….. and at every lattice point there is an H atom characterized by its wavefunction, ϕ_n, *i.e.*, the so called *1s* function. As stated above, the application of the translational symmetry results in infinite adapted Bloch functions:

$$\psi(k) = \sum_{n=0}^{n-1} e^{iknа}\phi_n$$

By evaluating this function at the centre, $k = 0$, and at the edge, $k = \frac{\pi}{a}$, of the first Brillouin zone, we obtain the most bonding, and the most antibonding wave functions, respectively.

The wave function at the top of the band is obtained for $k = 0$, $e^{ikna} = 1$ and for $k = \frac{\pi}{a}$, $e^{ikna} = e^{i\pi n}$, whereas $e^{i\pi n} = (-1)^n$, by always selecting an even value of the number of lattice sites. *Figure 20* presents the wave functions for these *k* values.

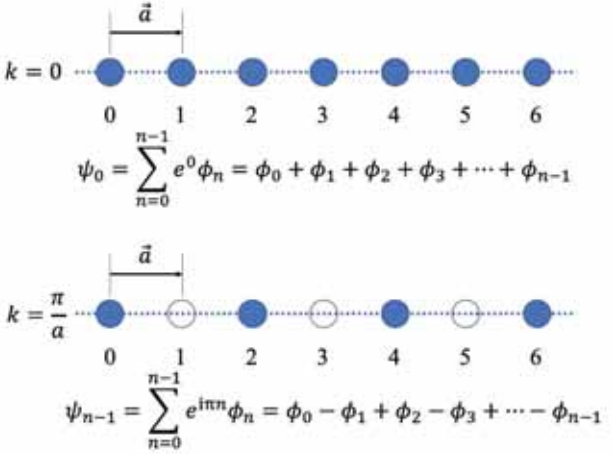

Figure 20. Wave functions for electrons moving along an equally spaced monoatomic hydrogen chain

It is clear that the wave function at the top of the band has the maximum number of nodes and the wave function has no nodes at the bottom. As the

energy increases the number of nodes increases and therefore *k* may also serve as a node counter.

The *Band Width* (BW) is defined by the energy separation between the top and the bottom of the band at $k = \frac{\pi}{a}$ and $k = 0$, respectively. Both the overlap and resonance integrals depend on the distance between the lattice points, as the lower the distance the higher the overlap between adjacent atoms A and B. In Mulliken's approach, the resonance integral is a function of the VSIE and the overlap integral, which is itself a function of the A-B interatomic distance:

$$\beta \propto \frac{\alpha_A + \alpha_B}{2} S_{AB}$$

It is clear that the greater the overlap, the smaller the interatomic distances, the greater the band width and the differences between the density of states at the top and bottom on the band, *Figure 21*. Notice that the area under the DOS curves must be the same, as the number of *crystal orbitals* is the same and, therefore, the thinner the band the higher the DOS.

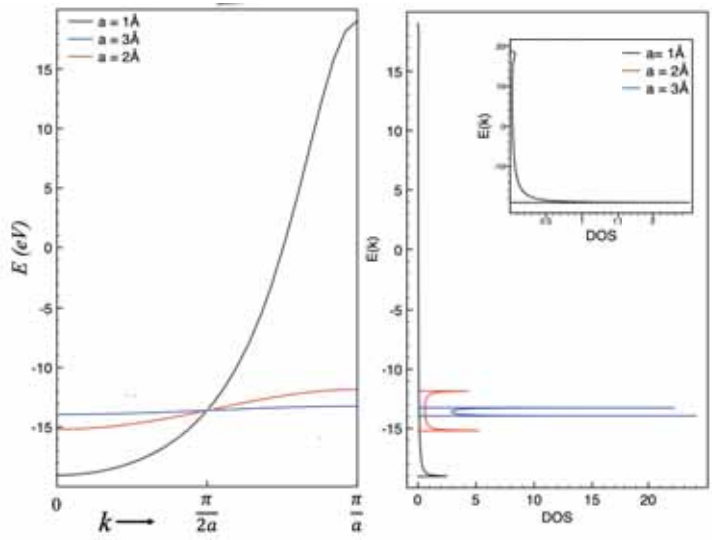

Figure 21. Left: Energy dispersion curves of equally spaced hydrogen chains, the lattice parameters are indicated in the figure. Right: Density of states for different interatomic distances, the insert reproduces the DOS for an interatomic distance of 1Å.

In general, the interactions are smaller for larger A-A distances and the band dispersion, the difference in energy between the top and the bottom of the band, decreases. On the contrary, the widest band width is for the shortest A-A distances.

The main conclusion is that the band dispersion is proportional to the strength of the atom–atom interaction between the unit cells, since as mentioned the interatomic interaction is proportional to the overlap integral that depends on the interatomic distance and the nature of the implied orbitals. In a rough approximation, this integral decreases in the order *of s–s > p–p > d–d > f–f.*

Interestingly, the nature of the atomic wavefunctions affects the way the energy dispersion curves run. According to the wave-function solutions, there is no implication that energy at the edge of the Brilloiun zone, $k = \frac{\pi}{a}$, is higher and energy at its centre, $k = 0$, is lower.

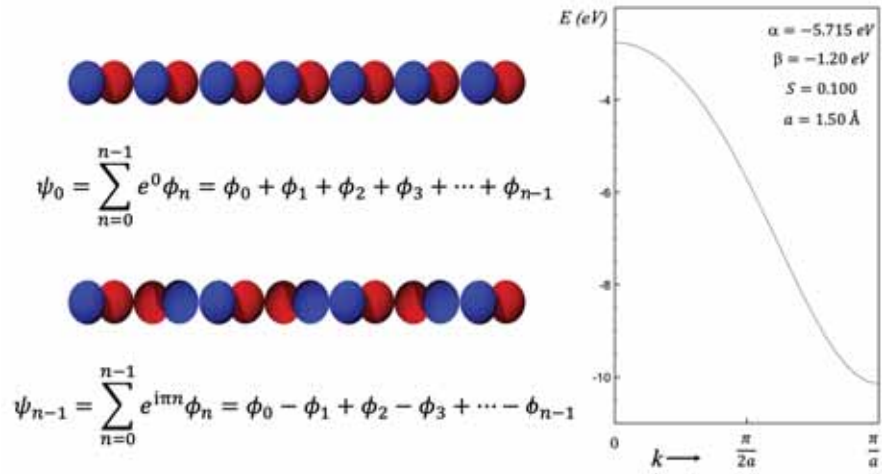

Figure 22. Wave functions and dispersion diagram for *p-p* σ interactions along an equally spaced monoatomic chain. Notice that this diagram "runs down" rather than up as in *Figure 21*.

Let us now consider the case of the wave function formed by the combination of p orbitals that are coaxial to the chain edge, *Figure 22*. As in the case of the s orbitals, the same combinations of the crystal orbital at $k = 0$ and at $k = \frac{\pi}{a}$ are obtained from the translational symmetry, but the

energy sequence is clearly different. For *p* orbitals coaxially aligned with the wave vector propagation direction, the highest energy level (top of the band) occurs at the centre of the first Brillouin zone ($k = 0$), whilst the lowest energy, at the bottom of the band, occurs at $k = \frac{\pi}{a}$, at the edge of the zone.

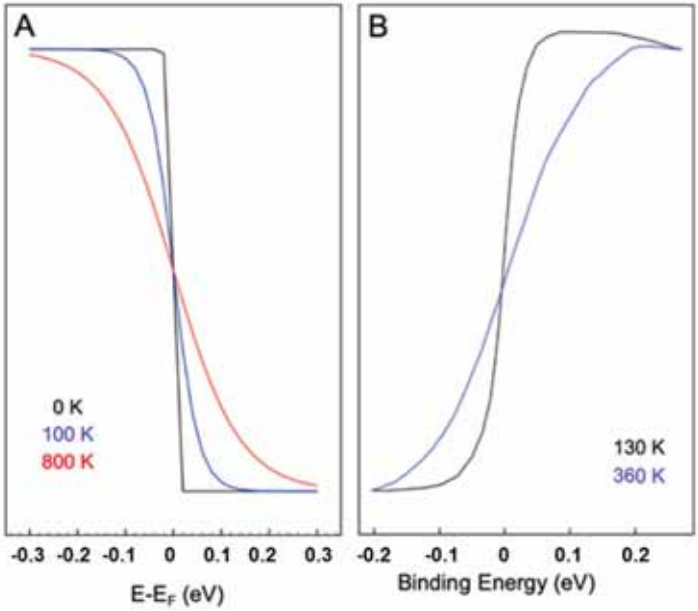

Figure 23. A) Fermi-Dirac distribution as a function of temperature; and, B) Photoemission spectra of Ru(001) around the Fermi edge at 130 and 360K.[4]

Properties of solids from the band picture

The electronic properties of solids depend on the energies and structures of bands, which are a function of the extent and the type of the bonding between the atoms forming that solid. Electrical conductivity is the most obvious electronic property of solids; it arises from the presence of empty energy levels with almost the same energy to the filled ones, which in the presence of an electric field will be a conduction pathway.

[4] G.K.L. Cranstoun *et al.*

Metallic solids are electrical conductors whatever the temperature, showing conductivity at the lowest attainable temperature. On the contrary, non-metallic solids show some conductivity at high temperatures, but as soon as the temperature goes down the electrical conductivity disappears. This behavior is related to the band-filling behavior. In a filled band there are no empty levels close in energy to the filled ones and electrical conduction is therefore hindered because an energy gap to the next energy band occurs. This behavior is typical of insulators. However, empty and filled levels are close in energy in partially filled bands, giving rise to a net motion of electrons and therefore to electrical conduction. A typical example of this behavior is found in metals.

If there is an energy difference between bands -a band gap- *why is it that insulators may show slight electrical conductivity at high temperatures?* The number of excited states is a function of temperature that for solids is described by the *Fermi-Dirac* distribution:

$$f(E) = \frac{1}{1 + e^{\frac{E-E_F}{kT}}}$$

This distribution, $f(E)$, accounts for the fraction of levels of energy, E, that is permissible at a given temperature, T. It is clear that there is a sharp cut-off at 0K between the top of the filled band, E_F, known as the *Fermi level*, and the empty band. However, electrons are thermally excited when the temperature increases and the distribution around the Fermi level is smoothed. *Figure 23* presents, as an example, the behavior of the Fermi-Dirac distribution as a function of temperature together with the photoemission spectra of Ru (001) as a function of temperature around the Fermi edge. As the temperature rises, the spread of excited energy levels broadens and, consequently, some electrical conduction even passes through the insulators. Several situations may be envisaged for electrical conductors. The simplest situations involve an insufficient number of electrons to fill the energy band completely. A second situation appears for completely filled bands that overlap with empty bands, thereby providing empty levels close enough to the filled levels, and finally a third possibility appears for filled bands separated from empty bands, although with a small energy gap between them in the order of *kT*. Examples of these situations are seen in *Figure 24*. The band gap clearly increases for solids with insulating behavior exceeding *kT*.

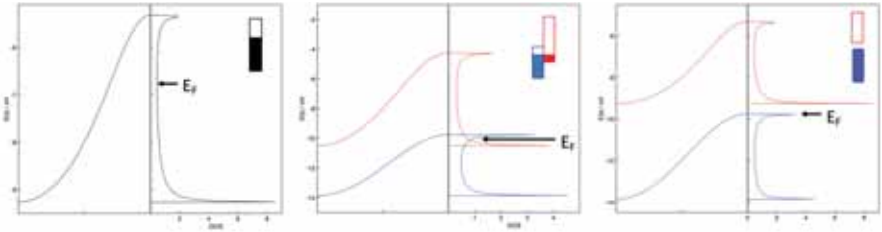

Figure 24. Dispersion diagrams and DOS curves for three equally spaced monoatomic chains of s and d orbitals aligned along the propagation of vector k. This figure illustrates different conduction pathways in electrically conductive solids. The inserted box plots schematize the filling of the bands.

Lowering symmetry: The two-atom cell problem

Let us now go back to the case of the equally spaced monoatomic chain of hydrogen atoms. For a chain of *n* atoms, it must be *n 1s* electrons, that according to the Aufbau principle would fill $\frac{n}{2}$ crystal orbitals. As we have seen before, it results in a dispersion curve "*running up*" that will contain *n* crystal orbitals and that will therefore require *2n* electrons to be completely filled.[5] It is clear that half of the band of this equally spaced hydrogen monoatomic chain will be filled and the chain will show a metallic character. Obviously, this could not be a proper description of solid hydrogen that does not show electrical conductivity.

By considering the molecular character of hydrogen, we may think of equally spaced H_2 entities along the direction of the propagation vector *k*. Of course, no observable change will appear since we have changed the dimension of the unit cell, not the interatomic distances, as represented in *Figure 25*. However, the dispersion diagram will change, because the lattice parameter and the number of orbitals per cell has been doubled.

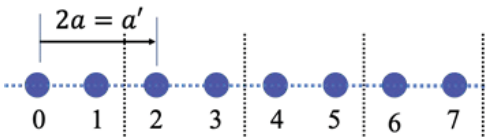

Figure 25. Two-atom cell for equally spaced 1D hydrogen chain.

[5] See for instance left panel on figure 22.

Let us raise the question of what the wave functions are at the centre of the first Brillouin zone, that is at $k = \frac{\pi}{2a}$. Following the formulation of the Bloch functions:

$$\psi_1(k) = \frac{1}{\sqrt{N}} \sum_{n=1}^{n} e^{ikna} \phi_n$$

The resulting wave function is:

$$\psi\left(k = \frac{\pi}{2a}\right) = \sum_{n=1}^{n} e^{\mathrm{i}\frac{\pi n}{2}} \phi_n = \sum_{n=1}^{n} i^{\mathrm{n}} \phi_n = i\,\phi_1 - \phi_2 - \mathrm{i}\,\phi_3 + \phi_4 + \mathrm{i}\,\phi_5 \ldots$$

This wave function for the negative value of $k = -\frac{\pi}{2a}$ is:

$$\psi\left(k = -\frac{\pi}{2a}\right) = \sum_{n=1}^{n} e^{\mathrm{i}\frac{\pi n}{2}} \phi_n = \sum_{n=1}^{n} (-i)^{\mathrm{n}} \phi_n = -i\,\phi_1 - \phi_2 + \mathrm{i}\,\phi_3 + \phi_4 - \mathrm{i}\,\phi_5 \ldots$$

Remember that all the solutions are doubly degenerate as seen on solving the cyclic polyenes π systems and Kramers theorem. Therefore, linear combinations may be created, to eliminate the complex form:

$$\psi_+ = \psi\left(k = \frac{\pi}{2a}\right) + \psi\left(k = -\frac{\pi}{2a}\right) = -\phi_2 + \phi_4 - \phi_6 + \phi_8 - \phi_{10} + \phi_{12} \cdots$$

$$\psi_- = \psi\left(k = \frac{\pi}{2a}\right) - \psi\left(k = -\frac{\pi}{2a}\right) = \phi_1 - \phi_3 + \phi_5 - \phi_7 + \phi_9 - \phi_{11} \cdots$$

The energy solutions are:

$$E_i(k) = \alpha \pm 2\beta \cos k \frac{a'}{2}$$

which will be exactly the same as before, since nothing has to be changed except for the lattice parameter. The dispersion diagram, *Figure 26*, appears similar to the one in *Figure 21*, but folded around the middle axis. In general, on increasing the cell size *n* times without lowering the symmetry of the lattice, the dispersion band is folded *n* times. Note the point of contact between the two bands at $k = \frac{\pi}{2a}$ and the two wave functions with degenerate energy levels. Obviously, this situation, as stated above, will not

change the properties of the 1D chain that will remain electrically conductive.

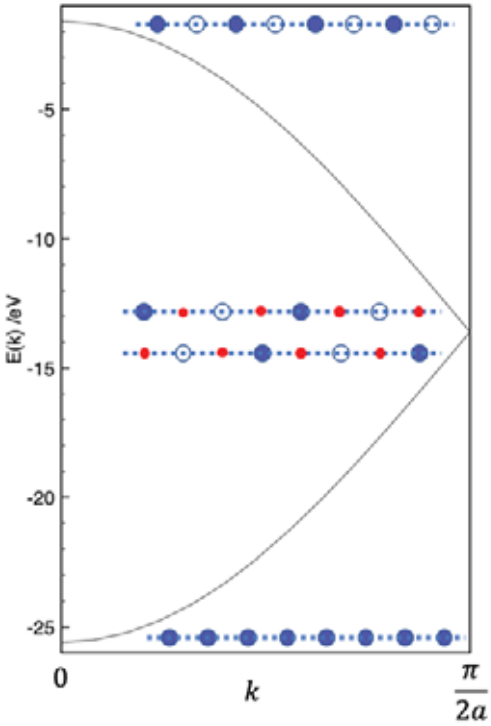

Figure 26. Dispersion diagram for equally spaced H_2 entities

Addressing this problem, it seems reasonable to assume that the 1D chain is formed by H_2 molecules with their axes coincident with the chain direction. This is equivalent to a 1D structure with a Bravais lattice characterized by a translation vector of dimension *2a* and a H_2 basis on every lattice site, as schematized in *Figure 27*. The band structure of the chain of horizontal H_2 molecules arises from the interaction of the σ_g and σ_u^* molecular orbitals. The σ_g level destabilizes (increase in energy) passing from Γ $(k = 0)$ to X $\left(k = \frac{\pi}{a}\right)$, because the bonding intramolecular interaction of the H_2 molecule in one cell changes to antibonding in the next cell.

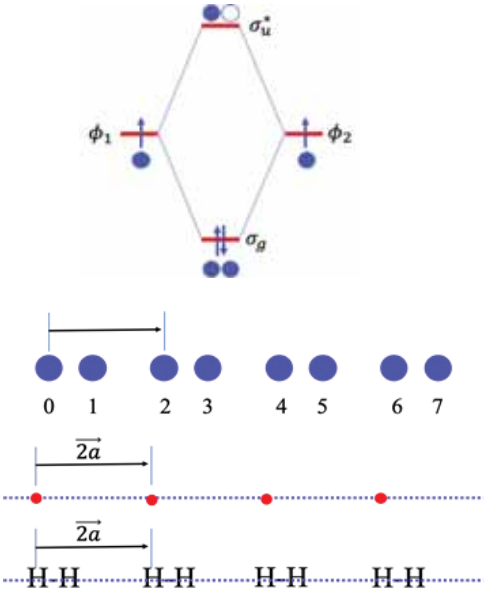

Figure 27. Molecular orbital diagram for H_2 and scheme of its solid 1D Bravais lattice

On the contrary, the σ_u^* level runs the opposite way, because the antibonding character changes to bonding on moving to the next cell.

Note the σ_g band where lower energy looks like an *s* band and "runs up" while the σ_u^* one that is higher in energy, has a similar shape (symmetry) to the shape of the p_z orbitals and, therefore, "runs down" in the dispersion energy diagram. The way that the bands run simply depends on the topology of the orbitals along the chosen direction.

The wave functions are therefore:

$$\psi_1(k) = \frac{1}{\sqrt{N}} \sum_{n=1}^{n} e^{ikna} \sigma_{g_n}$$

$$\psi_2(k) = \frac{1}{\sqrt{N}} \sum_{n=1}^{n} e^{ikna} \sigma_{u_n}$$

In the case of the equally spaced monoatomic chain of *n* hydrogen atoms, we obtain *n* crystal orbitals that are a combination of the *n* atomic wave functions. In the two-atom cell approach, we have $\frac{n}{2}$ cells (lattice sites) each containing a H_2 molecule with two molecular wave functions, σ_g and σ_u^* , resulting in two bands each with $\frac{n}{2}$ levels that may each allocate *n* electrons. The energy dispersion and DOS diagrams for this situation are shown in *Figure 28*.

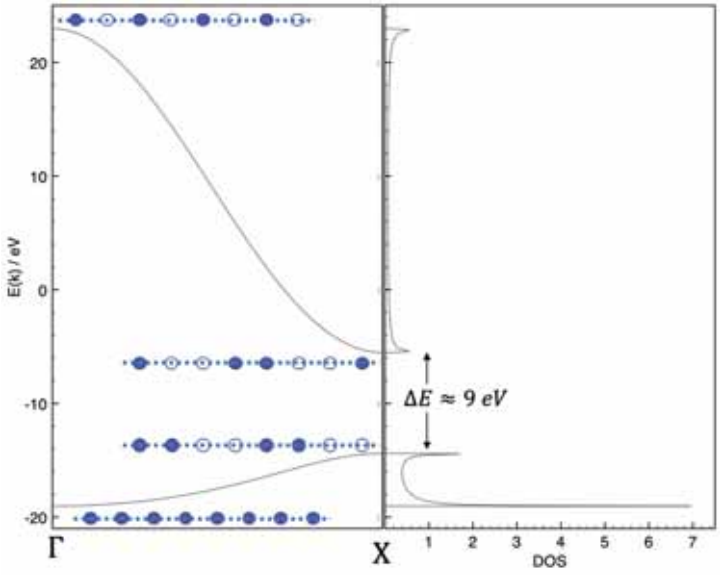

Figure 28. Energy dispersion and DOS diagrams for H_2 molecules aligned in the chain direction with different inter- and intra-molecular H-H distances

The energy gap between bands at the X point is just a function of the inter- and intra-molecular H-H distances. If these distances are identical, the band gap vanishes and we have the situation of *Figure 26*. It is clear that when the band gap vanishes there are two degenerate crystal orbitals that are phase shifted. Moreover, both bands have the same symmetry with respect to the mirror plane containing the 1D solid, both bands are totally symmetric and therefore interact with each other, raising the energy of the upper band and lowering the energy of the lower one. This distortion for 1D systems with half-filled bands is called *Peierls distortion*.

Peierls distortions are characterized by lower system symmetry. In the 1D hydrogen chain, the symmetry is reduced in the non-equally spaced case.

An analogy may be found in molecular chemistry in the well-known Jahn-Teller effect, stating that nonlinear molecules reduce symmetry to remove degenerate electronic states.

Infinite molecules: The Krogman salts

Among the solids with one-dimensional properties, the tetragonal compounds of platinum, first synthesized by Krogman, are of particular interest, *e.g.*, the mixed-valence $K_2Pt(CN)_4Br_{0.3}\cdot xH_2O$ exhibits 1D metallic conduction. The solid is built of square planar $Pt(CN)_4$ units linked together along the *c* axis of the structure. The Pt-Pt distance, 2.88 Å, is only slightly higher than in metallic platinum (2.77 Å). *Figure 29* presents a view of the staggered stack of tetragonal $K_2Pt(CN)_4Br_{0.3}\cdot xH_2O$ solid.

The electrical conductivity parallel to the c axis of the structure is 10^5 times higher than perpendicular to it, consistent with the 1D metallic character of this solid. Therefore, potassium platinocyanide, $K_2Pt(CN)_4$, shows an eclipsed stack of square planar PtL_4 complexes with a much longer Pt-Pt distance (3.3 Å) than in the mixed-valence compound. Note that d^8 Pt^{2+} in $K_2Pt(CN)_4$ is oxidized in mixed-valence $K_2Pt(CN)_4Br_{0.3}\cdot xH_2O$ that presents an average Pt oxidation state of *+2.3*, suggesting that the Pt-Pt distance correlates directly with the average oxidation state.

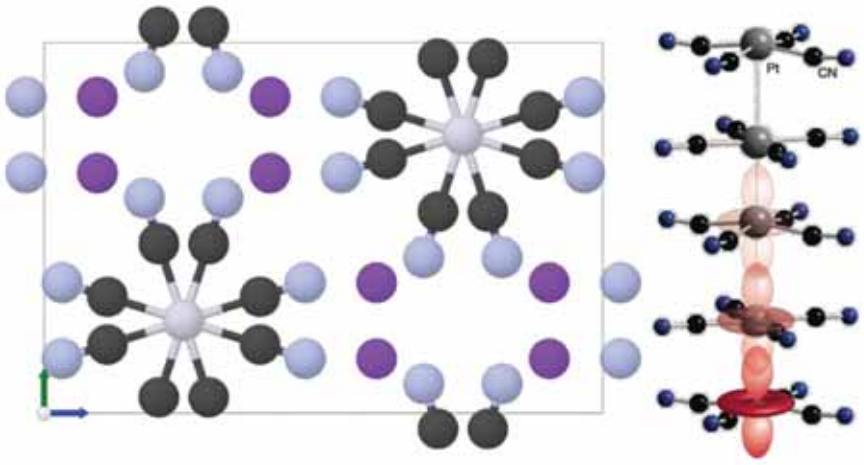

Figure 29. Projection along the [001] direction of the unit cell of staggered $K_2Pt(CN)_4Br_{0.3}\cdot xH_2O$ 1D metallic conductor and *d-d* Pt overlap along the *c* axis.

In addition, the square planar Iridium solids, $M_x[Ir(CO)_2X_2]$ (M= H, Na, K; X= Cl, Br, I), form 1D solids through metal-metal interactions that result in electrically conductive materials. Although these solids are less stable than the platinocyanide ones, it has been shown that the electrical conductivity is a function of the Ir-Ir distance and must be related to the average oxidation state of iridium metal.

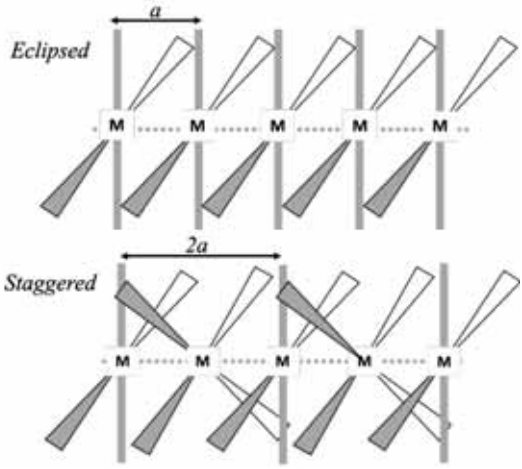

Figure 30. Possible configurations of the 1D metal chains

Although Pt 1D solids are slightly more complex than the monoatomic hydrogen chain, few differences in defining the band dispersion exist. The 1D chain will be defined by a set of lattice points separated by a translation vector, *a*, and the square planar complex will be the basis of each lattice point. It must be considered that if the M-M separation is characterized by a translation vector, *a*, it is double in the eclipsed configuration than in the staggered one (*Figure 30*).

Starting with the smaller unit cell, the eclipsed structure, as the main feature, the conductivity occurs along the axis, and the system may be simplified by substituting the cyanide ligand for the simpler hydride one. The molecular orbital diagram of this repeating unit may be easily deduced from the conventional picture of square planar complexes, *Figure 31*. Both $[Pt(CN)_4]^{2-}$ and $[Ir(CO)_2X_2]^{2-}$ are 16 electron complexes as expected for square planar complexes, which means that the d block splits into four occupied (d_{z^2}, d_{xy}, d_{xz}, d_{yz}) orbitals and one empty ($d_{x^2-y^2}$) one. As we

have simplified the problem using the H^- ligand, we may forget any π contribution of the M-ligand bonds and we will therefore have four σ bonds between the SALC of the ligands ($a_{1g}+ b_{1g}+e_g+b_{2g}$) and the atomic orbitals of the metal complex. The metal, $d_{x^2-y^2}$ (a_{1g} symmetry), participates in the M-L bond, but the symmetry remains the same.

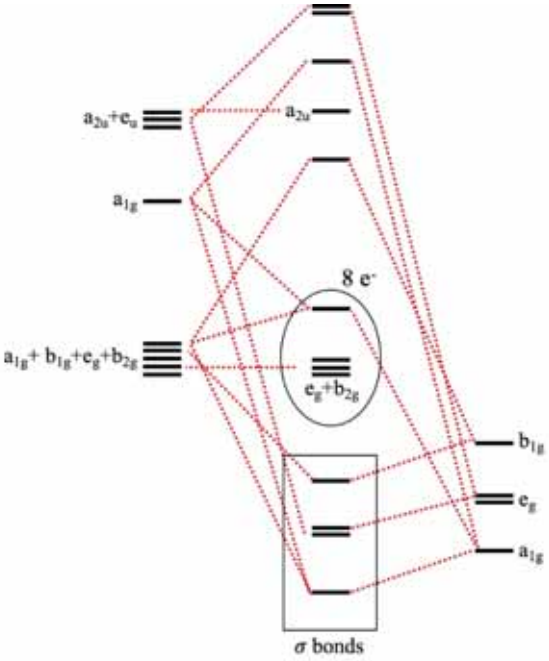

Figure 31. Qualitative MO diagram for 16 electron square planar complexes.

On forming the solid, each molecular orbital (MO) will form a band. Although, some bands will have the same symmetry, once they have formed, and will be mixed together in a first approximation, we may bypass this effect.

We can gain a qualitative idea of the interactions between the MO through basic chemistry knowledge. It is clear that the interaction strength follows $\sigma > \pi > \delta$ in the same way as the band width. Moreover, we must firstly analyze the set of orbitals close to the Highest Occupied Molecular Orbital (HOMO) and the Lowest Unoccupied Molecular Orbital (LUMO) levels. The next step should be the analysis of the way the bands runs.

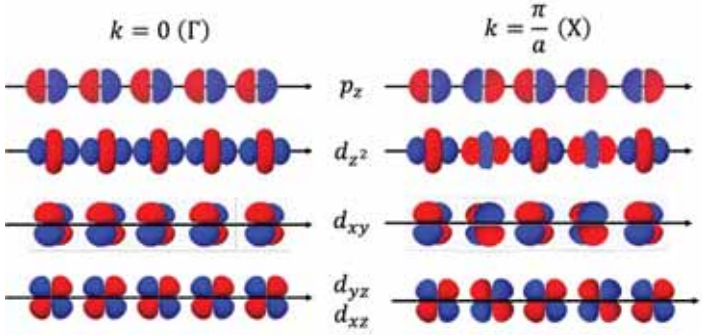

Figure 32. Bloch's functions of d orbitals at the centre and the edge of the Brillouin zone.

Figure 32 schematizes the Bloch functions for the bands formed with the participation of the metal *d* orbitals. Upon interaction along the *z* axis, p_z and d_{z^2} orbitals result in σ bands, d_{xz} and d_{yz} in π orbitals and the two d orbitals perpendicular to the solid axis (d_{xy}, $d_{x^2-y^2}$) in δ orbitals. The two δ functions and the σ function resulting from the d_{z^2} interaction have their lowest energy level at Γ and their highest at X. The two π functions (d_{xz}, d_{yz}) and the σ one (p_z) "*run down*" have their highest energy level at k = *0.*

The model 1D solid is formed by *N* cells, each containing one MH_4 unit and N number of levels per bond that may have room for two electrons each. As these complexes have 16 electrons, the set of MO shown in *Figure 31*, forming the sigma bonds (a_{1g}, b_{1g}, e_g), each hold two electrons, as well as the a_{1g}, b_{2g} and e_g *d* levels of the central atom. The metal d_{z^2} and the $d_{x^2-y^2}$ levels are the HOMO and the LUMO of the model unit.

The linear MH_4 solid has all the bands completely filled to the top of the d_{z^2} band. An energy gap appears between the latter band and the p_z one making this solid an insulator, *Figure 33*. The complete filling of the bands, in addition to providing clues on the electrical conductivity of the solid provides more information on the bonding. As can be easily seen, as the Bloch functions form, half of the orbitals of the band have a bonding character and the other half an antibonding character.

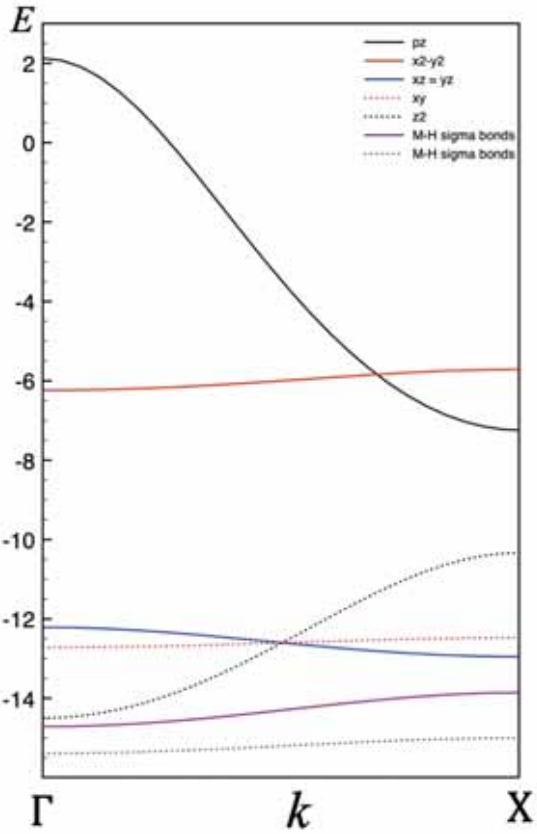

Figure 33. Energy dispersion diagram for 16 electron MH_4 complexes.

Moreover, if the destabilization of the antibonding levels is higher than the stabilization of the bonding levels, the net bonding character of these completely filled bands should be slightly antibonding. Let us for the moment justify this apparent non-bonding character assuming that mixing of bands with the same symmetry with respect to the *c* axis, mainly p_z and d_{z^2}, provide the required stabilization energy.

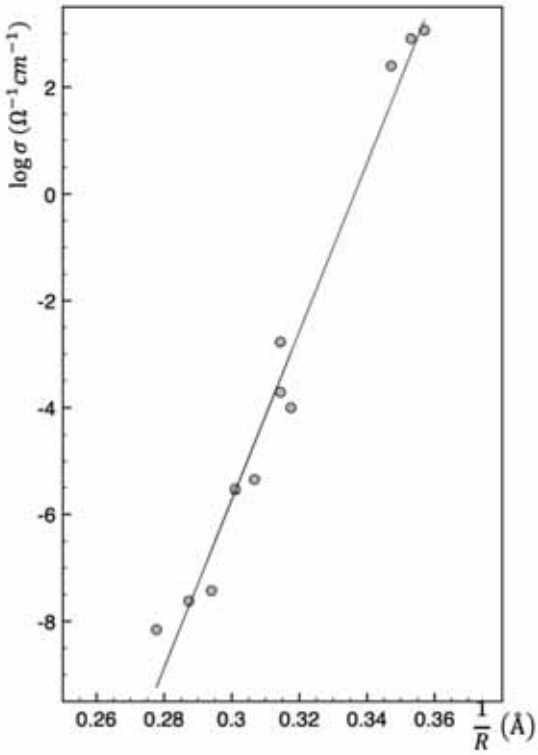

Figure 34. Electrical conductivity as a function of the reciprocal of Pt-Pt distance in platinocyanides [6]

Could the conductive properties be associated with the staggered configuration of the solid? To answer this question, we have to go back to the MH_4 unit. Let us assume, for a simpler analysis, that every band is now folded at $k = \frac{\pi}{2a}$ and we will therefore have two degenerate wave functions at point X for each band that according to Peierls distortion will split, generating small gaps between them. However, from the point of view of the electrical conductivity nothing changes since the *Fermi* level associated with the HOMO level remains the same and all the bands are completely filled with a gap appearing between the metal levels d_{z^2} and $d_{x^2-y^2}$.

The electrical conductivity, *Figure 34*, of platinocyanides is a function of the reciprocal of the Pt-Pt distance, the shortest of which are those with the highest Pt oxidation state:[6]

$$K_2[Pt(CN)_4] > K_2[Pt(CN)_4]Br_{0.30} > Cs_2[Pt(CN)_4](FHF)_{0.39} > Rb_2[Pt(CN)_4](FHF)_{0.40}$$

The spectacular increase in room temperature conductivity is directly proportional to the increase in the number of charge carriers and, therefore, to the presence of empty levels within the bands as a direct consequence of the higher oxidation state of Pt that reduces the number of *d* electrons. These electrons, typically in the 0.3-0.4 range, are from the highest occupied levels that are at the top of the d_{z^2} band. The oxidation state increase accounts for 15-20% of the population of this band that necessarily increases the bond order, because the highest levels have antibonding character that is lost on oxidizing Pt. The Fermi level should now be at the middle of the band and the empty levels should be close to filled levels in terms of their energy, favouring electrical conductivity.

The LCAO theory of the square lattice

2D models bridge the simple one-dimensional models considered above and the tridimensional structure of most solids, but we cannot forget the importance of 2D solids as graphene or other scientific and technological layered solids. Over the past few years, 2D materials have emerged as an opportunity to develop previously unimaginable technologies through the understanding of their unusual physical properties, *e.g.*, Transition Metal DichalCogenides (TMDC´s) show novel, diverse, and tuneable layer-dependent properties that can be controlled by their crystalline structure, number of stacking layers, and defect concentration. By controlling the direct bandgap of the material, it is possible to achieve enhanced photoluminescence, optoelectronic properties, and controllable electrical properties suitable for the fabrication of high-performance transistors; although, 2D materials promise a wide range of novel applications that are not possible with bulk materials. Silicones, hexagonal BN, graphene, black phosphorous, and germanene present extraordinary physical and chemical properties, among hundreds of others covering a whole range of materials that can be semiconductor, metals, semimetals, and superconductors. For instance, Germanane (GeH) shows an interlayer separation of 5.9Å, is not

[6] FHF is the bifluoride anion.

flat like graphene, and has a surprisingly high theoretical mobility, 5-fold higher than bulk Ge and 10-times if compared to silicon. TMDC´s have changed concepts in gene delivery opening up such opportunities as cancer theragnostic.

At first sight the use a 2D approach, neglecting interlayer interactions, appears to be appropriate for an understanding of the properties of these layered structures, as intralayer interactions are much stronger than interlayer ones.

The only difference with the previous treatment is the *k* vector in the reciprocal space that will have two dimensions. The Brillouin zone will therefore be characterized by an area

$$\vec{k} = \overrightarrow{k_x} + \overrightarrow{k_y}$$

An array of similar atoms, separated by a distance *a*, in a square lattice is the simplest possible 2D crystal.

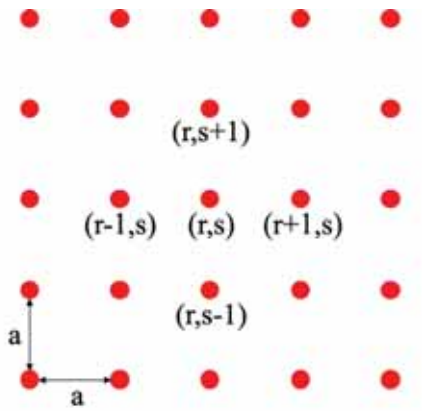

Figure 35. Labelling of points in square lattices

Figure 35 shows a square lattice with the labelling of the different lattice points. By placing an atom at every lattice point we may write functions describing the crystal orbitals as:

$$\psi(k) = \sum_{n=0}^{n-1} e^{iknа}\phi_n = \sum_{n=0}^{n-1} e^{i(k_x r + k_y s)a}\phi_n$$

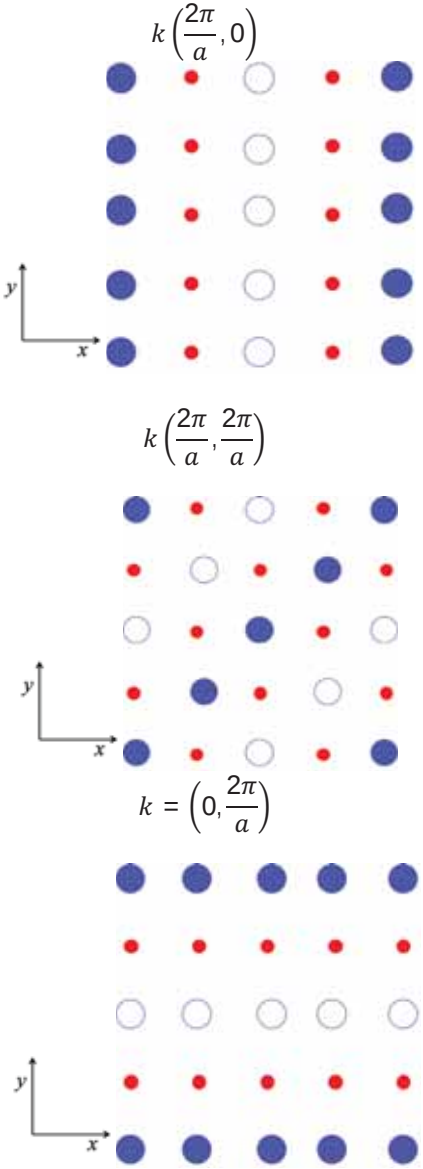

Figure 36. Bloch functions, real part, for an equally spaced linear chain of hydrogen atoms at the *k* vectors that are shown.

Let us suppose that ϕ_n describes a *1s* orbital of atomic hydrogen. The Schrödinger equation must therefore be factorized into two components along the x and y directions that are identical to the solutions of the 1D solid. As for the linear chain, k_x and k_y values are in the $0 < |k_x|, |k_y| < \frac{\pi}{a}$ range, making the construction of the Bloch functions in both directions straightforward. For the linear chain of equally spaced hydrogen atoms, we have seen that Bloch functions at $k = \frac{\pi}{2a}$ are:

$$\psi_+(k) = -\phi_2 + \phi_4 - \phi_6 + \phi_8 - \phi_{10} + \phi_{12} \cdots$$
$$\psi_-(k) = \phi_1 - \phi_3 + \phi_5 - \phi_7 + \phi_9 - \phi_{11} \cdots$$

Upon construction of the Bloch sums at $k\left(0, \frac{2\pi}{a}\right)$, $k\left(\frac{2\pi}{a}, 0\right)$ and $k\left(\frac{2\pi}{a}, \frac{2\pi}{a}\right)$, it is clear that there are also vectors that run along the square lattice diagonals, *Figure 36.*

Recall that the first Brillouin zone is a primitive cell in a reciprocal space. The two vectors defining this cell are the reciprocal of the $\vec{a}$ vector in real space and as a primitive cell, it contains only one lattice point. *Figure 37* shows the first Brillouin zone of the defined square lattice. The points Γ, M, and X correspond to *k* vectors $(0,0)$, $\left(\frac{\pi}{a}, \frac{\pi}{a}\right)$, and either $\left(o, \frac{\pi}{a}\right)$ or $\left(\frac{\pi}{a}, 0\right)$.

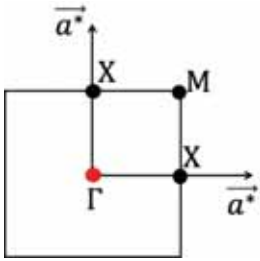

Figure 37. First Brillouin zone of the square lattice

Obviously, all bands modify their energies with k giving rise to an energy surface in the Brillouin zone. However, as for the 1D case, we plot the positive component of the *k* vector, which results in just one fourth of the Brillouin zone.

The Γ-X and X-M distances in reciprocal space are the same, but the Γ-M, at the diagonal of the Brillouin zone, is larger by a factor $\sqrt{2}$. Despite all

these the usual plot of the dispersion energy diagram takes no account of the differences and simply shows a two-dimensional plot with equal distances pointing to the highest and the lowest energies of the corresponding bands.

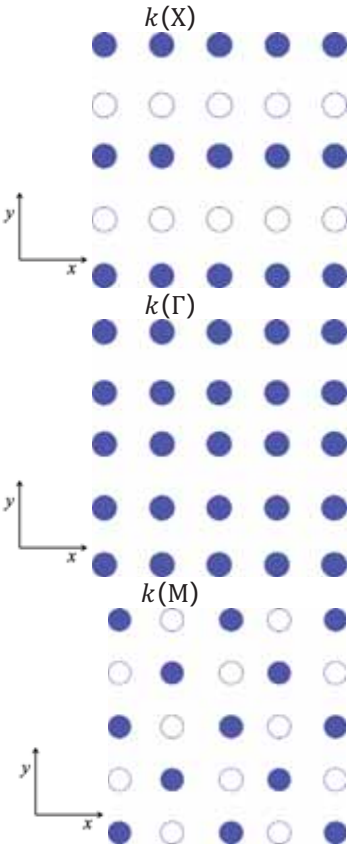

Figure 38. Bloch functions, real part, for an equally spaced square lattice of hydrogen atoms at the *k* vectors that are shown

Analysing the Bloch functions at the three following points Γ, M, and X, from the chemist's point of view, it can be easily concluded that the number of nodes, *Figure 38*,[7] is different at the three points of the Brillouin zone and, as the highest number is at M and the lowest at Γ, the highest energy corresponds to the former and the lowest to the latter point.

By solving the secular equations, the energy solutions for the square lattice take the form:

$$E_j = \alpha + 2\beta \cos\{(k_x a) + \cos(k_y a)\}$$

It is clear after observing *Figure 38* that the wave function at M is clearly antibonding and presents the maximum possible number of nodes in both the *x* and the *y* directions. *Figure 39* illustrates the dispersion energy diagram for this equally spaced 2D lattice of hydrogen atoms. At X the wave function is mostly non-bonding, because it shows the same number of bonding and antibonding interactions and is clearly bonding at Γ where all the interactions have a bonding character.

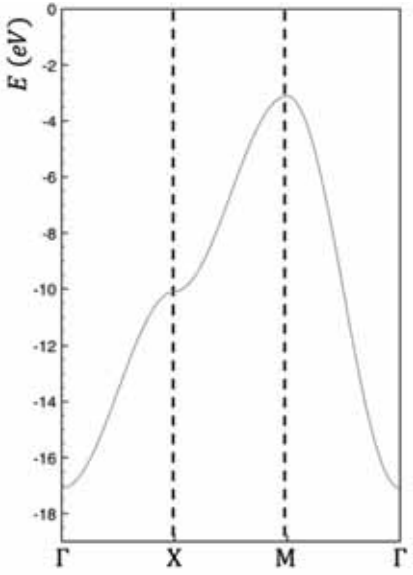

Figure 39. Dispersion energy diagram for a hydrogen square lattice.

[7] Note that full and empty symbols stand for different polarities of the wave function

Adding orbitals to the atoms forming our square lattice adds complexity. Two of the three *p* orbitals lie on the square lattice plane and the third one is perpendicular to our square lattice. Let us imagine an N atoms 2D lattice, for which a projection of the orbital icons on the *xy* plane is shown in *Figure 40* for the special points Γ, M, and X. It is clear that the crystal orbitals are characterized by σ and π interactions. These interactions at Γ, M, and X are schematized in *Table 5*.

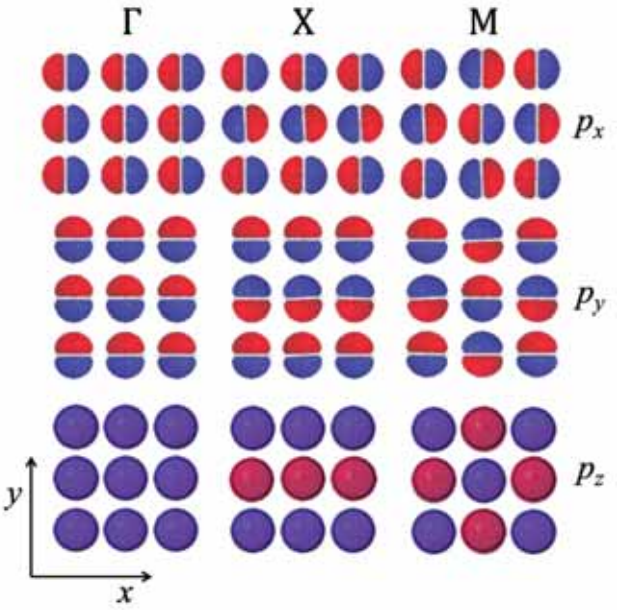

Figure 40. Sketch of the three *p* crystal orbitals formed at the special points Γ, M, and X of the first Brillouin zone.

Table 5. Interactions between p orbitals in a square lattice of nitrogen atoms.

	Γ		*X*		*M*	
	x	*y*	*x*	*y*	*x*	*y*
p_x	σ^*	π	σ^*	π^*	σ	π^*
p_y	π	σ^*	π	σ	π^*	σ
p_z	π	π	π	π^*	π^*	π^*

The p_x,p_y-p_x,p_y interactions are stronger than the p_z-p_z ones, because the σ overlap is greater than the π overlap. Recalling that both the stabilization and the destabilization energies are a function of the overlap integral, it is clear that the highest energy corresponds to p_x, the orbitals at point X, and the lowest energy to p_y at the same special point. At points Γ and M, p_x and p_y crystal orbitals are degenerate in energy, although the energy is higher at Γ, because the σ interaction is stronger than the π one.

Qualitatively this dispersion energy diagram is universal for all the square lattices, depending on the width of the interatomic distance, the shortest distances having the widest bands. However, we may expect complications due to the mixing of *s* and *p* orbitals and to the interaction of bands of the same symmetry. The universal dispersion energy diagram is shown in *Figure 41*.

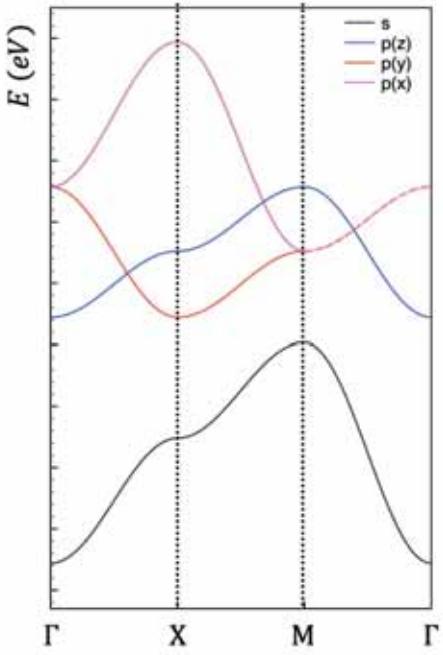

Figure 41. Qualitative energy dispersion diagram for a square lattice of *N* atoms

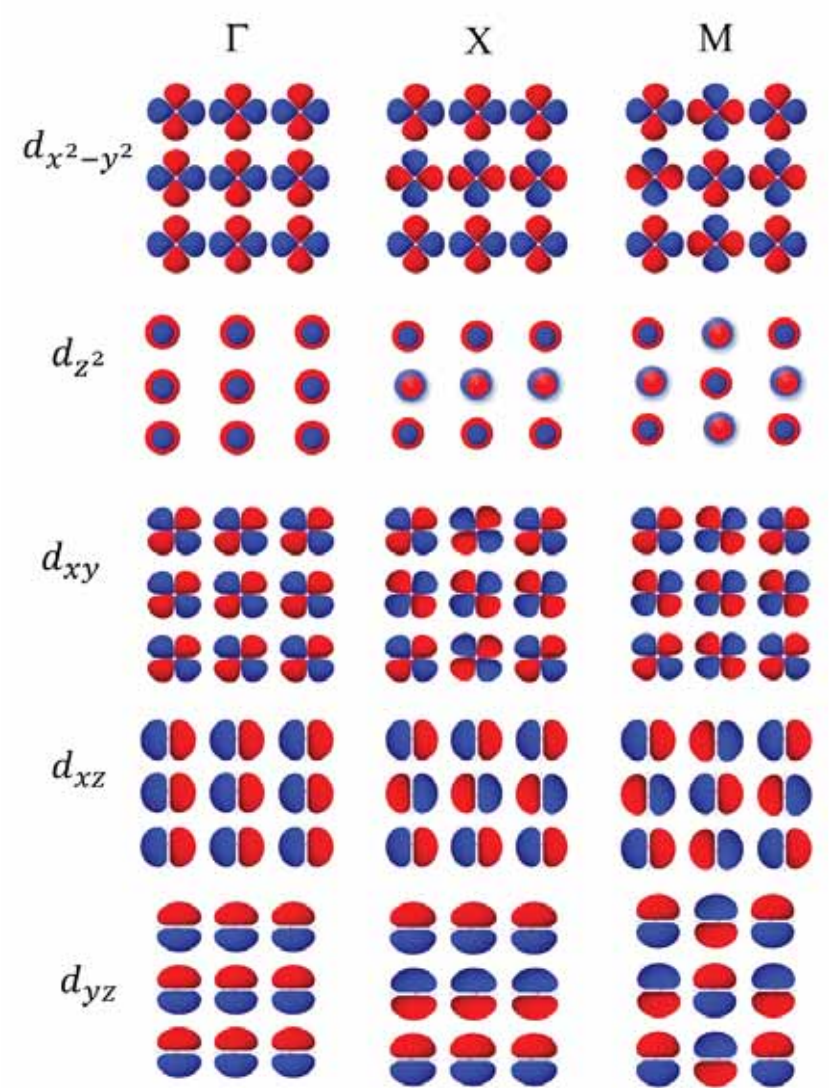

Figure 42. Sketch of the five *d* crystal orbitals formed at the special points Γ, M, and X of the first Brillouin zone. Note that all the sketches correspond to the projection on the *xy* plane

Let us consider a 2D ferrous crystal, in order for a comprehensive analysis of the behavior of the different atomic orbitals in this square lattice. There are no differences with the previous square lattice of hydrogen atoms except for the presence of a larger number of atomic orbitals including *p* and *d* orbitals.

Figure 42 outlines the icons and the orbital icons for the Bloch functions at the special points Γ, M, and X. The interaction between $d_{x^2-y^2}$ and d_{z^2} result in σ type functions, while π type functions result from interaction of the d_{xy} orbitals. The orbitals, d_{xz} and d_{yz}, that are perpendicular to the square lattice plane present both π and δ type interactions, as outlined in *Figure 43*.

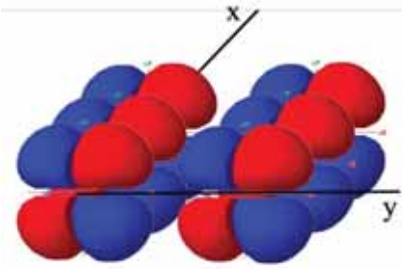

Figure 43. Representation of the π*-antibonding and δ-bonding interactions on a square array of d_{xz} orbitals.

These five *d* orbitals will result in five bands, because there is one iron atom per unit cell. Note that for the sake of clarity, bands *s* and *p* have been omitted from the structure, because the dispersion energy diagram for these bands is qualitatively exactly the same, as described in *Figure 41* and as stated above.

At Γ, the only degenerate bands are d_{xz} and d_{yz} that present δ-bonding and π*-antibonding interactions, respectively. The d_{xy} band has the highest energy, because it undergoes π*-antibonding interactions while the $d_{x^2-y^2}$ band has the lowest energy, characterized by σ-bonding interactions along both the *x* and the *y* axes. The d_{z^2} band of intermediate energy is perpendicular to the *xy* plane, which shows δ-bonding interactions along both the *x* and the *y* axes. Therefore, *d* orbitals are no longer degenerate at Γ.

From points Γ to X, both the $d_{x^2-y^2}$ and d_{z^2} bands, whose symmetry is independent of the Γ mix, and the resulting bands are linear combinations of both bands, $d_{x^2-y^2} \pm d_{z^2}$. This mixing point is marked by a dot in *Figure 43*. The d_{xz} and d_{yz} bands are no longer degenerate at X, because d_{xz} shows δ-and π-bonding interactions and the d_{yz} band shows δ*- and π*-antibonding interactions. Finally, at this point the d_{xy} band is essentially non-bonding, because it presents π-bonding in the *y* direction and π*-antibonding in the *x* direction.

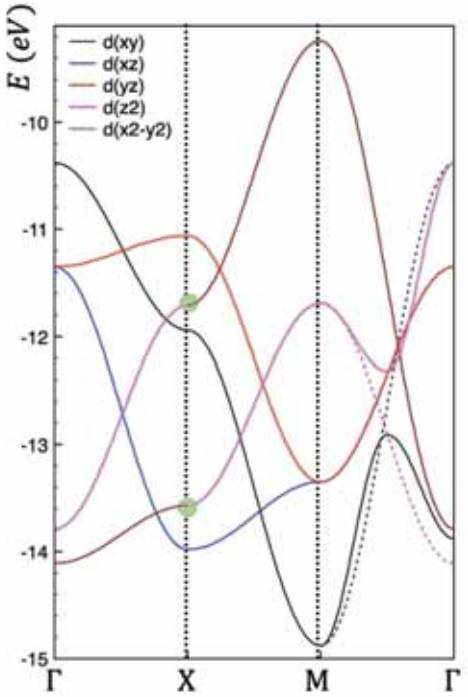

Figure 44. Energy dispersion diagram for the *d* bands of a square lattice of Fe atoms. The green dots indicate the point where the bands mixed

The d_{xz} and d_{yz} bands are degenerate at point M, showing δ*-antibonding and π-bonding interactions. The energy of the $d_{x^2-y^2}$ and d_{xy} bands from X to M is reversed, as the energy of the $d_{x^2-y^2}$ band is now higher (σ*-antibonding) than the one for d_{xy} (π-bonding). The symmetry of the $d_{x^2-y^2}$and d_{z^2} bands is no longer the same, but the d_{xy} and d_{z^2} bands now have the same symmetry and they strongly interact. The symmetry

properties avoid the crossing of bands of the same symmetry, between M and Γ. The degenerate bands, d_{xz} and d_{yz}, slightly differ in energy, although this aspect is not included in *Figure 44*.

The addition of a third dimension will not modify the solution scheme of the different Bloch functions, but complicate to an extreme the solution of the equation system. The first Brillouin zone accounts for a volume around every lattice point and the number of special lattice points at the edge of this zone multiply in as many different directions as the lattice symmetry may allow. Let us, therefore, leave the calculations of the dispersion energy bands to powerful computers.

The electronic structure of adsorbed monolayers

The 2D problem studied so far is clearly a relevant one for studying surface interactions that are of paramount importance in catalytic processes. Although, the most compact face of Ni is (111), we will analyze the effect of CO adsorption on Ni(100), because the simpler surface geometry of this face, which for the sake of simplicity we will assume remains unaltered after chemisorption, favours our qualitative treatment. This picture is clearly simplified, because we know that surfaces may reconstruct upon adsorption.

At low coverages, CO molecules form an ordered Ni(100)-(2x2) CO surface structure. In this structure, CO molecules are adsorbed on top of surface Ni atoms, essentially perpendicular to the surface with a Ni-C distance ~1.75Å, *Figure 45*.

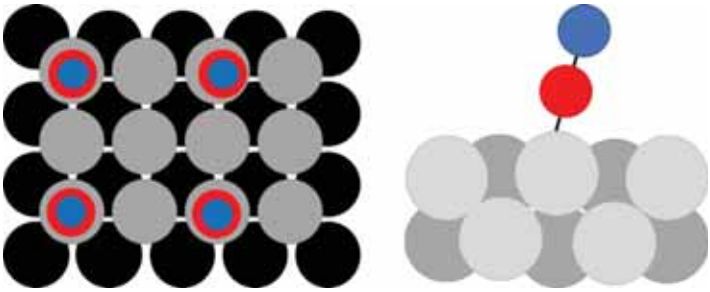

Figure 45. Front and side views of the Ni(100)-(2x2) CO surface structure

CO molecules interact with the Ni surface forming Ni–C covalent bonds mainly of a σ character, while there are further changes within the CO

molecule consistent with added charge in a molecular π-symmetry state. The bonding scheme is consistent with the traditional view of *σ*-donation from the CO to the metal and the *π* back-bonding from the metal to the molecule.[8]

The band structure was analyzed by Inverse Photoemission Spectroscopy and Photoelectron Spectroscopy for sampling both the filled and the empty valence band states. Experimentally, a broad empty band was observed at 4.5 eV above the Fermi level with a component at 1.8 eV, assigned to the bonding and antibonding components of the *2π*-derived band of adsorbed CO. Using Photoelectron Spectroscopy, it has been shown that the*1π* and 5σ bands of adsorbed CO overlap with a maximum in the density of states at ~-7 eV, and the thinner *4σ* band appears at ~-11 eV below the Femi level is placed in the middle of the Ni *d* band.[9] The bands arising from the interaction of the MO of adsorbed CO, *Figure 46*, show a similar behavior to those arising from atomic orbitals of the same symmetry.

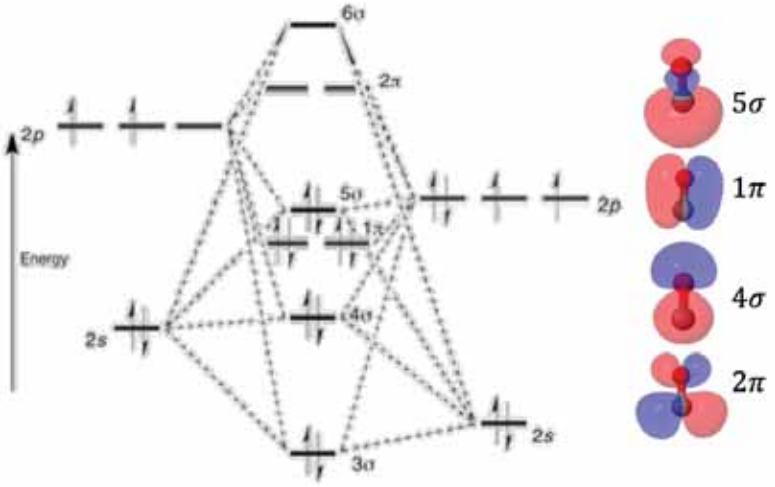

Figure 46. MO diagram and orbital shapes of the CO molecule

[8] J.T. Hoeft *et al.*
[9] W. Reimer *et al.*

The symmetry of the 2π orbital of CO is similar to that of *d* orbitals, *Figure 46*. Therefore, the dispersion energy diagram for these bands are quite similar to those originating in d_{xz} and d_{yz} in *3d* metals, *Figure 43*.

They are degenerated at Γ and M, but at X they split. A similar behavior was expected for the two degenerate 1π orbitals, but in this case its behaviour is *p*-like, *Figure 40*. The *4σ* and *5σ* orbitals present p_z and d_{z^2}-like behaviour, respectively with the lowest energy at Γ and the highest at M.

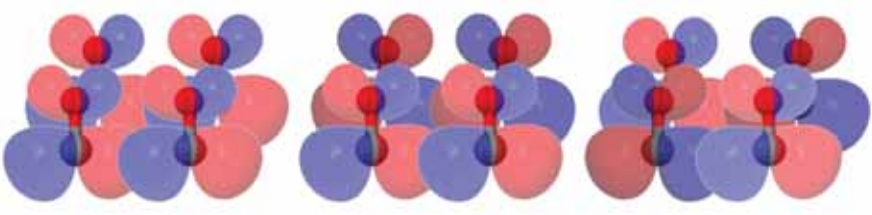

Figure 47. Overlap of 2π orbitals of adsorbed CO at Γ, M, and X

The spreading of the *s* band depends on the CO-CO distance on the Ni surface. As the coverage (the number of CO molecules per unit surface area) increases, the distance between the molecules will decrease, the interaction will be stronger, and the bands will widen. In addition, we have to consider the bands arising from the interaction of Ni orbitals. *Figure 47* provides a simplified view of the *3d* orbital interactions.

The CO molecules interact with the Ni orbitals and, from a rough approximation, the CO *4σ* and *5σ* orbitals that present p_z and d_{z^2}-like behavior clearly interact with the p_z and the d_{z^2} orbitals of Ni and the 2π one interacts with Ni d_{xz} and d_{yz} bands. This behavior is clearly seen in *Figure 47* that presents the calculated density of states of square lattices of unsupported and Ni-supported CO overlayers.

The most relevant features of these DOS is the strong modification of the *5σ* and the *2π* bands upon chemisorption on Ni(100). The *5σ* orbital energy levels shift downwards to form new states by mixing *5σ, 1π* and Ni d_{z^2} orbitals, and the *2π* band clearly interacts with the substrate orbitals, in such a way that the Ni charge density is transferred to these states, leading to a partial occupation of the antibonding *2π** states and of bonding states between C and Ni atoms.

Density of states

Throughout this chapter, we have been dealing with the density of states that is the number of levels between E and $E + dE$. This concept in some way returns to that of frontier orbitals.

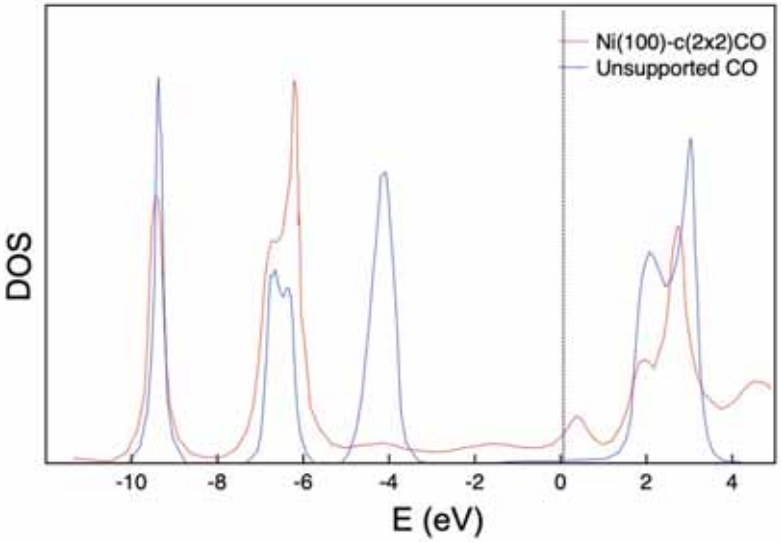

Figure 48. Density of states projected onto C spheres for square lattices of unsupported and Ni(100) supported CO overlayers. Adapted from Freeman *et al.*[10]

The shape of the DOS is predictable from the band structure, because they are by definition the derivative of the dispersion energy curve. For instance, *Figure 48* presents the DOS of half a monolayer of CO adsorbed on Ni(100). It is clear that the CO molecule has a 5σ HOMO orbital and a 2π LUMO orbital. The corresponding bands in the unsupported square lattice of CO at ~-4 and ~2-4 eV are the highest energy occupied and the lowest energy empty bands in a concept similar to the HOMO and LUMO orbitals. Upon interaction with the Ni surface energy, states appear close to the Fermi level of Ni, placed at zero, which is an indication of Ni-CO bond formation. An additional advantage of DOS curves is that they return to the real space

[10] A. J. Freeman *et al.*

showing an average charge density within the Brillouin zone and providing an intuitive interpretation of the bonding characteristics.

Let us return to our 1D platinocyanide linear chain. A portion of the energy dispersion diagram together with the calculated DOS is shown in *Figure 49*.

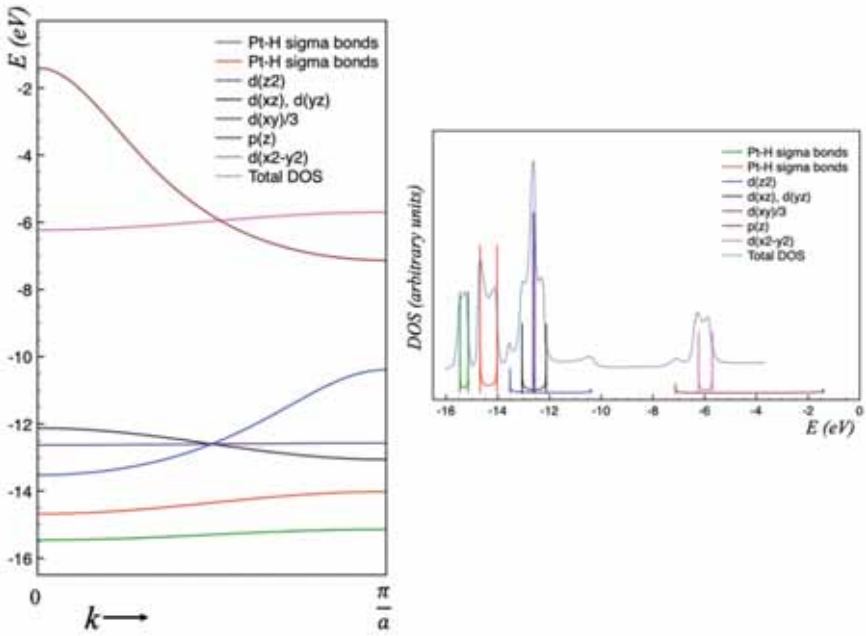

Figure 49. Qualitative dispersion energy diagram and DOS for linear 16 electron complexes. The DOS of each band is plotted together with the Total DOS subjected to Gaussian smoothing.

The main interactions within this linear chain are located along the solid axis between the d_{z^2} and p_z orbitals of platinum that form σ-type bonds followed by the π-type ones formed by the interaction of the d_{xz} and the d_{yz} orbitals, while all other interactions are quite small. The band width, as should be expected, is higher for the stronger interactions decreasing in width as the interactions are reduced.

The Density-Of-States (DOS) is a quite useful function. As stated above steep bands account for lower DOS while flat bands result in higher DOS. The diagram in *Figure 49* clearly shows that the completely flat d_{xy} band results in the highest DOS. The DOS is proportional to the velocity of electrons, *v*, in the band:

$$\left(\frac{dE}{dk}\right)^{-1} \propto v^{-1}$$

This relation between the DOS and electron velocity clearly indicates that the flatter the band the lower the mobility of electrons and therefore the electrons in these bands cannot be easily moved and are mainly located on atoms. On the contrary, wider bands mean high velocity electrons that are highly delocalized. Before increasing the number of dimensions, a crucial chemical question must be addressed: to characterize the electron structure in terms of bonding properties. Linking this concept to the well-known molecular case, we may start with the electronic structure of H_2^+. The electron density is given by the integral over all the space of the square of the wave function.

$$\int \psi^* \psi d\tau = \int \psi^2 d\tau = \int (c_1\phi_1 + c_2\phi_2)^2 \, d\tau = 1$$

$$\int \psi^2 d\tau = c_1^2 \int \phi_1^2 d\tau + c_2^2 \int \phi_2^2 d\tau + 2c_1c_2 \int \phi_1\phi_2 d\tau$$

As we have used normalized functions the three first integrals are just unity and the last one is the overlap integral, S_{12}. The last term, $2c_1c_2S_{12}$, is the *overlap population* or *Mulliken population* and accounts for the charge every atom holds in the bond. For an H-H distance of 0.74Å, Slater-type orbitals and the expression for the coefficients

$$c_1 = c_2 = \frac{1}{\sqrt{2(1 + S_{12})}}$$

It is possible to calculate the overlap integral, $S_{12} \approx 0{,}64$, and then the charge distribution in the bond.

$$1 = \frac{1}{2(1 + S_{12})} + \frac{1}{2(1 + S_{12})} + \frac{2}{2(1 + S_{12})} = 0.305 + 0.305 + 0.390$$

For the H_2 molecule, we simply have to multiply these figures by 2, thereby accounting for the total number of electrons of this molecule. We assume

that the *Mulliken population* consists of 0.78 bonding electrons, but it is obvious that electrons cannot be divided, which generates serious difficulties when interpreting the results.

This approach can be easily extended to crystal orbitals. The total number of electrons, *N*, is a function of the coefficients, $c_{\mu i}$, of the AOs, ϕ_i, centered on atom A forming the crystal orbital that has an occupation number, f_i, equal to 0.1 or 2.

$$N = \sum_A \sum_{\substack{\mu \\ \mu \in A}} \sum_i^m f_i c_{\mu i}^2 + 2 \sum_A \sum_{B>A} \sum_{\substack{\mu \\ \mu \in A}} \sum_{\substack{\nu \\ \nu \in A}} \sum_i^m f_i c_{\mu i} c_{\nu i} S_{\mu\nu}$$

Despite the alarming aspect of this expression, it is no different from the H_2 molecule, except for the number of atoms and the *k*-dependence of the coefficients. The mathematical treatment is clearly not as simple as it is for the H_2 molecule and powerful computers have to perform the sum of all the contributions for each atomic orbital at a given centre over every occupied crystal orbital. By averaging these results for the whole *k* range, we can divide up the total DOS into contributions of the different atoms.

Although the solution of this portioning function is complicated, we may obtain qualitative information in a relatively easy way. Let us recover our first example on the band structure of TiC, TiN and TiO to apply the knowledge obtained from developing band structures of simple transition metal compounds. All these solids present a structure that may be described as a cubic eutectic 3D array of oxide anions with metals occupying octahedral holes, or alternatively as the packing of MO_6 octahedra sharing edges with its neighbours. Therefore, both metal cation and anions lie in an octahedral environment and considering MO_6 as the basic bonding unit, we may start by describing the bonding in these "*monomeric units*". In the classic MO diagram for octahedral coordination, the σ bonds are formed by the interaction of the a_{1g}, t_{1u} and e_g *SALC* combination of *2s* and *2p* orbitals of the surrounding six anions and the *4s* (a_{1g}), *4p* (t_{1u}), $3d_{z^2}$ and $3d_{x^2-y^2}$ (e_g) orbitals of the Ti cation, respectively. The largest interactions are between the *s* and *p* orbitals of both Ti and the anion and the smallest between the *d* orbitals and the *SALC* of the anions, *Figure 50*.

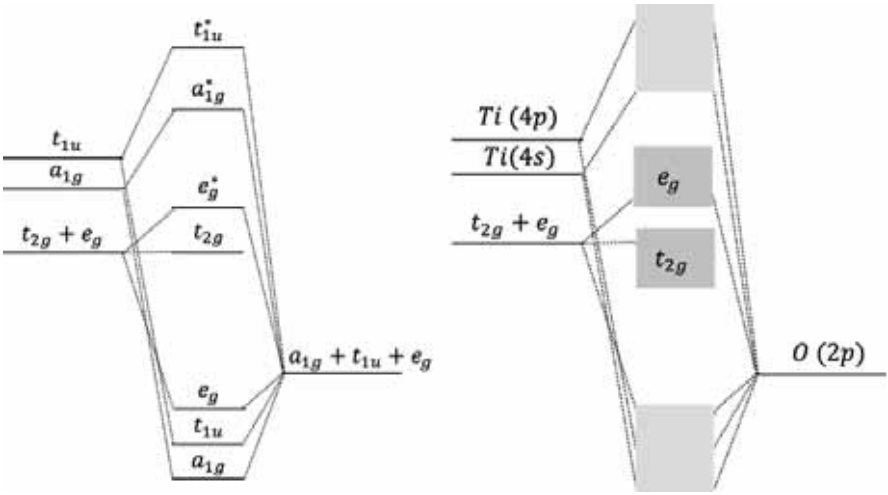

Figure 50. Octahedral coordination. Left: Qualitative MO diagrams. Right: schematic band diagrams. For the sake of simplicity, the π *p-d* interactions are omitted in the MO diagram.

If we only consider the σ bonds, the metal t_{2g} orbitals remain non-bonding and are localized on the Ti atoms. We may consider a weak π-type interaction of these *3d* orbitals with p orbitals of the anions. However, as shown in Figure 1, if we consider the interactions with the next-nearest neighbours, Ti t_{2g} orbitals give rise to metal-metal bonding. It should be noted that the M-M distance is $\sqrt{2}d_{M-O}$ and, for anions of the first row, these M-M distances are in fact close enough to form bonds. The Ti-Ti distances are in the 2,13-2,17 Å range for these three solids and the Ti-X ones close to 1.5 Å for all of them. The influence of the metal-metal bond is shown in the metallic conductivity of the three solids that is of a similar order of magnitude to the conductivity of bulk titanium. Considering all the interactions, the band structure may be schematized, as shown in *Figure 50*.

From the standpoint of chemistry, we may say that the deepest energy levels are mainly the non-metal *2p* levels and the levels above these are mainly *d* in character from titanium. As should be expected, the *d* band in the octahedral environment splits into t_{2g} and e_g orbitals, but they may overlap upon interactions in the solid. The presence or not of a gap between these levels depends on the relative sizes of cation and anion and the energy differences between the metal and non-metal atomic orbitals. *Figure 51* presents the atom-projected and orbital-projected density of states of these

solids. As should be expected, the anion character is higher in the deepest-lying bands while the *d* bands appear close to the Fermi level. Note the scale that represents the energy difference between the actual value and the value of the Fermi level. It is clear that there is no band gap between the t_{2g} and e_g bands that overlap in all these solids, which explains their metallic conductivity. The σ bond model shows that the e_g band is destabilized by the M-X interaction, its width being a function of the metal-non-metal overlap. The t_{2g} band is also destabilized by interaction with the oxygen *p* orbitals, forming π bonds, which may be observed in *Figure 51* by the small contribution of *p* orbitals in the uppermost levels of the *d* band. Therefore, most of the t_{2g} band accounts for Ti-Ti interactions.

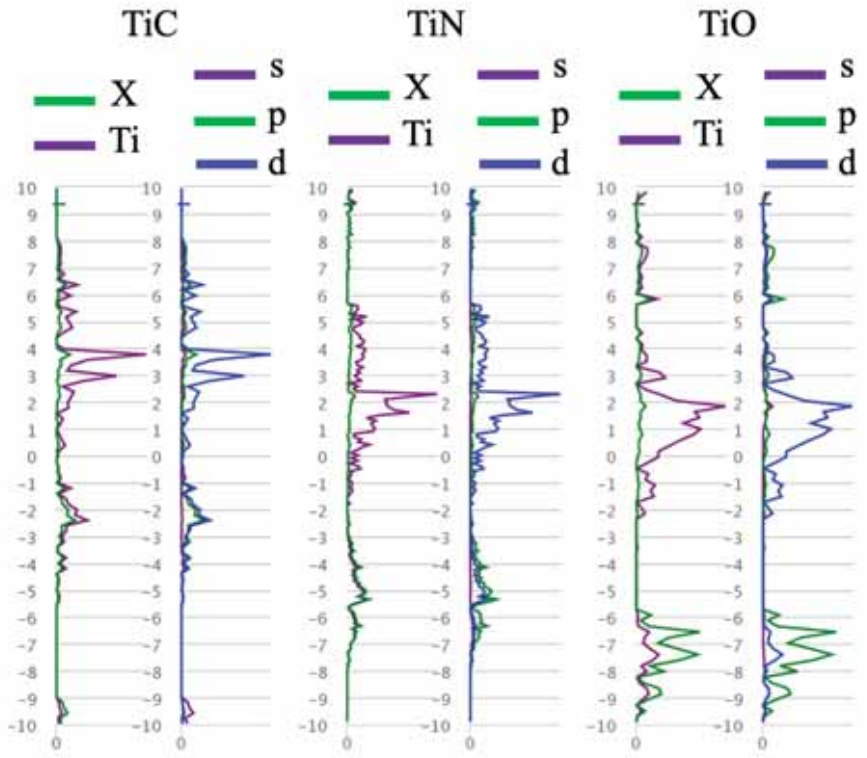

Figure 51. Atom-projected and orbital-projected density of states of TiC, TiN and TiO.[11]

[11] A. Jain *et al.*

This approach can be extended to the band structure of rocksalt-type first transition series metal monoxides. The first members of this series of compounds, TiO and VO, show properties that are characteristic of metallic or semi-metallic compounds (delocalized electrons) while MnO, FeO, CoO, and NiO behave as semiconductors and show properties of localized electrons. The differences between their properties must be understood on the basis of differences in orbital overlap. On increasing the nuclear charge, 3d orbitals contract and decrease the interaction between t_{2g} orbitals between the nearest-neighbour metals. Therefore, ongoing Ti to Ni metal-metal interactions decrease and increasingly the t_{2g} is localized on the metal atoms. The energy difference between the metal *d* orbitals and the oxygen *p* orbitals decreases throughout the series, increasing the interactions along the M-O-M axis that involves the e_g orbitals, the smaller the energy difference the higher the covalence of the bonding, a difference that reaches a minimum for NiO. Moreover, 180º of the M-O-M bonds permit cation-anion-cation super-exchange interactions through the metal e_g orbitals, which explains the antiferromagnetic behavior of MnO, FeO, CoO, and NiO.

References and used books

Chemical Bonding in Solids, J. Burdett, Oxford University Press, 1995

Solids and Surfaces: A Chemist's View of Bonding in Extended Structures, Roald Hoffmann, Wiley-Interscience, 1989.

Computational Chemistry of Solid State Materials, Richard Dronskovski, Willey-VCH, 2005.

H. Basch, A. Viste, H.B. Gray, *Theoret. Chim. Acta* 3, 1965, 458

Mater. Sci. Eng. 12, 2004, 21.G.K.L. Cranstoun, R.G. Egdell, M.D. Hill, R. Samson, *J. Electron Spectrosc. Phenom.* 33, 1984, 23.

J.T. Hoeft, M. Polcik, D.I. Sayago, M. Kittel, R. Terborg, R.L. Toomes, J. Robinson, D.P. Woodruff, M. Pascal, G. Nisbet, C.L.A. Lamont, *Surf. Sci.* 540, 2003, 441

W. Reimer, Th, Fink, J. Küppers, *Surf. Sci.* 193, 1988, 259

A. J. Freeman, C. L. Fu, E. Wimmer, *J. Vac. Sci. Technol.* A 4, 1986, 1265.

A. Jain, S.P. Ong, G. Hautier, W. Chen, W.D. Richards, S. Dacek, S. Cholia, D. Gunter, D. Skinner, G. Ceder, K.A. Persson, The Materials Project: A materials genome approach to accelerating materials innovation, *APL Materials*, 2013, 1, 011002.

CHAPTER 4

STRUCTURE DETERMINATION: X-RAY DIFFRACTION

"It seemed at first a new kind of invisible light.
It was clearly something new, something unrecorded"
W. C. Röntgen

Wilhelm Conrad Röntgen discovered X-rays in 1895, which rapidly found application in medicine due to their extraordinary ability to penetrate opaque objects. X-rays (wavelengths 0.1-100 Å) are a part of the electromagnetic spectrum situated in the interval between ultraviolet and gamma radiation (*Figure 1*).

X-rays can be classified as "hard" and "soft" based on their penetration ability and they are used in different techniques according to their interaction with matter. The wavelengths of conventional X-ray fluorescence are within the 0.3-10 Å range, whereas the interval employed in diffraction techniques is much shorter (0.5-2.5 Å). The order of magnitude of the latter range corresponds exactly to the order of packing observed for crystal structures. Although it was impossible to confirm those structures before the discovery of X-rays, the order of the solids was predicted on the basis of morphological data suggesting repetitive periodic construction of motifs at distances between 1 and 3 Å. Hence, X-ray diffraction has rapidly become fundamental for elucidating crystal structures and has come to be known as the chemical *fingerprint* of all crystalline materials.

Before considering how X-rays interact with crystals, it is worth mentioning how they originate. X-ray radiation is initiated when small-mass high-kinetic energy particles collide with matter (a target) and a loss of energy occurs. The largest part of the energy is lost as heat and a small part is emitted as X-rays. Experimentally, the X-rays are generated using electrons in so called X-ray tubes (*Figure 2*).

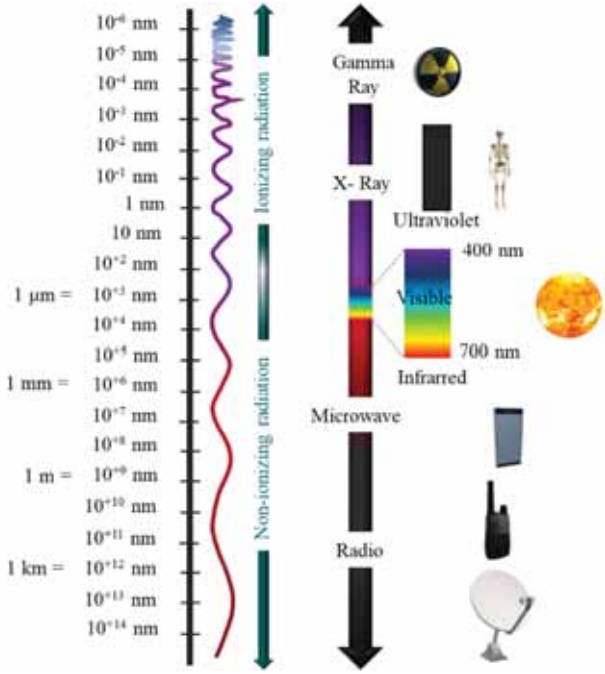

Figure 1. Electromagnetic spectrum

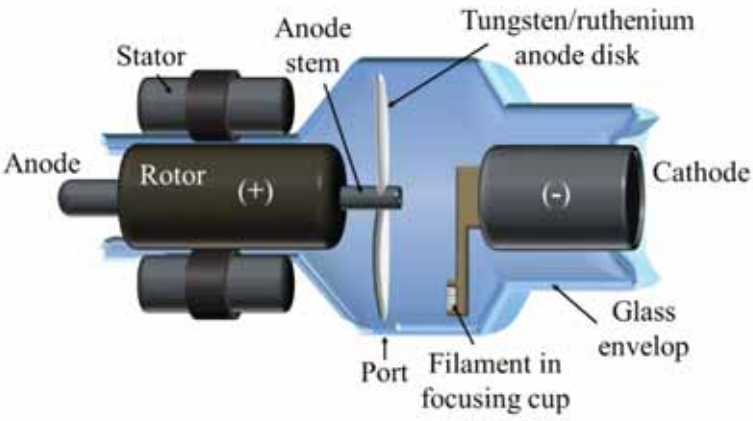

Figure 2. Schematic representation of an X-ray tube

X-ray tubes consists of anode, cathode and filament sealed all together in a glass cylinder in a vacuum (10^{-7} mm Hg). When applying a voltage, the electrons released by the incandescent filament are accelerated towards the anode (anticathode), collide with it, and initiate the emission of X-rays. The filament, a tungsten wire, is situated in a focusing cup and directs most of the electrons toward the anode, by applying a negative potential to repel all other directions. If we analyze the anode-emitted radiation at distinct voltages, we can see that under certain values the intensity distribution of the emitted wavelengths appears continuous (*Figure 3*).

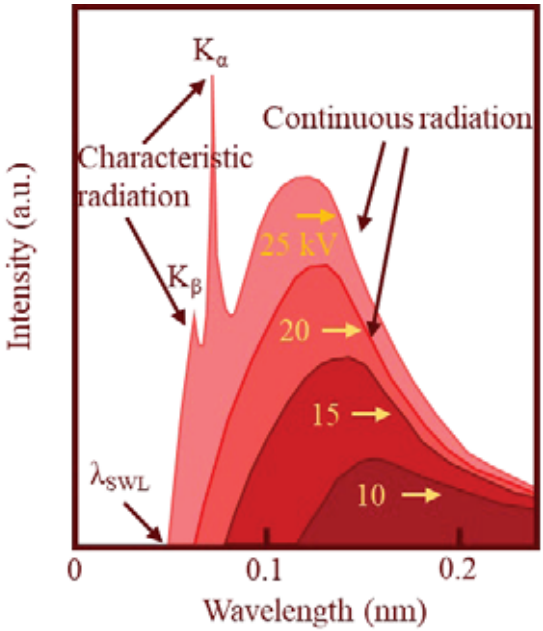

Figure 3. Intensity distribution of emitted X-rays from Mo filament at different voltages

This type of radiation is called *continuous* (*polychromatic* or *white*) spectrum radiation and results from the deceleration of the electrons hitting the anticathode. It is a monotonic function increasing with voltage and shifting to shorter wavelengths until reaching a zero value, known as the *short wavelength limit*. The total continuous X-ray energy emitted by the target depends on the atomic number of the target and the X-ray tube voltage. When the voltage exceeds a certain value, characteristic for every

material, discontinuities arise, i.e., a few intensity maxima superposed upon the continuous spectrum at specific wavelengths. Those maxima, discovered by W. H. Bragg and H. G. Moseley, are *characteristic lines* forming the *characteristic spectrum* of the anticathode (target) at a voltage value corresponding to the *critical excitation lim*it. In the case of molybdenum, the characteristic lines appear at voltages higher than 20 kV and in series, labelled ***K, L, M***, according to their atomistic roots. The series originates when a colliding electron with a sufficiently high energy ejects an electron from the inner shells of the target material. This situation is energetically unstable and the hole that is produced fills up with electrons from the outer shells, emitting characteristic radiation. All transitions must obey certain rules (*Figure 4*).

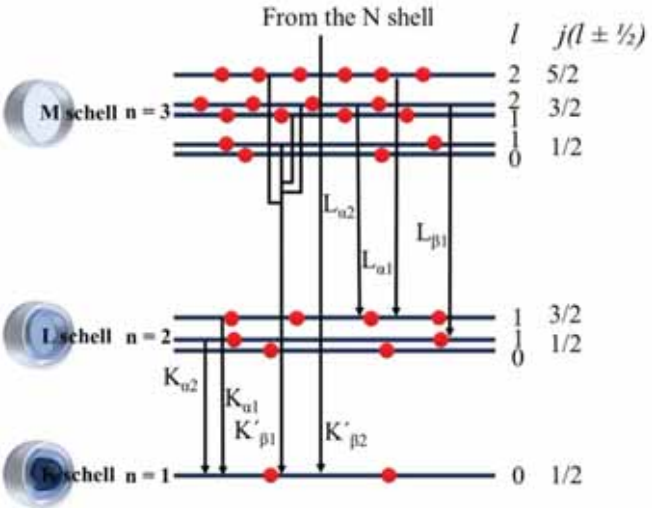

Figure 4. General energy level diagram.

Only the transitions with orbital angular momentum of electron (l=0, n-*1*) and total orbital angular momentum ($j=l+½$) are permitted, thus leading to the general *selection rules*:

$$\Delta l=\pm 1\ ,\ \Delta j=\pm 1 \text{ or } 0$$

Therefore, the radiation of the K series consists of frequencies with the same spectral term difference originated by the transition between the K shell and another of minor energy (L, M,…). The number of permitted transitions is important, but only those of high intensity are in practice detected in

conventional equipment. Thus, the most frequent transition of higher intensity begins with an electron that originates at the L_{III} sublevel and moves to the K level emitting the $K_{\alpha 1}$ line ($L_{III} \rightarrow K$ or $2p^{3/2} \rightarrow 1s$). Analogically, the $L_{II} \rightarrow K$ and $M_{III} \rightarrow K$ originates the $K_{\alpha 2}$ and $K_{\beta 1}$ lines. Sometimes, it is difficult to separate $K_{\alpha 1}$ and $K_{\alpha 2}$ lines; a doublet is formed when the L sublevels are similar in energy. In this case, an average value of both constitutes the K_{α} (av.) and is used as an X-ray wavelength. Some commonly used X-ray wavelengths are listed in Appendix 3.

X-ray interaction with matter

When the incident X-rays encounter matter, a series of phenomena are initiated conditioned by the radiation cross-path through the object. The X-rays can penetrate the object without interaction, or they can be completely absorbed, or scattered from their original direction, losing a part of their energy (*Figure 5*). Only a certain part of the energy is recovered, due to the absorption process, either as photoelectrons or by fluorescence emission. An additional mechanism is the scattering process, described as initial absorption and subsequent reemission of electromagnetic radiation. When the energy of the incident and the photon emissions coincide, the radiation is *elastically scattered*, unless a loss of energy occurs, in which case it is regarded as *inelastic scattering*.

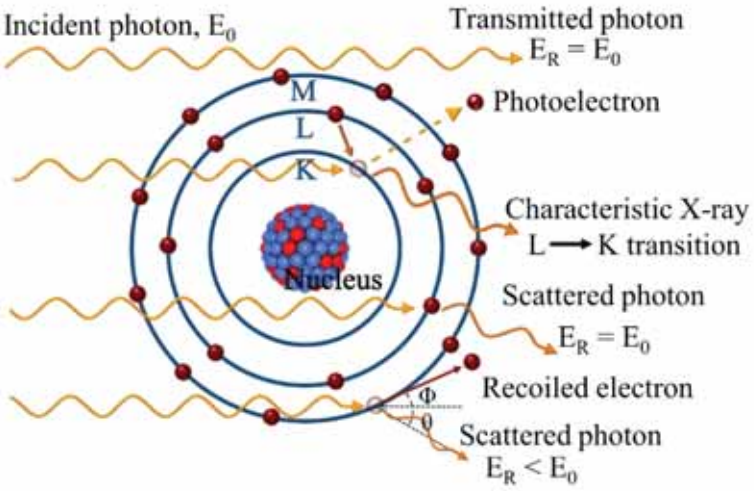

Figure 5. Interaction of X rays with matter

X-ray diffraction

The diffraction is characteristic for all waves and can be defined as the wave behavior modification upon interaction with an object. Crystal X-ray diffraction was demonstrated by M. von Laue, Friedrich and Knipping following their consideration of an analogy between X-rays and the behaviour of light. Laue, based on J.C. Maxwell's theory for wave propagation, postulated that if we consider X-ray radiation as a wave, and its wavelength has the same magnitude as the periodic distances found in a crystal (a few Å), the incident radiation should be diffracted.

Friedrich and Knipping were indeed able to observe the diffraction of the $CuSO_4.5H_2O$ crystal (*Figure 6*) and this observation, together with the theory proposed by Laue, was the foundation for a great advance, leading to the elucidation of the first crystal structure a year later by the Braggs, father and son.

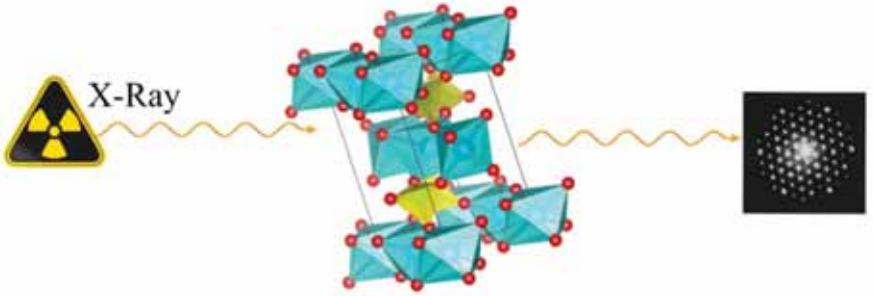

Figure 6. Schematic representation of Friedrich and Knipping's experiment and X-ray diffraction of $CuSO_4$.

Reciprocal space

Before entering into the fundamentals of X-ray diffraction we should define the concept of reciprocal space where the phenomena related to X-ray diffraction are more easily interpreted. The importance of this concept is based on the fact that any X-ray diffraction is the representation of a distorted 2D reciprocal space diagram corresponding to real space. The concept was introduced by P. P. Ewald in 1921 and it allows the complex set of family planes in the real lattice to be replaced by an equivalent simpler set of points in the reciprocal lattice. *But how to represent all possible sets of planes with one point?* To do so, a perpendicular to every set of planes,

Problem I *Construct the reciprocal lattice in the* ***x-z*** *plane of a primitive monoclinic lattice (****y****, direction perpendicular to the projection plane).*

1. On the *x-z* plane of the monoclinic lattice, planes (100) and (001) are identified and a perpendicular is traced from the point of origin.
2. The reciprocal lattice (001*) and (1*00) points on that normal are at distances of $1/d_{001}$ and $1/d_{100}$, respectively.

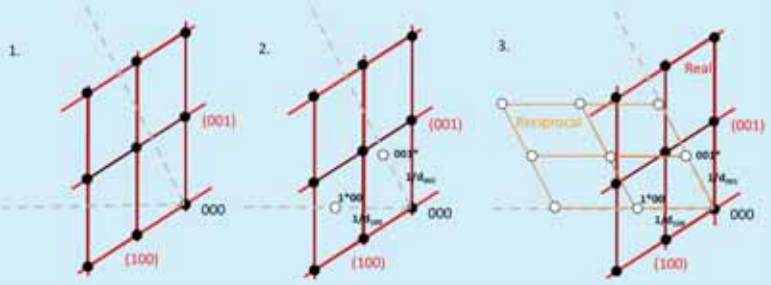

3. Points 001^* and 1^*00 on the reciprocal lattice represent the orientation of the relative planes (001) and (100) of the crystal. With this point and the origin, we can construct the reciprocal lattice, taking the two new vectors a^* and c^* as the reciprocal axes. Those parameters determine the points of separation and are monotonically repeated in both directions to produce reciprocal points corresponding to the set of planes with indices (h0k).

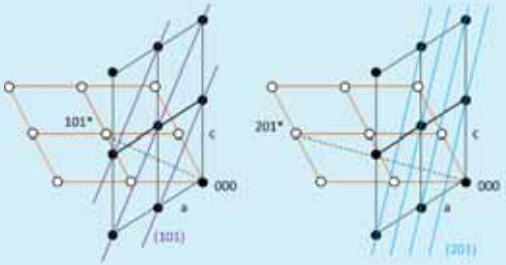

4.

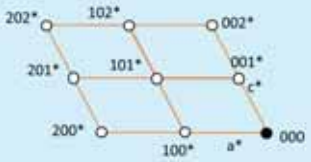

hkl, is traced to a distance d^* inversely proportional to the interplanar spacing, d_{hkl}, of the (*hkl*) family planes ($d^*=1/d_{hkl}$) where the reciprocal point is positioned. The direction of the reciprocal vector indicates the orientation of the direct lattice planes with respect to the crystallographic axis. The origin of both lattices is the same, being the starting point for the reciprocal lattice from the real one.

The parameters of the reciprocal lattice are conventionally defined as a^*, b^*, c^* and a^*, b^* and g^*. By definition, the reciprocal axes are perpendicular to the direct axes which define the lattice.

$$a^* \perp bc,\ b^* \perp ac \text{ and } c^* \perp ab$$

So, the parameters can be calculated as follows:

$$a^* = [b \bullet c]/V;\ b^* = [a \bullet c]/V \text{ and } c^* = [a \bullet b]/V$$

where, the square parenthesis indicates the vectorial product of the lattice parameters and V is the volume of the direct cell, defined as a scalar magnitude where $V=a[b \bullet c]$. As the reciprocal parameters are perpendicular to the real lattice parameters, the scalar product of each real parameter with its reciprocal homologue is equal to unity (or to 2π when the Brillouin zone is defined). Thus

$$a \bullet a^* = 1 = a[b \bullet c]/V = V/V = 1;\ b \bullet b^* = 1 \text{ and } c \bullet c^* = 1$$

And any product of a direct lattice parameter to another distinct reciprocal is zero, $c \bullet b^* = 0$. The relation between the area of the parallelogram face—defined by the axis in real space to which the reciprocal vector is perpendicular—and its volume is equal to the module of the reciprocal vector (perpendicular to that face). It is easier to understand, using the orthorhombic (or other orthogonal) real lattice as an example, where the reciprocal axes coincide with the real ones. The module in this case is $a^*=1/a$, $b^*=1/b$ and $c^*=1/c$, and it is equal to the projection of the vector $\boldsymbol{a}$ over the $\boldsymbol{a}^*$ direction.

So, for all orthogonal systems the reciprocal of the reciprocal lattice is the direct lattice.

Thus a^* is perpendicular to *c*, c^* to *a* and both are perpendicular to *b*. The construction of the 3D lattice is now possible (*Figure 7*)

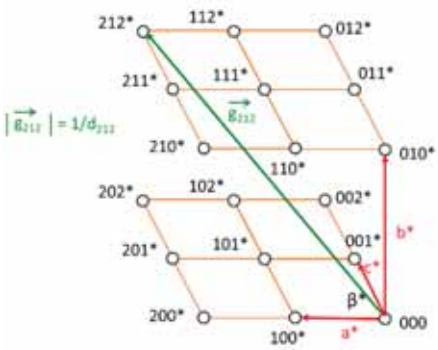

Figure 7. Construction of the 3D reciprocal lattice.

Problem II. *Using a cubic I lattice, draw the projection of the reciprocal lattice viewed along the c axis of the conventional cell.*

Among the properties of the reciprocal lattice, we can highlight that the separation of the reciprocal points is constant, as it is for the direct lattice. The greater the distance in the reciprocal lattice, the lesser the separation between the family of planes in the direct lattice. The distance between two reciprocal points can be measured by the module of the distance vector d*, which is inversely proportional to the spacing between planes defined by the *hkl* Miller indices in the direct lattice.

$$d_{hkl}{}^{*}=\frac{1}{d_{hkl}}=ha^{*}+kb^{*}+lc^{*}=g_{hkl}$$

where, $ha^{*}+kb^{*}+lc^{*}$ are the components of the reciprocal vector g_{hkl} (or $d_{hkl}{}^{*}$).

To describe a point of the reciprocal lattice corresponding to the (*hkl*) plane, we must add i) *h* units of a^{*} over the (h00) direction, k units of b^{*} over the (0*k*0) direction, and *l* units of c^{*} over the (00*l*) direction.

$$\text{with } a^{*} = |g_{hkl}| = \frac{1}{d_{100}},\ b^{*} = |g_{hkl}| = \frac{1}{d_{010}},\ c^{*} = |g_{hkl}| = \frac{1}{d_{100}}$$

And, we can calculate the distance between the planes of the (*hkl*) family for all crystal systems, using the following equation, $d_{hkl}^{*}=\frac{1}{d_{hkl}}=ha^{*}+kb^{*}+lc^{*}$, the module of the reciprocal vector:

$$d_{hkl}^{*}\cdot d_{hkl}^{*}= h^{2}a^{*}\cdot a^{*}+ k^{2}b^{*}\cdot b^{*}+ l^{2}\, c^{*}\cdot c^{*} + hk\, a^{*}\cdot b^{*}+ hl\, a^{*}\cdot c^{*}+ kh\, b^{*}\cdot a^{*}+ kl\, b^{*}\cdot c^{*}+ lh\, c^{*}\cdot a^{*}+lk\, c^{*}\cdot b^{*}$$

and the scalar product:

$$d_{hkl}^{*2}\cdot= h^{2}a^{*2}+ k^{2}b^{*2}+ l^{2}\, c^{*2}+2hka^{*}b^{*}cos\gamma^{*}+2hla^{*}c^{*}cos\beta^{*}+2klb^{*}c^{*}cos\alpha^{*}=1/d_{hkl}^{2}$$

This expression is simplified for all crystal systems, taking into account the relation between reciprocal and/or real lattice parameters (*Table 1*).

If the plane (*hkl*) belongs to a zone, the reciprocal vector, g_{hkl}, is perpendicular to the zone axis [UVW], and their scalar product is equal to zero:

$$(ha^{*}+kb^{*}+lc^{*})\cdot(aU+bV+cW)=0$$

Solving this equation, and taking into account that the scalar product between the corresponding reciprocal and the real lattice parameters is equal to one, and the multiple of different parameters is zero, the zone equation is as follows:

$$hU+kV+lW=0$$

This equation allows us to determine if a series of planes belongs to the same zone and *vice versa*.

Returning to the fundamental principles of X ray diffraction, we can now consider that this phenomenon consists in a constructive interference of electromagnetic waves propagated in well-defined directions. Imagine two waves traveling in the same region of space. At certain directions they will overlap and the resultant wave will be the sum of the wave amplitudes and, in other directions, their sum will be equal to zero (*Figure 8*).

Table 1. Direct and reciprocal parameter relation to the interplanar distance *d*.

System	d_{hkl} /reciprocal parameters relation	d_{hkl} /direct lattice parameters relation
Cubic	$\frac{1}{d^2} = (h^2 + k^2 + l^2)a^{*2}$	$\frac{1}{d^2} = \frac{1}{a^2}(h^2 + k^2 + l^2)$
Tetragonal	$\frac{1}{d^2} = (h^2 + k^2)\,a^{*2} + l^2c^{*2}$	$\frac{1}{d^2} = \frac{h^2 + k^2}{a^2} + \frac{l^2}{c^2}$
Hexagonal	$\frac{1}{d^2} = (h^2 + hk + k^2)a^{*2} + l^2c^{*2}$	$\frac{1}{d^2} = \frac{4}{3a^2}(h^2 + hk + k^2) + \frac{l^2}{c^2}$
Orthorhombic	$\frac{1}{d^2} = h^2a^{*2} + k^2b^{*2} + l^2c^{*2}$	$\frac{1}{d^2} = \frac{h^2}{a^2} + \frac{k^2}{b^2} + \frac{l^2}{c^2}$
Monoclinic	$\frac{1}{d^2} = h^2a^{*2} + k^2b^{*2} + l^2c^{*2} + 2hlc^*a^*\cos\beta^*$	$\frac{1}{d^2} = \frac{\frac{h^2}{a^2} + \frac{k^2}{b^2} - \frac{2hlcos\beta}{ac}}{sin^2\beta} + \frac{k^2}{b^2}$
Triclinic	$\frac{1}{d^2} = h^2a^{*2} + k^2b^{*2} + l^2c^{*2} + 2hka^*b^*\cos\gamma^* + 2klb^*c^*\cos\alpha^* + 2lha^*c^*\cos\gamma^*$	$\frac{\frac{h^2}{a^2}sin^2\alpha + \frac{k^2}{b^2}sin^2\beta + \frac{l^2}{c^2}sin^2\gamma + \frac{2hk}{ab}(cos\alpha cos\beta - cos\gamma) + \frac{2kl}{bc}(cos\beta cos\gamma - cos\alpha) + \frac{2hl}{ac}(cos\gamma cos\alpha - cos\beta)}{1 - cos^2\alpha - cos^2\beta - cos^2\gamma + 2cos\alpha cos\beta}$

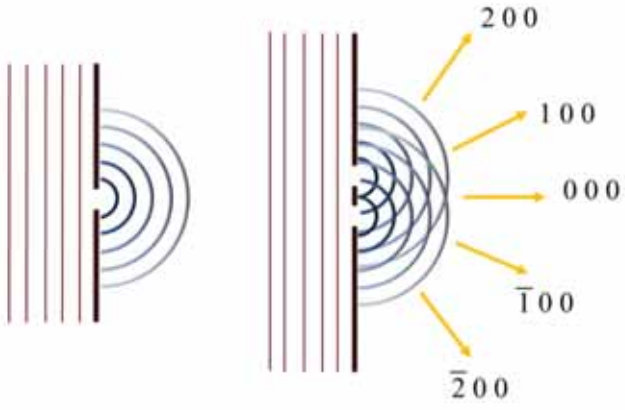

Figure 8. X ray wave propagation.

The wave motion can be described using harmonic motion of an oscillator of radius-vector, ***f***, and constant angular rotation velocity, **w**.

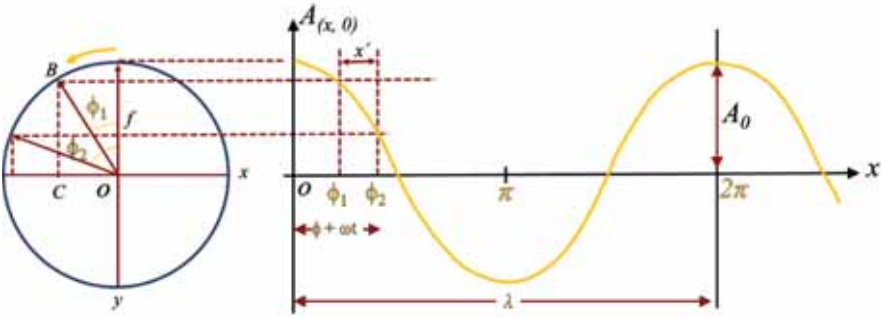

Figure 9. Oscillator motion.

If we describe the motion of point C (projected at point B through the rotational vector) *vs.* the angular displacement, ϕ ($\phi = \omega t$), a simple harmonic motion function is observed (*Figure 9*). The components of the vector, ***f*** (f_y), represent the periodic variations that the wave-associated electric field undergoes during a complete oscillation within the ϕ=0 – 2π range. In this case, the ϕ angle represents the wave phase with a defined position over the reference, O*y*.

The maximal value that could be adopted by the electric vector in the wave propagation direction is the amplitude of the wave, $A_{0,}$ with a magnitude equal to that of vector ***f***. Both magnitudes, phase and amplitude are periodically repeated in the wave propagation direction, which produces a wave motion at a complete 2π oscillator motion that is repeated at constant intervals, λ. Therefore, the variation of the phase angle, ϕ, between two points in the propagation direction *x* is:

$$\Delta\phi=\phi_2-\phi_1=2\pi/\lambda x'$$

and, the amplitude:

$$A(0,x) = A_0\cos\,\phi x=A_0\,\cos(2\pi/\lambda x)$$

or

$$A(0,t) =A_0\,\cos(\phi+\omega t)$$

when expressed as a function of time.

Suppose an interference of two waves, at the same frequency and amplitude: the interference is completely *constructive* when the wave amplitudes present the same magnitude and the same direction (sign). Both waves are *in phase* with greater amplitude than the partials of every component. The condition for *in-phase* wave propagation is that the difference of both waves in motion is zero or a multiple integer of the wavelength:

$$\Delta x = n\lambda \quad (n= 0, 1,2,\ldots.)$$

and the phase difference is also multiple pairs of p:

$$\Delta\phi=2\pi/\lambda x= 2n\pi$$

Thus, for $x = \lambda/2, 3\lambda2, 5\lambda/2....$ with corresponding difference $\Delta\phi=\pi, 3\pi, 5\pi$, a minimum value of the function occurs, *i.e.*, both waves present the same amplitudes, although with different signs, resulting in a zero interference. This interference is called *destructive*.

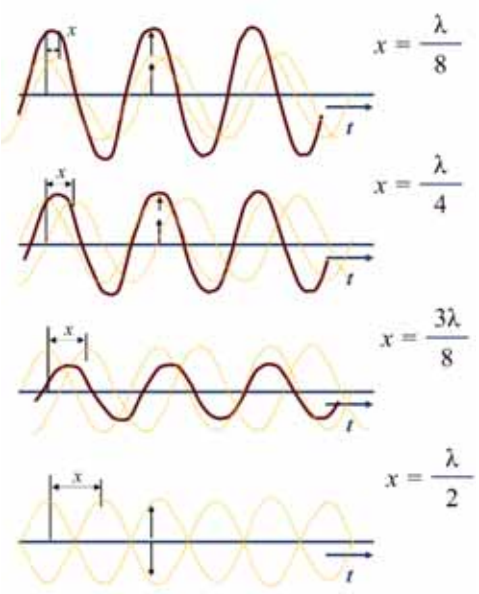

Figure 10. Examples of wave interferences

Between both limiting situations, multiple partial cases are possible with wave intensity equal to the transported energy by units of area perpendicular to its propagation direction (*Figure 10*). Or, in other words, the intensity will be proportional to the square of the resulting amplitude.

$$I \sim |A_0^2|$$

As the diffraction of crystals is a three-dimensional phenomenon, the translation must be taken into consideration. If we consider a chain of periodically separated atoms with translation *a*, *b*, and *c* and an incident X-ray with direction S_o, then the direction of the diffracted X-ray is given by the vector *S* (*Figure 11*). All atoms in a chain separated at a distance of *a (b* or *c)* must diffract in order to achieve a constructive interaction, with the difference $S\text{-}S_0$ being an integer number of the wavelengths:

$$a \cdot S - a \cdot S_0 = a \cdot (S - S_0) = h\lambda$$

For a crystal, this reaction must be satisfied in the three directions *a*, *b* and *c*.

$$a\cdot(S-S_0)=h\lambda \qquad a(\cos\psi-\cos\psi_0)=h\lambda$$
$$b\cdot(S-S_0)=k\lambda \quad \text{or } b(\cos\chi-\cos\chi_0)=k\lambda$$
$$c\cdot(S-S_0)=l\lambda \qquad c(\cos\omega-\cos\omega_0)=l\lambda$$

where *h, k, l* are integer numbers (positive, negative or zero) and ψ_0, χ_0, ω_0, ψ, χ, ω are the angles formed between the incident and the diffracted beams, S_0 and S, from a chain of atoms separated at distances of a, b and c. Those equations are known as the Laue equations for crystal diffraction.

Although Laue was the first to define the conditions of crystal diffraction, W. H. Bragg and W. L. Bragg synthesized all equations into one general condition for diffraction. The Braggs formulated the law based on the geometrical conditions for reflection, and applied it to a diffraction of the *(hkl)* crystal plane. The Bragg law was formulated as: *the difference in the optical paths of the diffracted rays by consecutive hkl planes must be equal to a multiple integer of the wavelength*.

To obey Bragg's Law, two geometrical conditions for reflection must be fulfilled; i) the incident and reflection angle must be the same; and, ii) the incident, reflection beam, and the normal to the reflection plane are within the same plane, perpendicular to the plane of reflection.

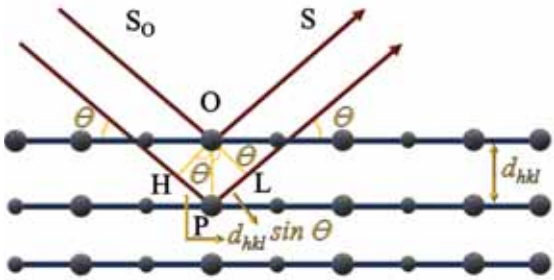

Figure 11. Schematic representation of Bragg's Law

In *Figure 11* a series of planes separated by a distance, d_{hkl}, are considered. We can deduce the following:

$$\delta=HP+PL=2d_{hkl}\sin\theta=n\lambda$$

Yielding Bragg's Law, that is expressed as:

$$\lambda=2\frac{d_{hkl}}{n}\sin\theta$$

Where ***n*** is the order of diffraction and is equal to 1 for planes with *nh, nk, nl* indices of spacing (1/n) d_{hkl}. The solution to Bragg's Law results in a reflection with indices H=*nh*, K=nk, L=nl, generally presented as *hkl* (without parentheses to distinguish them from the Miller indices). So, the reflections for indices 231, 462, 693 correspond to 1st, 2nd and 3rd order reflections of the planes with Miller indexes (231).

The reciprocal space vector of both Bragg's Law and the Laue equations can be related with the space vector of the Bravais lattices, giving the latter a physical reality. When we introduce the concept of reciprocal space into the Laue equation describing X-ray radiation vectors through a module, $1/\lambda$, with incident and diffracted beams, S_0/λ and S/λ, respectively, then the equation is transformed into:

$$a\cdot(S-S_0)=h\lambda \qquad aa^*\cdot(S-S_0)=ha^*\lambda$$
$$b\cdot(S-S_0)=k\lambda \qquad bb^*\cdot(S-S_0)=kb^*\lambda$$
$$c\cdot(S-S_0)=l\lambda \qquad cc^*\cdot(S-S_0)=lc^*\lambda$$

And their sum results in a relation showing the proportionality between the difference $S\text{-}S_0$ and the reciprocal vector. In other words, **the X-ray diffractogram is the reciprocal lattice of the real lattice**.

$$1/\lambda\,(S-S_0)= d_{hkl}^*$$

P.P. Ewald proposed a spherical graphical representation to relate the reciprocal lattice and the diffraction in the crystal (Figure 12).

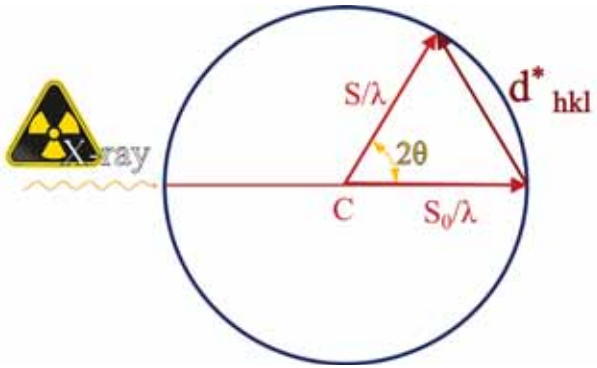

Figure 12. Ewald spherical representation.

The radius of that sphere is $1/\lambda$ where S_0 is the incident beam vector with a module that is coincident with that radius. The diffracted beam is represented by any vector of module S/λ. If a crystal is situated in the centre of the sphere **C**, the vector corresponding to the difference between the incident and diffracted beam is the reciprocal vector, d_{hkl}*. All points of the reciprocal lattice within the Ewald sphere satisfy the Laue equations and correspond to a diffracted plane in real space. The relation to Bragg's Law is evident as the angle formed by S_0/λ and S/λ is 2θ, and the plane perpendicular to d_{hkl}* is the (hkl) plane for which $\frac{1}{2}|d^*_{hkl}| = S/\lambda \sin\theta$ or, in relation to real space, $1/2d = 1/\lambda \sin\theta$.

All diffracting waves must fulfil the Laue (Bragg) equation and can be solved by using Ewald's sphere. If we consider spheres with origins at different reciprocal lattice points, the position vectors of their centres indicate the direction of propagation and their modules, the diffracted rays. For every concrete reciprocal point, we can obtain the geometrical plane of the centre of the sphere passing through the point and the lattice origin. All geometrical points on a plane at half-distance between two reciprocal lattice points in the direction of the reciprocal vector, d_{hkl}*, correspond to the (hkl) plane. All those planes enclose a volume known as the Brillouin zone (*Figure 13*). A vector originating from a point outside the Brillouin zone describes a non-diffracted wave, freely propagating within the lattice. The volume of the Brillouin zone is equal to the volume of the reduced reciprocal lattice and is the inverse of the reduced crystal lattice (a pseudo Wiegner Seitz cell). Various Brillouin zones are distinguished, the first zone is the closest to the origin, the second zone is the one that follows, when referring to the distance from the origin, and so on.

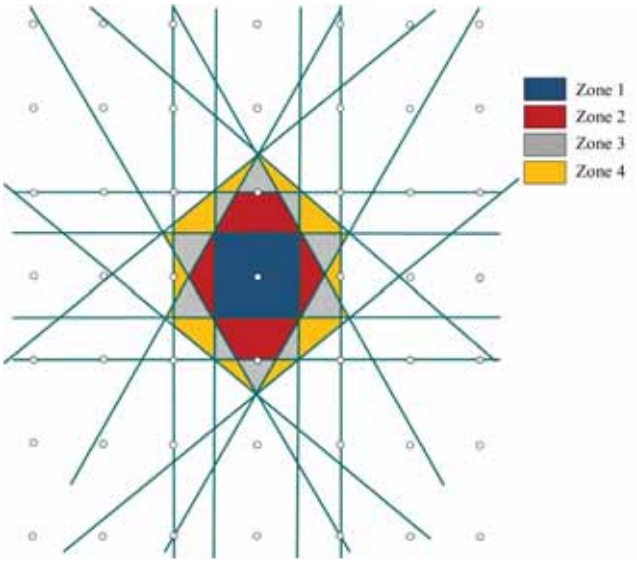

Figure 13. The first 4 Brillouin zones

Up until now, we have not considered the atoms as such in the equation (only their position); however, under an incident X-ray, all atoms re-emit waves of the same wavelength, a process known as elastic diffusion. The resulting wave is generally *in phase*, and the phase difference between incident and dispersed waves is known as π. This phenomenon is known as Rayleigh diffusion. The diffused wave amplitude is inversely proportional to the mass of the particle. Considering protons and electrons and an intensity of diffusion proportional to the amplitude, the intensity of the proton will be 10^{-6} times that of an electron. So we may only consider the effect of the electrons on X-ray diffraction, and its efficacy is measured by a factor called the atomic factor, f_a. This factor depends on the number of electrons and their distribution and it is defined as the amplitude of dispersion produced by the atom with respect to that of an electron, as a reference.

However, before studying the factors that influence the intensity of the diffraction, we must mention how X-ray diffraction analysis is performed. Experimentally speaking, the sample and the X-ray source remain stationary in X-ray diffraction analysis, whereas the detector moves at an angle of 2θ to analyze all diffracted beams within a chosen angle range (*Figure 14*). The pattern (diffractogram) that is obtained represents the "fingerprint" of the structure with position and intensity of the diffractions corresponding to compound composition and crystal structure symmetry.

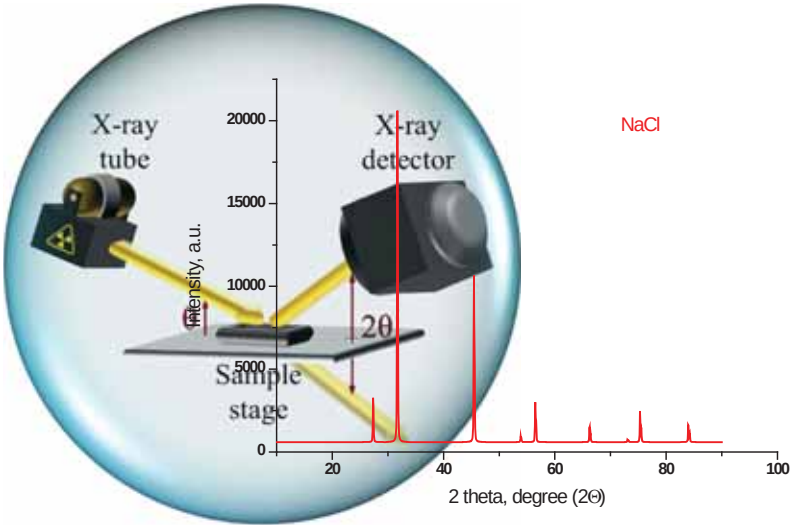

Figure 14. X-ray diffraction set up, and NaCl diffraction as an example.

The presence of all atoms must be considered, in order to analyze the intensity of the diffracted rays by a conventional lattice. The geometry of the X-ray diffractograms, such as that of NaCl in *Figure 14*, depends essentially on the interplanar distance and is not influenced by the type of atoms (all NaCl type structures present the same diffractions). However, the intensity of the diffraction lines is determined by the scattering factor of every atom present in the diffracted (hkl) plane. The intensity is proportional to the amplitude of the wave that is dispersed by each atom and is known as

the structure factor, $\mathbf{F_{hkl}}$. The structure factor is then defined as the amplitude of the wave scattered by the atoms of the lattice basis:

$$F_{hkl} = \sum_n f_n e^{2\pi i(hx+ky+lz)}$$
$$= \sum_n f_n \cos 2\pi\,(hx_n + ky_n + lz_n)$$
$$+ i \sum_n f_n \sin 2\pi\,(hx_n + ky_n + lz_n)$$

The positions of the atoms within the hkl plane are defined and the intensity of the diffracted wave is proportional to the square of the structure factor module, $I \sim \left|F_{hkl}{}^2\right|$.

Let us apply the structure factor to different structures. The primitive **P** lattice is defined by one atom with position (*0,0,0*). The corresponding structure factor is as follows:

$$F_{hkl} = f_a e^{2\pi i(h0+k0+l0)} = f_a$$

and, the intensity is independent of *h,k,l* and proportional to the square of the atomic factor, $F_{hkl}{}^2 = fa^2$.

Two atoms with positions (*0,0,0*) and (½, ½, 0) are necessary to describe the ***C***-centred lattice. The structure factor is:

$$F_{hkl} = f_a e^{2\pi i(h0+k0+l0)} + f_a e^{2\pi i(h/2+k/2)} = f_a \left[1 + e^{\pi i(h+k)}\right]$$

When h and k are of the same parity (even or odd number) the sum of both is always an even number h+k=2n, the $e^{\pi i(h+k)} = 1$ and the $F_{hkl}{}^2 = 4fa^2$

On the contrary, if h and k are of different parity (one even and one odd), then $e^{\pi i(h+k)} = -1$ and $F_{hkl}{}^2 = 0$.

Problem III. *Are there any systematic absences for the A-centred and B-centred lattices?*

Note: $e^{n\pi i} = 1$, *for n even number and* $e^{n\pi i} = -1$ *for n odd*

The diffracted intensity is null and the diffraction absent. This is called **systematic absence** or **extinction**. For the *C* centred lattice, only planes where *h* and *k* either both odd or both even diffract with no null intensity.

For the ***F*** lattice, 4 points are required to describe the cell: (0,0,0), (½, ½, 0), (0, ½, ½) and (½, 0, ½), and the structure factor is then:

$$\begin{aligned} F_{hkl} &= f_a e^{2\pi i(h0+k0+l0)} + f_a e^{2\pi i(h/2+k/2)} + f_a e^{2\pi i(k/2+l/2)} \\ &\quad + f_a e^{2\pi i(h/2+l/2)} \\ &= f_a \left[1 + e^{\pi i(h+k)} + e^{\pi i(l+k)} + e^{\pi i(h+l)}\right] \end{aligned}$$

It is easy to deduce that if all the indices *h*, *k*, or *l* are of same parity (all even or all odd), then the resulting diffractions are permitted and will be of high intensity ($F_{hkl}^2 = 16fa^2$). However, if at least one of the indices is of a different parity, then the resulting diffraction will be of null intensity.

Problem IV. *Are there any systematic absences for the* ***I*** *lattice?*
Note: *Two points structure (0,0,0) and (½, ½, ½)*

What happens if our structure is composed of more atoms, different in nature? For example, *NaCl* with positions for *Na* (0,0,0), (½, ½, 0), (0, ½, ½) and (½, 0, ½) and for *Cl* (½, ½, ½), (½, 0, 0), (0, ½, 0) and (0, 0, ½) the structure factor will become:

$$\begin{aligned} F_{hkl} &= f_{Na} e^{2\pi i(h0+k0+l0)} + f_{Na} e^{2\pi i(h/2+k/2)} + f_{Na} e^{2\pi i(k/2+l/2)} \\ &\quad + f_{Na} e^{2\pi i(h/2+k/2)} + f_{Cl} e^{2\pi i\left(\frac{h}{2}+\frac{k}{2}+\frac{l}{2}\right)} + f_{Cl} e^{2\pi i\left(\frac{h}{2}+k0+l0\right)} \\ &\quad + f_{Cl} e^{2\pi i(h0+k/2+l0)} + f_{Cl} e^{2\pi i(h0+k0+l/2)} \end{aligned}$$

Or

$$\begin{aligned} F_{hkl} &= f_{Na}\left[1 + e^{\pi i(h+k)} + e^{\pi i(k+l)} + e^{\pi i(h+l)}\right] \\ &\quad + f_{Cl}\left[e^{\pi i(h+k+l)} + e^{\pi i(h)} + e^{\pi i(k)} + e^{\pi i(l)}\right] \end{aligned}$$

We can reconstruct the second term, taking into account that $e^{n\pi i} = e^{-n\pi i}$:

So for *h, k, l* of the same parity we observe diffractions, and if the sum is even (*h+k+l=2n)* the intensity is maximal $F_{hkl}^2 = 16[f_{Na} + f_{Cl}]^2$; and for *h+k+l=2n+1*(odd) the $F_{hkl}^2 = 16[f_{Na} - f_{Cl}]^2$, less intense diffractions appear.

The presence of the translational element of symmetry also has to be taken into consideration to determine the systematic absences. The presence of glide planes and screw axes produces the cancellation of existing diffractions and the absence of reciprocal lattice points.

Let us consider glide plane *a* perpendicular to the *z* axis, which produces an equivalent atom at coordinates ($x+ ½, y, \bar{z}$) to the initial atom A with coordinates (*x, y, z*); the structure factor may be written as follows:

$$F_{hkl} = f_A e^{2\pi i(hx+ky+lz)} + f_A e^{2\pi i\left(h\left(x+\frac{1}{2}\right)+ky-lz\right)}$$

Only for *l=0*, for the *(hk0)* planes the structure factor becomes zero:

$$F_{hkl} = f_A e^{2\pi i(hx+ky)} + f_A e^{2\pi i\left(hx+\frac{h}{2}+ky\right)} = f_A e^{2\pi i(hx+ky)}[1 + e^{2\pi ih}]$$

When *h* is an odd number, the F_{hkl} is null for all reflection *(hk0)*, and all corresponding reciprocal points disappear.

For the screw axis, 2_1, parallel to z, the atom equivalent to A (*x,y,z*) is positioned at ($\bar{x}, \bar{y}, z+½$), and the structure factor is:

$$F_{hkl} = f_A e^{2\pi i(hx+ky+lz)} + f_A e^{2\pi i\left(-hx-ky+l\left(z+\frac{1}{2}\right)\right)}$$

This factor becomes zero only when *h=k=0* and can be expressed as follows:

$$F_{hkl} = f_A e^{2\pi i(lz)} + f_A e^{2\pi i\left(lz+\frac{l}{2}\right)} = f_A e^{2\pi i(lz)}\,[1 + e^{\pi i(l)}]$$

When *l* is an odd number, F_{hkl} is equal to zero. So systematic absences appear for all *h=k=0* and for *l* as an odd number within the reciprocal lattice, then one of two points disappears in the direction $[001]^*$.

From the last two examples it is clear that we can deduce the space group from X-ray diffraction analysis and, *vice versa*, an X-ray diffraction can be generated from the crystallographic table, indicating the positions of the atoms and the space group.

From the diffractograms we can extract information on the Bravais type lattice, presence of glide planes from *hk0*, *h0l* and *0kl* diffractions, and the presence of screw axes using the *h00*, *0k0* and *001* diffractions. Although the deduction of the Bravais lattice type is easier, the consideration of the translational symmetry elements is not trivial, and in some cases a refinement is required.

As for the opposite case, the relative intensity and systematic absences and the sequence of diffraction lines observed in an X-ray diffractogram may be determined with the crystallographic tables.

Although the structure factor yields an important approximation to the expected intensity, a few other important factors must be mentioned: the Lorenz, polarization and absorption correction factors. The Lorentz factor is a trigonometrical factor and depends on the geometry of the experimental technique and the shift of the crystallographic planes with respect to the incident beam. It is the coefficient resulting from the angular velocity of the crystal over the shifting rate of the plane along the diffracted beam.

The polarization factor is another trigonometrical function resulting from the orientation of the electrical field of the incident beam and the polarization produced upon beam diffusion. And the absorption correction is applied only when atoms with higher absorption coefficients are present. The sum of all factors rules out the diffraction lines intensity distribution over X-ray pattern of every studied phase.

Problem V. *Use the scheelite structure, space group $I4_1/a$, and determine the possible systematic absences in its diffraction pattern, list the indices of the first six largest d-spacings and discuss the expected X ray pattern.*

The I symbol specifies an inner centred lattice for which we need two points to describe the structure: (*x*,*y*,*z*) and (*x*+½ , *y*+½, *z*+½). The structure factor is therefore as follows:

$$F_{hkl} = f\left[e^{2\pi i(hx+ky+lz)} + e^{2\pi i\left(hx+\frac{h}{2}+ky+\frac{k}{2}+ly+\frac{l}{2}\right)}\right] = fe^{2\pi i(hx+ky+lz)}\left[1 + e^{\pi i(h+k+l)}\right]$$

All diffraction with $h+k+l=2n$ will be present in the pattern.

The *a* symbol indicates an axial glide plane with translation a/2 perpendicular to the z axis (the case resolved above for the glide plane). The (*x*, *y*, *z*) point moves to ($x+ ½, y, \bar{z}$) and the resulting structure factor is as follows:

$$F_{hkl} = fe^{2\pi i(hx+ky)}\left[1 + e^{2\pi ih}\right]$$

The second condition is that h must be an even number, h=2n. The space group is tetragonal (4 in first position and absence of 3 in the second position), and *a* and *b* are equivalent, so the k=2n condition will also appear (*h*,*k*=*2n*).

The 4_1 screw axis originates points at (*x*, *y*, *z*), ($\bar{x}$, $\bar{y}$, *z* +½), (*x*, $\bar{y}$, *z* + ¼) and (*x*, $\bar{y}$, *z* + ¾) and the translation at [001] direction implies the conditions of *00l* diffractions. The calculated structure factor results in the following expression:

$$F_{hkl} = f\left(e^{2\pi(lz)}\left[1 + e^{2\pi il} + e^{\pi il/2} + e^{\pi i3l/2}\right]\right)$$

With the general condition of extinction *l*=*4n*.

The interplanar distance for the tetragonal lattice can be calculated by the following equation:

$$\frac{1}{d^2} = \frac{h^2 + k^2}{a^2} + \frac{l^2}{c^2}$$

The largest *d*-spacing will occur at the lowest *hkl*. We have to order all possible diffractions in increasing order of *hkl*, and eliminate any systematic extinctions, in order to find the first six. For c=2a, *h* and *k* will vary from 0 to 2, and *l* from zero to four.

Index	Extinction	*d*-spacing	Index	Extinction	d-spacing
100	yes		211	no	2.30 Å
001	yes		220	no	1.85 Å
110	no	4.76 Å	202	no	2.38 Å
111	yes		221	yes	
200	no	2.62 Å	122	yes	
002	yes		222	no	1.76 Å
201	yes		003	yes	
210	yes		103	no	3.07 Å
102	yes		004	no	2.84 Å
112	no	3.10 Å	104	yes	

All the permitted diffractions will be present in the final diffraction pattern, the intensity of which is influenced by the type of atoms forming the structure (*f* is considered general in this example).

References

Cristalografia, Jose M. Amigo, Jose Luis Briansó, M. Claire Briansó, Ramon Coy Yll, Joaquin Solans Huguet, Rueda, Madrid,1981.

Solid State Chemistry, L. E. Smart and E. A. Moore (2012), CRC Press, Boca Raton, FL

Cristaloquímica de materiales de la estructura a las propiedades de los sólidos inorgánicos, 1st edition, Carlos Pico Marín, Maria Luisa Lopez Garcia, Maria Luisa Veiga Blanco, Editorial Sintesis, Spain 2008

Solid state chemistry and its application 2nd edition, Anthony R. West, 2014 John Wiley & Sons, Ltd, UK.

Metodos de Difraccion de Rayos X: Principios y aplicaciones, Joaquin Bermudez-Polonio, Piramide, 1981.

All structures are generated with Vesta software using the CIF from http://www.crystallography.net/cod/index.php and the references listed below in the same order as they appear in this chapter:

$CuSO_4$. P.A. Kokkoros, P.J. Rentzeperis, The crystal structure of the anhydrous sulfates of copper and zinc, Acta Crystallographica 1958, 11, 361-364.

CHAPTER 5

DEFECTS IN SOLIDS

"Certain defects are necessary
for the existence of individuality"
Johann Wolfgang von Goethe

One of the most important fields in present-day solid-state chemistry is undoubtedly the formation of defects and their relation to material physicochemical properties. A virtually perfect crystal could only exist at a temperature of absolute zero, while all crystals present certain imperfections at normal ambient temperatures. The definition of defect frequently refers to an irregularity of the crystal structure, such as missing atoms/ions, impurities, adatoms or a substitution of one atom for another. We can classify the defects according to their dimensional extension. The simplest defects are the 0-D dimensional ones known as **point defects**, where only one atom or site is involved. The second group includes the **linear defects**, where the defect is extended in 1-D but it is seen as a point defect in the other two directions. When an entire **plane of defects** is involved, the 2-D group arises, and when the defects **cluster** together, or precipitates appear, we can see this arrangement as a 3-D extension (*Figure 1*).

Defects can also be classified by the compositional change they produce. Defects that have no effect on the composition of the crystal are known as stoichiometric (intrinsic) defects. On the contrary, the presence of nonstoichiometric (extrinsic defects) produces compositional change in the crystal. All those defects are called structural/compositional defects and influence the unit cell. Generally, the irregularities are randomly distributed within the unit cell, but sometimes they can present an ordered arrangement resulting in virtually "defect-free" structures of regular vacancies (*Figure 2*).

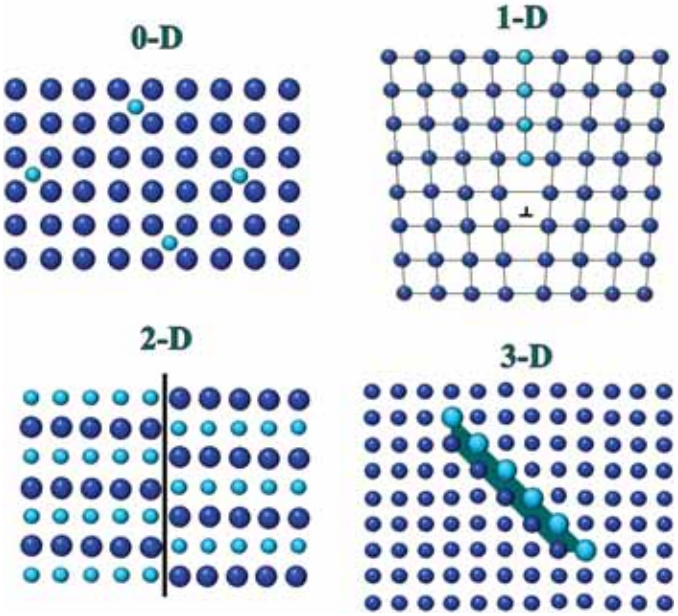

Figure 1. Defect organization according to the dimension of extension.

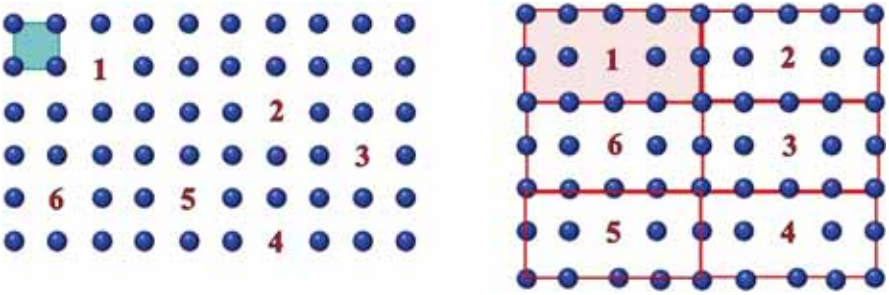

Figure 2. Randomly distributed vacancies in a defective structure and defect-free structure showing ordered vacancies.

Sometimes the generation of structural defects may entail the appearance of electronic defects, such as the presence of extra electrons or, in the absence of electrons, the generation of positive holes. Both are charged defects and are prone to influence the conductivity of materials, typical examples of which are *n*- and *p*-type semiconductors.

Whatever their organization, structural defects are always associated with crystalline solids, as they fulfil the condition of being composed of repetitive units of atoms/ions. Without attempting a full classification, some types of defects that will be considered in this chapter are listed in *Schema 1*.

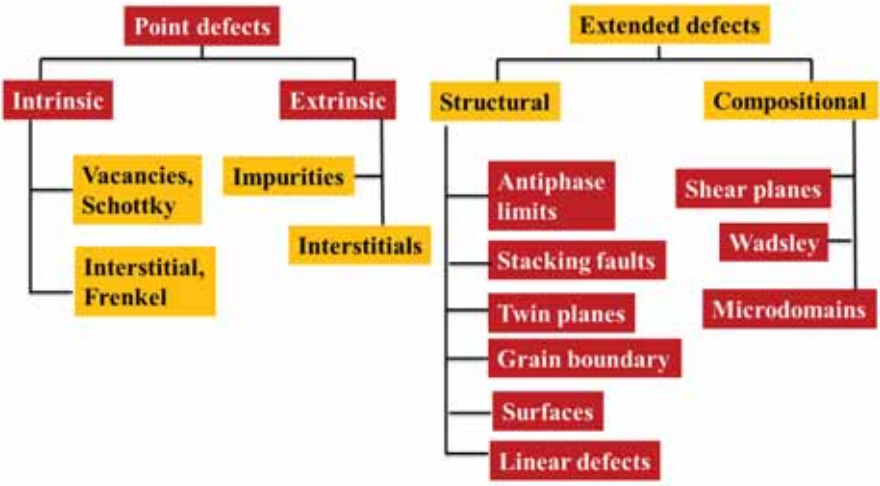

Schema 1. Defect classification chart

Point defects

Point defects can be divided in two groups, intrinsic and extrinsic defects. An atom that is missing from its original position in the lattice creates a **vacancy**, $\mathbf{V_M}$ or $\mathbf{V_X}$ (M associated with metal, X with a non-metal site). An extra atom in a normally empty position within the crystal is called an **interstitial** atom, $\mathbf{M_i}$, $\mathbf{X_i}$, and could be an atom of the same chemical nature (self-interstitial) or an impurity atom. When referring to ionic solids, the two different sets of metallic and non-metallic sites are divided into **sublattices**, and the impurities are called **dopants**. The dopants can either enter the interstitial site, A_i, or be substituted for an atom in an occupied site, producing a substitutional defect affecting one or another sublattice, $\mathbf{A_M}$ ($\mathbf{A_X}$). When the impurities are of different valence the substitution is called **aliovalent**. When discussing ionic crystals, the self-compensation mechanism must be taken into consideration; the charge neutrality must remain, and we can expect to see the introduction of additional vacancies and antisites balancing the charge. The compensation can also be achieved

by the introduction of electronic defects: electrons, **e´**, or holes, **h•**. When the impurities that are introduced are compensated by electrons, they are called **donor** impurities and when compensated by holes, they are called **acceptor** impurities. The set of symbols for differentiating the point defects is known as Kröger-Vink notation, which is used to denote the defects in the chemical equations, for which purpose the charge of the resulting defect must be indicated. We refer to it as the effective charge (q_e), and its relation to the real charges ($\boldsymbol{Z_d}$) is given below. The effective charge is the charge that the defect has with respect to the charge that would be present at this site in a defect-free crystal. The effective charge is represented as the difference between the real charge of the defect species, $\boldsymbol{Z_d}$, and the real charge of the site occupied in the crystal, $\boldsymbol{Z_s}$.

$$q_e = Z_d - Z_s$$

The effective charges are denoted with superscript ´ (prime), and • —for negative and positive charges, respectively.

Let us consider the CdO crystal. The effective charge of the cadmium vacancy, V_{Cd}, is the real charge of the defect (zero for vacancy) minus the real charge of the site that it occupies within the crystal (2 for Cd^{2+}):

$$q_e = 0-2= -2$$

The cadmium vacancy appears with negative effective charge and should be written as $V_{Cd}^{2´}$ where the multiple charge is indicated by $n´$. On the other hand, an anion vacancy, V_O will present an opposite effective charge, +2 , (q_e= 0 -(-2)=+2) indicated with $V_O^{2•}$. The interstitial sites are normally unoccupied and present no charge, so their effective charge is the same as the real charge of the entering species. Cadmium entering an interstitial site should be denoted as $Cd_i^{2•}$.

As for the substitutions, the replacement of Cd^{2+} by Mg^{2+} will not generate an effective charge, as the q_e= 2 - (2)=0 and it is denoted by x, Cd_{Ni}^{x}. The absence of charge is always emphasized with x. The replacement of an ion of one valence by an aliovalent dopant creates a charged defect. For example, the substitution of Cd^{2+} for Li^{+} (q_e =1-2= -1), $Li_{Cd}´$ and Fe^{3+} (q_e =3-2= 1), $Fe_{Cd}•$ can result in positively or negatively charged defects and the same is valid for the substitution of the O^{2-}, by F^{-} (q_e =-1-(-2)= 1), $F_O•$ and by N^{3-} (q_e =-3-(-2)= -1), $N_O´$. All the defects described above are illustrated in *Figure 3*.

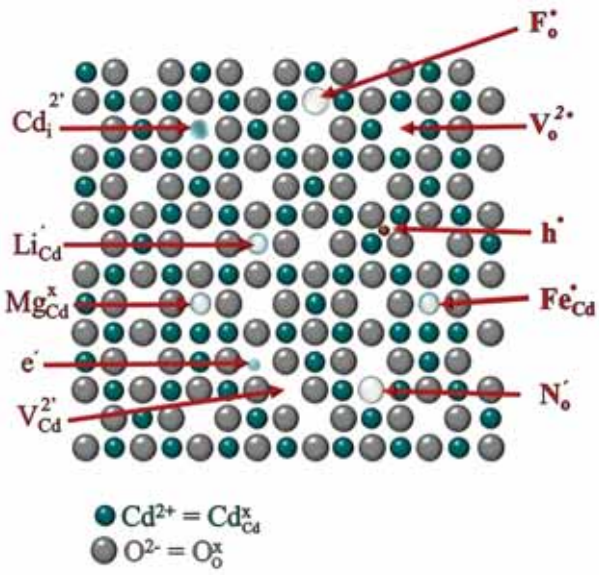

Figure 3. Point defects generated in the CdO crystal matrix.

Problem I. *What type of defects are generated upon substitution of the Na^+ and Cl^- in NaCl crystal by K^+, Ca^{2+} and O^{2-}? Calculate the effective charge of the resulting defects.*

In ionic solid crystals, the point defects must preserve their electroneutrality. A presence of cationic vacancy demands the presence of an extra charge or the absence of an anion. A balanced population of cationic and anionic vacancies is known as the **Schottky defect**. This kind of defect is very common for the alkali halides. The vacancies are not necessarily situated together and the number of defects is half of the resulting vacancies for an MX type solid (*Figure 4, NaCl*). For solids of different stoichiometry, the number of vacancies depends on the cation/anion relation.

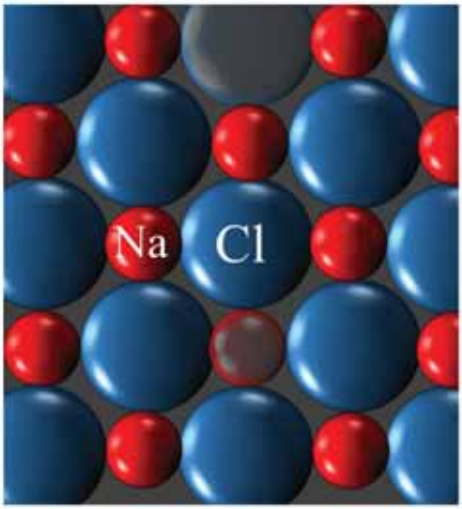

Figure 4. Schematic representation of a Schottky defect in NaCl.

Problem II. *How many vacancies stand for one Schottky defect in the Al_2O_3 crystal?*

A total number of 5 vacancies are associated with one Schottky defect within the Al_2O_3 crystal, two Al^{3+} and three O^{2-} ones.

Indicate the Kröger-Vink notation and the effective charge of both sites.

A **Frenkel defect** describes the movement of one atom or ion from its original position in the sublattice to an empty interstitial position. The electroneutrality is preserved as the vacancy that is created is compensated by the addition of a corresponding atom/ion in an interstitial site (*Figure 5, AgCl*). Both sublattices can be involved, although the smaller size ions are usually preferred.

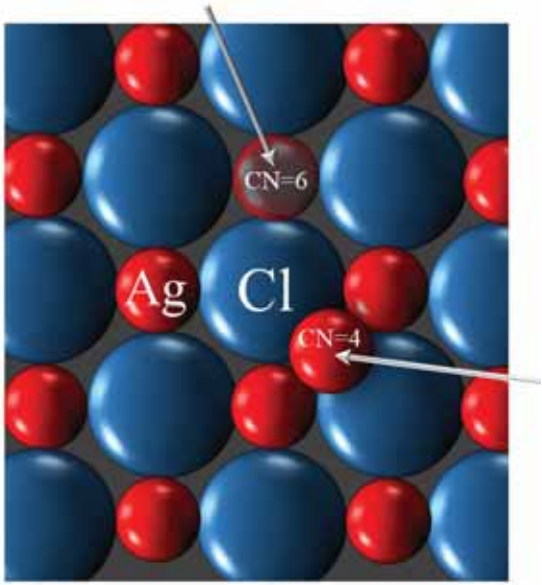

Figure 5. Frenkel defect formation for the AgCl.

Problem III. *Imagine a Frenkel defect for the CaF_2 fluorite structure. Which ion will be involved?*

In this case the Frenkel defect consists in F^- vacancy and interstitial F^- site.

Indicate the Kröger-Vink notation and the effective charge of both sites.

The Ag^+ changes from 6-fold coordination to 4-fold coordination. Although the latter appears less stable, the Ag^+ ions are stabilized by an important covalent interaction with the Cl^-. This kind of defect is observed for AgCl, but not for the parent structure, NaCl, where the more ionic character limits the stabilization of the interstitial Na ion.

Both for the Schottky and the Frenkel defects, the vacancy-vacancy and vacancy-interstitial pairs are randomly distributed, although sometimes they may associate into clusters. This tendency is easily explained, as the opposite charges within the pair of defects tend to attract each other.

An atom or ion that occupies a site normally occupied by another one forms an **antisite**. This kind of defect is unusual in binary ionic compounds, as the integrity of the lattice is affected. Nevertheless, it is very common in metal alloys (*Figure 6*) and multicationic compounds, such as spinels. In the direct spinel crystal $MgAl_2O_4$ the Mg^{2+} and Al^{3+} occupy tetrahedral and octahedral sites, respectively. However, some Mg^{2+} can exchange with the Al^{3+} to form antisite defects, as shown in the following equation:

$$Mg_{Mg} + Al_{Al} \rightarrow Mg_{Al}' + Al_{Mg}^{\bullet}$$

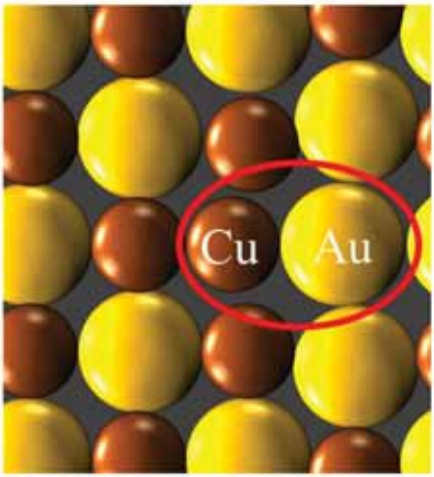

Figure 6. Illustration of an antisite defect.

And the inverse spinel structure is formed (*structures in chapter II, Figures 20, 21*).

But how to estimate the number of defects present in one solid?

Equilibrium defects population

Virtually perfect crystals only exist at absolute zero, but at normal temperature the solid presents a certain population of defects. The presence of a certain number of defects reduces the free energy of the crystal (*Figure 7*). Thermodynamics suggests an energy cost for defect formation (the energy necessary to break the bonds); however, that cost can be assumed by the energy gain from the structural disorder that is produced following the

creation of the defects (the large number of positions that defects can occupy).

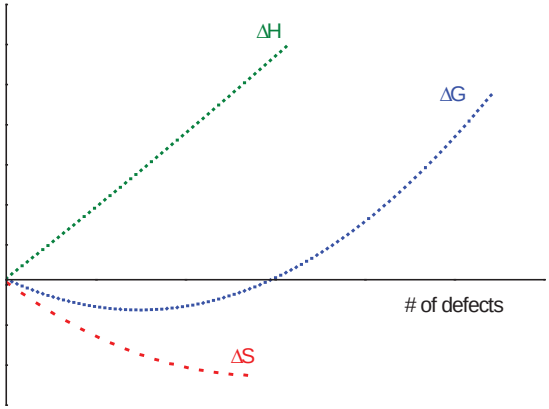

Figure 7. Gibbs energy change as a function of the number of defects

We can then quantify the energy of the system using the Gibbs free energy equation

$$\Delta G=\Delta H - T\Delta S$$

The introduction of defects lowers the Gibbs free energy to a certain point, but the introduction of more and more defects causes the destruction of the crystal. Minimal Gibbs energy therefore corresponds to an equilibrium population of defects.

Let us now consider the creation of a single vacancy (n_v). If we consider that the energy gain is caused only by configurational entropy, it can be expressed using the Boltzmann equation:

$$S = klnW$$

where, W is the number of ways for distributing n_v vacancies in N random sites, and k is the Boltzmann constant.

W is calculated by probability theory with the expression:

$$W = \frac{N!}{(N - n_v)!\, n_v}$$

Assuming that $lnN! \approx N\ lnN - N$ for N~∞ (Stirling's approximation), and removing the factorials, the entropy level for vacancy creation is:

$$\Delta S_v = k\,[NlnN - (N - n_v)\ln(N - n_v) - n_v ln\, n_v]$$

On the other hand, at a specified temperature, the enthalpy level for vacancy creationΔh_v is assumed to be constant, and the total enthalpy change is given by:

$$\Delta H_v = n_v \Delta h_v$$

The final expression for the Gibbs energy change is:

$$\Delta G_v = n_v \Delta h_v - k\,T[NlnN - (N - n_v)\ln(N - n_v) - n_v ln\, n_v]$$

The minimum of this curve corresponds to the equilibrium number of vacancies existing for temperatures above absolute zero. At equilibrium, $\Delta G_v = 0$; and the minimum is given by:

$$\left(\frac{d\Delta G_v}{dn_v}\right)_T = 0$$

and,

$$\left(\frac{d\Delta G_v}{dn_v}\right)_T = \frac{d}{dn_v}\{n_v \Delta h_v - k\,T[NlnN - (N - n_v)\ln(N - n_v) - n_v ln\, n_v]\} = 0$$

Assuming that the differential of a constant is zero, and that of $lnx = 1/x$ and $xlnx = 1 + lnx$, the equation becomes:

$$\Delta h_v = kTln\left[\frac{N - n_v}{n_v}\right]$$

or,

$$n_v = (N - n_v)e^{-h_v/kT}$$

and, for N>> n_v the

$$n_v \approx Ne^{-h_v/kT}$$

If we treat the defect population as chemical equilibrium (occupied site ↔ vacancy), we can apply the mass action law using concentrations, and express the equilibrium constant for vacancy creation (K_v):

$$K_v = \frac{n_v}{N} = e^{-\Delta G_v/RT}$$

where, n_v is the number of vacancies, N the total number of crystal sites ($\frac{n_v}{N}$ the fraction of vacancies in the crystal), ΔG_v the molar Gibbs energy of vacancy formation, R the gas constant, and T the temperature in K.

This equation is often given as the equation for the formation of one single defect:

$$n_v = Ne^{-\Delta g_v/kT}$$

ΔG_v is expressed in units J(eV)/defect paired with the Boltzmann constant (J K^{-1} or eV K^{-1}).

Problem IV. *Calculate the number of vacancies per cubic meter of copper in equilibrium at 1000ºC. Assume energy of vacancy formation to be 0.9 eV/atom, Cu atomic weight P_{Cu}= 63.5 g/mol and density of 8.4 g/cm^3.*

To calculate the number of vacancies, we must calculate the number of Cu atoms in 1m^3, using its density:

$$d = \frac{m}{V} = \frac{N * P_{Cu}}{V * N_A}$$

$$N = \frac{6.023\,10^{23}\,\frac{atoms}{mol} * 8.4\,\frac{g}{cm^3}\,10^6\ cm^3/m^3}{63.5\,\frac{g}{mol}} = 8 * 10^{28}\ atoms/m^3$$

And the number of vacancies, n_v, at 1000 ºC:

$$n_v = N\exp(-\frac{\Delta G_v}{kT}) = 8 * 10^{28}\frac{atoms}{m^3} * \exp\left(\frac{0.9\,\frac{eV}{atom}}{8.62 * \frac{10^{-5}eV}{K}\,1273\,K}\right)$$
$$= 2.25 * 10^{25}\ vacancies/m^3$$

Regularly, the entropy contribution is neglected and only the enthalpy of formation is taken into consideration:

$$n_v/N = e^{-\Delta H_v/RT}$$

and, expressed in energy per single defect:

$$n_v = Ne^{-\Delta h_v/kT}$$

Problem V. *Calculate the fraction of vacancies at 950ºC for pure silver, at an enthalpy of vacancy formation of 105.2 KJ/mol. Using the calculated fraction, determine the number of vacancies in 1 m^3 at the same temperature using the lattice parameter of a silver fcc lattice, a=4.086 Å. Repeat the calculation using the silver density and 10.5 g/cm^3 and atomic weight of 107.88 g/mol.*

We have considered up to now a single defect formation. *But what happens when a Schottky or Frenkel defect is involved?*

For the Schottky defect the chemical equilibrium could be imagined as follows:

$$\text{occupied site} \leftrightarrow \text{cationic vacancy } V_M^{\prime} + \text{anionic vacancy } V_X^{\bullet}$$

If there is no interaction between the defects, we can write the expression of the equilibrium constant for Schottky defect formation, K_s, as a multiple of the cationic and anionic vacancies fraction:

$$K_s = \frac{n_{cv}}{N}\frac{n_{av}}{N} = e^{-\Delta G_s/RT}$$

As the number of cationic vacancies, n_{cv}, is equal to the number of anionic vacancies, n_{av}, the equation can be rewritten as:

$$n_{cv} = n_{av} = n_s = Ne^{-\Delta G_s/2RT}$$

A factor **2** appears in the denominator of the exponent corresponding to creation of 2 vacancies for a one single Schottky defect.

Similarly, we can neglect the entropy term and the final equation becomes:

$$n_s = Ne^{-\Delta H_s/2RT}$$

or, per single Schottky defect:

$$n_s = Ne^{-\Delta h_s/2kT}$$

Applying the same reasoning for Frenkel defects and considering, for example, cationic defect formation, the equilibrium is as follows:

occupied site ↔ cationic vacancy + cationic interstitial

The above-mentioned expression for the equilibrium constant of Frenkel cationic defect formation, K_F, will be:

$$K_F = \frac{n_{cv}}{N}\frac{n_{ci}}{N_i} = e^{-\Delta G_F/RT}$$

where, N is the number of the occupied cationic sites and N_i is the number of available interstitial sites, and n_{cv} and n_{ci} denote the number of formed cation vacancies and occupied interstitial sites, respectively.

As n_{cv} is equal to n_{ci}, both are equal to the cationic Frenkel defects:

$$n_{cv} = n_{ci} = n_{cF} = \sqrt{NN_i}\, e^{-\Delta G_F/2RT}$$

If the number of normal and interstitial sites, $N = N_i$, is the same, the equation is identical to the equation of Schottky defects:

$$n_{cF} = Ne^{-\Delta H_F/2RT}$$

And when replaced by the enthalpy of formation of the Frenkel defect, it becomes:

$$n_{cF} = \sqrt{NN_i}\, e^{-\Delta H_F/2RT}$$

and, for a single defect,

$$n_{cF} = \sqrt{NN_i}\, e^{-\Delta h_F/2kT}$$

Problem VI. *Using the energy for Schottky defect formation for the NiO crystal of 198 kJ/mol and its lattice parameter (NaCl type) a= 4.17 Å, calculate the number of Schottky defects in 1 m^3 of NiO at 1000 ºC. How many vacancies are there, and how many Schottky defects are present in one gram of solid? (Note: determine and use the NiO density).*

The anionic Frenkel defect will result in the same expression.

Defect clustering

The presence of defects, especially vacancies, causes structural relaxation around the defect. In metals, the atoms move toward an empty position making the vacancy smaller, whereas the opposite occurs for the ionic solids: the surroundings move outwards. Closely situated charged vacancies could attract each other and form a pair or clusters of a larger size.

Problem VII. *Calculate the theoretical density for O-rich (O/Fe =1.058) and Fe-deficient (Fe/O=0.95) wüstite (lattice parameter 4.301Å) and compare it to the observed density for that compound (5.728 g/cm^3).*

A typical example of that is the FeO wüstite. The ideal stoichiometric structure presents a rock-salt structure with Fe^{2+} in octahedral sites, but the empirical structure presents an excess of oxygen. There are two possibilities where the latter is concerned: either an excess of oxygen (FeO_{1+x}) in the interstitial sites or an iron deficiency resulting in Fe vacancies ($Fe_{1-x}O$). We can determine which of the two mechanisms occurs by a comparison between real and theoretical density.

Density calculations show that the wüstite structure is better reflected by the $Fe_{1-x}O$ formula corresponding to iron deficiency. Obviously, the iron vacancies are compensated by the presence of oxygen vacancies, and electroneutrality is maintained, when Fe^{2+} is oxidized to Fe^{3+} for every anionic vacancy. However, the vacancies are not randomly distributed, and a small aggregate with a variety of clusters appears, the most stable configuration of which is four cationic vacancies (*Figure 8* in red) around an Fe^{3+} known as a 4:1 cluster. The generated Fe^{3+} ions occupy the empty interstitial tetrahedral positions instead of the normally occupied octahedral ones (rock salt structure type). This organization recalls that of iron spinel

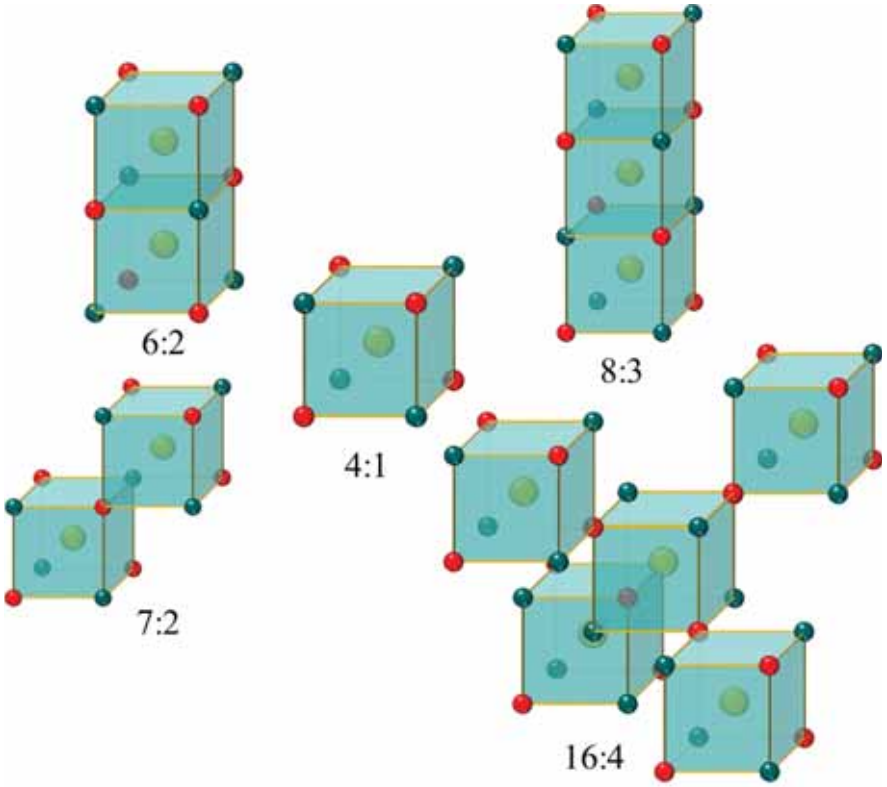

Figure 8. Defect cluster organization for wüstite structures (red circles Fe^{2+} vacancies, green circles O^{2-} in its normal sites and yellow circles Fe^{3+} ions

Another example is hyperstoichiometric UO_{2+x} with a fluorite type structure that can be represented by UO_8 cubes at the centre of the fluorite unit. Above 1100 ºC, the structure exists with x ranging between 0 and 0.25 and this variation is due to the presence of interstitial O^{2-}. The extra oxygen charge is compensated, and some of the U^{4+} ions convert to U^{5+} and U^{6+}. The defects cluster together in 2:2:2 Willis cluster chains, consisting of 4 oxygen cubes with one interstitial oxygen each, two placed along the <111> diagonal, and the other two along the <110> diagonal (*Figure 9*). This organization causes an additional effect: oxygen vacancies appear in the junction of every three cubes, so that in the cluster agglomerate we have 2 vacancies, two oxygen interstitials and 2 oxygen atoms in their normal positions. The introduction of oxygen alters the lattice parameters and

increases the cell volume up to a certain value, indicating the moment when the clustering of defects becomes significant, with a consequent decrease of the volume of the solid.

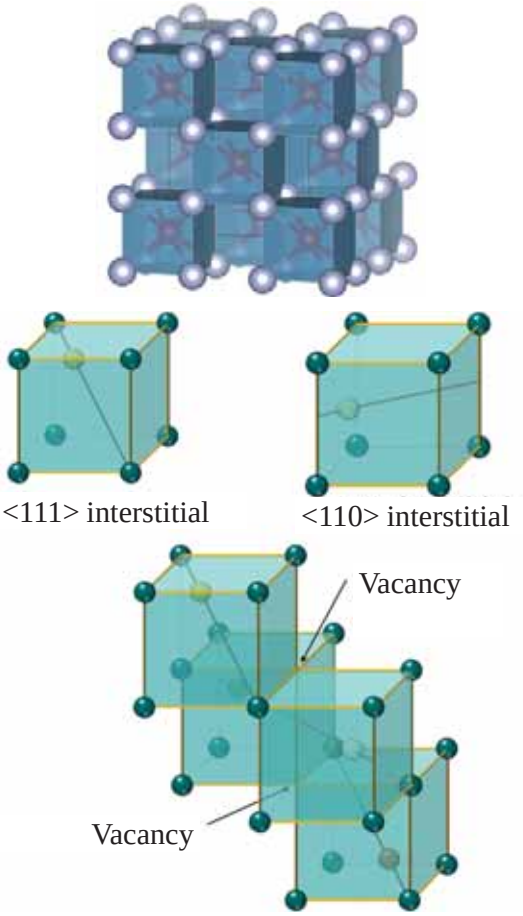

Figure 9. Cluster organization in a hyperstoichiometric UO_{2+x} compound (fluorite structure).

Solid solutions

Both compounds ($Fe_{1-x}O$ and UO_{2+x}) introduce a very important group of extrinsic defects non-stoichiometric compounds. The defects occupy interstitial sites of the oxides, but when the concentration of the dopant increases, substitution can arise, leading to the formation of **solid solutions**. The solid solution is a crystal structure with a different composition where the major component is called solvent and the add-component solute. We can differentiate solid solutions of two types: **substitutional**, when a component of the solvent is replaced by solute atoms or ions, and **interstitial** when the solute infiltrates empty interstitial sites.

The formation of an interstitial solid solution is conditioned by the size of the entering atom/ion. Elements such as H, C and N can easily enter a metal host structure, a typical example of which is the interstitial solid solution resulting from the introduction of C into iron. This process, where C enters the octahedral interstices of γ-Fe, is the basis of the steel industry.

An example of substitutional solid solution formation is the solid formed by Cr_2O_3 and Al_2O_3. The composition of this solid solution varies from a pure Al_2O_3 to a pure Cr_2O_3, although a very small part of its range compositions produces the synthetic red ruby used in lasers. The properties of this solid solution, especially the colour, depend strongly on the proportion of its Cr^{3+} content, as the colour gradually changes from colourless Al_2O_3 to intense red and finally green. A small amount of Cr^{3+} (0.04 to 0.5%) lends it the ruby colour and its optical properties. The ruby crystal is the basis of ruby laser emission (Light Amplification by Stimulated Emission Radiation). The Cr^{3+} ions substitute Al^{3+} in a distorted octahedral environment and the three d-electrons occupy the fundamental *d*-levels. Upon light absorption, one of these electrons may transit to a higher energy state—excited state—in two possible transitions (*Figure 10*).

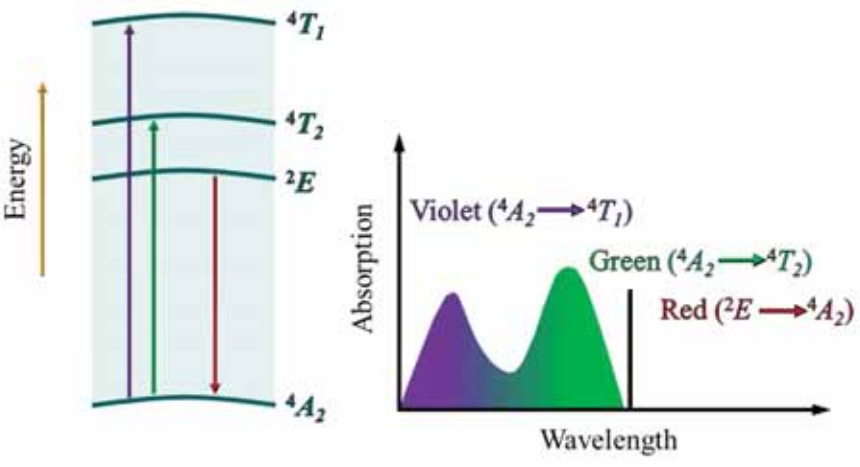

Figure 10. Cr $^{3+}$ excitation and ruby laser emission

After that, the electrons may return to the fundamental state, emitting the same energy as the absorbed energy, their level of excitation dissipating after non-radiative emissions. In this case, the energy release is assumed by the crystal as vibrational energy. The electron cannot go back to the fundamental level, because this transition is related to a spin change and it is doubly prohibited by Laporte and the spin rule, so the electron remains trapped. When the electron population is sufficiently high at this level, the emission of the first photons induces a spontaneous coherent emission, known as red laser emission.

As more Cr^{3+} is substituted for Al^{3+}, we also start to observe a change in the unit cell parameters. In 1921, Vegard postulated an empirical correlation between the lattice parameters of the solid solution and those of its parent compounds. The solid solution lattice parameter must fall on a straight line between the parameters of both parents, according to its composition (*Figure 11*).

For a solid solution with composition A_xB_{1-x} and a lattice parameter, a_{AB}, where A and B are the parent compounds with lattice parameters a_A and a_B, the expression of Vegard's law is:

$$a_{AB} = x a_A + 1\text{-}x\ a_B$$

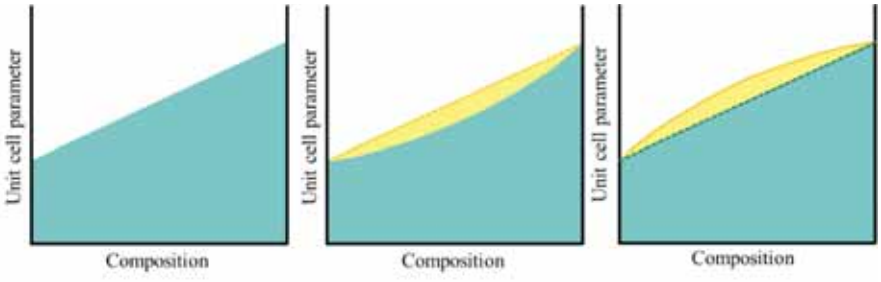

Figure 11. Behaviour according to Vegard's law

Taking into account that Vegard's law reflects the lattice parameter change as a consequence of the atomic/ionic radii variation within the cell, any deviations, whether "negative" (below the ideal straight line), or "positive" (above it), result only from the size effect.

The possibility of substitutional solid-solution formation is higher when some specific requirements are met. Those requirements, known as the Hume-Rottery solubility rules that were postulated in the twentieth century for metallic alloys, are summarized as follows:

i. The crystal structure of each element is identical;
ii. The atomic sizes could differ within 15 %;
iii. There is no important difference in electronegativity;
iv. The elements have the same valence.

They can be applied to ionic compounds, although an additional condition must be considered: crystal electroneutrality.

v. The total charge of positive and negative ions must remain zero.

Aliovalent substitutions are also possible when ions are substituted by ions of a different charge. The additional charges that appear are compensated, either by the creation of additional vacancies that fill the interstitials (ionic compensation), or by electrons and holes (electronic compensation).

If the entering ion is a cation of higher charge than the ion from the host structure, a cationic vacancy is created. Ca^{2+} ions can replace some Li^{+} ions in LiI, leaving one Li^{+} vacancy for each Li^{+} replaced by Ca^{2+}. This aliovalent substitution increases the population of the Li^{+} vacancies and promotes the conductivity of the Lithium Iodide battery.

This type of battery is used in pacemakers and consists of a Li anode where the oxidation reaction takes place ($Li \rightarrow Li^+ + e^-$) and an I_2/polymer hybrid cathode with a corresponding reduction reaction ($½\ I_2 + e^- \rightarrow I^- + e^-$). The electrons travel through an external circuit closed by ions moving across the electrolyte (*Figure 12*). A key component is the electrolyte that can support ionic, but not electronic, conduction, i.e., LiI only transfer ions. LiI has a rock salt structure and the only way to sustain an ionic transfer is the presence of a Schottky defect population.

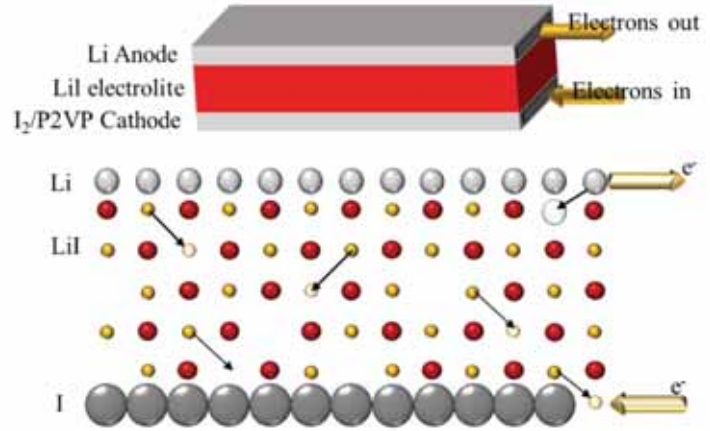

Figure 12. LiI battery

This population is rather low for pure LiI and a CaI_2 doping is used to improve the ionic conductivity of the electrolyte, the introduction of one Ca^{2+} generates one additional Li^+ vacancy.

The introduction of a higher valence cation into the structure can also create interstitial anions. That is the case of uranium oxide UO_{2+x}, listed above, where, upon oxidation, the O^{2-} ions are introduced into interstitials, and a part of U^{4+} is oxidized to U^{5+} and U^{6+}, resulting in a mixed valence solid solution: $U^{4+}{}_xU^{6+}{}_{1-x}\,O_{2+x}$.

If the entering ion is of lower charge than that in the host structure, the charge balance is maintained by creating anion vacancies or cation interstitials. One example is the replacement of Zr^{4+} in ZrO_2 by Ca^{2+}; for every calcium ion, one anion vacancy is created.

The interstitial cation addition mechanism, well known in aluminosilicates, has a compensatory effect. The charge generated through Si^{4+} replacement

by Al^{3+} is compensated by the introduction of interstitial alkali metal cations or protons. These materials are known as molecular sieves or zeolites, used as absorbents and catalystss in the petrochemical industry.

The charge compensation during aliovalent substitutions is not always ionic; electronic compensation can also occur, altering the conduction behaviour of solids. One typical example is the rock salt-type NiO structure. Upon heating, an excess of O^{2-} appears in the structure and cation vacancies, and the holes that are created are responsible for the semiconductive behaviour of NiO (*p*-type semiconductor). The final structure is often described as Ni^{3+}, replacing Ni^{2+} with one effective positive charge on a defect.

Another example is CdO (rock salt structure) where an excess of metal is observed. The defects are usually described as interstitial Cd^{2+}, with charges that are compensated by electrons. The appearance of extra electrons converts the oxide into an *n*-type semiconductor and its conductivity depends on O_2 partial pressure.

Interstitial cation intercalation can result from the insertion of cations between the sheets of a layered structure. A weak chemical bonding results between the layers in contrast to the strong bonding within the layer. An example of such a compound is the non-stoichiometric TiS_2 layered structure with Li^+ intercalation between the layers (*Figure 13*). The non-stoichiometry of the structure arises from the gradual filling of the empty octahedral sites with Ti, resulting in $Ti_{1+x}S_2$ (x ranging between 0 and 1). The Li interlayer intercalation creates another family of non-stoichiometric phases with the general formula Li_xTiS_2.

The open layered structure allows Li movement, and this type of compound is used as an alkali reservoir for alkaline batteries. Commercially available batteries are now designed with Li_xMO_2 phases, where M is a transition metal such as Ni, Co or Mn.

When the space to be occupied is larger and usually unoccupied, the entering species is called an interpolated species and occupies tunnelled or caged spaces in the structure. Typical examples are the tungsten bronzes with the formula M_xWO_3, where M is practically any metal of the periodic table. The interpolated species occupy the cubic or pentagonal interstices originated by WO_6 octahedral organization. The variation in the metal filling originates an important family of non-stoichiometric compounds with a wide compositional range.

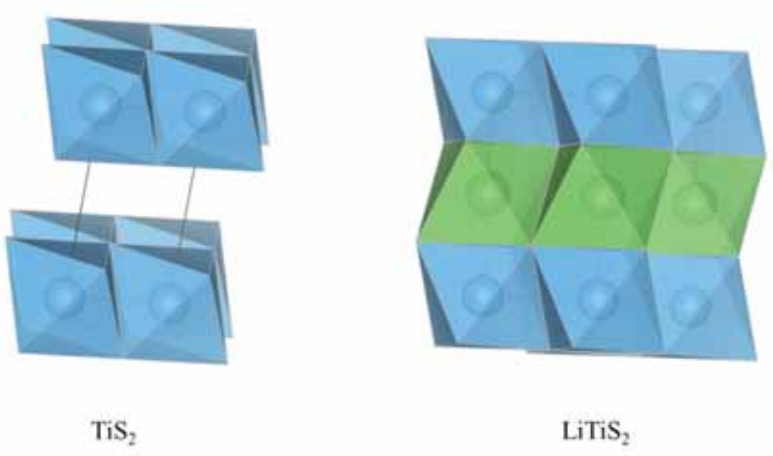

Figure 13. TiS_2 layered structure and Li intercalation behavior

Another structure of this type is the hollandite structure $A_2M_8X_{16}$, with cryptomelane $K_2Mn_8O_{16}$ as an example. The structure is organized by edge-sharing MnO_6 octahedra, forming wide tunnels occupied by K (*Figure 14*). The variation of the tunnel filling makes the structure non-stoichiometric, and a mixed Mn valence organization is found.

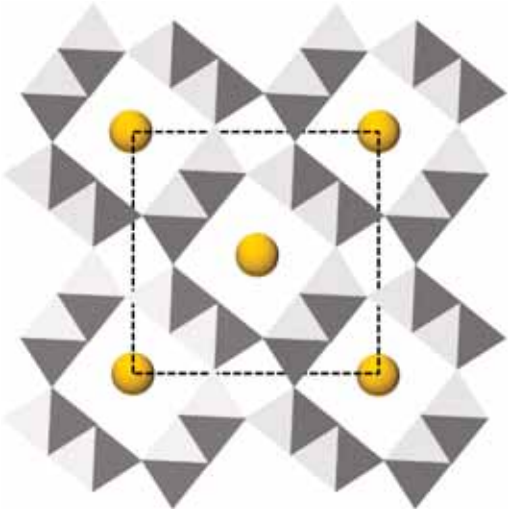

Figure 14. Hollandite type structure.

All groups enumerated so far correspond to the presence of point defects which introduce some degree of non-stoichiometry into the solids and produce significant changes within their optical and bulk properties and conductivity. The possibility of agglomeration of the point defect introduces another important group of defects, known as extended defects.

Extended defects

Starting with the linear defects, dislocations are among those with greatest influence on the mechanical properties of solids, particularly metallic solids. **Edge dislocation** appears when an extra half plane of atoms is added to the crystal. This defect is stoichiometric and involves a distortion of the crystal in the environment of the added half line of atoms. We can define a dislocation line as a line perpendicular to the plane of the figure, localized on the tip of the inserted plane (*Figure 15*, indicated by ⊥).

When shear stress is applied, the opposite ends of the crystal are pushed in opposite directions (left and right arrows in *Figure 15*). At that point in time, the dislocation glides, atom number 3 breaks its bond with number 6, and a new bond 2-6 is created that leaves atom number 3 on the top of the dislocation. The movement, called *slip*, can continue until it reaches the surface.

The magnitude of the dislocation is measured by the so-called Burgers vector, $\vec{b}$, and can be determined by drawing a closed circuit around the dislocation in clockwise direction. For a perfect crystal A-B-C-D the resulting circuit is closed, whereas the circuit of the dislocation remains open. In that case the vector (in red) needed to close the circuit is the Burgers vector. The Burgers vector of an edge dislocation is perpendicular to the dislocation line.

Another type of dislocation is the screw dislocation that creates a defect like a spiral staircase. Its virtual formation cuts halfway through the crystal, sliding the sides parallel to the cutting edge (*Figure 16*). The slip plane contains the dislocation line and the Burgers vector is parallel to that line.

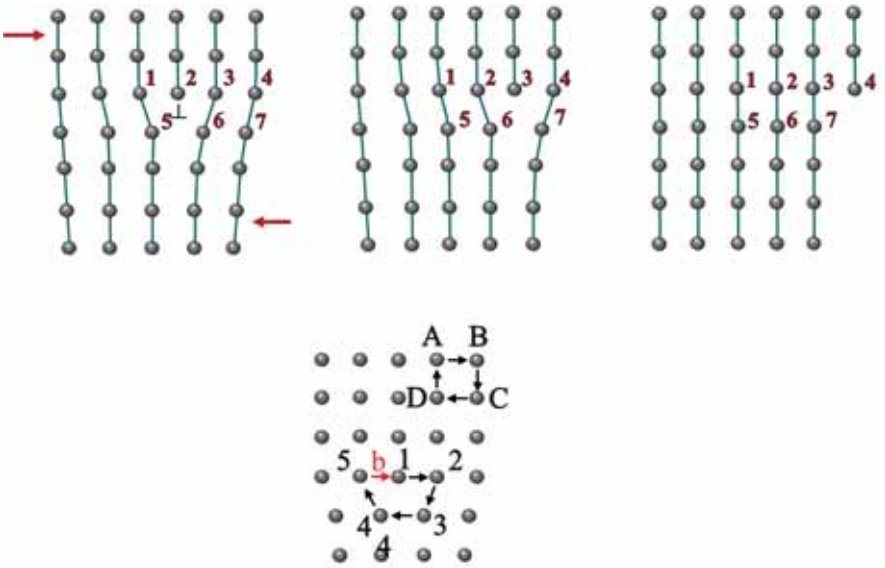

Figure 15. Edge dislocation migration

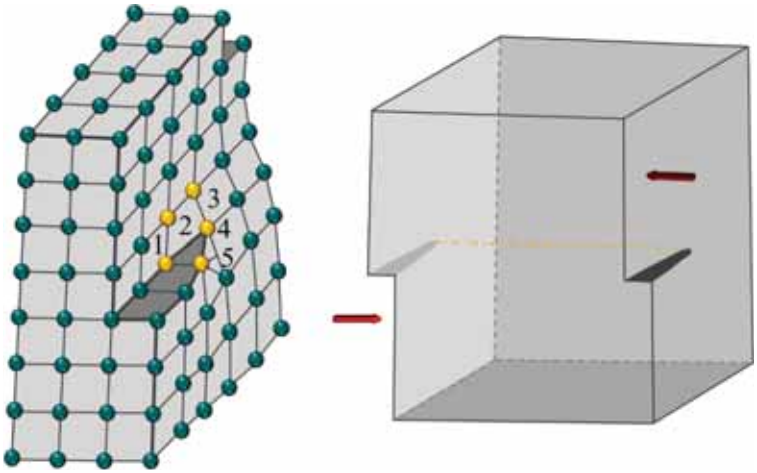

Figure 16. Screw dislocation

Generally, the dislocations observed in solids are of various types: edge and screw dislocations coexist; the atom shifting in that region is a combination of both and recalls a **loop** movement as a part of a ring configuration. The movement of the dislocation toward the surface leaves a step of height equal to the Burgers vector. The formations of **loops**, considered frequently as a significant **clustering of vacancies** and a weakening of the structure, is responsible for the reduction of the metal's mechanical strength. However, the addition of some impurity atoms may produce the opposite effect by "locking" the dislocation movement; which is the role of the C interstitial atoms in the iron metal matrix when forming a steel. Hardening can also be achieved by hammering the material (work-hardening): an important number of dislocations arise and start moving in all directions. The majority of the dislocations are stopped at the grain boundaries and the mechanical properties of the materials are improved. Although all directions for movement are possible, there are some preferred planes, or a set of planes, where the dislocation originates and from which it prefers to migrate. For metals, that direction is parallel to the direction of close packing. For copper (*fcc* stacking), the slip plane is (111) and the direction of dislocation is [110]. The shortest vector describing the run starts at the corner atom and finishes at the middle face atom.

Although the crystal appears well-ordered, an important number of "domains" exist, each slightly misaligned to the others, that are separated by **internal boundaries**. Such boundaries are considered a 2-D defect and, when disordered, form extended defects. They can produce local alterations in the composition of the solid and are characterized by the variation of atom ordering, frequently leading to **antiphase boundaries** (*Figure 17*). The antiphase boundary is a displacement defect characterized by a vector specifying the displacement of one part with respect to the other. The antiphase boundaries for metals such as copper are identical to other types of defect referred to as stacking faults; these describe changes in the stacking sequence corresponding to the lattice type. When *ABCABCABC* stacking is disrupted, yielding an *ABCACABC* sequence, the antiphase boundary lies between A and C in the second stacking group. For ionic solids, the antiphase may affect only one type of ion due to the unchanged composition left after the formation of that boundary.

All the extended defects considered above are structural defects, due to disruption within the order of the crystal. No change of composition is found in them. The same is true for the surface, which is itself regarded as one of the major defects, due to the presence of unsaturated bonds, adatoms, gas occlusion and adsorbed molecules (*Figure 18*).

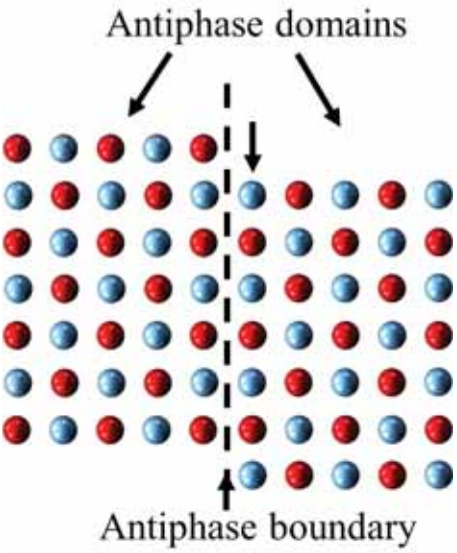

Figure 17. Antiphase boundary

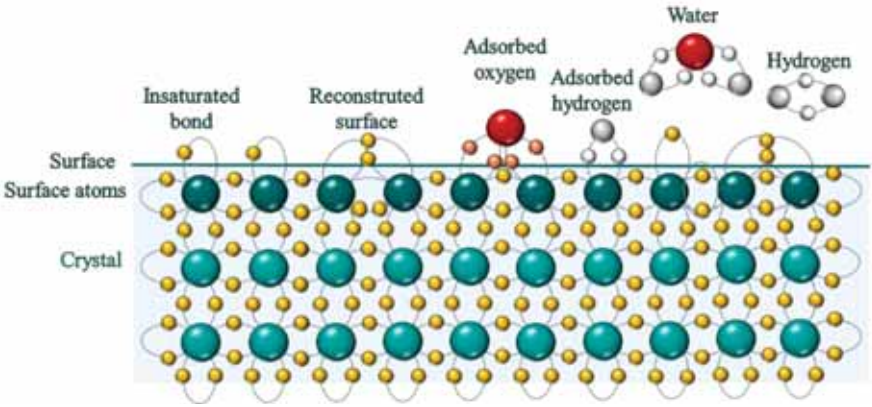

Figure 18. Schematic representation of solid surface.

The surface is continuously exposed to gases, liquids, or is in contact with other solids, and it is almost always covered by a layer of atoms or molecules of another phase. The surface is studied in a separate field of science, *Surface Science*, dealing with all phenomena that may occur over

that extended defect and some of them will be the subject of the last two chapters of this book, dedicated to heterogeneous catalysis.

Shear planes

Shear planes are compositional extended defects and correspond to a plane of atoms intentionally removed from the crystal. The removal of atoms causes a reconstruction of the crystal through structural arrangements that eliminate the defects (Figure 19).

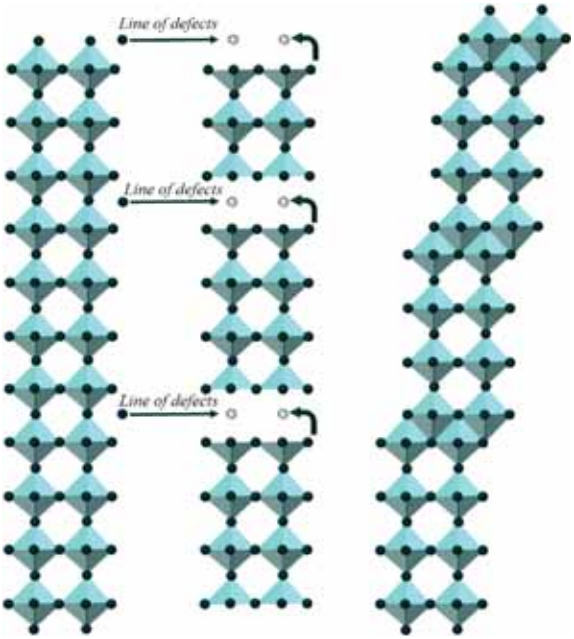

Figure 19. Shear plane formation

These defects are very typical of the structures known as *berthollides*—substitute bronze materials with the general formula $Na_xW^{5+}{}_xW^{6+}{}_{1-x}\ O_3$. When reduced under hydrogen, some of the oxygen atoms are converted into water. The line of defects thus formed introduces instability into the structure, which is removed by the creation of new bonds, bringing the oxygen defects of the environments closer and regenerating the 6-fold coordination. The block formed of 4 organized octahedra generates a

practically linear and periodically sheared chain, sharing one oxygen per octahedron, *Figure 20*.

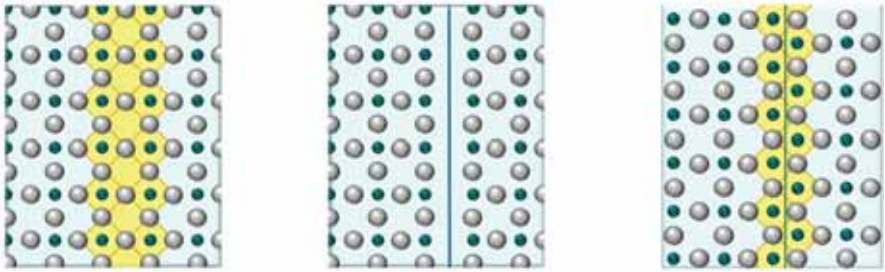

Figure 20. Shear plane organization

The mechanism of shear plane formation for WO_3 solids is believed to proceed through aggregation of the oxygen vacancies on the {102} and {103} planes, strictly dependent on the degree of reduction or oxygen removal. This process, which is not limited, may occur in all dimensions with the formation of rectangular or square blocks of different size; block structures are then formed. Excellent examples are the structures based on Nb_2O_5, presenting two types of blocks (3x4) and (4x4) octahedra (*Figure 21*).

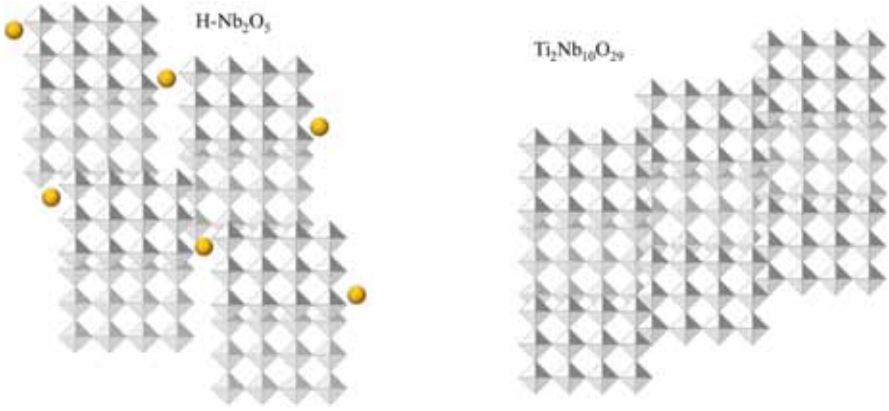

Figure 21. Nb_2O_5 based block structures (shaded blocks differ in height).

Both arrangements, shear planes and block structures, produce additional rectangular or tetrahedral interstices that can be filled by rearrangement of blocks and are known as **Wadsley defects**.

Compositional defects of another type are the **Suzuki phases** obtained when an alkali halide is doped with a divalent cationic impurity above the solubility limit; the latter results in new phase precipitation. The resulting structure can be described as a cubic phase with lattice parameter twice that of NaCl and formed by 3D arrays of impurity-vacancy organizations. The dipole organization results in 2x2x2 blocks and the whole structure is organized by alternate layers of NaCl and impurity-vacancy planes (*Figure 22*).

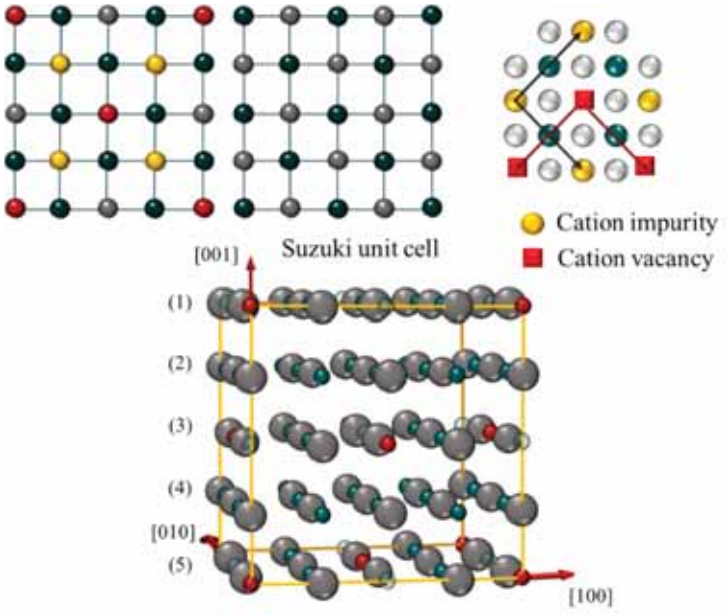

Figure 22. Organization of Suzuki phases

It is clear that the presence of defects within solids is inevitable and that their type and concentration will influence the structure and, as a consequence, their properties. Typical examples are: the behaviour change of extrinsic semiconductors after doping, the appearance of colour in otherwise transparent solids, the improvement of mechanical properties by the addition of impurities or variations in magnetic properties. The literature is full of structure-property relationships in every branch of Materials Science. In the following two chapters, however, we will focus on the catalytic behaviour of solids as an unconditional part of heterogeneous catalysis.

References

Defects in solids, Richard J. D. Tiley, John Wiley & Sons Inc. USA, 2008.

Crystal chemistry from basic tools to materials creation Gérard Férey, World Scientific, Singapore, 2017

Solid state chemistry and its application 2nd edition, Anthony R. West, 2014 John Wiley & Sons, Ltd, UK

Solid State Chemistry, L. E. Smart and E. A. Moore (2012), CRC Press, Boca Raton, FL

P. Aceituno, F. Cussó, A. de Andres, F. Jacque, Aggregation pathways and Suzuki phase formation in doped alkali halides, Solid state communications, 49, 1984, 209-212.

All structures are generated with Vesta software using the CIF from http://www.crystallography.net/cod/index.php and references listed below in order of appearance:

TiS_2: I. Oftedal, Roentgenographische Untersuchungen von SnS_2, Ti S_2 $TiSe_2$, $TiTe_2$, Zeitschrift fuer Physikalische Chemie (Leipzig), 1928, 134, 301-310.

$LiTiS_2$: J. R. Dahn, W. R. McKinnon, R. R. Haering, W. J. L. Buyers, B.M. Powell, Structure determination of Li_xTiS_2 by neutron diffraction, Canadian Journal of Physics, 1980, 58, 207-213.

CHAPTER 6

REACTIONS ON SOLID SURFACES: INTRODUCTION TO HETEROGENEOUS CATALYSIS

"It is, then, proved that several simple or compound bodies, soluble and insoluble, have the property of exercising on other bodies an action very different from chemical affinity. By means of this action they produce, in these bodies, decompositions of their elements and different recombinations of these same elements to which they remain indifferent"
Jöns Jacob Berzelius (1779 – 1848)

Catalysts, of vital importance to the modern global economy, can transform raw materials through economically efficient, and environmentally friendly processes that produce high-grade chemicals and fuels. A large number of pharmaceuticals, fertilizers, food, energy vectors or materials of everyday use are produced via catalytic processes, 90% of which are heterogeneously catalysed. Heterogeneous catalysis is also finding new applications in emerging areas such as green chemistry, fuel cells, nanotechnology, and biotechnology.

A detailed understanding of heterogeneous processes entails knowledge of both the catalyst surface and the reactant-catalyst interface. As a consequence, *Surface Chemistry* has emerged as an exciting discipline in heterogeneous catalysis, and powerful tools for probing the atomic and molecular species in the topmost layers of solids are under continuous development to refine the understanding of catalyst action and behaviour. While the previous chapters have treated the fundamental principles of solid-state chemistry in detail, these last two chapters are focused on the application of solid materials as heterogeneous catalysts. It is difficult to achieve a simple discussion of the principles of heterogeneous catalysis, as catalysts involve a rich range of physicochemical surface properties and can be used in a wide range of reactions. This chapter only provides a global and simple view of heterogeneous catalysis, explaining, as concisely as possible, all principal aspects, including some recent developments.

Historic overview of catalysis as scientific discipline

Catalysis is a well-known phenomenon, discovered at the dawn of human history, and practiced since ancient times in the art of wine and beer production by fermentation. The theoretical concepts defining catalysis as a scientific discipline were, however, only introduced in the nineteenth century by Berzelius, Davy, Faraday, and Ostwald, among others. During the twentieth century catalysis became one of the fundamental pillars of the present-day chemical and manufacturing industry. A chronological list of the most significant discoveries below provides a historic illustration of the most important scientific advances that gave rise to the modern science of catalysis:

- **5000 B.C.** – *Production of wine by **fermentation** of sugars (enzymatic catalysis).*
- **1575** – *V. Cordus used sulphuric acid to catalyse the **transformation of alcohol** to ether.*
- **1811** – *Kirchhoff observed that heating an aqueous solution of **starch with mineral acids** transformed it into a gum (dextrin) and then into grape-sugar.*
- **1817** – *H. Davy evidenced a reaction between two gas reactants on a metal surface, which itself remains unaltered.* ***He discovered the use of platinum in catalysis.***
- **1818** – *Thénard investigated the production of oxygen by **decomposition of oxygenated water** in the presence of Ag, Au, Mn and Pt.*
- **1820** – *E. Davy reported the **oxidation of ethanol to acetic acid** in the presence of finely divided platinum.*
- **1822** – *Döbereiner studied the **reaction of hydrogen and oxygen** in the presence of platinum sponge.*
- **1825** – *Henry discovered the deactivation of Pt-based catalysts in presence of hydrogen sulphide and carbon disulphide.*
- **1834** – *Faraday provided the first scientific basis of **electrocatalysis** (metal-catalysed hydrolysis, oxygen reduction, and fuel cells).*
- **1836** – *Berzelius proposed the **first definition of catalysis** inspired by acid-, base-catalysed reactions.*

- **1877** – *Lemoine showed that the reaction rate at which **chemical equilibrium** is achieved could be increased, but the **position** of equilibrium cannot be altered.*
- **1878** – *Kühne coined the name **enzymes** for biological catalysts.*
- **1905** – *Haber developed a process for producing **ammonia** from its elements using a Fe-based catalyst, and received the Nobel prize in 1918.*
- **1909** – *Ostwald received the Nobel prize for his work on catalysis and investigation into fundamental principles in chemical equilibrium and **reaction rates**.*
- **1912** –*Sabatier was awarded the Nobel prize for his work on hydrogenation of organic compounds in the presence of finely disintegrated nickel*
- **1925** – ***Fischer** and **Tropsch** synthesized hydrocarbons from CO and H_2 at high pressures.*
- **1926** – The ***DuPont** company started the first large scale industrial production of **methanol**.*
- **1927** – *Hinshelwood published his kinetic theory based on earlier findings of Langmuir.*
- **1931** – *Bosh and Bergius received the Nobel prize in recognition of their contribution for the development of **high-pressure reactions**.*
- **1932** – *Langmuir received the Nobel prize for his discoveries relating to **surface chemistry**.*
- **1936** – *Houdry developed the **catalytic cracking of crude oil**, which was improved by Lewis and Gilliland in **1941** by their introduction of **fluid catalytic cracking (FCC) technology**.*
- **1951** – *Wheeler discovered the influence of **gas diffusion** on catalyst activity and selectivity.*
- **1953** – *Ziegler and Natta were both awarded the Nobel prize in 1963 for new chemical formulations related to technology for **high-polymer production**.*
- **1954** – *Eischen developed a method for characterization of metal and metal oxide active surfaces by adsorption, distinguishing between **Brønsted and Lewis acid sites**.*

- **1956** – *Hinshelwood and Semenov received the Nobel prize for their research into* ***reaction mechanisms****.*
- **1960** – *Three important industrial processes were commercialized: ethylene to acetaldehyde (****Wacker process****), benzene to cyclohexene (****Hydrar process****), and the first acrylonitrile production plant (****SOHIO process****).*
- **1964** – *Mobil Oil developed an efficient rare earth metal stabilized X-zeolite for* ***catalytic cracking****. This* ***zeolite*** *revolutionized the petrochemical industry and is today one of the most important industrial catalysts.*
- **1965** – *Wilkinson designed a homogeneous Rh-based catalyst for* ***hydrogenation,*** *widely used in pharmaceutical and fine-chemical industries.*
- **1968** – *Heck and Mizoroki independently discovered the* ***Heck reaction****, widely used today in fine chemistry.*
- **1973** – *Fischer and Wilkinson received the Nobel prize for the development of* ***sandwich-type organometallic compounds****.*
- **1975** – *Engelhard corporation developed the first commercial* ***exhaust after-treatment*** *catalytic system for reducing the pollutant emissions from automobiles.*
- **1976** – *Mobil Oil commercialized a* ***methanol-to-gasoline process*** *operating with ZSM-5 zeolite catalyst.*
- **1978** – *Introduction of* ***selective catalytic reduction (SCR)*** *for stationary power plants NO_x emission control.*
- **1990** – *Commercialization of* ***benzene-to-phenol oxidation*** *process over Fe-ZSM-5 catalyst.*
- **1992** – *Ertl patented the first* ***non-based iron catalyst for ammonia synthesis****.*
- **1994** – *Olah was awarded the Nobel prize for his contribution to the carbocation chemistry.*
- **2001** – *Knowles, Noyori and Sharpless received the Nobel prize for* ***chirally catalysed hydrogenation reactions****.*
- **2002** – *The Latin term* ***operando*** *was introduced to highlight the importance of studying catalyst materials under working conditions.*

- **2005** – *Chauvin, Grubbs and Schrock received the Nobel prize for the development of* ***metathesis reactions*** *in organic synthesis.*
- **2007** – *Ertl was awarded the Nobel prize for his studies on* ***chemical processes on solid surfaces****.*
- **2010** – *Heck, Negishi and Suzuki received the Nobel prize for their discovery of* ***Pd-catalysed cross-coupling reactions*** *in organic synthesis.*
- **2020** – *Quo Vadis*

Ever since the early years of the twenty-first century, catalysis as a scientific discipline has been enjoying a "new golden age", due to the continuous necessity for research into the complex environmental and energy issues faced by our industrialized society. The development of the bio-economy sector related with the creation of next-generation biorefineries makes it necessary to find novel strategies for efficiently treating bio-based molecules and materials. From a more fundamental point of view, advances within the field of computational and molecular chemistry are expected to provide a robust basis for the formulation of a molecular theory of catalysis. The application of advanced characterization techniques under realistic conditions in investigating the dynamic behaviour of catalysts offers one of the best perspectives for successful research and the rational design of a new generation of catalysts. In the field of reaction engineering, innovative reactors must be developed using 3D-printing technology. The microreactors technology is an interdisciplinary field that has attracted enormous interest, due to its numerous advantages in comparison to conventional reactors, such as improved heat and mass transfer and safety operations. Therefore, the possibilities offered by catalysis science are virtually infinite and depend only on the creativity of researchers and the new developments required by a future sustainable society.

Definition and classification of catalysis

After the first definition, suggested by Berzelius in 1835, as *"the decomposition of bodies by a catalytic force"*, the concept of catalyst has been remastered many times. In 1895, Ostwald proposed a definition still in use nowadays describing a catalyst as *"a material that accelerates a chemical reaction without affecting the equilibrium position and thermodynamics of the reaction"*. Finally, the modern definition includes the concept of catalytic cycle and describes a catalyst as *"any substance that*

transforms reactants into products, through an uninterrupted and repeated cycle of elementary steps in which the catalyst participates while being regenerated to its original form at the end of each cycle during its lifetime".

The catalytic reaction consists of various steps in which the reactants are bonded to the catalyst and react to form the products that are finally released from it (*Figure 1*), leaving it available for a new catalytic cycle. The catalysed reactions may comprise several intermediate and transition-state complexes, completely different from the one involved in the non-catalysed reaction. Therefore, the catalyst offers an alternative path for the reaction—more complex, but energetically much more favourable, as is confirmed by the potential energy curve in *Figure 1*.

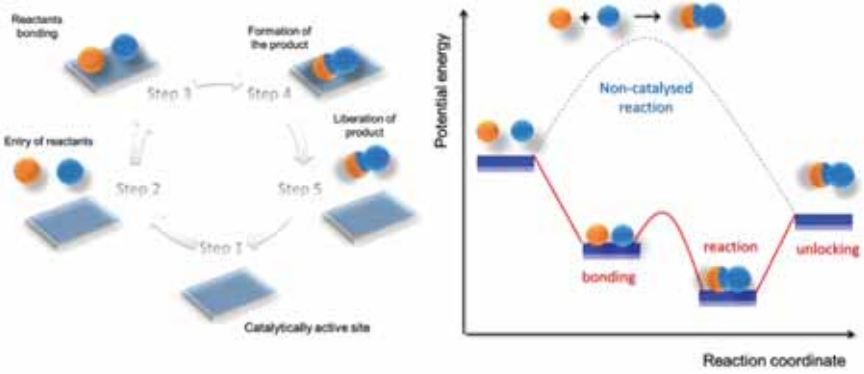

Figure 1. Catalytic reaction cycle: sequence of elementary steps and potential energy diagram.

Catalysts can be found in a multiplicity of forms ranging from single-atoms or molecules to large crystalline solids or even biological structures like enzymes. Furthermore, catalysts can operate in different reaction environments and phases: liquids, gases or solid surfaces. The vast variety of catalysts can be classified on the basis of two criteria: structure and phase composition. Accordingly, catalysis can be classified in three categories: *homogeneous catalysis* (molecular/organometallic catalysts), *biocatalysis* (enzymes), and *heterogeneous catalysis* (solid catalysts). *Homogeneous catalysis* and *biocatalysis* take place usually in uniform phases, gas or liquid, whereas *heterogeneous catalysis* typically occurs in a biphasic system. Enzymes are positioned somewhere between molecular-homogeneous and macroscopic-heterogeneous catalysts (*Figure 2*).

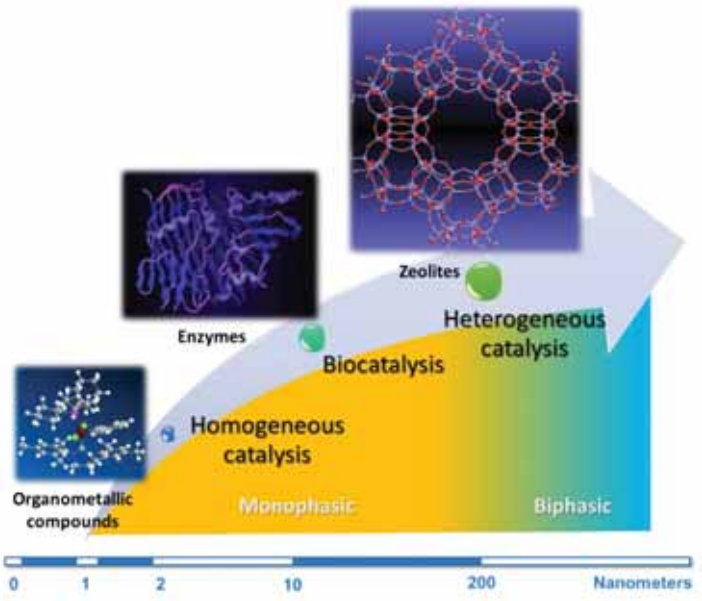

Figure 2. Classification of the three types of catalysis on the basis of structure and phase composition.

In *homogeneous catalysis*, the processes occur in a uniform and mostly liquid phase, in which both catalyst and reactants are molecularly dispersed in the reaction medium. Organometallic complexes, organic acid metal salts, or even mineral acids or bases constitute the typical examples of homogeneous catalysts. One industrial process that uses homogenous catalysts is the carbonylation of methanol to acetic acid, known as the Monsanto process, which employs an Rh-complex based catalyst. Despite presenting important advantages such as excellent selectivity and single active sites, homogeneous catalysts are industrially limited, due to their low thermal stability and high recovery costs.

In the second category, the term of *biocatalysis* refers to the utilization of enzymes as catalysts. Enzymes are large organizations of proteins that present adequate structure for a shape-specific active site that improves rates and selectivities of biologically relevant reactions necessary for living cells. The enzymatic reactions are not uniquely confined to the *in vivo* systems, but can also operate in aqueous media and organic solvents in highly specific reactions. Nowadays, biocatalysis offers excellent opportunities in the pharmaceutical and food industries, for which the enantioselective

reactions are extremely important for the development of many drugs, flavours and food additives. Although very expensive and inadequate for the traditionally conservative chemical industries, it is increasingly evident that enzymes will play a key role in the replacement of some traditional chemical manufacturing routes in the production of biofuels within the near future.

The last category, *heterogeneous catalysis*, involves the participation of several phases, in which the catalyst is usually solid and the reactants gases or liquids. The main advantage of using solid material is the ease of separation of reactants or products and catalysts. Heterogeneous catalytic processes are the basis of the existing petrochemical and bulk-chemicals industries, since only solid catalysts can adequately satisfy the large installations, continuous processing and high temperatures required for these industrial processes.

Problem I. *Compare homogeneous and heterogeneous catalysis using the following table and discuss it in details.*

	Heterogeneous	Homogeneous
Active centres	Atoms exposed on the surface	All atoms
Selectivity	Minor selectivity	Very selective
Reaction conditions	Severe (often temperatures superior to 250 ºC)	Mild conditions (25 – 200 ºC)
Activity loss	Sintering of metal particles or poisoning	Cluster formation and poisoning
Structure / Stoichiometry	Undefined	Defined
Thermal stability	Very high	Low
Catalyst recycling	Unnecessary (fixed-bed reactors)	Very laborious (distillation or extraction)
Cost	Low	High

Catalysis as multidisciplinary science: spatial-time multiscale approach

Catalysis, heterogeneous in particular, is not a mere subfield of chemistry and chemical engineering but a broad area involving disciplines such as materials and solid-state chemistry and physics, surface science, chemical kinetics and reaction engineering. None of these disciplines is more important than the others; rather, their mutual integration and cooperation is a real necessity.

Heterogeneous catalysis involves a spatial and time-dependent multiscale approach starting with design and characterization at molecular level and going through activation, spectroscopic characterization of the working surface, and system processing on an industrial scale involving catalyst shaping before activation in scientifically designed reactors (*Figure 3*). All those steps include the application of fundamental and applied concepts on three length scales: (i) *microscopic*, dealing with solid structure details, adsorption and reaction mechanisms, molecular modelling, and surface chemistry; (ii) *mesoscopic*, comprising kinetic and transport phenomena and their relation with catalyst physicochemical and catalytic properties; and (iii) *macroscopic*, including the most relevant aspects of reaction engineering, reactor design, mechanical strength and catalyst shaping (monoliths or extrudates). At a microscopic and mesoscopic level, catalytic activity is usually expressed in terms of intrinsic reaction rates, while the activity at macroscopic level is presented as productivity (activity per unit volume).

The time-scale of heterogeneous catalytic processes varies, in parallel with the different length scales discussed above. The activation and chemical bond breaking of a molecule occurs in a picosecond range, whereas the complete reaction cycle may last some microseconds for fast reactions and minutes for complicated reactions on surfaces. At the mesoscopic level, transport phenomena measure the facility of reactants and products to move across the catalyst packed bed. This diffusion through the catalyst particles and their pores may last seconds or minutes, and the residence time of molecules inside the reactor may last seconds or infinity if the reactants are transformed into undesirable products remaining on the catalyst's surface. Furthermore, the heat released in exothermic reactions may diffuse through the packed-bed reactor walls originating a thermal gradient, a process that, as in microreactors, can take several seconds or microseconds if the heat exchange is efficient. Finally, at the macroscopic level, the reactors are

designed for large-scale and long-term performance and the time-scale can last several years.

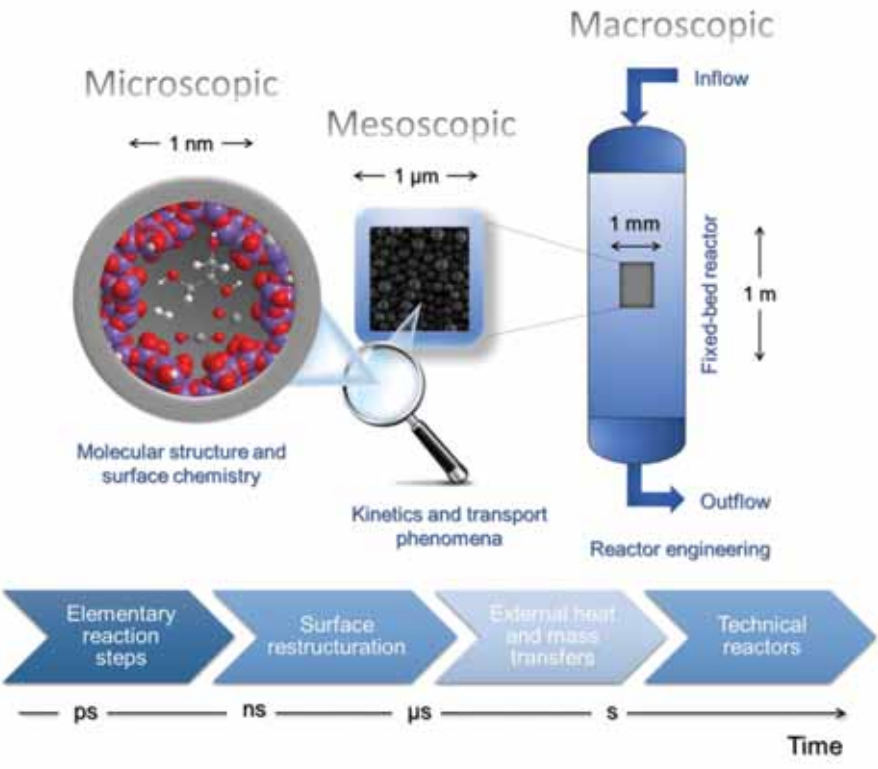

Figure 3. Schematic representation of the time-space multiscale approach.

Economic impact of the heterogeneous catalysis

Worldwide, approximately 85% of all chemical products are manufactured using catalysts and 15-20 % of the economic activities of industrialized countries depend directly on catalysis. The economic impact of the technology is reflected by the annual growth in demand for heterogeneous catalysts within such diverse sectors as the petrochemical and oil-processing industry, the chemical industry and environmental protection. *Table 1* illustrates the importance of heterogeneous catalysis, underlined by the enormous variety of industrial processes in which solid catalysts are involved.

Table 1. Some examples of industrially relevant catalytic processes using solid catalysts

Product	Process	Reaction	Catalyst	Area of application
Sulphuric acid	Contact	$2SO_2 + O_2 \rightarrow 2SO_3$	Pt or V_2O_5	Chemical manufacture, metal processing, fertilizers, explosives and drugs
Chlorine	Deacon	$4HCl + O_2 \rightarrow 2Cl_2 + H_2O$	$CuCl_2$ or RuO_2	Chemical manufacture, polymers (PVC, polyurethanes), pulp and paper industry and water sanitation.
Ammonia	Haber-Bosh	$N_2 + 3H_2 \rightarrow 2NH_3$	Fe	Chemicals, explosives, fertilizers, and gunpowder
Hydrogen	Steam reforming	$CH_4 + H_2O \rightarrow 3H_2 + CO$	Ni/Al_2O_3	Hydrogenation processes, ammonia synthesis
Nitric acid	Ostwald	$4NH_3 + 5O_2 \rightarrow 4NO + 6H_2O$	Pt-Rh	Chemicals, explosives, fertilizers, dyes, fragrances and metal purification
Methane	Sabatier	$CO_2 + H_2 \rightarrow CH_4 + H_2O$	Ni	Fuels and energy
Formaldehyde	Methanol oxidation	$CH_3OH + O_2 \rightarrow CH_2O + H_2O$	Fe-Mo mixed oxides	Chemical manufacture, resins production, coatings, textile industry, explosives
Methanol	Methanol synthesis	$CO + 2H_2 \rightarrow CH_3OH$	Cu-Zn	Bulk chemicals and fuels
Fuels	Fischer-Tropsch synthesis	$CO + H_2 \rightarrow (-CH_2-)_n + H_2O$	Fe, Co	Production of fuels, olefins, paraffin waxes, lubricants, etc.
Polyethylene	Ziegler-Natta	$CH_2{=}CH_2 \rightarrow (-CH_2-CH_2-)_n$	Ti compounds, $TiCl_3/AlR_3$	Polymers and bulk chemicals
Gasolines	Reforming of Naphtha	Dehydrogenation and isomerization of paraffins	Pt, Pt-Re, Pt-Ir	High-octane fuels
Syngas	Coal gasification	$C + H_2O \rightarrow H_2 + CO$	Ni, alkali metals	Synthetic fuels
Acrylonitrile	Sohio	$2CH_3{-}CH{=}CH_2 + NH_3 + O_2 \rightarrow 6H_2O + 2CH_2{=}CH{-}CN$	Bi-P-Mo oxides	Preparation of thermoplastics and synthetic rubbers, acrylamide and acrylic acid

They are widely used for nitric and sulphuric acids, ammonia and methanol production and in the petrochemical industry for obtaining platform chemicals and polymers. Catalysis also plays a fundamental role in environmental abatement processes, *e.g.*, for sulphur removal from crude oil and methane for low-sulphur fuels, removal of NO, CO and hydrocarbons from stationary and mobile exhaust emissions, etc.

Properties of the solid catalysts

In general, the properties of solid catalysts are either physical, chemical or strictly catalytic in nature. The physical properties include porosity, surface area, density, mechanical properties such as crush strength and attrition resistance, and morphological properties such as catalyst shaping and thermal stability. Chemical properties comprise chemical composition, redox behaviour, acidity and basicity, surface properties and structure. Catalytic properties are focused on all dynamic parameters that describe catalyst behaviour during a chemical reaction, *i.e.*, activity, selectivity and stability. An insightful correlation between all properties constitutes the basis of structure-activity relationship and establishes that of rational solid catalyst design.

In 1989, Richardson introduced the concept of the catalyst design triangle, illustrated in *Figure 4*, suggesting that the ideal design is an optimized combination of interdependent physical/mechanical, chemical/structural and catalytic/dynamic properties.

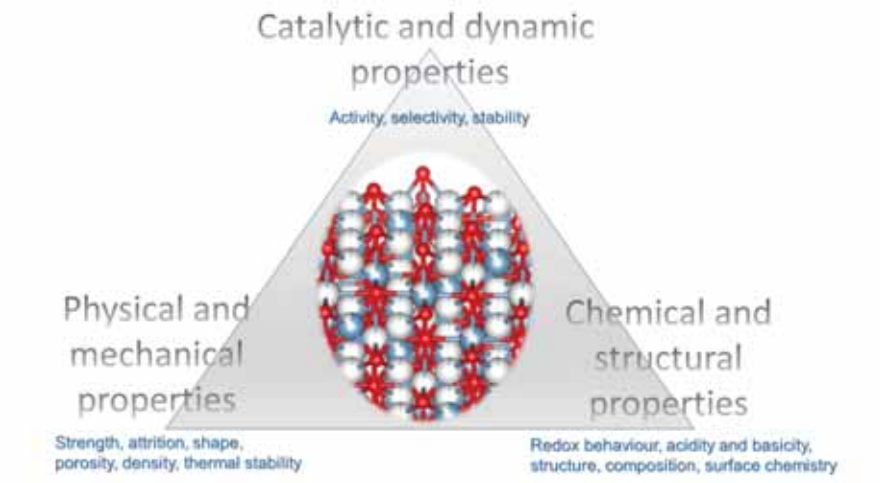

Figure 4. Catalyst triangle design concept proposed by Richardson.

The optimization of those properties requires a careful choice of solid catalyst components. Two types of solid catalysts can be distinguished, taking as a base the type of catalytic reaction:

- *Supported catalysts:* catalytically active sites are dispersed on a support with high specific surface areas. The materials used as supports are usually oxides such as γ-alumina, silica, magnesia, titania, ceria and zirconia, or mixed oxides such as $MgAl_2O_4$ and $CeZrO_4$. All supports provide a porous network where the active phase, usually metallic, is spread. This type of catalyst optimizes the reactive surface and provides better use of expensive catalytic materials such as Rh, Pt, Pd, Ru and Ir metals.

- *Unsupported or bulk catalysts:* as the name suggests, these catalysts are composed entirely of catalytically active material although only their surfaces will be accessible for the reactants. For example, γ-Al_2O_3 is a bulk catalyst with surface acidic properties, typically used in dehydration reactions. Multicomponent oxides are also representative examples of this group, *e.g.*, Cu-Zn mixed oxides for methanol synthesis; Al_2O_3-SiO_2 for hydrocarbon cracking; Mo-V-Te-Se mixed oxides for ammoxidation of propane. Another special group of more sophisticated bulk catalysts with well-defined porous networks is the *molecular sieves* variety with zeolites as the main example. Zeolites are crystalline aluminosilicates with three-dimensional cavity structures and interconnected channels where only molecules of a suitable size and shape can enter and pass through. These materials find important applications, in general, as solid acid catalysts in the petrochemical industry and particularly for fluid catalytic cracking (FCC) of crude oil.

There is an almost unlimited variety of supported and bulk solids that can potentially catalyse; however, the main objective of catalyst science is to design the best formulation for a given process with optimized properties.

Physical and mechanical properties

Catalysts can be manufactured in diverse shapes. Mass and heat transport phenomena depend on particle shape and typically extrudates (pellets) are used to avoid pressure-drop problems and to reduce the thermal gradients. Physical and mechanical properties are particularly important to achieve a successful solid catalyst. Considering extrudate catalysts, high mechanical strength against crushing and high attrition resistance become essential.

These properties are fundamental to avoid reactor plugging by pulverization and to maximize the energy efficiency of the process. The catalyst must have also sufficient thermal stability to prevent structural changes, sintering or volatilization under reaction conditions.

Catalysts are commonly porous solids and their density, surface area and porosity are of extreme importance. Commercial extrudates are prepared by compacting ultrafine catalyst particles and during this process *macropores* with diameters around 100 nm are formed due to the voids left between all agglomerated particles. This empty space is commonly called *bed porosity* (ε_b) and presents typical values of 30 – 40 %. On the other hand, the individual particles possess intraparticle porous structure consisting of *micropores* with characteristic dimensions less than 2 nm and/or *mesopores* in the 2 – 50 nm size range. The total volume of intraparticle voids is called *particle porosity* (ε_p). The interparticle voids must be sufficiently large to allow fast diffusion of the reactants to the particles, while the pore size of each individual particle must be as large as the dimensions of the molecules themselves, in order to enable their diffusion through the pores to the active sites located inside the pores. Both pore structure and pore-size distribution depend strongly on catalyst preparation method, and pores can have all varieties of geometrical shapes. Catalyst density is related to its porosity and three types of density can be defined: (i) *true density*, representing the mass of catalyst per unit volume; (ii) *apparent density*, related to the mass of catalyst per unit volume of porous particle; and (iii) *packed density*, referring to the mass of catalytic bed per unit volume of packed bed. The relation between *particle porosity* (ε_p) and *true density* (ρ_{true}) is given by the following equation:

$$\varepsilon_p = \frac{V_{pore}}{V_{pore}+V_{solid}} = \frac{V_{pore}}{V_{pore}+(\rho_{true})^{-1}} = \frac{V_{pore}+(\rho_{true})}{1+(\rho_{true})}$$

where V_{solid} and V_{pore} correspond to the volume of solids, and the total pore volume, respectively. A similar equation can be deduced for the estimation of *bed porosity* (ε_b) from measurable parameters, including the total mass of bed catalyst, total bed volume, packed density and true density.

$$\varepsilon_{bed} = \frac{V_{bed} - V_{solid}}{V_{bed}} = \frac{V_{bed} - (\rho_{true})^{-1}}{V_{bed}} = 1 - \frac{(\rho_{true})^{-1}}{(\rho_{bed})^{-1}} = 1 - \frac{\rho_{bed}}{\rho_{true}}$$

The specific surface area is another parameter that depends directly on porosity, and practically all internal surface area resides within the micro- and/or mesopores. The specific surface area of a solid catalyst can be

determined by adsorbing nitrogen at its boiling temperature (77 K). The adsorption curves are called *adsorption isotherms*, and their analysis with suitable mathematical models determines the total solid surface area.

Problem II. *How do adsorption isotherms relate to the porosity of solids?*

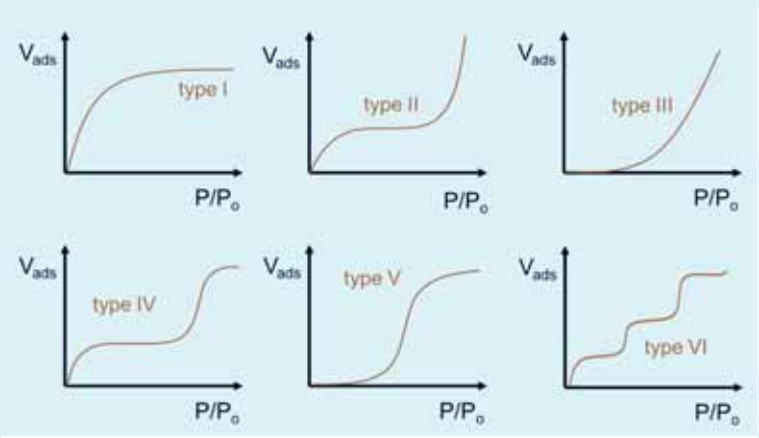

Isotherm shape provides useful information and it is related to the porosity of the solids. According to IUPAC, we can distinguish six types of isotherms, in what is known as *Brunauer classification*

Isotherm *type I* is characteristic for microporous solids such as activated carbons or zeolites: nitrogen is adsorbed as a monolayer until saturation is reached, and pore filling occurs without capillary condensation. When the micropores are filled, adsorption follows on the external surface. The *Type II* isotherm describes the adsorption on macroporous and non-porous solids; adsorption first takes place in a monolayer and subsequently grows in multilayers.

On the contrary, for *type III* and *V* isotherms no monolayer formation is observed and the entering molecules are preferentially adsorbed on another already adsorbed molecule rather than on an empty surface. These types of isotherms are rarely found in solid catalysts and the most typical example is represented by the adsorption of water on hydrophobic surfaces.

The *type VI* isotherm is obtained for uniform ultramicroporous solids, for which the surface contains only a few groups of energetically uniform adsorption sites. This type of "stepped" isotherm was measured for well-crystallized zeolite X and silicalite. Finally, the *type IV* isotherm group corresponds to mesoporous solids and it is typical for most oxides used as supports in heterogeneous catalysis. This isotherm firstly shows monolayer formation, followed by mesopore filling and capillary condensation giving a sharp adsorption volume. After saturation of adsorption sites, desorption occurs in a different way from adsorption and "hysteresis" appears as a result of capillary condensation within the mesopores. The specific surface area, pore size, distribution and pore volume can be estimated from the adsorption curves, while the type of hysteresis provides information about the pore shape.

The *BET model*, the most commonly employed model for specific surface determination, was developed by Brunauer, Emmett and Teller in the 1930s. Typical oxides such as alumina or silica present BET surface areas of 200 – 300 $m^2\ g^{-1}$ while other materials like porous carbon can achieve areas superior to 1000 $m^2\ g^{-1}$.

Brunauer, Emmert & Teller (1938)

The BET model is only applicable to the *type II* and the *type IV* isotherms. This model assumes a multilayer adsorption where the adsorption energy for the first layer (monolayer) is uniform, while the binding of the second and subsequent layers is of the same nature as the forces responsible for gas

condensation. Consequently, when saturation pressure is reached, the number of multilayers becomes infinite and the adsorbent condenses to bulk liquid on the solid surface. Under dynamic equilibrium, the rate of condensation (adsorption) is equal to the rate of evaporation (desorption). BET equation establishes the relationship between monolayer volume capacity and overall amount of adsorbed gas, often rewritten in its linearized form

$$\frac{P}{V(P_0 - P)} = \frac{1}{cV_m} + \frac{(c-1)}{cV_m}\frac{P}{P_0}$$

where P is the pressure, P_0 is the saturation pressure, V is the total volume of adsorbed gas, V_m is the volume of adsorbed gas in the monolayer, and c is a constant related with the heat of adsorption of the first layer and the vaporization heat for a chosen adsorbent. The plot of $P/[V(P_0-P)]$ against P/P_0 gives a straight line with intercept $1/cV_m$ and a slope $(c-1)/cV_m$. Thus, the values of c and V_m are derived, and the BET surface is estimated from:

$$S_{BET} = n_m \cdot \sigma \cdot N_A$$

where n_m is the monolayer capacity expressed in moles of adsorbate per gram of solid, σ is the average area occupied by the adsorbate in a full monolayer (16.2×10^{-20} m^2 for N_2), and N_A is the Avogadro number.

The BET model fits reasonably only with experimental observation in a limited range of partial pressures (P/P_0 = 0.05 – 0.3) leading to the conclusion that the BET equation cannot be applied for the description of solid materials containing micropores or small mesopores where the conditions of multilayer adsorption would not be satisfied.

As a surface phenomenon, heterogeneous catalysis usually requires larger specific surface areas, in order to maximize particle exposure to reactants. In this sense, *dispersion* is a very important parameter defined as the fraction of surface available atoms with respect to the total number of atoms for the specified solid. The dispersion is an average property that varies from 0 to 1 although typically expressed as a percentage. The estimation of the dispersion is particularly useful for supported catalysts, for which optimal dispersion is achieved when a maximum number of available active sites are homogeneously distributed on the surface. Dispersion is usually determined by selective chemisorption of a gas that is adsorbed, preferentially on the supported metal particles but not on the support. For instance, metallic dispersion, measured by H_2 chemisorption in commercial

Pt/Al_2O_3 catalyst with metal loading of 0.5 wt.%, can achieve values of platinum dispersion of around 90% practically corresponding to single atom distributions on a carrier surface. For unsupported catalysts, specific adsorption sites can be deduced by finding an appropriate region of pressure and temperature to adsorb a model reactant, commonly participating in the reaction. Examples can be found with N_2O and NO adsorption on Mn_2O_3 and Mn_3O_4, catalysts used normally for nitrogen-oxide decomposition.

Chemical and structural properties

Catalytic behaviour can also be correlated with the geometric and electronic properties of the surface. Therefore, precise knowledge of chemical structure and composition and bonding of the reactants on the surface is of primary significance.

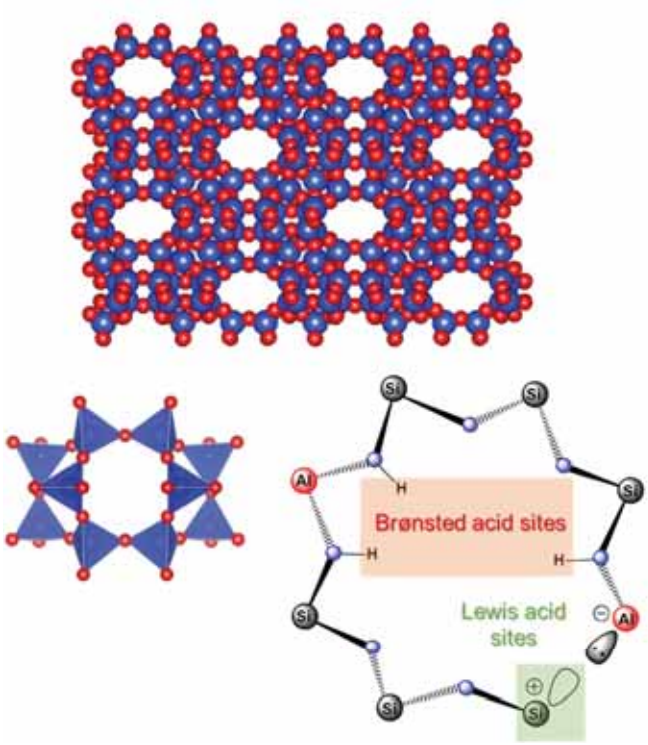

Figure 5. ZSM-5 structure and illustrative representation of acid sites types.

Surface acidity plays a key role in many catalytic processes involving hydrocarbon transformations such as cracking, oligomerization and isomerization. Understanding the nature of the acid sites is essential for designing catalysts with optimal properties. The acidic properties are mostly discussed in terms of Brønsted and Lewis definitions. Brønsted-type acid is any hydrogen containing species capable of releasing a proton, while Lewis-type acid is any species with unoccupied orbitals that can accept an electron pair to form dative or coordination bonds. An example of acid catalysts is the group of zeolites, containing cations compensating the negative charge created when Al^{3+} replace Si^{4+} atoms in the tetrahedral units of a silicate framework. When the cations are replaced by protons, zeolites acquire unique acidic properties, exemplified by the schematic representation of the characteristic Brønsted and Lewis acid sites for ZSM-5 zeolite in *Figure 5*. The acidity strength of zeolites depends on the local environment of the protons, and the number of acid sites can be improved by increasing the Si/Al molar ratio up to 1 in accordance with Lowenstein's rule, in the presence of two neighbouring AlO_4 tetrahedral units virtually forbidden.

Basicity is also another important facet of catalyst design, since many reactions are catalysed by basic solids. A Brønsted-type base is any substance capable of combining with protons while a Lewis-type base is any species that possess a free electron pair that can be donated to form an adduct compound. The alkali-earth metals oxides are the strongest bases and exhibit excellent catalytic performance in numerous fine-chemical synthesis processes. The rapid development of solid-state and materials chemistry has led to more advanced basic catalysts: for example, hydrotalcites, also called layered double hydroxides (LDHs)—solids that present abundant quantities of hydroxyls, and Brønsted-type basic sites, located in brucite-like layers (*Figure 6A*). The hydrotalcites are anionic clays with the general formula $[M_{(1-x)}^{2+}M_x^{3+}(OH_2)]^{x+}(A_{x/n}^{n-})\cdot yH_2O$, in which a part of the bivalent cations are isomorphically replaced by trivalent cations resulting in the formation of layers with positive charge. This positive charge is compensated by anions such as NO_3^-, CO_3^{2-} and Cl^- located in the interlayer space. One of the most popular hydrotalcites has the chemical formula $Mg_6Al_2(OH)_{16}CO_3\cdot 4H_2O$, and its thermal decomposition results in highly homogeneous mixed oxides with composition $MgAl_2O_4$ and direct spinel structure (*Figure 6B*).

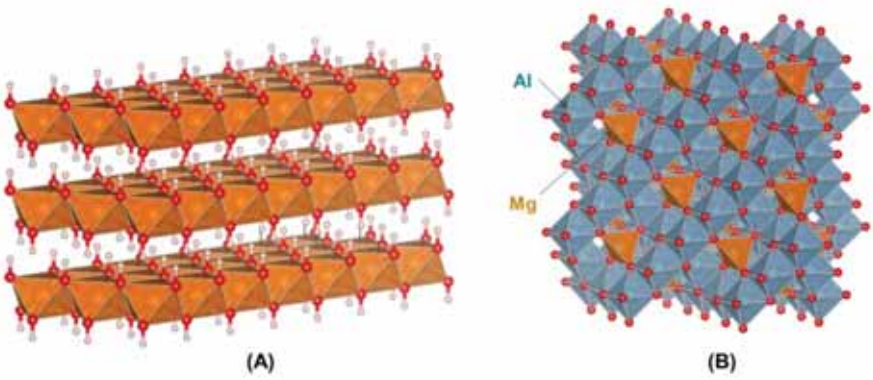

Figure 6. Crystal structure of brucite ($Mg(OH)_2$) **(A)**, and direct spinel structure ($MgAl_2O_4$) **(B)**.

The redox properties and electronic and ionic conductivity of solids also exercise an important effect on catalytic performance. The reducibility of solid catalysts is directly associated with electron and/or lattice oxygen mobility within surface and bulk layers. Redox properties are involved in reaction mechanism control and notably influence catalyst activity/selectivity. Perovskite-type oxides are largely used in catalytic processes due to their intrinsic redox properties. The perovskites are double oxides with chemical formula ABO_3, where A occupies the centre of a cube coordinated with 12 oxygen anions, and B locates at cube vertices in octahedral oxygen environment (*Figure 7A*). The A-site cations are usually rare- or alkaline-earth metals, whereas the B-site cations are transition metals responsible for catalytic activity. The wide variety of chemical compositions of these compounds is derived from the fact that around 90% of the metallic elements present in the periodic table are able to form a stable perovskite-type structure. Moreover, partial substitution of both A- and B-type sites by other cations with different valences leads to the formation of oxygen vacancies and redistribution of the redox sites of the solid. Therefore, perovskite-based catalysts present an excellent catalytic performance due to their intrinsic oxygen mobility within the lattice, oxygen adsorption capacity and controlled reducibility. Perovskite-type mixed oxides are active in many reactions, such as catalytic combustion of CO and hydrocarbons, selective reduction of NO_x, and oxidative coupling of methane. Other relevant applications include electrodes for fuel cells, gas sensors, and membrane reactors. Other types of multicomponent oxides are the Scheelite-type compounds with the general formula ABO_4, the redox

properties of which, associated with cation vacancies, are of special interest in catalysis. The scheelite structure crystalizes in tetragonal unit cells with *I41/a* space groups and consists of four formula units of AO_8 bisdisphenoid polyhedral, and four BO_4 tetrahedral units where A is the larger cation (*Figure 7B*). Scheelite-type structures, with $CaWO_4$ as a representative example, tolerate the incorporation of trivalent into divalent cation sites, creating cation vacancies to maintain electroneutrality. The resulting empirical formula can be written as $A_2\square(BO_4)_3$, where the symbol □ represents a cation vacancy, the defect structures of which, even with more than 30% of vacancies in the A sites, are stable. The scheelite-type structure has served as a framework for many multicomponent oxides widely employed as catalysts in industrially important processes such as selective oxidation and ammoxidation of alkenes. The production of acrylonitrile from propylene, air and ammonia in a fluidized-bed reactor (SOHIO process) uses $BiMoO_4$ scheelite-type oxide as catalyst. The presence of cationic vacancies governs the catalytic properties of such a material.

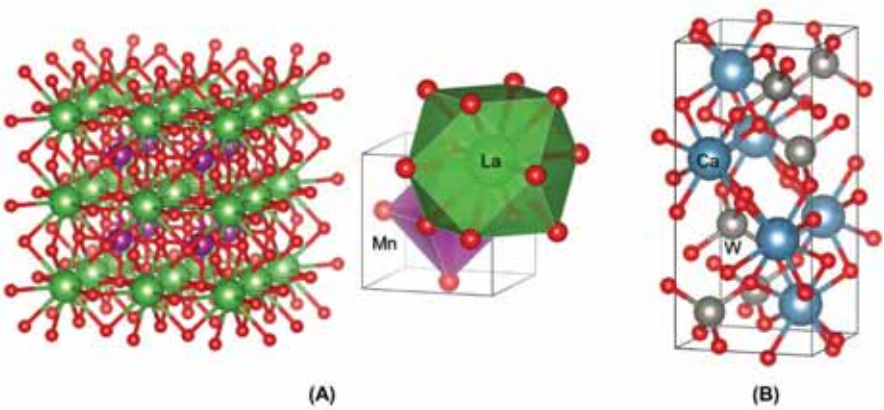

Figure 7. Examples of solids with redox properties: **(A)** Perovskite-type structure ($LaMnO_3$) and **(B)** Scheelite-type structure ($CaWO_4$)

Depending on the reaction, solid catalysts can contain acid – base sites, redox sites or a combination of both when multifunctional properties are required. Many metal-supported catalysts present bifunctional properties and are used in catalytic reactions that require this duality. The reforming reactions of naphtha transformation into high-octane gasoline is the typical example. Pt or Pd supported on γ-Al_2O_3 are used as catalysts, while the acid sites of alumina isomerize the naphtha and Pt or Pd metallic sites dehydrogenate and hydrogenate to produce gasoline. Another interesting

example is found in metal-zeolite materials, in which a multiple combination of redox metal zeolite acidity and the shape selectivity of the micropores provides a multifunctional catalyst in numerous chemical processes.

Catalytic properties

The catalytic behaviour of a solid is determined by its *activity*, *selectivity*, and *stability*. The catalytic *activity* is a measure of how many reactant molecules are transformed per unit time and per amount of catalyst. In general, the activity can be expressed either in terms of conversion (moles of transformed reactants per moles of feed reactants) or using the concept of *turnover frequency* (TOF), defined by the number of transformed reactant molecules per unit time and per active site and reported in reciprocal time units. Sometimes, it is difficult to determine the number of active sites, and the activity is normalized by the area of exposed catalyst. In situations where the reaction rates are non-uniform within the catalytic bed, it is more appropriate to express the catalytic activity as *space-time yield* (STY), defined as the amount of product obtained in the reactor per unit time and unit reactor volume.

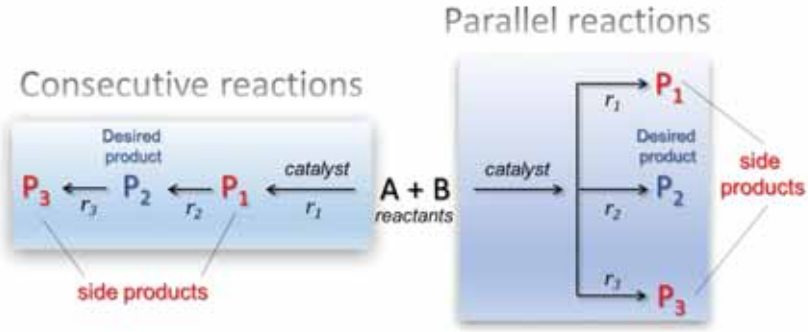

Figure 8. Types of reactions affecting catalyst selectivity.

Another even more important parameter than activity is catalyst *selectivity*, which describes the relative rates of two or more competing reactions and measures the ability of the catalyst to accelerate one reaction with respect to all other possible reactions. As illustrated in *Figure 8*, competitive reactions occur when two reactants are transformed into several products through parallel or consecutive pathways. Therefore, selectivity is defined as the ratio between the rate of desired product formation and the rate of

reactant consumption, *i.e.*, the moles of desired product with respect to the moles of converted reactants.

The stability of catalysts is as important as activity and selectivity. The *stability* of a catalyst is often measured by the loss in activity and/or selectivity as a function of time. A catalyst's lifetime can be expressed in terms of desired chemicals produced per charge of spent catalyst within a period of time from a few seconds to years. An optimal catalyst design must present both high activity and long-term stability, but probably the most important criterion is its selectivity. A selective catalyst might be able to accelerate the formation of the desired products in the process, reducing the costs of separation, purification and waste treatment, as well as the amount of necessary reagents. On the contrary, high conversions and long-term stability are not strictly necessary, since the unconverted reactants can be recirculated and solid catalysts can be regenerated.

Promoters and modifiers

The physicochemical properties of catalysts are influenced by the presence of *promoters* or *modifiers*. These substances are not intrinsically active, but induce a tremendous effect on catalytic properties when introduced into the catalyst formulation in small amounts. We can classify the promoters under four categories:

- *Chemical promoters*: species that modify catalyst selectivity by decreasing the number of possible secondary reactions and favouring only one reaction path. One excellent example is the use of promoters in steam reforming reactions to suppress coke formation. Coke is formed from CH_x species produced in cracking reactions and their subsequent acid-catalysed polymerization to carbonaceous deposits that cover the active sites. The addition of alkali and alkaline earth metals neutralizes the acid sites and decreases the formation of coke. In addition, they promote steam carbon gasification, thus considerably increasing the lifetime of the catalysts.

- *Electronic promoters:* usually highly dispersed, these species directly affect the electronic properties of the active phase. As a consequence, these promoters are involved in the chemical bonding between active sites and adsorbates. Potassium is typically used as a promoter for Fe-based catalysts for ammonia synthesis, due to its facility to donate electrons to the active metal and to facilitate, in this case, the dissociation of N_2 through π back-donation.

- *Textural promoters:* these additives prevent the sintering of the active surface and help the stabilization of the specific surface. These promoters also increase the thermal stability and mechanical resistance of the catalyst. For example, the addition of 1 wt.% of SiO_2 or ZrO_2 to γ-Al_2O_3 with a high surface area (250 m^2 g^{-1}) notably enhances its mechanical properties and prevents the loss of surface area associated with γ-to-α alumina phase transition.

- *Selective poisoning promoters:* these promoters are used to selectively block specific sites of the active phase and to avoid certain side reactions. For example, partial poisoning of nickel sites with certain sulphur or boron coverages tends to inhibit the formation of whisker carbon due to blocking of carbon nucleation sites. As a result, boron- or sulphur-promoted Ni catalysts decrease carbon formation during hydrocarbon steam reforming reactions and increase catalyst stability. Nevertheless, it is also known that activity in steam reforming notably decreases above a certain threshold concentration of dopant. Therefore, loading of selective poisoning promoters must be optimized to avoid coke formation while guaranteeing a sufficient rate of reaction.

Promoters have attracted huge interest in catalyst science due to their remarkable influence on the activity, selectivity, and stability of catalysts. In practice, a solid catalyst may contain more than one promoter where the overlapping effects complicate the precise understanding of the promoter function. In fact, the great majority of promoters have been discovered by chance and only few of them were a result of systematic research. In more recent years, the development of *in situ/operando* techniques and the advances in computational methods have introduced new insights into the role of promoters.

Requirements for a successful solid catalyst

Catalysts are usually designed specifically for a particular process and their development is intimately related with reaction engineering. It is essential to integrate the catalyst design within the overall reaction process, and some key properties are required to achieve a successful catalyst for a specific process under certain reaction conditions:

- The catalyst must present an optimal specific activity and high selectivity in rendering the desired products and minimizing the production of waste.
- The catalyst must have a sufficiently long lifetime, or else it must be easy to regenerate if deactivation is necessary after short periods.
- Porosity and catalyst shape must be adequate, to ensure a fast diffusion of reactants through the catalyst bed and to allow accessibility within the pores.
- Solid catalysts should have high mechanical strength and good thermal stability.
- Toxicity and safety in handling ought also to be considered. "Green catalysts" must be designed.
- The cost of catalysts must be low and, if any precious metals are involved, their loading should be minimized.

The originality of the catalyst design is another factor that, although not strictly necessary, could increase the competitiveness of the industrial process.

How does the heterogeneous solid catalyst work?

The mode of action of a solid catalyst can be described by a sequence of individual elementary steps (*Figure 9*) that are fundamental for the progress of the overall catalytic cycle:

i. External diffusion of the reactants through the catalytic bed and boundary layer surrounding catalyst particles.
ii. Internal diffusion of the reactants into pores in the solid to access the active sites.
iii. Adsorption of the reactants onto the active sites.
iv. Surface chemical reaction of the adsorbed reactants involving formation of intermediates and conversion into the products.
v. Desorption of the formed products from catalyst surface.
vi. Internal diffusion of the products through the pores.
vii. External diffusion of the products away from the catalyst surface through the boundary layer.

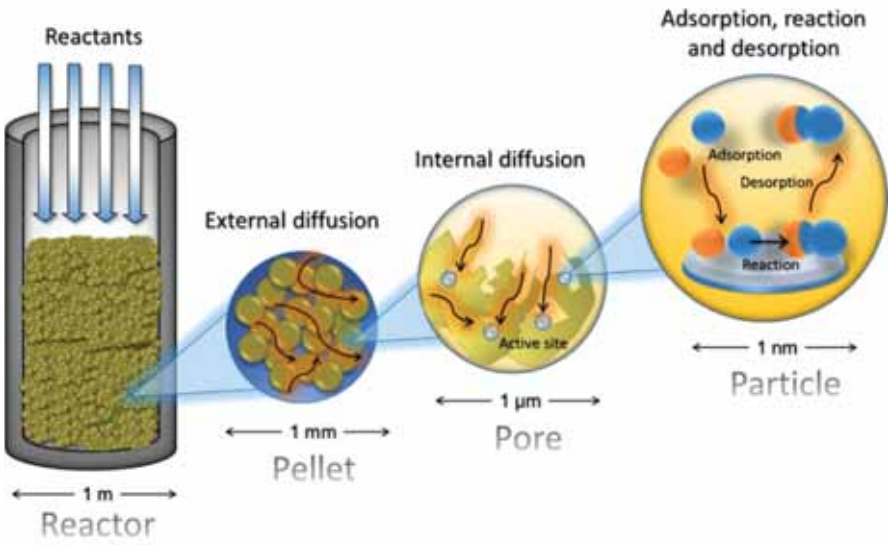

Figure 9. Individual steps of heterogeneous catalytic reaction at different length scales

The overall process is controlled by the slowest step, the rate-determining step. Three regimes of catalytic rate control can exist: external diffusion control (steps *i* and *vii*), pore diffusion (steps *ii* and *vi*), and kinetics control (steps *iii*, *iv* and *v*). *Microkinetic* models are used to describe the kinetic phenomena (adsorption, chemical reaction and desorption) at a molecular level, while the term *macrokinetic* is considered when the transport phenomena play an important role. Additionally, heat transfer effects can also participate for highly endothermic or exothermic reactions; the temperature of the process influences the diffusion phenomena to a considerable extent. At low temperatures, the diffusion through a catalytic bed, a boundary layer and the pores is much faster than the surface reaction rate, *i.e.*, the overall process will be kinetically controlled. In contrast, at higher temperatures the reaction rates increase more rapidly than the diffusion rates, and the overall process is controlled by pore diffusion and, at even higher temperatures, by external diffusion. Diffusion-limited regimes can be altered by modifying the reactor design (type/geometry), catalyst morphology and porous structure or the specific flow conditions. Any microkinetic study performed to deduce the relevant reaction mechanisms requires a system that is not controlled by diffusion limitations,

i.e., the reaction rates measurements must be completed under kinetic regime conditions.

Diffusion and transport phenomena

In heterogeneous catalysis, diffusion is an imperative step to overcome a chemical reaction. The reactant molecules diffuse, first toward the external surface of catalyst particles, and they then enter the pores to attain the active sites. Once the reactants are transformed, the product molecules follow the reverse path. In case of catalytic reactions in gas-solid systems, external diffusion is governed by the classical laws of gaseous diffusion, in which a gas flow passing through catalyst particles generates a static layer of gas molecules resulting from the gradual transition between this layer and the flowing gas phase. The thickness of this boundary layer is inversely proportional to the linear flow rate, and the rate of diffusion through this layer is given by the equation:

$$r_{external} = k_m(C_g - C_s)$$

where C_g is the gas concentration in the gas stream, C_s is the concentration of the gas in the boundary layer, and k_m is the mass transfer coefficient.

The k_m value can be estimated from the physical properties of the gas mixture and from the aerodynamic flow conditions and depends on the dimensionless Schmidt (*Sc*), Reynolds (*Re*), and Sherwood (*Sh*) numbers. The rate of diffusion through the boundary layer must be sufficiently high to ensure concentrations of the reactants and products at the catalyst surface, the same as for the gas passing through the catalytic bed. This occurs when the gas flow rate is high, and under these conditions the external diffusion will have no effect on the measured reaction rate. On the contrary, if the gas flow rate is too low, the boundary layer thickness would be significant and the diffusion rate through the layer will contribute notably to the observed reaction rate.

In the case of internal or pore diffusion, the collisions of the molecules with the walls of the pores become as important as the intermolecular collisions. Diffusion inside the pores occurs according to the so-called Knudsen diffusion and depends basically on pore dimensions. In 1939, Ernest Thiele developed a mathematical model estimating the pore diffusion effect on a chemical reaction defining the Thiele modulus (∅), a dimensionless quantity given by:

$$\emptyset = l \cdot \lambda = l \cdot \sqrt{\frac{4k_r^{''}}{d_p \cdot D_{eff}}}$$

where λ is the mean free path, l is the pore length, $k_r^{''}$ is the diffusion rate coefficient, d_p is the pore diameter, and D_{eff} is the effective diffusivity. This expression of the Thiele modulus is only appropriate for first-order reactions occurring on solid catalysts with straight cylindrical or irregular pores. More generally, the Thiele modulus equation for a reaction of order – *n* is given by:

$$\emptyset = \frac{V_P}{A_E} \cdot \sqrt{\frac{n+1}{2} \cdot \frac{4k_r^{''}}{d_p \cdot D_{eff}}}$$

where V_P is the geometric volume of the catalyst particle, A_E is the external surface area of the catalyst, and *n* is the reaction order. This equation is valid for reactions with $n > 0$ and for non-idealized pore shapes.

The effectiveness factor (η) is another dimensionless number that expresses any deviation from the ideal behaviour, *i.e.*, this parameter describes the effect of internal diffusion on the reaction rate. For a first-order reaction and catalyst particles with slab geometry, this factor is expressed as a function of the Thiele modulus:

$$\eta = \frac{observed\ reaction\ rate}{reaction\ rate\ in\ the\ absence\ of\ internal\ gradients} = \frac{\tanh \phi}{\phi}$$

The values of the effectiveness factor and the Thiele modulus may be used to predict the rate of the catalytic reaction and its relation to the rate of diffusion of the reactants inside the pores (internal mass transfer). The effectiveness factor tends to unity at low Thiele modulus values, and indicates that all available catalytic sites are contributing to the measured reaction rate with rapid diffusion of the reactants through the pores under such conditions (*Figure 10*). On the contrary, low values of the effectiveness factor and high Thiele modulus values correspond to situations where internal mass transfer determines the effective rate of reaction, reactants are unable to penetrate into the pores and the reaction rate is low over much of the catalyst particles. Rigorous evaluation of the effectiveness factor requires a definition of reactant concentration profiles within the catalyst particles, schematically illustrated in *Figure 10B.*

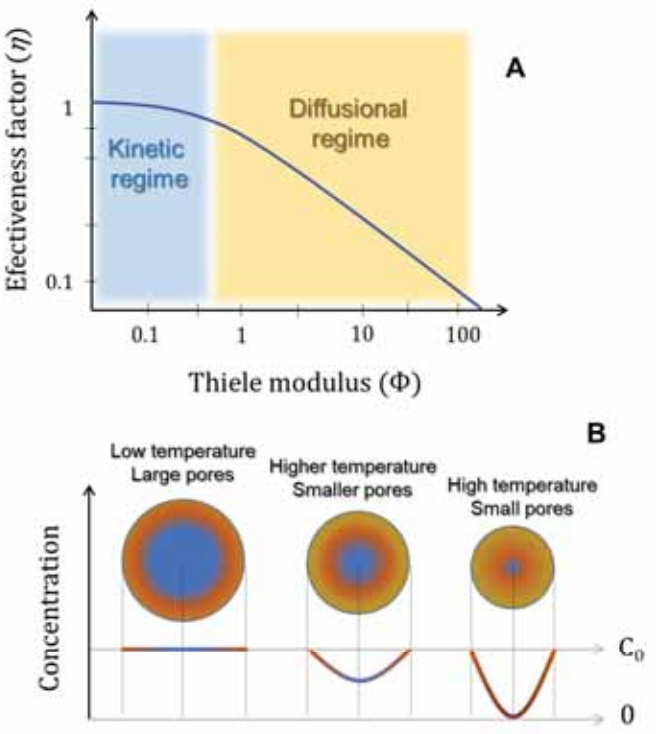

Figure 10. A Effectiveness factor *vs.* Thiele modulus, and **B** Reactant concentration profiles through the catalyst particles as a function of pore size and reaction temperature

Concentration profiles depend on catalyst particle pore dimensions and on the reaction temperature. Diffusion through large pores takes place in the same manner as outside the pores, and concentration gradients are absent. Thus, for low temperature (low $\emptyset$) and large pores, the concentration profile will remain constant through the particles, and the effectiveness factor will be close to 1. When the pore dimension is close to the reactant size, Knudsen diffusion becomes more important and the effective diffusivity is proportional to the square root of the temperature ($T^{1/2}$). As the Thiele modulus ($\emptyset$) is inversely proportional to effective diffusivity, significant concentration gradients will appear at higher temperatures, and the concentration in the particle centre can drop to zero (very high $\emptyset$ and η close to zero) at very high temperatures. Therefore, the mass transfer limitation can be minimized by using particle geometries and wide pores that improve

the accessibility of reactants to the active surfaces, and at low reaction temperatures. A treatment of this subject in greater depth is beyond the scope of this book, but interested readers can find an especially readable discussion of the topic in O. Levenspiel's book "Chemical Reaction Engineering", Wiley, 2nd Edition, 1972.

Adsorption and desorption processes

The adsorption of reactants on the active sites of the catalyst surface is another key step in heterogeneous reaction. In general, two types of interactions determine the adsorption: *physisorption* and *chemisorption*. *Physisorption* is a multilayer phenomenon in which molecules are adsorbed on the surface of the solid via cohesive van der Waals' interactions and the heat of adsorption is similar in magnitude to the vaporization enthalpy (ΔH_{vap}) of adsorbed gas. The *chemisorption* process involves the formation of chemical bonds between adsorbed molecules and active site surfaces, and the heat of adsorption (Q_{ads}) is comparable in magnitude to the heat of chemical reaction. Both *physisorption* and *chemisorption* phenomena can be described using the Lennard-Jones potential energy diagram, *Figure 11*, which represents the potential energy of molecules (H_2 as example) as a function of the distance between the adsorbate and the solid surface.

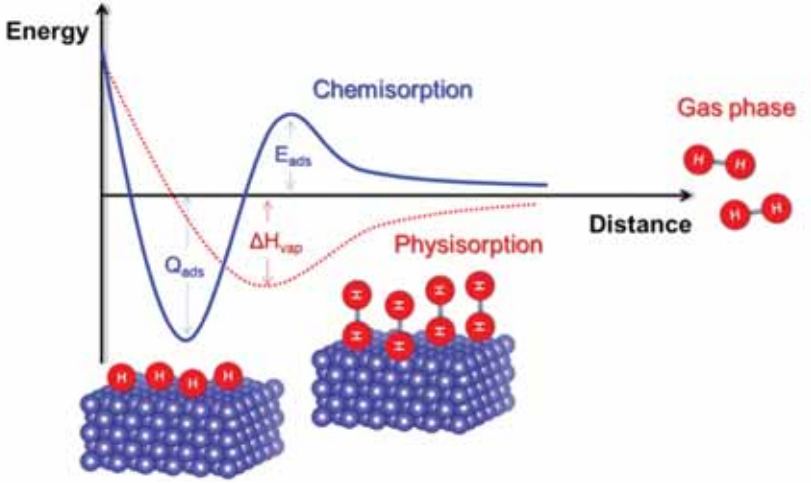

Figure 11. Lennard-Jones potential energy diagram for adsorption of hydrogen on metal sites

At infinite distance, hydrogen molecules are not attracted by the metal surface, but as H_2 approaches the surface the molecules undergo physical adsorption and lose energy when trapped by the surface. At shorter distances, the molecules interact tightly with the surface as their degree of freedom decreases notably. This situation causes strong repulsion between the electron clouds of molecules and the solid surface, and the molecule can become dissociated, producing hydrogen atoms chemisorbed on the metal surface. The dissociation only occurs when the activation energy (E_{ads}) necessary for chemical bonds to break is lower than the chemisorption heat. As a consequence, this dissociative chemisorption is a highly specific phenomenon and, in the case of hydrogen, frequently occurs on platinum or nickel but rarely on gold. On the contrary, the physisorption process is not specific and depends on a solid surface area; molecules of different natures can physisorb on any surface, forming multilayers.

The physisorption process is a necessary requisite but it is not sufficient to ensure the reaction of molecules on the surface. The basis of heterogeneous catalysis is *chemisorption*, which involves the breaking and building of specific chemical bonds, processes that occur preferentially on the active sites of the catalyst's solid surface. Therefore, a chemical reaction may occur only when the gas molecule incident on the catalyst surface is adsorbed and migrates to the nearest active sites forming a chemisorbed state. The probability of adsorption and migration decreases as the average number of adsorbed molecules per unit surface area increases. The *sticking probability* (S) is a parameter which describes the probability of adsorption as a function of the surface coverage, and can be defined as the ratio between the adsorption rate and the number of molecules colliding with the surface, according to the equation:

$$S(\theta) = \frac{d\theta/dt}{F}$$

where θ represents the surface coverage, ranging between 0 (bare surface) and 1 (all adsorption sites are covered), and F is the collision frequency, a statistic parameter that can be calculated from the Langmuir-Hertz equation:

$$F = \frac{P}{N_0\sqrt{2\pi m k_B T}}$$

where P is the gas pressure, N_0 is the number of collision sites per unit of surface, m is the mass of the adsorbing molecule, k_b is the Boltzmann constant, and T the temperature.

As not all collisions result in chemisorption, the *sticking probability* represents the fraction of collisions that produce chemisorption. Considering that only the molecules exceeding a required activation energy for chemisorption will be able to form "activated intermediates", the *sticking probability* can be written as:

$$S(\theta) = \sigma(\theta)\, f(\theta)\, e^{-E_{ads}/RT}$$

where σ is the steric factor, varying with the surface coverage (θ), which represents the probability of a molecule with sufficient energy (E_{ads}) to collide with an empty active site and adsorb. The term $e^{-E_{ads}/RT}$ indicates the fraction of molecules with sufficient energy for adsorption at temperature *T*, with R the universal gas constant. And finally, the function $f(\theta)$ represents the probability of the collision occurring with an unoccupied active site. Collisions with occupied active sites can obviously decrease the chemisorption activity, but the molecules can be adsorbed in a second layer and migrate over the occupied sites till an empty site appears. On clean surfaces with $\theta = 0$, the initial *sticking probability* (S_0) should be theoretically equal to unity, but surface heterogeneities can affect the observable *sticking probability* and certain divergences may therefore be expected.

With this background, we can formulate the rate equation that describes simple activated adsorption processes with the expression for the adsorption rate:

$$r_{ads} = \frac{d\theta}{dt} = F\, S(\theta) = F\, \sigma(\theta)\, f(\theta)\, e^{-E_{ads}/RT} = \frac{P}{N_0\sqrt{2\pi m k_B T}}\, \sigma(\theta)\, f(\theta)\, e^{-E_{ads}/RT}$$

The opposite of adsorption is the desorption process, and similarly, its rate from occupied active sites can be expressed as:

$$r_{des} = -\frac{d\theta}{dt} = k_{des}\, f'(\theta)\, e^{-E_{des}/RT}$$

where k_{des} is the desorption kinetic constant, $f'(\theta)$ is the covered sites fraction available for desorption and E_{des} is the desorption energy, equal to the sum of E_{ads} and Q_{ads}.

At equilibrium, the rates of adsorption (r_{ads}) and desorption (r_{des}) are equal and the equations can be rearranged to derive the adsorption isotherm, representing the equilibrium process. Adsorption isotherms are typically used to characterize the reactants' chemisorption on the solid surfaces. Depending on adsorbate molecule nature, adsorbent surface and experimental conditions, different empirical models can be considered. Among them, the Langmuir, Temkin and Freundlich models assume different surface site distribution according to the variation of the adsorption heat with the surface coverage (*Figure 12*).

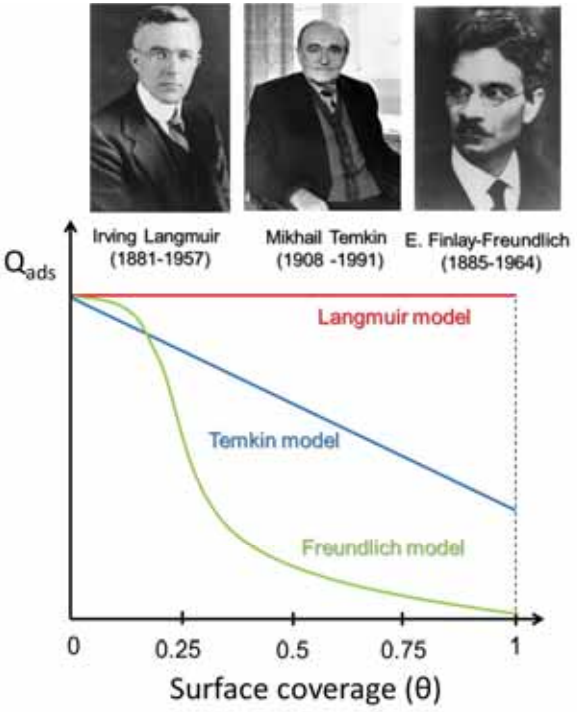

Figure 12. Variation of adsorption heat with surface coverage for the three models typically used to describe adsorption.

The simplest model is the *Langmuir isotherm*, developed by Langmuir in 1916 while working in General Electric on gas adsorption on the tungsten filaments of lamps. This model assumes an ideal uniform surface with

identical adsorption sites for which the adsorption heat is constant and independent of surface coverage where no interaction between adsorbed molecules occurs. Mathematically, the Langmuir isotherm can be expressed by the following equation:

$$\theta = \frac{KP}{1+KP}$$

where K is the equilibrium constant, P is the gas pressure, and θ is the surface coverage.

One of the major limitations of the Langmuir model is that the experimental data only fit at low surface coverages. In 1926, Freundlich proposed another empirical isotherm expression, in order to correlate the data measured at higher pressures:

$$\theta = \frac{n}{n_m} = \alpha P^{1/\beta}$$

where α and β are parameters dependent on temperature with both terms decreasing as temperature increases. This isotherm model simulates a non-uniform surface with complex distribution of active sites with adsorption heats dependent on surface coverage. As the numbers of adsorbed molecules are proportional to the fractional power of pressure, this isotherm is similar to the Langmuir isotherm at low pressures with the initial number of occupied sites presenting similar adsorption heats. Nevertheless, as surface coverage increases, the adsorption sites become more heterogeneous and the adsorption heat decays exponentially till full coverage is attained.

In the third model proposed by Temkin in 1940, the heat of adsorption decreases linearly with surface coverage. This model considers non-uniform surfaces with randomly distributed active sites with different affinities towards the adsorbent molecules. The sites of highest affinity are occupied first and the following molecules interact subsequently with the remaining empty sites till saturation. Assuming these considerations, the Tenkim equation presents a linear relationship between surface coverage (θ) and pressure ($\ln(P)$):

$$\theta = a \ln(bP)$$

where a and b are two fitting parameters related with the adsorption heat. An illustrative example of this model is the variation of the adsorption heat observed for chemisorbed CO on platinum epitaxial surfaces.

In general, the three models satisfactorily represent the majority of catalysts and their active phase distribution. The adsorption isotherms provide the basis for the formulation of the kinetic expressions that describe heterogeneously catalysed reactions.

Surface reactivity: kinetic and reaction mechanisms

The next step involves surface reaction of the adsorbed molecules via surface intermediates that are subsequently transformed into products. In the final catalytic step, the products are desorbed from the surface and the catalytic cycle starts again. At a microscopic level, the surface reaction proceeds through a series of elementary steps which are used to derive an expression of the rate associated with unknown concentrations of surface intermediates and measurable macroscopic concentrations of reactants. The aim of kinetics is to establish mathematical expressions and to apply them to a possible reaction mechanism relating the overall reaction rate with experimental parameters, such as temperature, pressure and concentration of reactants. If the conversions are very high or very close to the equilibrium conversion, the kinetic study may become complex, since the influence of the products themselves cannot be overlooked with regard to their competitive adsorption or participation in reverse reaction. In order to facilitate the interpretation, rate data must be recorded under differential reactor conditions (very low conversions) in which the concentrations of the reactants are considered constant and the concentrations of products are so small that their influence can be completely ignored. Moreover, data must be collected under a kinetic regime to avoid the impact of mass and heat transport. By considering both approaches, we can measure the intrinsic reaction rates and estimate all kinetic parameters (rate constant, reaction orders, pre-exponential factor and apparent activation energy). The determination of those parameters is fundamental because:

- Kinetic and reaction mechanisms are interconnected, and the knowledge of the reaction orders with respect to the reactants and products is crucial to suggest a reaction mechanism.
- Detailed kinetic equations are necessary to evaluate the intrinsic activity of the catalyst and to optimize reactor scale-up.
- The influence of temperature on the reaction rate can provide helpful information about the rate determining step (the slowest reaction step).

It is particularly important to mention that the catalyst affects reaction kinetics but never changes the equilibrium point. *Catalysis is a kinetic*

phenomenon and cannot change the thermodynamic equilibrium. The *principle of microscopic reversibility* establishes that at equilibrium any microscopic process is reversible, which means that

- the chemical reaction must proceed in both directions through the same intermediate species
- adsorption and desorption processes in both directions must be identical
- active sites should be the same in both directions
- If the reaction occurs through a set of elementary steps in the forward direction, the reverse process ought to occur through the same set.
- The rate-determining step (*RDS*) should be the same in both directions

Hence, the effective reaction rate can be expressed as the ratio of kinetic and driving force (distance from equilibrium) terms over the resistance term:

$$r_{eff} = \frac{(kinetic\ term)\cdot(driving\ force)}{(resistance\ term)^n}$$

where *n* takes a value of 1 or 2 and depends on the number of catalytic active sites involved in the rate-determining step, *i.e.*, the slowest step. Consequently, for a complete derivation of the kinetics equation that shows the relationship between r_{eff} and variables such as concentration, temperature, and pressure, the reaction mechanism must be known.

Except for very simple reactions, it is extremely rare to gain complete knowledge of the reaction pathways, and different approaches are usually considered to elucidate the kinetic models. *Steady-State Approximation* (*SSA*) is commonly used when the concentration of surface intermediates during the reaction is lower than those of the major species in the mechanism. This approach is very useful for obtaining kinetic models of two-first order reactions in series, but for complex reaction schemes that involve parallel or competitive reactions the equations are virtually impossible to solve. In this case, other approaches such as the *Most Abundant Reaction Intermediate* (*MARI*) approximation are used to simplify the system. This method assumes that one of the intermediates is much more abundant than others, allowing their coverage in the global balance to be ignored. Nowadays, the use of computer-assisted kinetic models facilitates the efficient solution of extremely complex cases.

Only the basic aspects of the heterogeneous kinetic approach, originally employed by Langmuir in 1921 and later expanded by Hinshelwood, are discussed in this book. This approach allows us to obtain the rate equations directly from molecular adsorption and desorption modelling over uniform surface catalysts, excluding complex mass and heat transfer phenomena. We can formally classify the mechanistic aspects and formal kinetic expressions in models describing the adsorption of one (*unimolecular*) or two (*bimolecular*) reactants and reaction rates on a uniform catalyst surface.

Unimolecular reactions: Langmuir model

The simplest method to describe the kinetics of a chemical reaction involves the use of the Langmuir isotherm. Let us consider the following sequence of reactions:

(i) $A_{gas} + * \rightleftharpoons A^*$

(ii) $A^* \rightleftharpoons X^*$

(iii) $X^* \rightleftharpoons X_{gas}$

in which the reactant, *A*, is firstly adsorbed on the surface forming the specie *A**, and then *A** is transformed into the adsorbed species *X**, and finally *X** is desorbed giving the final gas product, *X*. If we suppose that the adsorption of A is the Rate-Determining Step (*RDS*), the surface reaction goes to completion, and the third reaction is an equilibrium; the reaction rate can therefore be expressed as:

$$r = \frac{k_{ads(A)}\, P_A}{1 + \lambda_X P_X}$$

where $\lambda_X = k_{des(X)}/k_{ads(X)}$, P_i is the partial pressures of the reactant, and k_i is the adsorption/desorption rate constant. This model assumes that the reactant A adsorbs on the active sites of the surface in a non-dissociative manner. The accumulation of adsorbed product, X*, decreases the reaction rate and consequently inhibits the reaction.

Bimolecular reactions: Langmuir-Hinshelwood and Eley-Rideal models

We can now consider a bimolecular reaction in which two molecules, A and B, react to give a product P. Assuming that the reaction-determining step

(*RDS*) is the surface reaction, and the adsorption of reactants (A and/or B) and desorption of product (P) are quasi-equilibrated, three different situations can be found:

(i) *Langmuir-Hinshelwood competitive model:* the reactants A and B are adsorbed on the same site with the reaction rate conditioned by the surface coverage fractions:

$$r = k\theta_A\theta_B.$$

(ii) *Langmuir-Hinshelwood non-competitive model:* in this case, the reactants A and B are adsorbed independently on two different sites, and the reaction rate is expressed as:

$$r = k\theta_A\theta'_B.$$

(iii) *Eley-Rideal model:* the reaction takes place between adsorbed A and B molecules from the gas phase with reaction rate dependent on surface coverage and partial pressure:

$$r = k\theta_A P_B.$$

For the initial kinetics; where the concentration of product is negligible, the following expressions are deduced:

$$r = k\frac{\lambda_A P_A \lambda_B P_B}{(1+\lambda_A P_A+\lambda_B P_B)^2} \qquad \textit{Langmuir-Hinshelwood competitive}$$

$$r = k\frac{\lambda_A P_A \lambda_B P_B}{(1+\lambda_A P_A)(1+\lambda_B P_B)} \qquad \textit{Langmuir-Hinshelwood non-competitive}$$

$$r = k\frac{\lambda_A P_A P_B}{1+\lambda_A P_A} \qquad \textit{Eley-Rideal model}$$

where $\lambda_{A\ or\ B} = k_{des(A\ or\ B)}/k_{ads(A\ or\ B)}$, P_i is the partial pressure of the component *i*, k_i are the adsorption/desorption rate constants, and *k* is the kinetic rate constant.

CO hydrogenation to methanol on a ZnO catalyst, hydrogenation of ethylene on Cu catalyst, or benzene hydrogenation on an Fe catalyst represent examples of the Langmuir-Hinshelwood mechanism. Oxidation of ammonia on Pt catalysts and selective hydrogenation of acetylene to

ethylene on Ni or Fe catalysts are important examples of the Eley-Rideal mechanism.

Problem III. *What is the application of the power rate law in heterogeneous catalysis?*

The formulation of heterogeneous kinetics based on the Langmuir-Hinshelwood and Eley-Rideal models is based on the assumption that the catalyst surface is energetically uniform. However, numerous experimental data on chemisorption rates and equilibria indicate that surfaces are not uniform. Many of these kinetic data can be expressed in terms of the Freundlich isotherm, which supposes that the chemisorption heat and the activation energy are linear functions of surface coverage. Moreover, it has been demonstrated that some chemisorption rate data obey the power rate law. Therefore, the kinetics of many heterogeneous reactions can be developed on the basis of the power rate law and the corresponding Freundlich isotherm. For instance, the reaction rate of a gas-phase bimolecular reaction A + B → C could be expressed as:

$$r = kP_A^{\alpha} P_B^{\beta}$$

where r is the reaction rate, k is the specific rate constant, P_A and P_B are the partial pressures of the reactants, A and B, and the exponents, α and β, represent the partial reaction orders of A and B, respectively. The overall reaction order is $n = \alpha + \beta$.

And the relationship between the rate constant, k, and the temperature is given by the Arrhenius equation:

$$k = Ae^{\frac{-E_a}{RT}}$$

where A is the pre-exponential factor, R is the universal gas constant ($8.31\ \mathrm{J\ K^{-1}\ mol^{-1}}$), T is the absolute temperature, and E_a is the reaction activation energy. The greater the activation energy, the higher the temperature sensitivity of k and, accordingly, the higher the reaction rate. By measuring the reaction rate at different temperatures and plotting $ln(r)$ *vs.* $1/T$, a straight line is obtained and its slope allows the estimation of reaction activation energy.

Typically, when the activation energy presents values lower than 20 kJ mol^{-1}, we can assume that the reaction is diffusion-controlled. This means that the reaction is not in a kinetic regime and the reaction rate is controlled by molecule diffusion throughout the catalyst bed and the pores.

The applicability of this approach is limited by the fact that the exponents, α and β, are not always constants, and are sometimes dependent on temperature and pressure. Thus, the validity of the power rate law is restricted to narrow pressure ranges with coverages sufficiently far removed from equilibrium, as demonstrated in numerous kinetic studies.

Energetic aspects of heterogeneous catalysis

All catalytic processes entail energetic changes associated with the strength of molecule adsorption on the catalyst surface. The surface provides active sites on which the adsorbed reactant bonds weaken to such an extent that chemical reactions readily take place. By plotting the variation of potential energy *vs.* the reaction coordinate, it is possible to evaluate the course of the heterogeneously catalysed reaction, *Figure 13*. This type of energetic diagram includes the energy of all transition states and surface intermediates. Catalysed surface monomolecular reaction ($A_{gas} \rightarrow B_{gas}$) proceeds in three elementary steps, whereas the non-catalysed reaction occurs directly in one step.

For non-catalysed reactions, the activation energy is equal to the energy barrier for the transition state, while for the catalysed reaction a distinction should be made between the *true activation energy* (E'_{act}), related to the chemisorbed state, and the *apparent activation energy* (E''_{act}), the energy barrier from ground to transition state. The Arrhenius equation provides the *apparent activation energy* estimation, but the *true activation energy* is more important from the heterogeneous catalysis point of view. The use of surface catalysts provides a new reaction route that decreases the activation energy, but the Gibbs free energy (ΔG^0) remains unaltered. This means that a thermodynamically unfavourable reaction cannot become favourable in the presence of a catalyst.

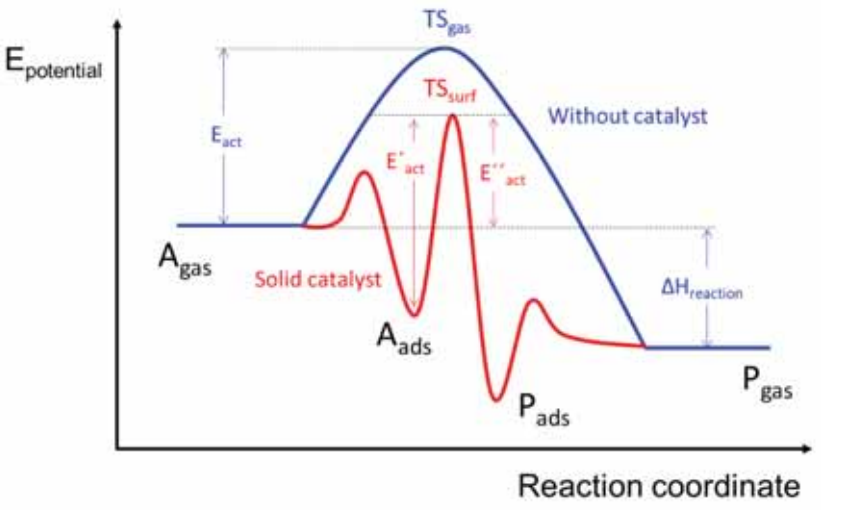

Figure 13. Energy diagram of heterogeneously catalysed monomolecular reaction, TS_{gas} and TS_{surf} transition state of gas-phase and surface reaction, respectively, $\Delta H_{reaction}$ reaction enthalpy, E_{act} activation energy of the non-catalysed reaction, E'_{act} true activation energy, and E''_{act} apparent activation energy

The strength of adsorption of reactants and products is also decisive for an optimal catalyst performance. In 1905, Sabatier postulated that a good catalyst is one that provides an optimum strength of bonding between the adsorbed reactants and catalyst surface (*Sabatier's principle*). This principle was experimentally demonstrated in 1960 by Rootsaert and Sachtler, using formic acid decomposition to carbon dioxide and hydrogen over various metal surfaces as their reaction model. It is reasonable to assume the intermediate formate formation, and the strength of the bond between that species and the metal surface is related to the formation enthalpy ($\Delta H^0_{formation}$) of the corresponding metal formate. If we represent the temperature needed to achieve the determined reaction rate ($\log r = 0.8$) versus the enthalpy of formation of metal formates, a *volcano curve* results, with the most active metals for formic acid decomposition situated at the top of the curve (*Figure 14*). The platinum group metals (Pt and Ir) are the most active for this reaction and lower temperatures are required to reach optimal reaction rate of decomposition. For all metals appearing on the left (Au and Ag), the metal-adsorbate bond is too weak and the intermediates are formed at an insufficient rate. Meanwhile, the formation enthalpy of metal formate is very negative for the metals on the right (W, Fe, Co or Ni)

as too strong a bond is formed, and the rate of intermediate decomposition is also insufficient. The *volcano curves* were described for the first time in 1958 by A.A. Balandin and provide a comprehensive basis to understand the catalytic activity of different catalysts. Empirically, this representation is used as descriptor-based catalyst screening for designing optimal catalysts.

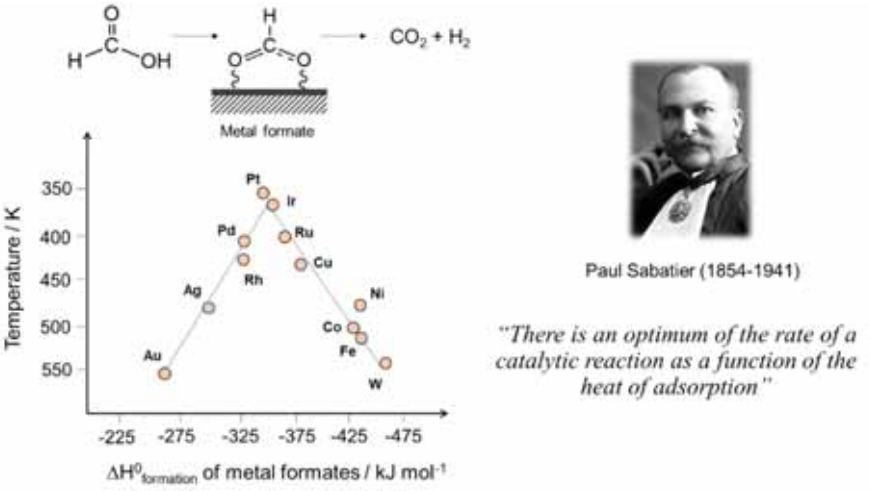

Figure 14. Experimental demonstration of Sabatier´s principle.

Understanding heterogeneous catalysis from first principles requires knowledge of surface reactivity and energy analysis. Thus, if we want to explain the differences in reactivity, the interactions of molecules in their transition states with catalyst surfaces must be understood. A very useful procedure for analysing transition states in heterogeneous catalysis is the *Brønsted–Evans–Polanyi relationship*, which expresses a linear relation between the modification in elementary reaction step activation energy with the change in the overall step reaction enthalpy over a family of similar catalysts. Moreover, the *Density-Functional Theory* (DFT) is an important tool for making reliable predictions based on *Brønsted–Evans–Polanyi relationship*, in particular for situations where experimental values are not available or are difficult to obtain. First-principle calculations are currently applied to construct *volcano curves* based on theoretical fundaments and to improve on the traditional *trial-and-error method* in catalyst design. Access to *volcano curves* provides the possibility to screen computationally many metal combinations, and allows a trade-off choice between the lowest price

and the best performance. A full description on the conceptual and computational approach for designing heterogeneous catalysts can be found in the book by R.A. van Santen and M. Neurock (*Molecular heterogeneous catalysis*, Wiley-VCH, 2006).

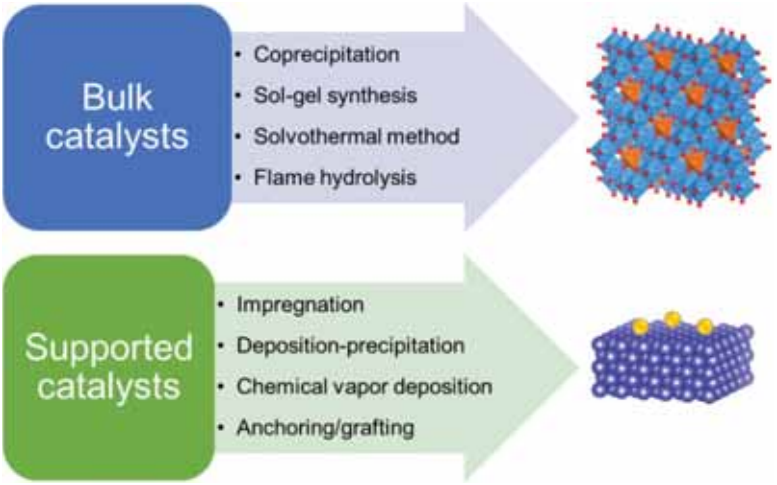

Figure 15. Classification of bulk and supported catalyst preparation methods

Preparation methods and characterization techniques of solid catalysts

The catalytic properties of solids are strongly influenced by the preparation procedure used and the quality of the starting precursors. Small variations in aging times, drying and calcination procedures, solvents used, agitation rates and precursor salts can affect catalyst performance. Different synthesis methods can be used to prepare bulk or supported catalysts (*Figure 15*). Bulk catalysts are typically prepared by precipitation, coprecipitation, sol-gel, solvothermal and flame hydrolysis methods among others. For the supported catalysts, the supports are firstly prepared (and optionally shaped) using the methods employed for the bulk catalysts and then the active catalytic phase is introduced into the porous structure of the support usually by impregnation or deposition-precipitation. The active phase can also be introduced using other methods such as chemical vapour deposition (CVD), anchoring or grafting. No matter what method is employed, a final activation treatment is usually required to obtain the active phase of the catalyst. The activation might be reduction with hydrogen (activation of

active metals), sulphidation with H_2S (activation of Mo-based catalyst for desulphurization), oxidation (oxide-based catalysts) and dehydroxylation (water removal from zeolites and clays). The activation procedures also depend on temperature, heating rate, flow rate and gas partial pressures. As the preparation includes different parameters to control it, it is fundamental to verify the reproducibility of the methods.

Preparation of bulk catalysts

Bulk catalysts are entirely composed of active material, the typical examples being silica-alumina for hydrocarbon cracking, iron-molybdate for methanol oxidation, Cu-Zn-Al oxides for methanol synthesis or zeolites for fluid catalytic cracking (FCC). The preparation techniques used are normally those that are easy to reproduce. In *precipitation* and *coprecipitation* methods, precursor solutions are precipitated by controlled pH variation leading to high-purity stoichiometric solids with well-defined crystalline structures. An example is $FeSbO_4$ catalyst used in SOHIO process (ammoxidation of propene to acrylonitrile), prepared by coprecipitation of Sb_2O_3 powder and warm aqueous solution of $FeNO_3 \cdot 9H_2O$, and using ammonia as precipitating agent. The solid precipitate is filtered, dried, and calcined to obtain rutile-type mixed oxide solids.

The *sol-gel method* is also successfully applied for the preparation of bulk catalysts. In this procedure, organic (alkoxides) or inorganic compounds are hydrolyzed to "gel" via intermediate formation of colloidal suspension "sol". The gel obtained is dried and calcined obtaining homogeneous solids with controlled surface area, pore volume and pore size distribution. The preparation of high surface area silica-alumina with accessible pore structures using aluminium isopropoxide and tetraethyl orthosilicate (TEOS) as precursors is an example of the synthesis method and its application.

Solvothermal synthesis is typically used to prepare molecular sieves and zeolites. As the name indicates, solvothermal treatment involves heating gels, precipitates or flocculates in the presence of solvent (known as *hydrothermal synthesis* when water is used as solvent) at 100 – 300 ºC under autogenous pressure in closed vessels (autoclaves). During this process, textural and structural changes are produced leading to the transformation of amorphous particles that are converted into crystalline materials. The crystallization process is kinetically slow, and material structure and crystal size depend on synthesis conditions (temperature and time). This method is used for large-scale production of zeolites. In the early 1970s, the Mobil Oil

company developed an innovative hydrothermal procedure using small amounts of alkyl ammonium salts as templates for directing crystal growth and obtaining zeolites with unusual pore dimensions. Zeolite catalysts prepared by hydrothermal methods (ultrastable zeolite Y, mordenite, MCM-22, zeolite beta, ferrierite, ZSM-5, ZSM-22, ZSM-23, and TS-1) are used in the refinery and petrochemical industries.

Flame hydrolysis, also called the AEROSIL® method, was invented by H. Kloepfer in 1942 to obtain nanoscale metal oxides via gas-to-particle conversion processes, based on the decomposition of suitable precursors on hot-wall and plasma reactors and through laser ablation. This method is typically used for the production of pyrogenic silica, in which silicon tetrachloride ($SiCl_4$) is vaporized, mixed with air and hydrogen, and then fed into a flame reactor. The water vapour generated during the combustion of hydrogen hydrolyses $SiCl_4$ forming nanoscale SiO_2 particles. The particle size and solid specific properties can be tailored by adjusting the flame parameters. This method leads to defined particle-size distributions of non-porous spherical particles of high purity.

Preparation of supported catalysts

The preparation of supported catalysts involves dispersion of the active phase on a carrier with high surface area. The role of the carrier in supported catalysts is not limited to active metal nucleation and dispersion but also affects activity, selectivity and stability. The most common methods for dispersing the active metal on the support are *impregnation*, *adsorption* and *precipitation-deposition*. The *impregnation method* consists of support immersion into a solution containing the required metal salt precursor concentrations and subsequent solvent removal under controlled temperature over time. After impregnation, the catalyst is dried and calcined. A variation of this method is known as *incipient wetness impregnation* when the volume of the precursor solution is at a level necessary to fill the pores of the support. For higher metal loadings when the precursor salt shows limited solubility, multiple impregnations may be required. The active phase distribution on the support is strongly influenced by many parameters such as rate of drying, calcination temperature and gas atmosphere during the final thermal treatment. Slow solvent evaporation from the narrow pores of the solid causes metal salt recrystallization within the pores and leads to the so-called *egg-yolk* distribution. In contrast, when the drying occurs too fast the evaporation starts within the pores and metal salt migrates to pore openings, producing an *egg-shell* distribution (*Figure 16*). If the metal is

very expensive (Pt, Rh or Pd), or if the reaction takes place predominantly on the outer surface as a result of pore diffusion limitations, then the formation of an *egg-shell* distribution with active components concentrated on the outer surface may be desirable. In general, the *impregnation method* leads to non-uniform active phase distribution and crystallite sizes within the 2–200 nm range. Some examples of industrial impregnated catalysts are $Ag/\gamma\text{-}Al_2O_3$ used for ethylene oxide production or $Ni/\alpha\text{-}Al_2O_3$, a catalyst for methane steam reforming for hydrogen production as a primary step of ammonia synthesis.

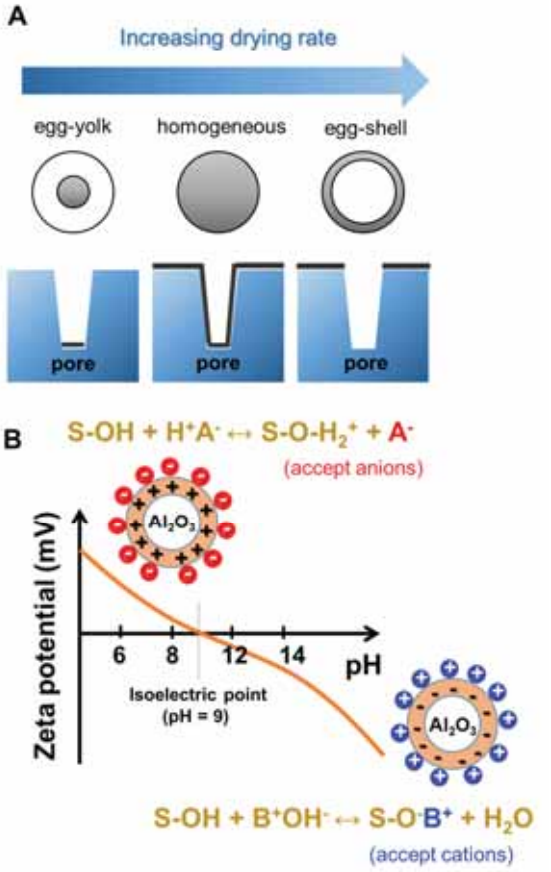

Figure 16. A Influence of the drying rate on active phase distribution; **B** adsorption of anions and cations on alumina surface as a function of pH

Problem IV. *If you want to prepare a benzene hydrogenation catalyst based on nickel supported on alumina (specific surface of alumina is 200 $m^2\ g^{-1}$) how much nickel do you need to impregnate to obtain separated active sites?*

The term "separated sites" indicates that each nickel atom must be sufficiently far away from other nickel atoms to ensure a reaction occurring at a site not influenced by the others. If we consider hydrogenation of thin substrates such as benzene, then an area of 1 nm^2 per active site will be sufficient. Since 200 $m^2\ g^{-1}$ is equal to $2 \cdot 10^{20}$ nm^2, one gram of alumina can accommodate roughly $2 \cdot 10^{20}$ atoms of nickel on "separated sites". Dividing by the Avogadro number, 0.3 mmol of nickel must be impregnated on 1 g of alumina support. It should be mentioned that this estimation supposes only single-atom sites, but in an actual catalyst, the active components are often formed by small metal clusters or nanoparticles.

In the *adsorption method*, the impregnation of precursor salts takes place via interaction with the groups present on the support surface. Ion-exchange reactions between the precursor ions and the support surface occur during salt impregnation, and the overall process is governed by kinetic and equilibrium constants. The polarization of the support surface depends on the pH of the solution and the isoelectric point of the solid—the pH at which the net charge of the surface is zero. For example, at pH below the isoelectric point the surface of alumina is protonated and positively charged adsorbing preferentially anions from the solution, while at pH above the isoelectric point the surface is negatively charged and cationic species adsorb (*Figure 16*). The adsorption method leads to a very homogeneous distribution of the active phase on the support, although a maximum adsorption capacity is found around 3 wt.% metal loading.

In the *deposition-precipitation method*, the support is impregnated by a metal-salt solution containing urea (or other base) at room temperature. When the temperature is raised to 70 – 90 ºC the urea decomposes and the formed hydroxyl ions precipitate homogeneously onto the metal precursor. Finally, the catalyst is calcined or reduced, resulting in highly homogeneous active metal distribution on support surface. This method has been extensively used to prepare highly dispersed gold nanoparticles on oxide supports.

Chemical vapour deposition (CVD) consists in vaporization and deposition of organometallic precursors on a support surface. This method can be used to produce supported metal catalysts, on both a large scale and in a controlled manner; it has been applied for synthesis of the Fischer-Tropsch Co/SiO_2 catalyst using $Co(CO)_8$ as a metallic precursor. The precursor to be used must fulfil several conditions, such as good volatility and thermal stability, simple preparation, high purity, low toxicity, easy and clean decomposition and stability under storage conditions. Compared to the conventional methods, the absence of solvent favours metal diffusion within the pores and prevents active phase redistribution during drying. Nonetheless, a final step that includes a thermal post-treatment is required to eliminate organic/inorganic residues and to activate the catalyst.

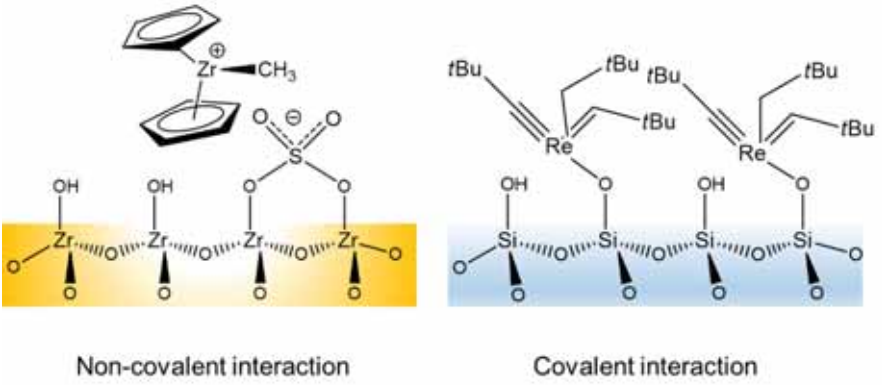

Figure 17. Examples of interaction of organometallic complexes with inorganic surfaces

Over the last two decades, extensive studies have been performed on the development of supported homogeneous catalysts on solid surfaces. Immobilization techniques seek to combine the advantages of homogeneous catalysts, such as high selectivity and yield, with those of heterogeneous catalysts: robustness, ease of separation and metal recovery. For this purpose, the *homogeneous catalyst heterogenization by anchoring* on a solid support is the most common approach. There are several ways to immobilize the metal complexes, with the main objective of bonding unaltered complexes to the surface. Organometallic complexes can be immobilized on the inner surface of porous supports by physisorption or cation exchange. However, this procedure is often ineffective, because of weak interaction between complex and support and consequent catalyst

leaching in liquid medium reactions. A more successful method is achieved when the organometallic complex is covalently bonded onto the support. In this context, the term *grafting* is used and involves a slight modification of the ligands, to facilitate the formation of covalent bond between the complex and the solid surface. Typical inorganic supports successfully employed are silica, alumina, zirconia, zeolites, and clays (*Figure 17*).

Characterization techniques

The available techniques include conventional procedures and more sophisticated methods used to investigate the physics and chemistry of surfaces. The characterization techniques encompass various types of spectroscopy, diffraction and imaging, all providing information on size, shape, morphology, topology, structure, chemical composition, surface acid-base and redox properties, and porosity. Some of these methods require ultra-high vacuum conditions and low temperatures, while others work at high pressures and elevated temperatures. In this section, we will focus our attention on the methods routinely used for characterizing solid catalysts. For more details, interested reader can consult the book "*Characterization of Solid Materials and Heterogeneous Catalysts: From Structure to Surface Reactivity*" by Michel Che and Jacques Védrine (Wiley, 2012).

The most common characterization techniques used in heterogeneous catalysis are schematically illustrated in *Figure 17*.

The chemical composition of catalysts can be determined using conventional analytical techniques (volumetric or gravimetric) or spectroscopic methods such as *atomic absorption spectroscopy* (AAS). Another technique commonly applied to obtain the elemental composition of the solid catalyst is *X-ray fluorescence* (XRF), although it is only applicable for elements heavier than sodium.

As heterogeneous catalysis involves essentially reaction on the surface, its surface composition is pivotal in determining the behaviour of a solid catalyst. Currently, many surface sensitive analytical methods under ultra-high vacuum conditions are available such as *X-ray photoemission spectroscopy* (XPS), *Auger spectroscopy* (AES), *Secondary ion mass spectrometry* (SIMS), *Ion scattering spectroscopy* (ISS), and measuring back-scattered X-rays by electron microscopy—a technique known as *Energy dispersive analysis of X-rays* (EDX).

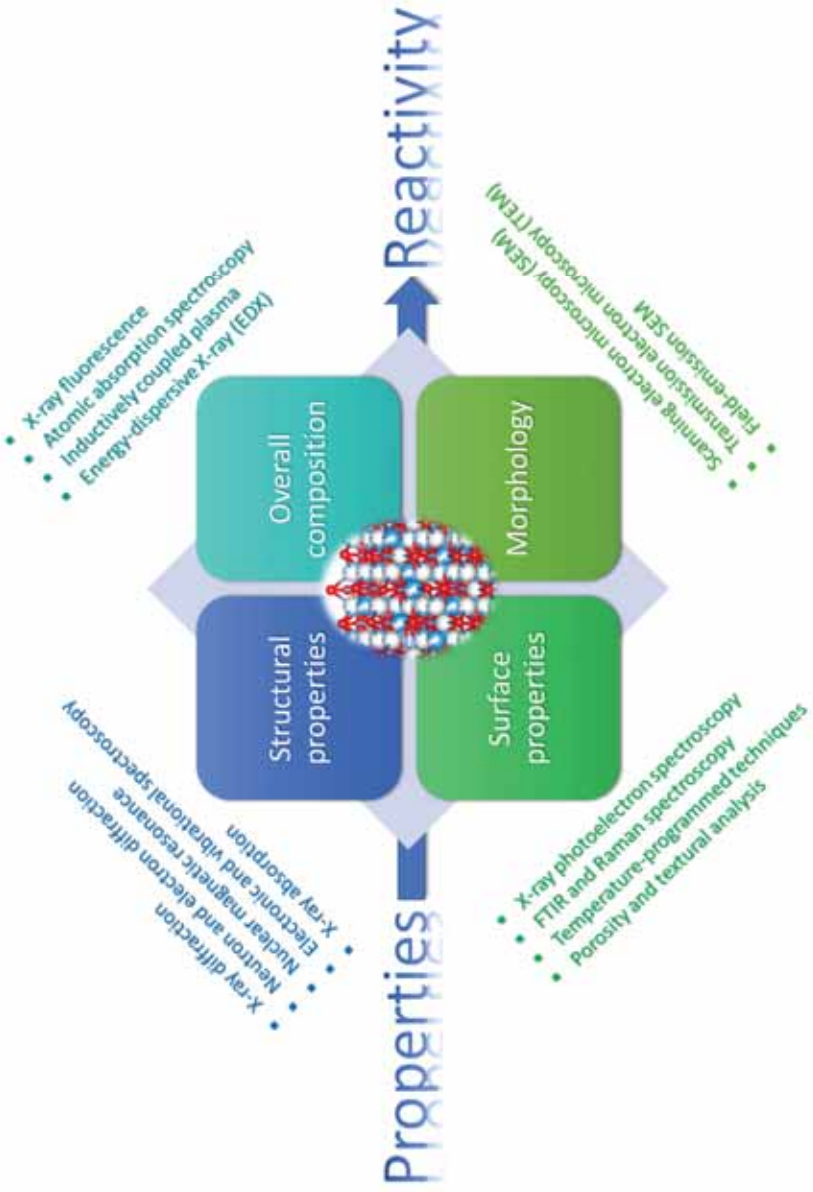

Figure 17. Most common characterization techniques used in heterogeneous catalysis

The nature of phases and their structure is generally analysed with *X-ray diffraction* (XRD). This technique can also be used to determine average crystallite sizes, using the extent of X-ray diffraction line broadening and applying the Scherrer equation:

$$\tau = \frac{K\lambda}{\beta cos\theta}$$

where τ is the mean crystallite size, K is a dimensionless shape factor close to unity, λ is the X-ray wavelength, β, broadening at half maximum intensity (FWMH: full width half maximum), and θ is the Bragg angle.

Furthermore, structural refinement methods such as Rietveld can be used to optimize both structural and non-structural parameters and to enable the precise determination of cell parameters and the distribution of crystalline phases. From a structural point of view, the technique of *X-ray absorption* (XAS), with which the coordination number, the interatomic distances and the symmetry of the solids can be determined, is also of particular interest in catalysis. Nevertheless, this technique presents the limitation that it is not easily accessible and requires synchrotron radiation.

Nitrogen physisorption is the conventional technique applied to analyse the textural properties of solid materials. The shape of the adsorption/desorption isotherms provides information on the overall type of porous network and more detailed information (pore size distribution, pore volume, specific surface area, etc.) can be obtained using mathematical methods such as the *Brunauer-Emmet-Teller* (BET) equation or the *Barrett-Joyner-Halenda* (BJH) method. The physical texture and morphology of a solid catalyst can be examined by *Scanning Electron Microscopy* (SEM), where information about shape and size of micropores and surface topology is obtained. On the other hand, *transmission electron microscopy* (TEM) possesses much higher resolution and facilitates observation of small metal particles (even single-atom catalysts) and the estimation of their dispersion on the support.

Thermo-programmed methods all involve techniques in which the variation of a physical parameter is analysed as a function of temperature at constant heating rate. Among these methods, we can distinguish *thermogravimetry* (TG), *differential thermal analysis* (DTA), *differential scanning calorimetry* (DSC), *temperature-programmed reduction* (TPR), and *oxidation* (TPO). Concerning the information revealed by these techniques, TG/DTA/DSC methods are typically employed to study the thermal stability of the catalysts and the occurrence of phase transitions with temperature, whereas

TPR/TPO experiments are carried out to evaluate the reduction/oxidation capacity of the solids as a function of temperature.

Many catalytic reactions depend on surface acidity or basicity and it is of great importance to know their concentration, nature and strength. Commonly, these sites are probed by surface titration using bases or acids, respectively. This process can be monitored using single colorimetric methods, in which the colour change is followed by indicators, or by using other techniques such as *infrared spectroscopy* (IR) or *nuclear magnetic resonance* (NMR). In these methods, the probe molecule needs to be of an adequate size, to ensure accessibility to all sites, and the interaction with the surface sites must be easily studied. Some examples of the probe molecules typically used are CO, CO_2, NH_3, pyridine or 2,6-lutidine. Another routine technique is *thermal-programmed desorption* (TPD), in which ammonia or CO_2 is firstly adsorbed and subsequently desorbed using temperature to assess the quantity of desorbed molecules and their strength. Furthermore, the acid-basic properties can also be characterized by catalytic reaction tests such as 2-propanol dehydration, in which the strength and number of acid sites is evaluated.

A large number of available characterization techniques offer numerous possibilities for understanding the physicochemical properties of solid catalysts and for establishing a relationship with their catalytic performance. *From a fundamental point of view, solid state chemistry is the starting point for designing a solid with the composition, structure and properties suitable for practical applications that include heterogeneous catalysis processes.*

In situ/operando approach: study of solid catalyst "in action"

Although interesting, the information gathered by the conventional characterization methods provides no direct insight into what is really happening on the catalyst surface under working conditions. Equally insufficient is the information that we receive before and after the reaction, since that on the spatiotemporal performance of a solid catalyst in the course of the catalytic reaction is missing. In other words, as indicated by G. Somorjai, *"it would be like studying a life with access only to the prenatal and postmortem states"*. The solution is to couple a characterization method to a reaction system to monitor catalysis "*in action*".

The term *in situ* is the Latin expression for "in place", and the *in-situ* characterization approaches provide useful information for the physicochemical properties of the catalysts under working conditions. The simultaneous measurement of catalytic activity and selectivity accompanied with *in-situ* characterization is commonly known as the *operando* approach (from Latin "working"). The potential impact of the *operando* approach on catalysis science is its capability to establish the fundamental molecular structure-performance relationship. In an illustrative example presented by M. Daturi in the *International Congress on Operando Spectroscopy* (2012, Brookhaven, USA), the catalyst surface can be visualized as a chessboard on which the motion of the pieces represents the adsorption of molecules. A "chess tournament" would be a representation of the real reaction occurring on the catalyst surface and the final objective of the *operando* approach is to monitor the "chess game".

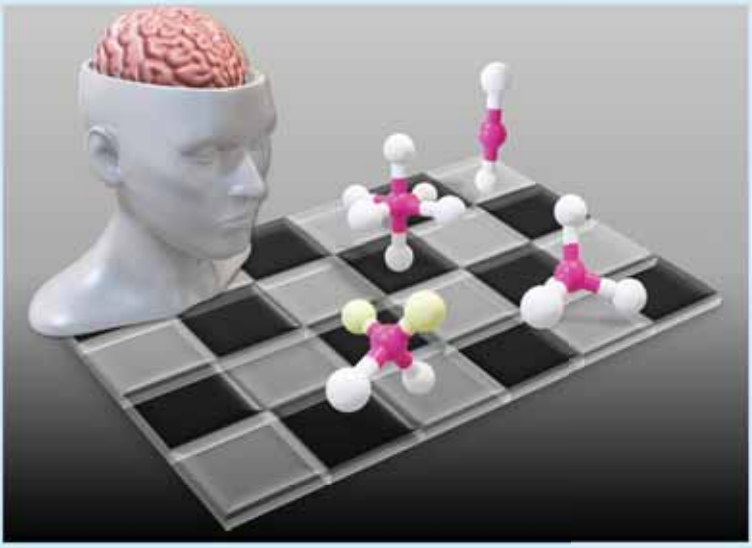

Applications of heterogeneous catalysis

Heterogeneous catalysis deals with a vast number of applications including oil refining and the petrochemical industry, production of bulk chemicals,

pollutants abatements, green chemistry and the production of fine chemicals. The relevance of heterogeneous catalysis will be illustrated with a few examples.

Industrial catalysis

Nowadays, more than 85% of industrial chemical processes depend on the efficient use of solid catalysts. Heterogeneous catalysts are crucial in many large-scale processes including hydrogenation, oxidation, hydrocarbon cracking, reforming, coal gasification, isomerization, and polymerization reactions, and are involved in the following industrial areas:

- Crude oil refining and petrochemistry
- Production of bulk and fine chemicals
- Plastics industry and manufacture of polymer materials
- Energy conversion processes

As an example, zeolites are typically used as catalysts in the petroleum refining processes, due to their excellent properties for selective chemical conversion of hydrocarbons into more valuable products such as diesel, gasolines, aromatic hydrocarbons, olefins, heating oil or liquid petroleum gas (LPG). Zeolite-based catalysts possess channels of specific dimensions offering different degrees of accessibility for organic molecules and present what is known as shape selectivity on reactants, products or transition-state. For example, protonated ZSM-5 zeolite catalyses alkylation of benzene with ethylene to obtain selectively monoethylbenzene against diethylbenzene, too voluminous to pass through the channels. Faujasite Type Y zeolites are also very efficient solid catalysts in reactions of fluid catalytic cracking (FCC) and hydrocracking. In these processes, the heavy fractions of crude oil are transformed into more valuable products such as gasoline, smaller branched olefins and aromatics.

The production of bulk chemicals can involve both inorganic and organic processes. The inorganic processes are the oldest known catalytic process as for example the Contact process for sulphuric acid production (1832) using V_2O_5 catalyst or Deacon process for chlorine production (1860) using $CuCl_2$. Heterogeneous catalysts are also used on a large industrial scale in the production of organic chemicals. For example, CO hydrogenation to methanol is typically carried out on Cu/Zn oxide catalysts. Heterogeneous metal oxide catalysts are also widely used for aerobic oxidation of $C_1 – C_4$ alkanes to produce olefins (ethylene, propylene and butadiene), oxygenates (acetaldehyde, acrolein, maleic anhydride and acrylic acid) and nitriles

(acrylonitrile). These compounds are very important feedstocks for the manufacture of special chemicals and many of them are fundamental for the production of polymers. For example, in 1957 the Standard Ohio Oil Company patented the SOHIO process, by which more than 7 million metric tons of acrylonitrile are produced annually by ammoxidation of propene over silica-supported bismuth molybdate catalysts (*Figure 18*).

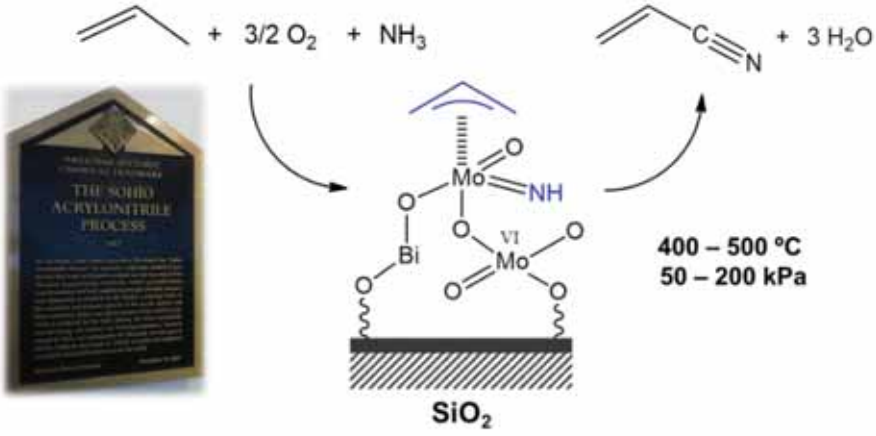

Figure 18. Schematic representation of acrylonitrile manufacture using the SOHIO process

Large numbers of polymers of industrial relevance involve olefin polymerization reactions. From the mid-1950s, the Ziegler-Natta process has been largely employed for polypropylene and polyethylene production at moderate pressures and temperatures (10 bar, 50 – 150 ºC). Although the traditional catalyst of Ziegler-Natta is based on Ti, Zr, or Hf organometallic compounds, the modern heterogeneous catalysts are $TiCl_4$ and $MgCl_2$ packed into spheres of amorphous silica in combination with an organoaluminium compound such as $Al(C_2H_5)_3$. In the early 1950s, the Phillips Petroleum company in the US developed another polymerization catalyst based on Cr_2O_3 supported on silica. The Phillips catalyst is manufactured by chromate (1-2 wt.%) impregnation on amorphous silica gel and calcination of the dried solid at 500 – 700 ºC. For both Ziegler-Natta and Phillips catalysts, it is assumed that coordinatively unsaturated transition metal centres are necessary for olefin polymerization providing the possibility of the simultaneous bonding of the monomers and the growing chain. The chain-growth mechanism involves insertion of two CH_2 units into a transition metal centre and increasing the original alkyl chain

while avoiding branched chain formation, *Figure 19*. Branched polymers can be obtained by copolymerization of ethylene with small short-chain alkenes. The ratio linear-to-branched chains greatly affects polymer properties.

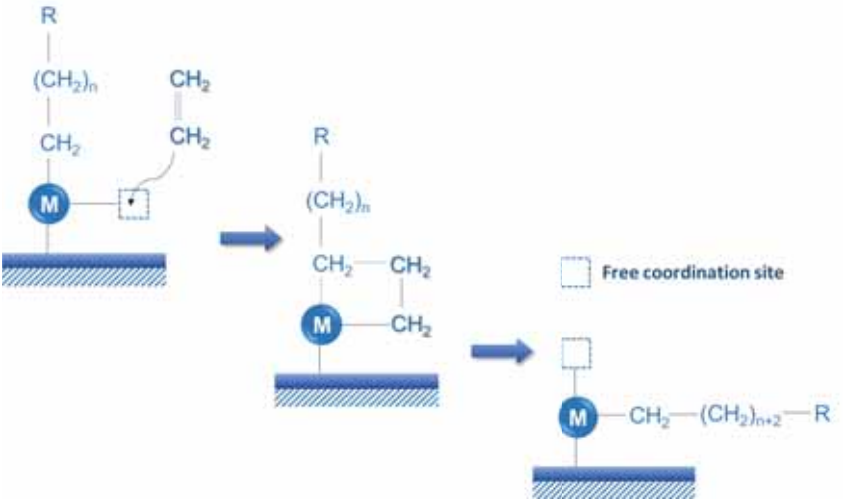

Figure 19. Ethylene polymerization reaction on coordinatively unsaturated metal centres

Heterogeneous catalysis also plays a pivotal role in energy conversion processes. Fossil fuels such as petroleum, natural gas, coal, shale gas or renewable sources such as biomass can be used for hydrogen and syngas production. The worldwide production of hydrogen derives mainly from natural gas steam reforming, a mature and well-established technology. In this process, methane and steam react at high temperatures (800 – 1000 ºC) to produce a mixture of hydrogen, CO and CO_2 of compositional ratio depending on operation conditions and the catalyst in use. The overall process involves additional steps such as natural gas purification (sulphur removal) and hydrogen purification (water gas shift and methanation converters), both necessary for using the produced hydrogen in ammonia and synthesis of other bulk chemicals. Steam reforming catalysts are typically based on nickel supported on alumina and promoted with alkali metals, shaped in pellets with large external diameters and high void fractions.

Problem V. *Why is the same catalyst (Ni supported on alumina) used in both methanation and methane steam reforming reactions?*

Methanation and methane steam reforming reactions are reversible (forward and backward) equilibrium reactions:

$$CO_2 + 4H_2 \rightleftharpoons CH_4 + 2H_2O$$

According to the principle of microscopic reversibility, the Ni/Al_2O_3 catalyst should work in both, methanation and steam reforming reactions. Furthermore, from a thermodynamic point of view both reactions require different operation conditions: low temperature for methanation (exothermic) and high temperature for steam reforming (endothermic). A more stable α-Al_2O_3 support is preferable for steam reforming reaction while less stable γ-Al_2O_3 support can be used for methanation.

Another relevant energy conversion process is related to the production of *syngas* and its subsequent transformation into synthetic transportation fuels. Syngas has traditionally been produced by coal gasification, although current changes in energy sources have redirected interest towards the gasification of biomass. Syngas, a mixture of CO and H_2, is the starting raw material for producing high quality transportation fuels through an important process discovered by Franz Fischer and Hans Tropsch in 1926. The Fischer-Trosch reaction has been widely investigated and the combined characteristics of solid catalyst and reactor type are essential. In 1993, SASOL successfully implemented slurry-bed reactors, due to their excellent heat-transfer properties. The commonly used catalysts are based on iron, cobalt and, to a lesser extent, on ruthenium supported on silica or alumina. Cobalt-based catalysts are preferred for diesel and jet-fuel production while iron-based catalysts produce waxes and olefin products of low molecular weight.

Environmental catalysis

Air pollution caused by emission of damaging substances from stationary and mobile sources is one of the most serious environmental problems facing society today. Among the pollutants emitted into the atmosphere, the most harmful for human health and the environment are nitrogen oxides (NO_x), sulphur oxides (SO_x), carbon monoxide (CO), volatile organic

compounds (VOCs), ammonia and particulate matter. Environmental abatement catalysts are fundamental to improve air quality.

The most representative example of environmental catalysis is the automotive exhaust catalyst. The exhaust gas emitted by automobiles contains typically unburnt hydrocarbons and CO and NO_x formed by the reaction between N_2 and O_2 air components at the high temperatures reached in the internal combustion engines. In the late 1970s and early 1980s, three-way catalytic (TWC) converters were introduced in vehicle emission control devices in USA and Canada. Basically, a three-way catalytic converter facilitates the removal of three pollutants—CO, NO and hydrocarbons—through the following reactions:

1) *Oxidation of unburnt hydrocarbons*: $C_xH_y + O_2 \rightarrow CO_2 + H_2O$
2) *CO oxidation*: $CO + O_2 \rightarrow CO_2$
3) *NO reduction by CO and hydrocarbons:* $NO + CO + C_xH_y \rightarrow CO_2 + H_2O + N_2$

It is remarkable that the first two reactions take place under oxidative conditions, whereas the third is a reduction reaction. All reactions are carried out in a single catalytic converter with the use of three precious metals (Pt, Pd and Rh) supported on high surface alumina (γ-Al_2O_3), and with ceria (CeO_2) and other minor additives (ZrO_2, MgO, La_2O_3) as promoters. Platinum and palladium are responsible for the oxidation reactions while rhodium sites catalyse the reduction reaction and can perform preferential adsorption and dissociation of NO in presence of O_2. The chemisorbed O* species oxidise CO and unburnt hydrocarbons into CO_2 and H_2O, whereas N* adsorbed species react, releasing N_2. Ceria is an oxygen-storage component that can release oxygen under fuel-rich conditions, guaranteeing the oxidation of CO and hydrocarbons (*Figure 20*). The minor compounds are used as structural or thermal stabilizers (La_2O_3). All catalytic components are coated on the honeycomb monolithic structure walls, typically made of cordierite ($Mg_2Al_4Si_5O_{18}$). The purpose of the coated honeycomb monolith is to provide a catalytic layer with a high surface area and to ensure high dispersion of the precious metals. This structure provides excellent thermal stability and prevents metal particles from sintering even at temperatures as high as 1000ºC. Finally, the monolithic structure is wrapped in metallic foil to ensure thermal insulation and to protect the catalyst from dampening and mechanical stress.

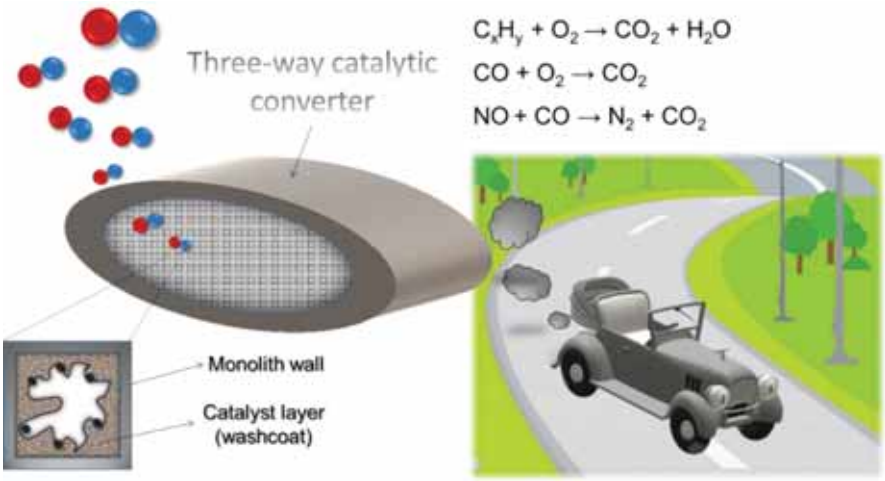

Figure 20. Three-way exhaust gas emissions catalytic converter.

Currently, worldwide standard legislation requires the reduction of emissions, and—due to continuing reductions in emission limits—the importance of environmental catalysis will increase in the near future to achieve an ultralow emission vehicle. Nevertheless, a virtually ideal zero-emission may only be attained by a hydrogen-powered vehicle.

Green chemistry

Green chemistry, also known as sustainable chemistry, involves the reduction or elimination of all hazardous substances from chemical processing. Heterogeneous catalysis is a fundamental pillar of green chemistry and offers the following benefits:

- Increased selectivity and yield
- Stoichiometric reactions replaced with catalytic cycles
- Minimized use of reagents and solvents
- Decreased energy requirements
- Enhanced process safety
- Waste-generation prevention and management

Heterogeneous catalysis is inherently a green technology. Several indicators can be used to measure the greenness of chemical processes and to establish the influence of catalysts on sustainability, such as the environmental factor

(*E*-factor) and atom economy. The *E*-factor represents the ratio between mass (kg) of generated waste and mass (kg) of desired product. For this indicator, waste is any substance other than the desired product, *i.e.*, solvent, products, catalyst and excess of reactants. There is a substantial increase of the *E*-factor from oil refining and bulk chemical industries (< 0.1 – 5) to fine chemicals and pharmaceuticals (25 – 100). In the oil refining industry and the production of bulk chemicals such as sulphuric acid and ammonia, almost all chemical conversions are catalysed by solids and the use of solvents is limited. In contrast, active pharmaceutical design and fine chemical manufacture require multistep stoichiometric organic synthesis with limited use of solid catalysts.

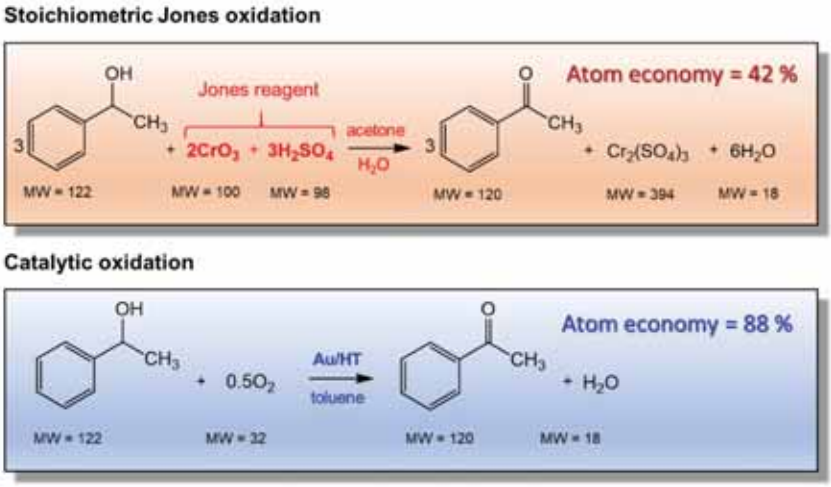

Figure 21. Oxidation of secondary alcohols into ketones as an example of green catalysis.

Another parameter typically used to measure the environmental impact of chemical processes is atom economy, defined as the ratio between the molecular weight of the desired product and the sum of the molecular weights of the stoichiometric starting reactants. According to this parameter, any synthetic method must be designed to maximise the incorporation of all atoms of the reactants into the final desired product, ideally approximating 100 %. One example is the Jones oxidation reaction, in which a secondary alcohol is oxidised to ketone in the presence of Jones reagent (chromium trioxide and sulphuric acid dissolved in a mixture of water and acetone). This process is very efficient and achieves high yields

of ketone, but the atom economy is only 42 % and due to the toxicity of CrO_3, the Jones oxidation is environmentally unacceptable (*Figure 21*). In recent years, this reaction has been replaced by greener chemical processes such as aerobic oxidation of alcohols under mild conditions (40 ºC in air and atmospheric pressure) in the presence of heterogeneous catalysts. The catalyst is based on gold nanoparticles supported on hydrotalcite (HT). It is a very effective process with an atom economy of 88 %.

Production of fine chemicals

Traditionally, fine and specialty chemicals have been produced by means of non-catalytic organic synthesis. Nonetheless, there are numerous examples demonstrating that heterogeneous catalysis offers an excellent opportunity for better processes in the flavour, fragrance and pharmaceutical industries. Even though solid catalysts are less active and selective than homogeneous catalysts or biocatalysts, their use is economically viable because of the ease of separation and reutilisation. Advanced solid materials with custom-designed properties—such as optimized metallic dispersion, redox ability and efficient control of acidity and basicity, high activity, specificity and long-term stability—have been developed for the synthesis of perfumery chemicals. High chemo-, regio-, stereo- and enantioselectivity can be obtained using the shape selectivity control of the porous materials functionalized with surface redox or acidic – basic sites. An example can be found in the isomerization of epoxides of terpenes to produce oxygenated compounds of perfumery interest. The isomerization of α-pinene oxide leads to a sandalwood-like fragrance chemical, called campholenic aldehyde (*Figure 22*). Selective production of campholenic aldehyde is conventionally catalysed by homogeneous Lewis acids such as the zinc halogenides $ZnCl_2$ or $ZnBr_2$, achieving high yields around 85%. However, these catalysts are not environmentally friendly due to their toxicity and corrosiveness, to which the impossibility of separation and regeneration can be added. Numerous efforts to find an optimal solid catalyst that will overcome these drawbacks have been reported, and zeolites with large pores such as USY (pores of 1.2 nm) have proved to be very effective. Selectivity of 75% campholenic aldehyde was achieved over commercial USY zeolite at 273 K. The conversion increased to 100% when the zeolite was dealuminated by diluted acid treatment, suggesting that Brønsted acidity associated with aluminium was not responsible for this isomerization.

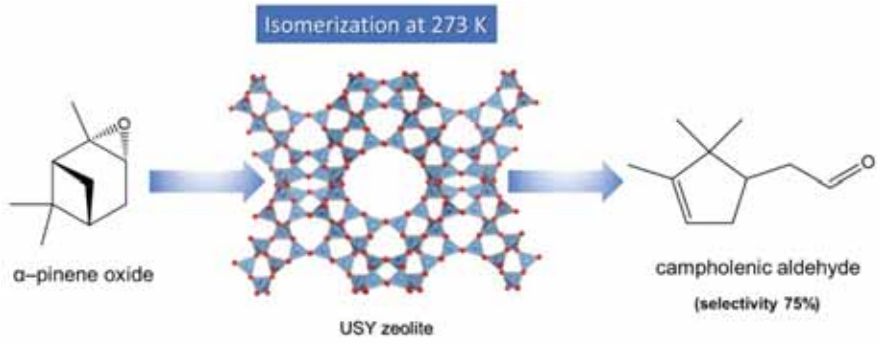

Figure 22 Isomerization of α-pinene oxide to camphonelic oxide on USY zeolite catalyst

Other interesting examples of heterogeneous catalysis application for the production of fine chemicals is the synthesis of propargylamines, which are versatile therapeutic drug molecules. Conventionally, these compounds can be obtained by amination of propargylic precursors, but the precursors are moisture sensitive and require strictly controlled reaction conditions. An interesting alternative synthesis is the so-called A^3 coupling reaction between alkyne, aldehyde and amine over heterogeneous catalysts. A large variety of solid catalysts based on supported metals have been tested in this reaction, and amongst the cationic types, gold shows an excellent activity (*Figure 23*).

Figure 23 A^3 coupling reaction scheme over gold-supported catalyst

Dispersed cationic gold species are able to activate alkyne molecules forming an acetylide intermediate, which reacts with immonium ions, generated *in situ* from the aldehyde and secondary amine, to form the desired propargylamine. This process presents important advantages

because it is an atom-economical and environmentally-friendly approach and clearly exemplifies the importance of heterogeneous catalysis in fine chemical production.

Used books and References

Introduction to catalysis and industrial catalytic processes, R.J. Farrauto, L. Dorazio and C.H. Bartholomew, Wiley-AIChE (2016)

Preparation of Solid Catalysts, G. Ertl, H. Knözinger and J. Weitkamp (Eds.), Wiley-VCH (1999)

Industrial Catalysis – A practical approach, Jens Hagen, Wiley-VCH (1999)

Handbook of Heterogeneous Catalysis, G. Ertl, H. Knözinger and J. Weitkamp (Eds.), Wiley-VCH (1997)

In situ spectroscopy of Catalysts, Bert Weckhuysen (Ed.), American Scientific Publishers (2004)

Catalysis – From Principles to Applications, M. Beller, A. Renken and R.A. van Santen (Eds.), Wiley-VCH (2012)

Introduction to heterogeneous catalysis, Roel Prins, Anjie Wang and Xiang Li, World Scientific Production (2016)

Catalysis: Concepts and Green Applications, Gadi Rothenberg, Wiley-VCH (2008)

Kinetics of heterogeneous catalytic reactions, Michel Boudart and G. Djéga-Mariadassou, Princeton University Press (1984)

Environmental catalysis, F.J.J.G. Janssen and R.A. van Santen (Eds.), Imperial College Press (1999)

Molecular Heterogeneous Catalysis – A conceptual and computational approach, R.A. van Santen and M. Neurock, Wiley-VCH (2006)

Metal Oxides – Chemistry and Applications, J.L.G. Fierro (Ed.), CRC Press - Taylor & Francis Group (2006)

Chemical Reaction Engineering, O. Levenspiel, Wiley, 2nd Edition (1972)

Heterogeneous Catalysis – Fundamentals and Applications, Julian R.H. Ross (Ed.), Elsevier (2011)

W.F. Hölderich et al., The use of zeolites in the synthesis of fine and intermediate chemicals, *Catal. Today* 37 (1997) 353-366

P. Bazin, O. Marie and M. Daturi, *Stud. Surf. Sci. Catal.* 171 (2007) 97-143

G. Leofanti, M. Padovan, G. Tozzola and B. Venturelli, Surface area and pore texture of catalysts, *Catal. Today* 41 (1998) 207-219

G. Leofanti *et al*., Pelletization of catalysts supported on activated carbon. A Case Study: clean synthesis of dimethyl carbonate from methanol and CO_2, *Catal. Today* 34 (1997) 307-327

A. Corma, Heterogeneous Catalysis: Understanding for Designing, and Designing for Applications, *Angew. Chem. Int. Ed.* 55 (2016) 6112-6113

F. Dumeignil, Jean-François Paul and Sébastien Paul, *J. Chem. Educ.* 94 (2017) 675-689

J.C. Védrine, Importance, features and uses of metal oxide catalysts in heterogeneous catalysis, *Chin. J. Catal.* 40 (2019) 1627-1636

D. Sanfilippo (Ed.), The catalytic process from the laboratory to the industrial plant, *Catal. Today*, 34 (1994) 259-552

CHAPTER 7

STRUCTURE-SENSITIVE REACTIONS

"Most finely divided catalysts must have structures of great complexity… we should look upon the surface as consisting of a checkerboard".
Irving Langmuir (1881-1957)

Introduction: the principle of active sites

Heterogeneous catalysis is based on surface phenomena, and the reactions occur when the reactants are chemisorbed on the most energetic sites of a crystal surface. The first model, formulated by Langmuir in 1916 for explaining chemisorption on metal surfaces, had assumed an arrangement of energetically identical sites non-interactive between each other where just one molecule from the gas phase is adsorbed per site. According to the model, the surface must be uniform and highly homogeneous with equivalent positions for chemisorption. Nevertheless, Langmuir was aware that this assumed approximation hardly satisfied real surface state.

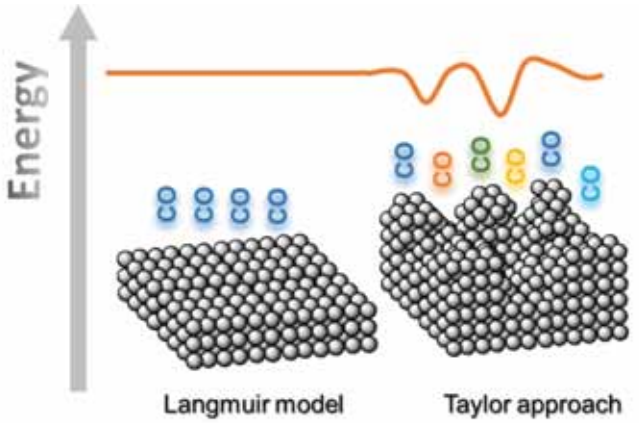

Figure 1. Illustration of Taylor approach

Indeed, the real catalyst surfaces are heterogeneous, and not all the sites that are present but only the "active sites" participate in the reaction. In 1925, Taylor established that the crystal defects present in real solids are the origin of the active sites. This proposal, commonly referred as *principle of active sites*, expounds that the activity related to those sites can be attributed to their low coordination (unsaturation) and the irregular geometry of the surface. The sites are distinguishable by the distinct coordination numbers of their surface atoms, resulting in different reactivity. This was originally evidenced by Taylor, focusing on CO adsorption and nickel carbonyl formation on heterogeneous nickel surfaces (*Figure 1*). Contrary to the uniform surface, heterogeneous surfaces present numerous coordination sites in which the molecules are adsorbed with differing energy. "*Only a small fraction of the surface is active*" and "*the amount of surface which is catalytically active is determined by the catalysed reaction*". A quantification of the active sites is also introduced by the *Taylor ratio*, defined as the fraction of active sites relative to the total number of sites on the catalyst surface for a particular reaction.

Modern surface science techniques provide a detailed inspection of crystal surfaces and reveal the presence of large regions where the atoms are organized in parallel planes separated by ledges. The presence of these ledges causes growth of new atomic planes and terrace formation, which are considered as crystalline defects. An atomic-scale model of the surface structure of crystalline solid with its different surface sites is represented in *Figure 2*. The surface is heterogeneous and atoms in terraces are surrounded by a large number of nearest neighbours whereas the atoms situated in steps and kinks present few neighbours.

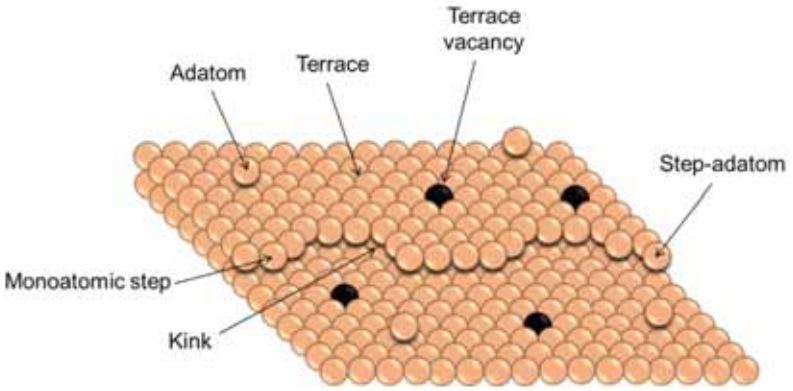

Figure 2. Schematic representation of a heterogeneous surface

In the late 1960s, Boudart classified catalytic reactions in two groups: structure-sensitive and structure-insensitive reactions. Structure-sensitive reactions alter their specific activity as a function of particle size, while in structure-insensitive reactions the rate remains constant whatever the particle size. Since then, advances in surface science have revolutionized our understanding of the participation, at the atomic scale and molecular level, of surface in catalytic processes. Gerhard Ertl (Nobel Prize of Chemistry in 2007) and Gabor A. Somorjai among others are the scientists that have contributed most to the development of molecular scale surface science, focusing exclusively on adsorption chemistry on single crystal surface and model catalysts.

The heterogeneity of the active sites on solid catalyst surfaces and its effect on catalytic activity have been widely investigated by means of different surface techniques: low energy electron diffraction (LEED), electron energy loss spectroscopy (EELS), atomic force microscopy (AFM), ion-scattering spectroscopy (ISS), X-ray photoemission spectroscopy (XPS), infrared reflexion absorption spectroscopy (IRAS) and Auger electron spectroscopy (AES), among others. Their ultimate goal is to study the surface atom by atom under working catalytic reaction.

Heterogeneous catalysts often consist of small metal oxide or sulphide particles dispersed on high surface area support materials. The supported catalysts typically used in industrial applications are multicomponent non-uniform systems, sometimes quite complex. Moreover, the state of the catalytic surface depends on the conditions under which it is used. Therefore, in many fundamental studies the complex real catalyst is replaced by a simplified model catalyst. Single crystals are highly uniform, crystalline and pure solids, and these model systems have traditionally been employed to explore the relationship between structure and properties of the supported industrial catalysts. However, the acquired fundamental understanding often suffers from “materials gaps” and “pressure gaps” when extended to the real-world operation and working at atmospheric or higher pressures. In the past few years, a great effort has been invested in the design of more sophisticated model catalysts: what is known as the concept of “bridging the material gap”, aimed at the deposition of nanoparticles with specific sizes and geometries on well-defined support surfaces (*e.g.*, metal nanoparticles supported on thin films of oxides deposited on single crystal metal surfaces, or non-metallic nanoparticles supported directly on single crystal metal surfaces). The model systems allow studies under high-pressure conditions and directs the interpretation of behaviour towards more realistic conditions.

Surface structure of solid catalysts

On the basis of their chemical nature the active phases can be categorized in three main groups as shown in *Table 1*. In the case of metals, important progress has been made in understanding surface atomic structure. However, this knowledge is more limited when more complex materials such as oxides or sulphides are considered.

Table 1. Classification of solid catalysts based on their chemical nature

Chemical nature	Catalytic phases	Main catalytic application
Metal	Fe, Co, Ni, Pt, Pd, Rh, Au, Ag, Cu	*Hydrogenation, oxidation, hydrogenolysis*
Non-stoichiometric oxides and sulphur compounds	NiO, ZnO, CeO_2, TiO_2, MgO, α-MnO_2, α-$Mo(W)O_3$, $Mo(W)S_2$	*Oxidation, desulphurization*
Stoichiometric oxides	Al_2O_3, SiO_2, zeolites	*Polymerization, isomerization, cracking, alkylation*

Metal surface structures

The great majority of metals used in catalysis are situated in groups 8, 9, 10, 11 and 12 of the periodic table. These metals tend to form densely-packed structures like body-centred cubic (*bcc*), faced-centred cubic (*fcc*) and close-packed hexagonal (*hcp*) (*Figure 3*). Most of them adopt *fcc* or *hcp* structures in which the packing arrangement maximizes the occupation of space, with only 26% empty space. In both structures each atom is surrounded by 12 nearest neighbours, *i.e.*, the coordination number of each atom is 12. Amongst all the metals in those groups iron is the only exception presenting a *bcc* lattice less densely packed structure with 32% of empty space and coordination number 8.

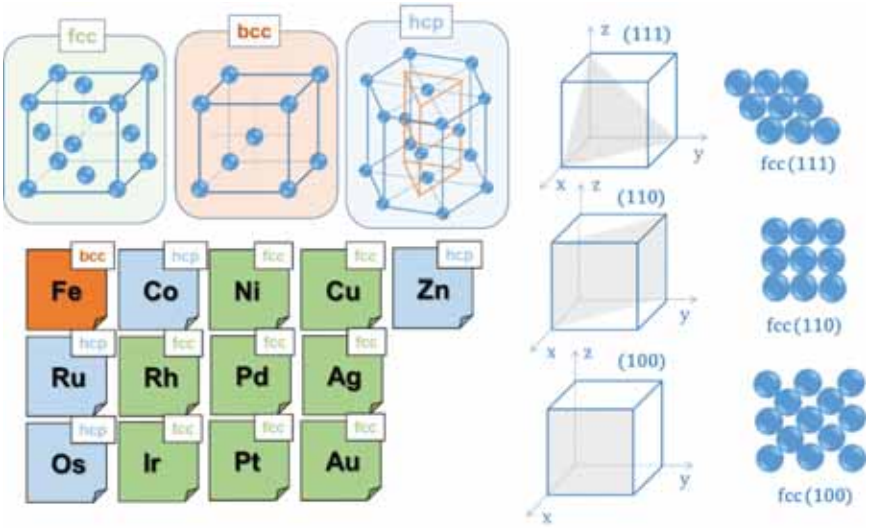

Figure 3. Representation of face-centred cubic (*fcc*), body-centred cubic (*bcc*) and hexagonal closed packed (*hcp*) lattices and representation of the *fcc* (111), (110) and (100) surfaces.

Heterogeneous catalysis occurs on the surface of solids and, therefore, it is important to establish which crystal planes are directly exposed to the reactants. The three basal planes of the cubic crystals are (111), (110) and (100) and their representative cross-section in the *fcc* unit cell is presented in *Figure 3*. It should be mentioned that the *hcp* crystal system presents four principal axes and the *hcp* planes are represented by four Miller-Bravais indices as (*hkil*) where the *i* index is the negative sum of indices *h* and *k*.

In highly homogeneous surfaces, the planes consist of atoms surrounded with many neighbours and low energy. These surfaces correspond to low-Miller-index planes such as (111), (110) and (100). Nevertheless, much more complicated surfaces composed of terraces separated by steps and even containing kinks are usually found. These rough surfaces are characterized by high-Miller-index planes and the typical notation is adopted, $n(h_t, k_t, l_t)$ x (h_s, k_{ts}, l_s), indicating that the surface is composed by *n* rows of atoms forming a (h_t, k_t, l_t) terrace and one step plane of (h_s, k_{ts}, l_s) indices. The *fcc* (111) surface variations produced in the presence of steps and kinks are illustrated in *Figure 4*. The *fcc* (755) surface is equivalent to 7(111) x (100). Theoretically all surface varieties can be constructed, but not all of them are thermodynamically stable, and restructuration frequently

occurs. Heterogeneous surfaces suffer dynamic rearrangement of the surface atoms on chemisorption time scale (10^{-13} s), on catalytic reaction time scale (s) or over longer periods (h) depending on the diffusion rate.

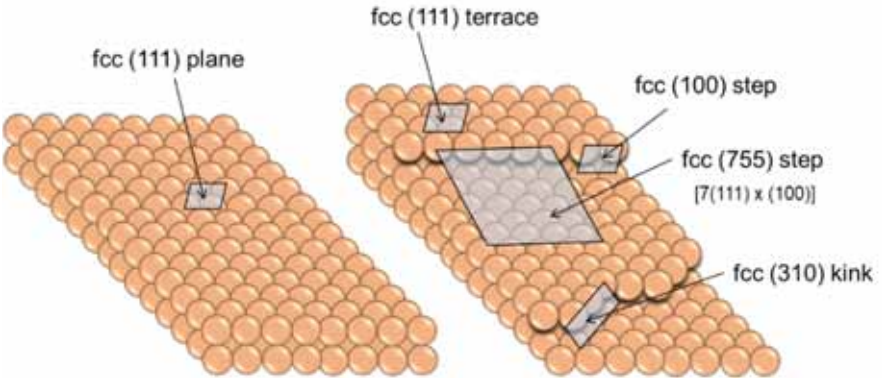

Figure 4. Model of *fcc* (111) surface in absence and in presence of steps/kinks.

Problem I *Draw the (332) and (430) surface structures for fcc metals.*

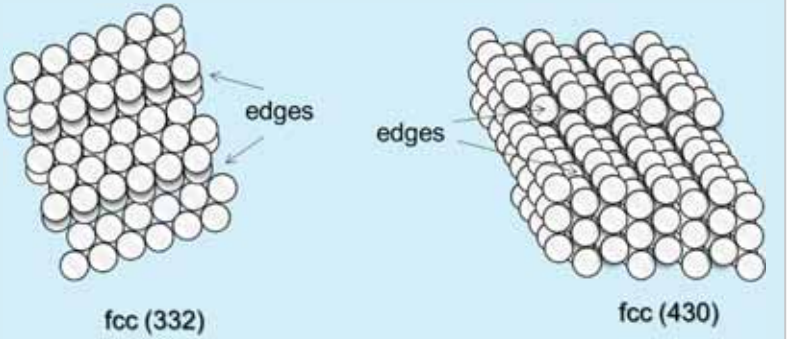

Oxide and sulphide surface structures

In comparison to the vast amount of data available for metal surfaces, direct knowledge of oxide and sulphide surface geometry and electronic systems is still very limited. The reason is that such surfaces are thermodynamically not well defined under ultrahigh vacuum conditions and in absence of a gas

phase. The geometric and electronic structures of these surfaces have been indirectly studied using diverse surface science techniques and electron spectroscopic methods by means of probe molecule adsorption studies (CO, H_2, O_2, CO_2, H_2O and NO). The probe molecules are adsorbed creating differences in the electric field distributions on the surface which are measured and contrasted with theoretical studies allowing the bonding behaviour of molecules with the surface structure to be rationalized.

Magnesium oxide (MgO) is one of the most frequently investigated oxide surface structures, due to its simple atomic structure and strong ionic bonding behaviour. This oxide presents a typical rock-salt structure where (100) and (110) surfaces are non-polar, while the (111) surface represents a polar oxide surface (*Figure 5*). The non-polar (100) and (110) surfaces exhibit nearly terminated surfaces (bulk like) with equal number of magnesium and oxygen atoms. In contrast, two different (111) surfaces are available, those terminating in magnesium and those in oxygen atoms. Such surfaces are called polar due to the existing net dipole moment. Densely packed non polar oxide surfaces, like MgO (100) or (110), are largely inactive but the creation of surface defects (corners, edges, steps, etc) associated with oxygen vacancies plays a significant role in their catalytic behaviour.

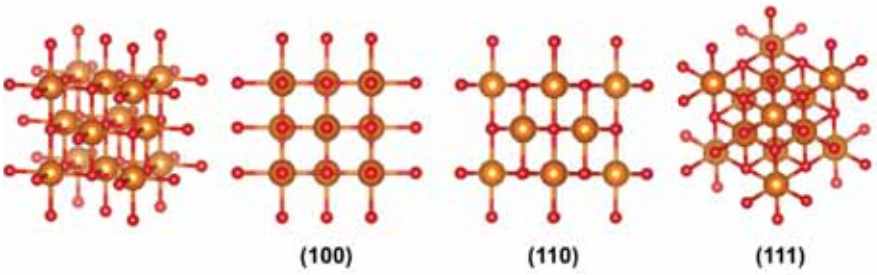

Figure 5. Structure of bare MgO and projection of the (100), (110) and (111) surfaces, magnesium in orange and oxygen in red.

Cerium dioxide (CeO_2), also called ceria, is another important oxide in catalysis due to its unique redox properties and high oxygen storage capacity (OSC). Cerium dioxide presents cubic fluorite structures with space group *Fm3m (Figure 6)*. The coordination environment of the surface atoms and the oxidation state of the ceria surface structures with low Miller index (100), (110) and (111) have been extensively studied. The (100) surface presents charged planes with a repeating O-Ce bilayer unit with a

dipole moment perpendicular to the surface. This surface becomes very unstable. On the contrary, the (110) surface exposes layers of cerium cations and oxygen anions with identical composition and balanced charges. Therefore, this surface is non-polar and much more stable. In the case of the (111) surface, a repeating unit of O-Ce-O in a symmetrical configuration results in very stable surface without surface dipole moment.

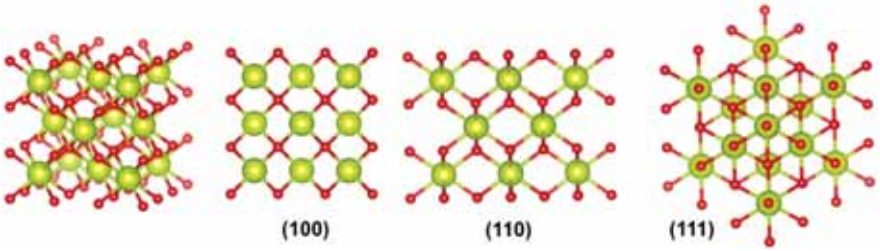

Figure 6. Structure of bare CeO_2 and projection of the (100), (110) and (111) surfaces, cerium atoms in green and oxygen in red.

In the majority of oxides, the surface is highly reactive and is affected when exposed to ambient atmosphere. The symmetry and coordination of the surface metal ions is very low in comparison to the bulk, and these ions exhibit a high tendency to achieve surface saturation by reacting with gas molecules from the atmosphere, and particularly with moisture. The reaction with moisture on the surface of metal oxides (*e.g.*, alumina) can be evidenced with different techniques, and infrared spectroscopy easily reveals the heterogeneity of the formed hydroxyls on the surface. The structure of γ-Al_2O_3 is organized in two types of layers, A and B, containing two different cation distributions corresponding to a defective spinel lattice parallel to the (111) plane (*Figure 7*). Both layers contain 24 aluminium cations and, while for the B-layer, all cations present octahedral coordination, only eight of the aluminium sites in the A layer are octahedral; all the remaining sixteen are located in tetrahedral interstices. Consequently, the structure of γ-Al_2O_3 is organised either in an octahedral structure formed by aluminium atoms surrounded by oxygen atoms (67% of Al atoms) or by aluminium atoms in a tetrahedral geometry (33% of Al atoms). This originates a wide variety of surface aluminium atoms that can adopt coordination numbers in the range from 3 to 6 originating a large population of surface hydroxyl groups with different geometries upon hydroxylation. These surface hydroxyl groups present vibrational modes that are very active in IR spectroscopy; hence, this technique is often used to characterize these species. *Figure 7* includes a schematic representation of all the

different types of hydroxyls formed on alumina surfaces with their corresponding stretching vibrational frequencies, measured by IR spectroscopy. A simple electrostatic model was proposed by Knözinger and Ratnasamy for the interpretation of the stretching vibrations of hydroxyl groups on alumina surfaces. This model is based on the assumption that the OH stretching vibration is determined by the coordination of the corresponding hydroxyl group with Al^{3+} cation. For the hydroxyls on the top A-layer of the (111) plane, two types of configurations are possible: (i) *type Ia*, associated with terminal hydroxyl groups coordinated to a single tetrahedral Al^{3+} cation), and (ii) *type IIa* characteristic of bridging hydroxyl groups linked to tetrahedral and octahedral cations). Similarly, in hydroxyls located on the top B-layer in the (111) plane, two more likely configurations arise: (i) *type IIb* associated with bridging hydroxyl linked to two octahedral cations, and (ii) *type III* configuration, typical of hydroxyl groups coordinated to three aluminium cation in octahedral interstices. If the spinel structure of alumina contains a large number of cationic vacancies a fifth configuration designated as *type Ib* can also exist, associated with terminal hydroxyl coordinated to a single octahedral aluminium cation. A maximum of five types of hydroxyl groups are expected on the surface of aluminas with spinel structure, and their relative abundance depends on the relative contribution of the different crystal faces.

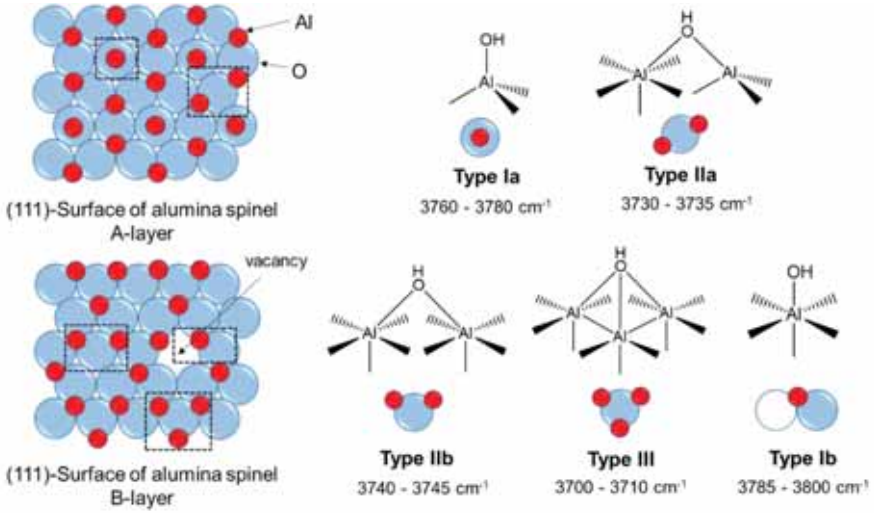

Figure 7. Types of aluminium sites and hydroxyl stretching frequencies in IR spectroscopy for the (111) surface of alumina spinel structure.

For other oxides, such as silica (SiO_2), the hydroxylation reaction is strongly limited by the high activation barrier on its hydrophobic surface. The hydroxylation of silica is only achieved under severe steam treatments at high temperatures.

These few examples provide some highlights regarding the chemical nature and structural features of oxide surfaces and this approach can be extended to many other oxides with catalytic properties such as ZrO_2, TiO_2, ZnO, Y_2O_3, La_2O_3, or even mixed-oxides ($MgAl_2O_4$, $FeCr_2O_4$, $CeZrO_4$, $LaAlO_3$). For more extensive information we recommend the excellent book by Henrich and Cox (V.E. Henrich and P.A. Cox, *The Surface Science of Metal Oxides* (1994), Cambridge University Press, Cambridge).

Sulphides such as MoS_2 or WS_2 play important roles in crude-oil refinement and hydrotreatments from petroleum destillates. In contrast to the oxides, which are ionic structures, sulphides show predominant largely covalent character; hence the crystal structures of sulphides differ greatly from those of oxides. The most representative example of sulphide surface is that of MoS_2 (*Figure 8*). The MoS_2 structure consists of Mo cation layers sandwiched between sulphur atom layers. Each molybdenum atom is surrounded by six sulphur atoms forming a trigonal-prismatic geometry and each atom of sulphur has three Mo neighbours. The MoS_2 layers are separated at 6.5 Å distance and the interaction between layers is controlled by weak van der Waals forces. Moreover, the layers are shifted one against another and it is necessary to include two layers in the unit cell, 2H-MoS_2 structure (2H stands for the two slabs in the cell). The reactivity of sulphides is associated with the edges, since the basal plane of sulphur atoms remains inactive. Two different reactive surfaces are formed when the MoS_2 structure is cut perpendicularly to the surface plane, one terminating with Mo atoms (Mo edges), and another associated with sulphur (S edges). Both surfaces are polar, one contains excess of positive charges (Mo edges), the other excess of negative charges (S edge). These surfaces are energetically very unstable and highly reactive in the presence of hydrogen. Consequently, the surface covers itself with SH^- groups when exposed to H_2S and H_2 mixtures during the hydrodesulphurization reactions.

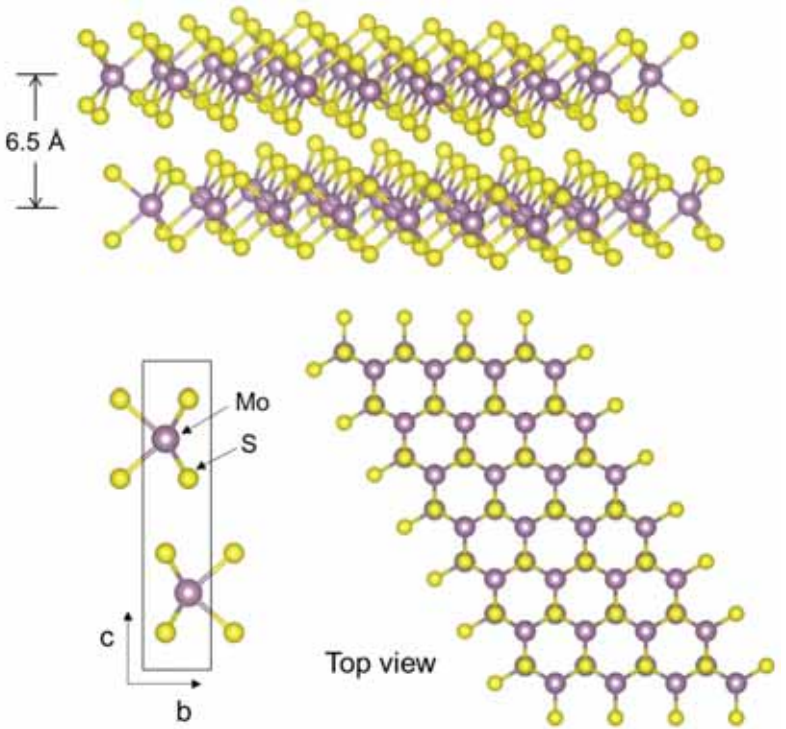

Figure 8. Structure of molybdenum sulphide.

Surface chemistry: the frontier of solid-state chemistry

Modern surface science is capable of investigating surfaces in detail on the atomic scale in the great majority of solids. The surface organization of crystalline solids differs notably from the structure exhibited by the bulk, and influences the chemical, mechanical, electrical, magnetic and optical properties of the material. In catalysis, the interest resides in the influence that the surface exercises on adsorption behaviour. The surface is not a mere spectator but "lives" during catalytic reaction. A number of dynamic mobility phenomena of surface atoms —such as surface relaxation and reconstruction, adsorbate induced restructuring— takes place, which this merits discussion of the influences that these exercise on the rate of heterogeneous reaction.

Relaxation and reconstruction of surfaces

From the thermodynamic point of view, the creation of surfaces implies an energetic cost due to the bonds that must be broken and as a consequence, the surface free energy remains always positive. The surface free energy (γ) is related to the cohesive energy of the solid (ΔH_{coh}) and to the number of bonds that must be broken according to the equation:

$$\gamma = \Delta H_{coh} \frac{Z_s}{Z} N_s$$

where Z_S is the number of the missing nearest neighbours missing on the surface, Z is the coordination number of a bulk atom, and N_S is the density of atoms on the surface. Normally, metals have the highest values of surface free energies, in the 1.5 to 3 J m^{-2} order, while ionic solids and oxides present much lower values, between 0.2 and 0.5 J m^{-2}.

The minimization of surface free energy is the motif that governs processes occurring on surfaces. This force leads to surface relaxation resulting in changes of the equilibrium position and bonding of the surface atoms. As a result, the atoms are displaced in directions perpendicular and parallel to the surface initiating the formation of new surface unit cells (reconstruction of the most external layers). This phenomenon is called *surface reconstruction* and the resulting atomic surface structure can differ fundamentally from that expected after abrupt termination of the bulk structure at the surface. Surface reconstruction is commonly observed in less closely packed metal surfaces like *fcc* (110) and *bcc* (100). After reconstruction the surface atoms show a maximal coordination number. For example, the (110) crystal face of iridium presents the so-called “missing-row” reconstruction, in which a whole row of Ir atoms is periodically removed (*Figure 9*).

In the case of the (100) crystal surface, the interatomic distance in the topmost layer undergoes shrinking parallel to the surface and the square unit cell collapses into hexagonal close-packed arrangements (*Figure 9*). This type of reconstruction is typical for many *fcc* metals, such as Ir, Au and Pt.

On the other hand, MgO (100) and NiO (100) crystal surfaces are typical examples of bulk terminated non-polar surfaces with moderate relaxations of the interlayer spacings. They present a nearly terminated rocksalt lattice surface. In contrast, a completely different situation is encountered for the polar (111) surface, in which the bulk-like terminated surface is reconstructed via octopolar reconstruction, illustrated for NiO in *Figure 10*.

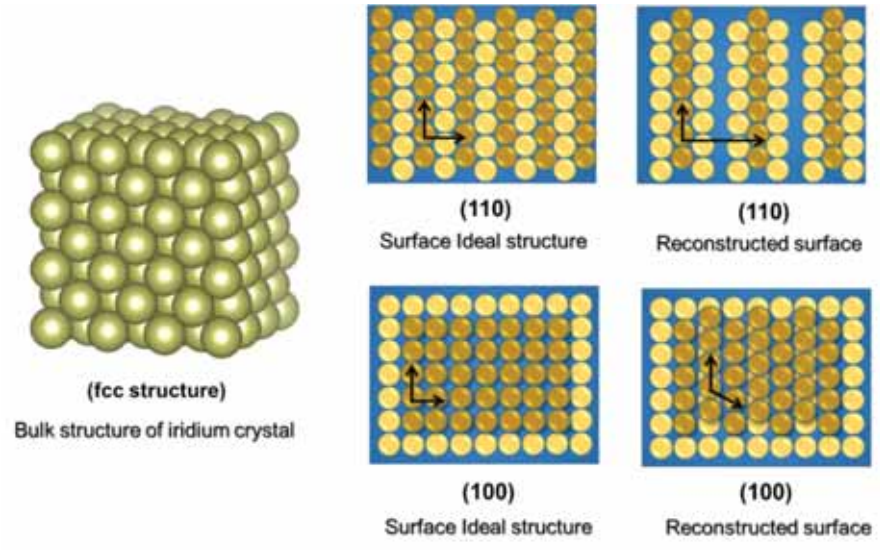

Figure 9. Reconstruction of Ir (110) and (100) surfaces.

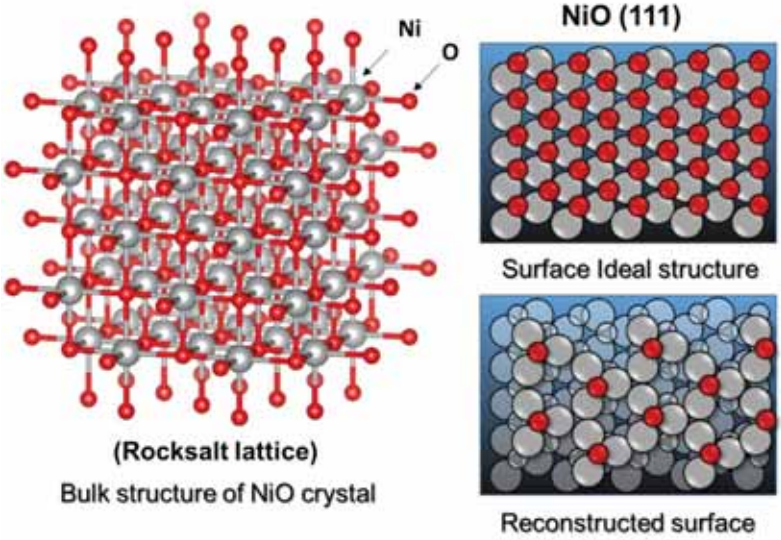

Figure 10. Reconstruction of NiO (111) surface, first transparent and second coloured layer

Low Energy Electron Diffraction (LEED)

Low Energy Electron Diffraction (LEED) is the surface analogue of the X-ray diffraction technique. As the name indicates, the major difference is that electrons are used instead of X-rays. The LEED techniques provides direct information on the surface structure and its basic principle is summarized in the following figure:

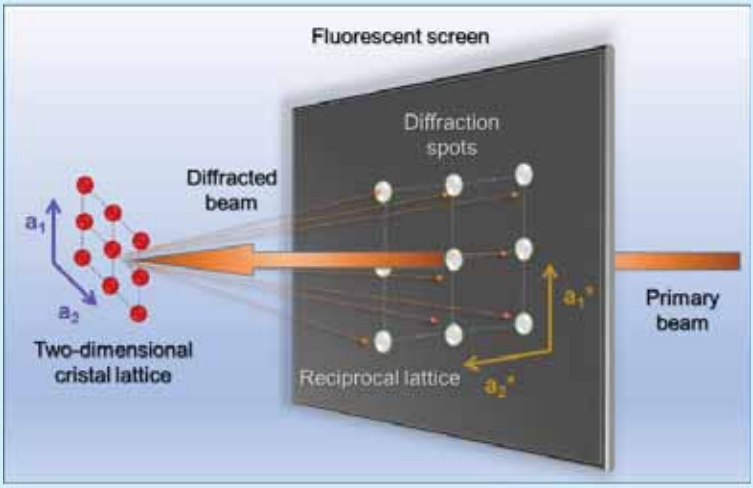

A primary electron beam is directed at the surface of a single crystal with unit cell having $\mathbf{a_1}$ and $\mathbf{a_2}$ vectors. A part of the incoming electrons is backscattered and, after removal of all inelastic backscattered electrons, the elastic backscattered electrons are post-accelerated towards a phosphorous screen where the LEED diffraction pattern is visualized. The LEED image thus obtained matches the reciprocal lattice described by vectors $\mathbf{a_1^*}$ and $\mathbf{a_2^*}$.

The single-crystal and the detection system are enclosed in an ultrahigh vacuum (UHV) chamber to assure a clean surface. In the last 50 years, LEED surface crystallography has successfully determined the precise location of atoms within the surface unit cell, the bond lengths and ordered adsorbed molecule orientations. More than 3000 surface structure LEED patterns are tabulated and classified on the basis of rotational symmetry of the substrate surfaces. These patterns are frequently characterized by an abbreviated notation of simple structures, known as Wood notation, in which the surface unit cell is expressed in terms of (*m* x *n*), where *m* and *n* are integer multiples of the translation vector $m\mathbf{a_1} + n\mathbf{a_2}$.

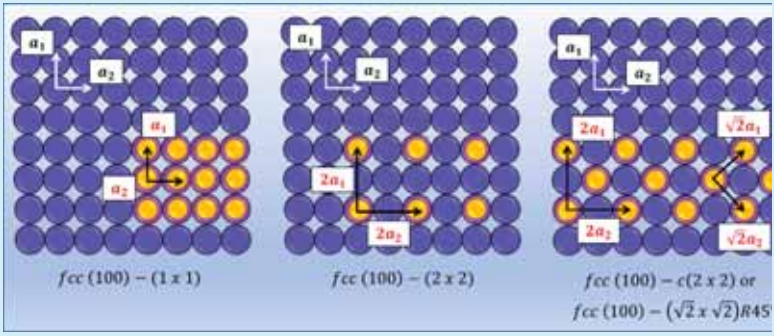

The Wood notation is adequate for simple geometries and very useful for describing the surface structure of chemisorbed adatoms and molecules. However, it is not easily applicable if the surface structure is rotated with respect to the bulk unit cell. The 2 x 2 matrix notation used above expresses how vectors $\mathbf{a_1}$ and $\mathbf{a_2}$ of the substrate unit cell transform into the vectors of the overlayer.

Other surface oxides, such as α-Al_2O_3 (0001), Cr_2O_3 (0001), Fe_2O_3 (0001) and V_2O_3 (0001), are also very polar surfaces with strong relaxations affecting several surface layers. These surfaces are characteristic of bulk corundum structures and exhibit relatively strong relaxations similar to the polar (111) rocksalt type surfaces. As the (0001) surface terminates either in an oxygen or metal layer, the polar surface can present a diverging surface potential. But if terminated with a half metal layer a charge-neutralized polar surface results.

Adsorbate-induced surface restructuring

The adsorption of adatoms or molecules on crystal surfaces usually induces new surface restructuring over a wide range of temperature and surface coverages. Depending on the type of adsorption, physi- or chemisorption, an important distinction is made between adsorbate-adsorbate and adsorbate-substrate interaction. During chemisorption strong chemical bonding is formed between adsorbate and substrate atoms and induces restructuring in the topmost surface layer where atoms near the chemisorption site are moved or rotated by the adsorbed species. The most common surface sites for chemisorption can be classified as bridge sites, top-sites, and hollow sites (three- and fourfold), *Figure 11*. The number of available sites on a surface depends on its geometry and the unit-cell lattice parameters. During physisorption, at suitably low temperatures, the adsorbate-adsorbate interaction predominates over adsorbate-substrate interactions. This type of interaction is governed by van der Waals forces and can be attractive or repulsive. If the interaction between adsorbate molecules is attractive, the adsorbate tend to form islands that grow with the coverage. By contrast, the repulsive interaction leads to a random coverage until relatively significant coverage provokes a close-packing of the adsorbate molecules on the surface. In this situation, the overlayer and the substrate can behave as independent lattices. In fact, the adsorbed phase can present more-or-less closely packed structures, and new classes of fluid or liquid-phases have been detected for physisorbed gases on solid substrates.

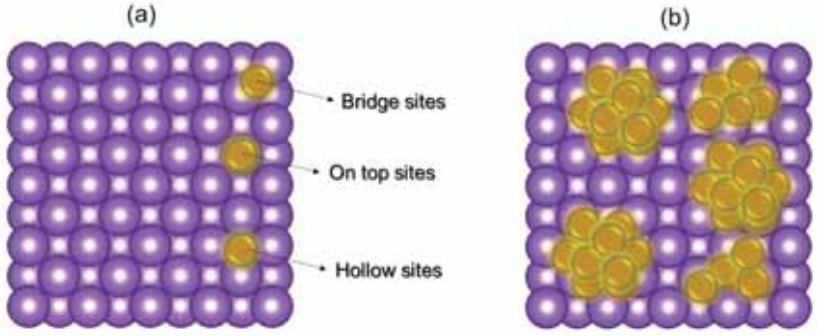

Figure 11 (a) Different types of adsorption sites on the surface during chemisorption, and (b) formation of islands of molecules during physisorption

Adsorbate-induced restructuring has been widely studied in the case of chemisorbed oxygen, sulphur and carbon adatoms. The localization of

different adatoms and their rearrangement have been established in numerous studies (*Figure 12*). For example, the adsorption of ¼ of a monolayer of carbon atoms on Ni (100) induces the restructuration of the topmost layer of Ni atoms in such a manner that four Ni atoms surrounding each carbon atom are rotated with respect to their underlying layers. The energetic cost of rearrangement of surface nickel atoms is compensated by the higher bonding energy of the carbon atoms chemisorbed on nickel, and the total energy decreases. In another example, sulphur atoms are chemisorbed on closely packed Fe (100) surfaces creating restructuration in which the formation of four strong Fe-S bonds weakens the nearest Fe-Fe bonds. On both examples, the adatoms are preferentially located on sites of high coordination. However, these atoms can also penetrate within and even below the first layer. For instance, on the Cu (110) surface, oxygen is coplanar with the surface metal atoms and could be represented as a single layer Cu-O surface compound.

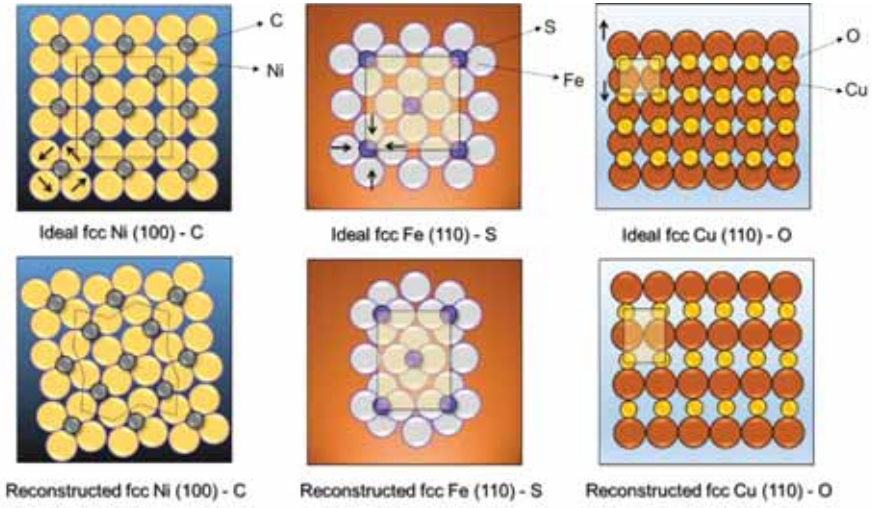

Figure 12. Carbon, sulphur and oxygen chemisorption induced restructuring of Ni (100), Fe (110) and Cu (110) surfaces.

The adsorption of metallic adsorbates on metal substrates has been extensively studied and these systems present many interesting catalytic properties. When the atomic sizes of the adsorbed and substrate metal atoms are close, a single-monolayer is formed in which adsorbate atoms occupy the unit cell of the substrate. This effect, commonly known as *epitaxial growth*, and the substrate orders the orientation and the lattice parameter of

the adsorbed crystal structure. The epitaxial growth provokes a change in the lattice constant accompanied by dislocations occurring within the interface layers. Therefore, metal adsorbates frequently form multilayers or three-dimensional crystallites over the metal substrate. A good example of epitaxial growth is given by the adsorption of Pd over Ag (100) substrate. Since Ag and Pd have similar atomic sizes and the same bulk *fcc* structure, Pd grows epitaxially on Ag (100) substrate, expanding its interatomic spacing by 5.1% over the substrate surface. In a suitable combination of metals, alloy formation is also possible and frequently observed at higher temperatures. During alloy formation, components with lower surface free energy segregate at the surface thus enriching the surface composition with respect to the bulk composition. Based on sublimation enthalpy data on metals, surface enrichment may be qualitatively predicted, *Figure 13*. For example, the sublimation energy of Zn is lower than that of Cu and consequently the surface of a CuZn alloy under vacuum conditions will be enriched in Zn, and similarly a PtCu alloy will be enriched in Cu. This thermodynamic prediction is directly associated with the cohesive energy of transition metals and its contribution is related to the electrons occupying the spatially extended *d*-valence atomic orbitals. These electrons play a key role in the formation of disordered alloys and directly contribute to the cohesive atom-bonding forces on the alloy surface.

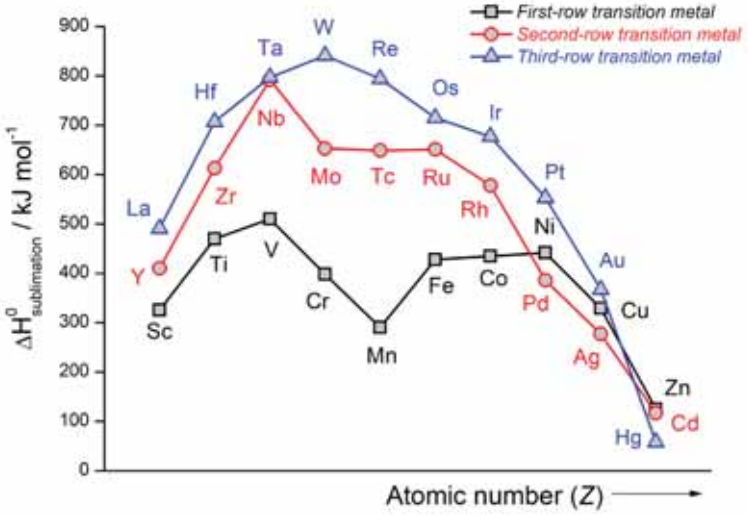

Figure 13. Variation of the sublimation enthalpy of metals in the first-, second- and third-row transition metals.

Another possibility is minority atom dissolution in the bulk forming a homogenous solid solution. An interesting example of surface alloy formation is found for the adsorption of aluminium on Ni (100) surfaces; in this case, surface alloy with Ni_3Al stoichiometry is formed and retains the bulk ordering at the surface. The overlayer exhibits the periodicity expected for the alternating bulk stacking of 50-50 mixed Ni-Al layers and pure Ni layers.

Problem II *The adsorption of gold occurs preferentially on the defect sites of Ru (0001) surface. Explain briefly this observation.*

As shown in *Figure 13*, Au has lower sublimation enthalpy than Ru. Thermodynamics, therefore, predicts that the Au-Ru alloy surface will be enriched in Au and the Au atoms will cover the unfavourable kink and step positions of the Ru (0001) surface. The diffusion of gold atoms in Ru bulk is thermodynamically unstable.

The structure of metal surfaces undergoes profound modifications when covered with a close monolayer of small chemisorbed molecules. For instance, CO adsorption provokes a rich variety of restructured surfaces. In general, the adsorption sites for CO depend on the nature, crystallographic orientations and CO coverage of the metal. At low coverages, CO occupies the bridge sites on Ni (111) surface and the threefold hollow sites on Pd (111). Meanwhile, the top sites are preferably occupied on Rh (111). At higher CO coverages, the repulsive adsorbate-adsorbate interactions force the adsorption of CO molecules in unusual sites of lower symmetry in order to maximize the intermolecular distance of adsorbed molecules. In the majority of metal surfaces the massive restructuring provoked by CO is reversible, and the surface is recovered after heating in vacuum.

Ethylene is another molecule commonly used as adsorbate to investigate adsorption-induced restructuring phenomena on metallic surfaces. However, in this case the chemisorption of ethylene is an irreversible process. When the surface is heated, the adsorbed ethylene is decomposed into hydrogen and carbon fragments which partially cover the surface. The typical example is the adsorption of ethylene on the Rh (111) surface illustrated in *Figure 14*. At low temperature (77 K), ethylene is adsorbed on Rh (111) through π-type interaction following Dewar-Chatt-Duncanson model. Accordingly, electron donation from ethylene π orbitals to the empty *d* states on the metal surface occurs as well as back-donation of electronic density from the occupied metal *d* band into the empty antibonding π^*-type

orbital. When we increase the temperature of a Rh (111) surface the adsorbed ethylene transforms to ethylidyne species and the surface metal atoms are moved on a three-fold hollow site. Two different three-fold hollow sites are available: the close packed hexagonal (*hcp*) and face-centred cubic (*fcc*). The latter does not present an atom in the downmost layer and ethylydine is only adsorbed on *hcp* hollow sites on Rh (111) surface. Therefore, ethylene adsorption produces ethylydine strongly chemisorbed on *hcp* hollow sites, thus restructuring the metal surface. Ethylydyne species decompose at temperatures over 450 K and polymeric chains with general formula C_xH are formed. Further increasing the temperature causes concurrent polymerization and dehydrogenation resulting in a graphitic monolayer.

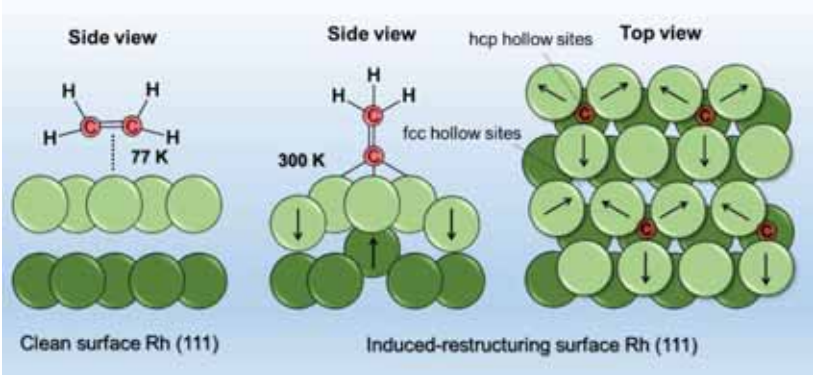

Figure 14. Ethylydine formation as result of ethylene chemisorption-induced restructuring of the Rh (111)

Problem III *Pyridine can be adsorbed on several metal surfaces and can modify its spatial orientation as a function of coverage and temperature. Its adsorption depends on the nature and structure of the metal substrate. Describe the fundamental aspects regarding bonding and pyridine orientation and provide the reasons for the different bonding geometries.*

The bonding or coordination of pyridine to metal surfaces can involve a π-aromatic ring or can otherwise occur through the lone pair of electrons on the nitrogen atom, as illustrated below:

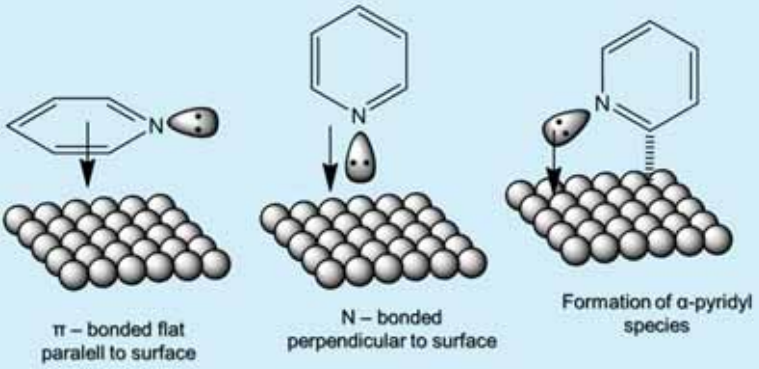

The transition between one or another type of interaction depends on pyridine coverage and temperature and it has been observed in Pt (110), Ni (100), Ag (111) and Pd (111) surfaces. A more specific form of interaction has been observed on Ni (100) and Pt (111) where the bonding species is α-pyridyl obtained after α-hydrogen abstraction in pyridine and formation of C-Me bond.

Dynamic surface restructuring during catalytic reactions

During the surface reaction the chemisorbed reactants induce surface restructuration, because the adsorbate-substrate bonds are energetically of the same magnitude as the strengths of the substrate-substrate bonds. Reconstructed surfaces constitute the most thermodynamically stable surface compositions and structures in equilibrium with the environment as long as the reconstruction kinetics is fast enough. This dynamic

adatoms or produce more active surfaces on which particular elementary steps are favoured. In these circumstances, the study of surface catalytic reactions should include the prediction of the restructuring phenomena that will take place under working conditions. Theoretical analysis of the surface reconstruction dynamics using first principle calculations and the application of *in situ* characterization techniques on model catalysts under working conditions are important for predicting and confirming this phenomenon.

An example is the use of metal oxides as catalysts for selective oxidation reactions where a disordered overlayer is created at the surface under reaction conditions and acts as active phase. Another interesting example is the dynamic surface reconstruction found for propene hydroformylation reaction over Rh single atoms supported on a CoO surface. During the reaction, propene adsorbs weakly on Rh/CoO surface, but adsorption significantly increases in the presence of H_2 and CO. Theoretical calculations suggest that the position of Rh single atoms does not change during the adsorption of CO, H_2 or propene separately, but Rh single atoms deviate from their lattice point after the co-adsorption of H_2 and CO on Rh/CoO surface. The displacement of Rh atoms promotes the adsorption and activation of propene. Another example of surface restructuring is found for the high-temperature Otswald process, in which ammonia is oxidized at temperatures above 1000 K on Pt/Rh gauze. Restructuring of this catalyst takes place in two stages with initial formation of parallel facets that grow to microscopic crystallites in the second stage.

Surface reconstruction is inherent in the reaction environment and involves formation of surface compounds. The state of the surface can change from metallic to oxide, sulphide, carbide or other alloys depending on the reaction environment. Thermodynamics dictates all changes occurring on the surface. For instance, the oxidation of CO over Ru surfaces can readily lead to the formation of RuO_2 surfaces; transition metals can transform to sulphides in desulphurization reactions, and iron catalyst surfaces can convert to Fe_3C phase during the Fischer-Tropsch reaction. Another illustrative example is found during the ethylene epoxidation reaction catalysed by Ag single-atoms. At low levels of O-surface coverage, the selectivity to epoxide is low and the reaction predominantly leads to acetaldehyde formation, subsequently oxidized to CO_2 and H_2O. Nevertheless, when the surface concentration of oxygen adsorbed species increases, the Ag_2O phases appear, and selectivity to epoxide significantly increases.

One way to study the compositional surface changes and surface enrichment that occur in alloys during chemical reaction is to measure the surface composition changes associated with the change of adsorbate coverage by *in situ* near-ambient pressure X-ray photoelectron spectroscopy (NAP-XPS). For instance, the chemical reaction $2H_2 + O_2 \rightarrow H_2O$ was selected as a model to study the changes produced on the surface of a $Pt_{50}Rh_{50}(100)$ alloy. A continuous atom exchange in the first subsurface layers and an unexpected Pt surface enrichment was found under slightly oxidizing conditions, as opposed to the observations in a highly oxidizing atmosphere. The evolution of the surface composition was assigned to a combination of single adsorbate-induced segregation processes and to adsorbates-surface interactions in the presence of short-lived reactive intermediate species.

Finally, it should be mentioned that adsorbate-induced restructuring can also occur over longer time scales (hours), necessary when atoms must diffuse along the surface. In this situation, the surface-induced restructuring can be considered as the initial step of a solid-state reaction kinetically controlled by diffusion.

Surface defects and reactivity

Surface defects or irregularities such as atomic steps and kinks are very effective sites for adsorbates chemical bonds breaking. The thermodynamic driving force for molecular dissociation is superior at the defect sites, due to their better bond-cleavage activity. Moreover, the population of surface defects increases under reaction conditions, due to the structural modification of surface atomic arrangements. It is therefore fundamental to investigate the role of the defects and correlate their properties to catalyst reactivity.

Of particular interest is the study of extended defects formation during the fast oxygen diffusion and exchange typical for “redox” type metal oxides. It is well-known that a slight reduction of certain oxides such as CeO_2, TiO_2, V_2O_5, MoO_3 or WO_3, leads to lattice oxygen loss, oxygen vacancies generation and non-stoichiometric oxide formation. These materials are commonly used in many selective oxidation reactions and the presence of oxygen vacancies have a deep effect on their catalytic behaviour. For instance, MoO_3 based catalysts are extensively employed for partial oxidation of alkenes. The α-MoO_3 is the most common polymorph of molybdenum oxide presenting an orthorhombic unit cell with a *Pbnm* spatial group in which distorted MoO_6 octahedra are ordered in bilayers with Van der Waals interactions maintaining the layers tightly packed (*Figure*

15). As discussed in the previous chapter, the partial reduction of α-MoO_3 at moderate temperatures induces the formation of *crystallographic shear* (CS). These planes form arrays with regular spacings and the metal ions in each shear plane retain their original octahedral coordination; the excess metal is compensated by the change from corner- to edge-sharing octahedral environment. These structures have been extensively studied since their discovery by A. Magnéli in 1953 and are known as *Magnéli phases* with general formula Mo_nO_{3n-1}. In *Figure 15*, the unit cell lattices of some intermediate Magnéli phases usually detected during the reduction of MoO_3 are drawn. All molybdenum substoichiometric oxides contain CS planes, i.e., $Mo_{18}O_{52}$, Mo_8O_{23} and Mo_4O_{11}, but an important difference exists between them. While the $Mo_{18}O_{52}$ structure can be derived directly from the α-MoO_3 structure, Mo_8O_{23} and Mo_4O_{11} structures result from the perfect cubic ReO_3 type structure consisting of vertex-sharing [MoO_6] octahedra.

The formation of these extended crystallographic shear (CS) planes and resulting structural sites with altered cation coordination are thought to be the main active sites for fast oxygen exchange. An illustrative example of assumption is found in the work reported by Ressler and co-workers in 2002 on selective oxidation of propene to acrolein using MoO_3 heterogeneous catalyst. Typically, this oxidation process proceeds via the *Mars–Van Kreevelen* mechanism, that involves activation of the organic molecule and the subsequent insertion of either surface oxygen atoms or lattice oxygen into a surface propene intermediate. Finally, the oxygen is replenished by the dissociation of O_2 molecules on the surface thus closing the catalytic redox cycle. The redox mechanism on MoO_3 involves the following fundamental steps: (i) generation of oxygen vacancies at the (100) or (001) facets by reaction with propene; (ii) diffusion of vacancies in bulk MoO_3; and (iii) formation of substoichiometric Magnéli phases like $Mo_{18}O_{52}$-type shear structure in the lattice. Depending on the reaction temperature, three possibilities can be distinguished: (i) temperatures below 600 K at which the participation of oxygen from the bulk MoO_3 is negligible; (ii) temperatures in the 600 – 700 K range where oxygen vacancy diffusion is sufficient to achieve a redox mechanism resulting in partially reduced MoO_3 under reaction conditions; and (iii) temperatures above 700 K, at which sufficiently fast diffusion of the lattice oxygen and rapid formation and annihilation of crystallographic-shear planes permits the participation of considerable amounts of lattice oxygen. Apparently, the latter regime is the most adequate for achieving a redox mechanism and ensuring complete reoxidation of the catalyst with oxygen from the gas phase to close the catalytic cycle. This example clearly illustrates the positive correlation between defect density and the catalytic activity of the material.

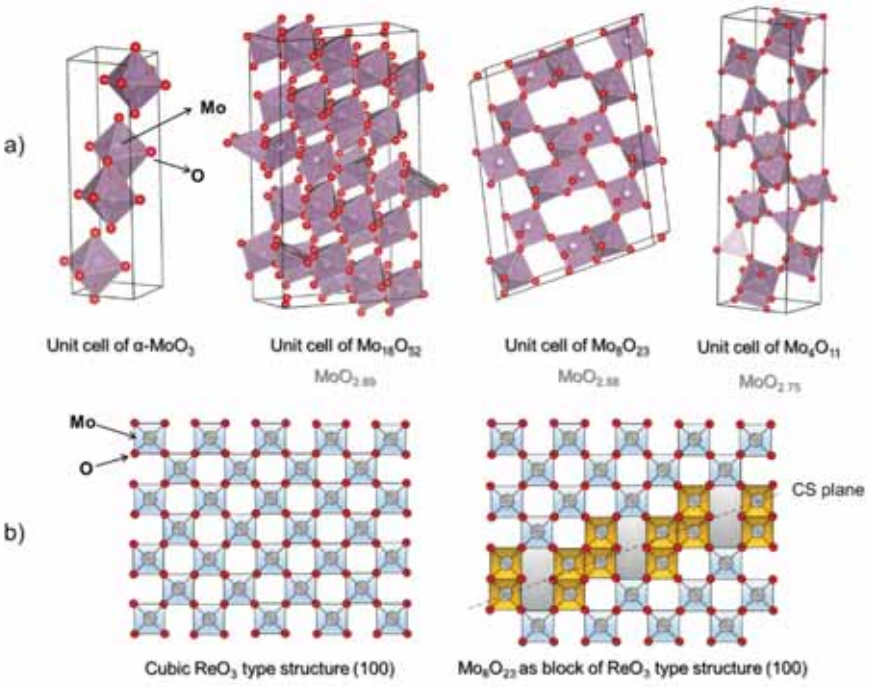

Figure 15 a) Crystal structures of orthorhombic α-MoO_3 and three characteristic substoichiometric Magnéli phases $Mo_{18}O_{52}$, Mo_8O_{23} and Mo_4O_{11}. b) Cubic ReO_3 type structure projected in (100) and (100) projection of Mo_8O_{23} structure showing ReO_3 type blocks and the formation of crystallographic shear (CS) planes

Structure-sensitivity of surface catalytic reactions

The term structure-sensitivity was first suggested to indicate the dependence of the reaction rate on metal catalyst particle size. A catalysed surface reaction is defined as *structure-sensitive* if the reaction rate varies noticeably with the change of particle size. The structure of the surface is dependent on particle size; the smaller the particle, the higher the proportion of edge and corner atoms, and the higher the exposure of high-energy faces, the greater will be their influence on the reaction rate. On the contrary, the reaction on a particular catalyst is defined as *structure-insensitive*, if the reaction rate is not influenced appreciably by particle size variation nor affected by the relative concentration of atoms in steps, kinks, and terraces.

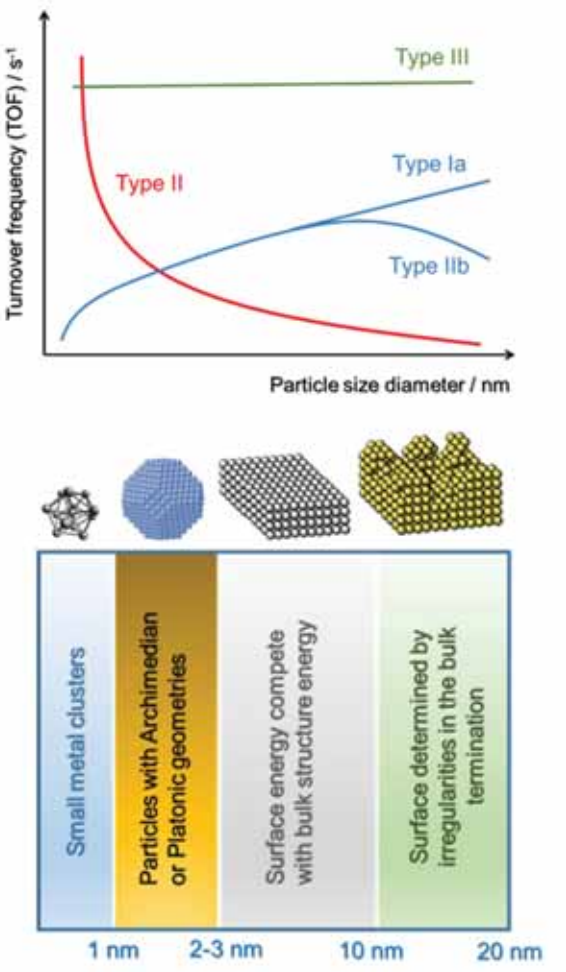

Figure 16 Schematic representation of the particle size length scale (left), and the three different types of observed structure-sensitivity.

Different length scales for metal particles can be discerned (*Figure 16*). The first corresponds to metal clusters of dimensions less than 1 nm, and in this case internal and external atoms cannot be differentiated. These small metal clusters are structurally reformed in contact with adsorbing molecules, and typically react as molecular catalysts. Their reactivity is directly related to

their orbital structure, which depends on the number of atoms. The second particle size length scale extends to a size range between 1 and 3 nm, in which the number of surface atoms is greater than the number of bulk atoms. The shape of these particles is often close to an ideal Platonian geometry—regular polyhedra, or Archimedian bodies built from different regular polyhedra. When the particle size falls into the 3 to 10 nm range, the number of surface atoms decreases in respect of the bulk atoms, and surface energy competes with bulk structure energy. In this situation, the bulk atoms rarely present structures similar to the corresponding most stable structure, and the relative stability of different surface geometries competes with the bulk structure energy. Finally, for particles sizes in the 10 to 20 nm domain, the number of bulk atoms is considerably superior to that of the surface atoms and irregularities such as corners, edge-sites, kinks, and step-sites are formed on the surface. These uncoordinated sites are expected to present different tendencies when engaging in chemical reactions. As a consequence, these sites are the main contributors to the structure-sensitivity of surface reactions and can be used to explain the particle size dependency observed in heterogeneous catalysis.

Three classes of structure-sensitivity can be distinguished on the base of reaction rate variation with particle size (*Figure 16*). An increase (*type I*), decrease (*type II*), or no effect on the reaction rates of a given catalytic reaction (*type III*) with the particles size could be observed. In 2009, Rutger A. van Santen formulated a molecular theory to explain the three classes of structure-sensitivity, based on theoretical calculations of the activation energies on the transition metal surfaces at each elementary reaction step. The reactions that involve cleavage or formation of molecular π-bonds, as in CO or N_2, must be distinguished from reactions that include σ-bonds activation, such as CH bonds in methane. *"Type I"* reactions take place when the rate limiting step involves formation or dissociation of π type bond. The reaction rate may uniformly increase (*type Ia*) as a function of increasing particle size or may present a maximum (*type Ib*). The prototype reaction for this class is the dissociation of CO or N_2 molecules. The activation of π type bonds requires step-edge sites, geometrically impossible below a certain particle size and the relative probability of such sites presents a maximum. The Fischer-Tropsch synthesis, in which CO is hydrogenated to form long hydrocarbon chains, presents the *"type I"* behaviour. The activation of σ-type bonds enters the prototype class *"type-II"* for which a uniform decrease of turnover frequency with increasing particle size is observed. Dissociative adsorption with C-H chemical bond cleavage is strongly affected by the presence of surface atoms at particle' edges and the relative number of this coordinatively unsaturated edge and

corner atoms decrease with the increase in particle size. On the contrary, the hydrogenation reaction of surface adsorbed alkyl species is independent of particle size variations, and corresponds to a class *"type-III"* reaction. The rate-limiting step for these *"type-III"* reactions is the recombination of an adsorbed H atom with surface alkyl intermediate to form σ-type bond.

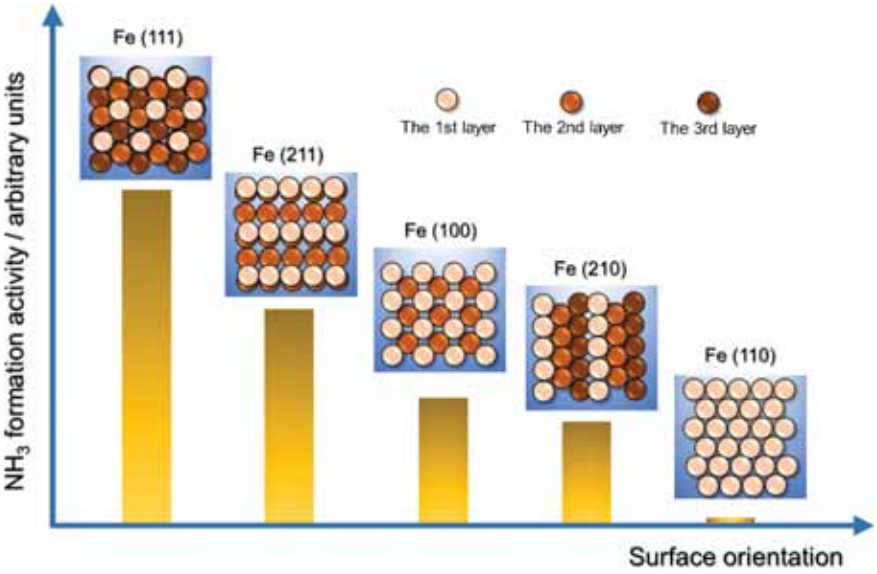

Figure 17 Ammonia formation rates over five idealized iron surface structures (111), (211), (100), (210), and (110); representative example of a structure-sensitive reaction. Reaction conditions: 400 ºC, 20 bar, and 3:1 H_2:N_2 molar ratio

A classical example of structure-sensitive reaction is ammonia synthesis from N_2 and H_2 on Fe single-crystal surfaces. The rates of ammonia formation depend on the crystallographic plane orientations. Fe (111) and Fe (211) surfaces present superior activity in NH_3 synthesis, followed by Fe (100), Fe (210) and Fe (110) crystal surfaces (*Figure 17*). There are two possible reasons for the different reaction rates. Fe (111) and Fe (211) faces demonstrate an exceptionally high surface roughness in which the second- and third-sublayer atoms are exposed to the reactants. In contrast, only the first layer of atoms is accessible to the reactants on the Fe (110) surface. Moreover, the Fe (111) and Fe (211) surfaces present unique active sites not present in the other planes. Indeed, Falikov and Somorjai, demonstrated that Fe (111) and Fe (211) are the only crystallographic orientations that expose 7-fold Fe sites and suggested that these are the most active sites for ammonia

synthesis on iron-single crystals. Moreover, the major concentration of Fe (111) explains the higher activity registered for this crystallographic orientation.

Examples of structure-insensitive reactions are the hydrogenation of cyclohexene over Pt surfaces, the methanation of CO over Rh and, especially, the hydrogenation of ethylene over a wide range of Pt-based catalysts. This reaction occurs through consecutive surface-catalysed additions of H atoms via the *Horiuti-Polaty* mechanism, and their classification as structure-insensitive is based on the complete absence of reaction-rate dependence with Pt crystal orientations. Studies of this system suggest that the formation of ethylidyne during the reaction leads to metal surface saturation, thus masking the participation of the different crystallographic orientations into the reaction.

Structure-sensitivity is also dependent on reaction conditions and the rate-determining step can change due to the variations of the amount and/or type of surface species. For instance, the oxidation of carbon monoxide by oxygen can be catalysed by several transition metals, and is either structure-sensitive or insensitive, depending on the reaction conditions, elegantly demonstrated by Engel and Ertl in 1978 over Pt single crystals.

A range of possible elementary steps involved in CO oxidation can be summarized as follows:

Step 1: $O_2\,(g) \rightarrow 2O_{ads}$
Step 2: $CO\,(g) \leftrightarrow CO_{ads}$
Step 3a: $O_{ads} + CO_{ads} \rightarrow CO_2\,(g)$
Step 3b: $O_{ads} + CO(g) \rightarrow CO_2\,(g)$
Step 3c: $O_2 + 2CO_{ads} \rightarrow 2CO_2\,(g)$

The kinetic results show that CO oxidation reactions occur through *step 3a*, *i.e.* via the *Langmuir-Hinshelwood* mechanism in which both reactants are adsorbed. Besides, *step 3b* and *step 3c* (*Eley-Rideal* mechanism) are not possible. At high pressures of molecular oxygen, the dissociative adsorption of oxygen on the surface is in equilibrium and the rate-determining step for the reaction is given by *step 3a*. The fact that the reaction rate increases with particle size suggests that oxygen atoms adsorbed on terraces or flat surfaces should react faster with carbon monoxide than the oxygen atoms adsorbed on steps and kinks. This observation indicates that CO oxidation is a structure-sensitive reaction at high partial pressures of O_2, which has been experimentally confirmed using kinked Pt single-crystals. However, at high

CO pressures, the surface is almost completely saturated, and the dissociation of oxygen on the surface becomes the rate-determining step, inhibited by the presence of high coverages of CO on the surface. In this situation, the reaction is structure-insensitive, as was experimentally evidenced using Pd single crystals.

Problem IV. *The formation of methane from syngas is a structure-insensitive reaction while the reverse reaction, steam reforming, is structure-sensitive. Is it true?*

The ratio of the forward and reverse reaction depends on thermodynamic constant and temperature, but not on the catalyst. As a consequence, if the rate of the forward reaction changes with the metal surface metal the rate of the backward reaction should change accordingly. Therefore, both reactions, whether structure-sensitive or structure-insensitive, must proceed in identical ways. So the above statement is contradictory and false.

Surface-structure selectivity

As explained in the previous chapter, one of the most relevant parameters for efficient catalysts design is selectivity control. Our knowledge regarding the effect of surface properties on reaction selectivity is much poorer than that on reaction rate and turnover frequency. Again, the development of surface-science techniques over past decades has facilitated detailed study of the molecular factors that controls the selectivity.

The reactions of *n*-hexane and *n*-heptane aromatization to benzene and toluene on Pt single crystals are the classic examples for introducing selectivity dependence on crystal orientation facets. These reactions can proceed at least via four reaction routes to form either aromatic, or cyclic, or branched isomers or to undergo C–C bond breaking leading to hydrogenolysis. It has been demonstrated that the Pt (111) surface with a hexagonal atomic arrangement is several times more active and selective to aromatic compounds than the Pt (100) surface with square unit cells. This behaviour can be explained by considering that the aromatization reaction rates increase with the greater concentration of irregularities (steps and kinks) on a hexagonal Pt surface with respect to a Pt square one. Moreover, the composition of an alloy can notably affect product selectivity and resistance to poisoning. The conversion of *n*-hexane in the presence of

hydrogen over Au-Pt (100) and Au-Pt (111) alloy systems decreases linearly with the addition of gold atoms on Pt (100), while it markedly increases with the addition of gold on a Pt (111) surface. A twofold increase in the isomerization reaction and an exponential decay in hydrogenolysis and aromatization reaction rates are responsible for the observed effect on Au-Pt (111) alloy selectivity. The formation of alloys leads to the creation of new sites and selectivity change in consequence.

Fischer-Tropsch synthesis is another interesting example that clearly illustrates the importance of edge and kink sites in the control of selectivity. The activation of CO is one of the crucial steps that controls this reaction, and it is well established that CO can dissociate to form surface carbon and oxygen species. The surface carbon is subsequently hydrogenated to form -CH_x fragments which can react further with hydrogen to give methane or to couple with other -CH_x fragments for larger chain hydrocarbon products. CO bond activation can also proceed through interaction with the metal surface forming a metal-CO bond where CO hydrogenation subsequently forms oxygenated hydrocarbons such as formaldehyde or methanol. This path proceeds through the formation of surface formyl (-CHO) intermediates. Experimental evidence and calculations of the barrier energies involved in each elementary step demonstrate that both CO dissociation and CO insertion depend on the distribution of edge/kinks and terrace sites on catalyst surfaces. The factor that controls the selectivity is the steps-to-terrace ratio. The kink/steps sites provide the ability to separate the reaction fragments and favour bond-breaking and bond-forming reactions. Hence the rates of CO dissociation and CH_x fragment coupling significantly increase on the edge sites due to the decrease in the possibility of metal atom sharing. In contrast, CO adsorption and hydrogen addition forming formyl intermediates is energetically more favoured on terrace sites and the CO bond cleavage is the preferred path. In this case, the weak metal adsorbate bonds promote the formation of oxygenated compounds in an exothermic reaction, while the CO dissociation presents a fairly high activation barrier and is highly endothermic (*Figure 18*). It is clear that careful control of the relative distribution kink/edges versus terrace sites on the catalyst surface permits the optimization to higher chain hydrocarbons (paraffins and olefins).

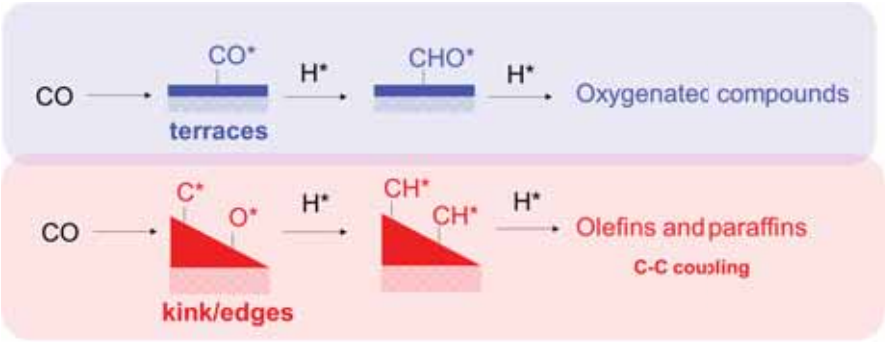

Figure 18 Schematic representation of the two possible paths for CO activation in Fischer-Tropsch synthesis

Problem V. *Is it possible to prove a non-dissociative chemisorption of CO for the production of methanol by a double isotopic labelling experiment using* $^{12}C^{16}O$ and $^{13}C^{16}O$*?*

When methanol is formed by non-dissociative chemisorption, only two methanol isotopes can be observed, $^{12}C^{16}O$ will produce $^{12}CH_3{}^{16}OH$ and $^{13}C^{18}O$ reacts $^{13}CH_3{}^{18}OH$ respectively. In dissociative chemisorption, $^{12}C^{16}O$ dissociates into $^{12}C + {}^{16}O$, and $^{13}C^{18}O$ splits into $^{13}C + {}^{18}O$. In this way, ^{12}C might combine with ^{18}O, and ^{13}C with ^{16}O during the formation of methanol, and four isotopes of methanol should be observed: $^{12}CH_3{}^{16}OH$, $^{12}CH_3{}^{18}OH$, $^{13}CH_3{}^{16}OH$ and $^{13}CH_3{}^{18}OH$. Therefore, a double isotopic labelling experiment can distinguish between dissociative and non-dissociative chemisorption of CO.

Considerable research efforts have been made to investigate the surface characteristics of oxides and many publications deal with such oxides as TiO_2, CeO_2, and α-Fe_2O_3, all of them with well-defined crystalline structures. However, what is much more difficult to understand is the structural effect of intrinsically complex undefined crystals such as γ-Al_2O_3 (defect-spinel or non-spinel structure). Recent advances in nanotechnology have facilitated the preparation of various Al_2O_3 molecules with different morphologies, and an increase in the rate of ethanol dehydration into ethylene was observed on the 100 facets of γ-Al_2O_3. It is clear that, by adjusting the preparation conditions, a desired selectivity towards a certain reaction can be obtained. Model single-crystals or alloyed single-crystals and metal oxides can be cut at various angles to expose surfaces containing different types of sites, at terraces, steps, or kinks. The relative distribution of these diverse surface sites determines the activity and selectivity of the catalyst.

support interactions. There is, therefore, a clear need to develop more complex models that may address all issues related to small nanoparticles and their interactions with the support.

The advances in catalysis science during the past four decades have resulted in two major breakthroughs: nanocatalyst design and *in situ* characterization techniques. Current chemical methods used for preparing metal nanoparticles dispersed on high-surface-area supports typically lead to monodisperse metal nanoparticles. This allows a fine tuning of metal nanoparticle size and shape and comprehensive study of the nanostructure-induced catalytic properties. On the other hand, the recent progress in *in situ* techniques provide a burgeoning opportunity to correlate the structure-reactivity relationship at atomic and molecular scales to the chemical nature of the active sites at nanometric level and to the role of the metal-support interface under realistic reaction conditions.

Metal-support interaction

The crystal morphology in vacuum conditions is determined by the *Wulff construction*; this postulates that the minimization of the total free surface energy of a crystal at constant volume and fixed temperature leads to the preferential orientation of certain crystal planes over others, defining an equilibrium crystal shape. The construction relies on the Wulff assumption that the distance from a specific surface plane to the centre of the crystal (h_i) is proportional to the surface energy (γ_i). Therefore, in a surface plane with small surface energy will present short distance to the centre and this plane will dominate the shape of polyhedron (*Figure 20*).

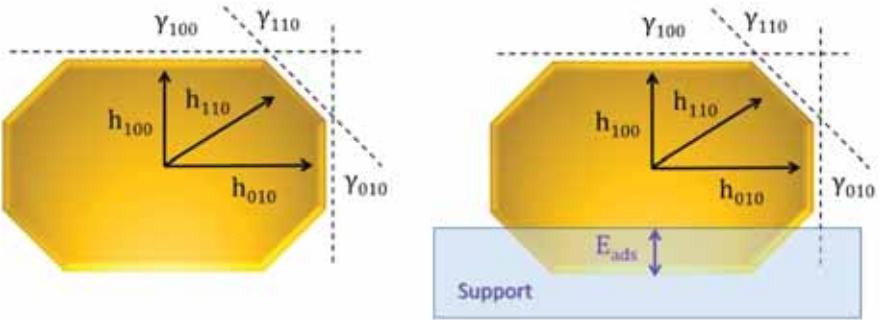

Figure 7.20 Illustration of the Wulff construction for a two-dimensional crystal (left), and of a truncated Wulff polyhedron on a support.

In supported catalysts, metal particles tend to minimize their free energy forming agglomerates. Nevertheless, the support usually hinders this sintering process and the equilibrium shape of the supported nanoparticle is usually a truncated Wulff polyhedron (*Figure 20*) described by the *Wulff–Kaischew theorem*. The adhesion energy (E_{ads}), also called interface energy, measures the bonding strength between the metal nanoparticle and the support, and plays a crucial role in determining the size/shape of the supported metal nanoparticle. The interface energy is difficult to measure, but can be estimated by quantifying the shape of the supported metal nanoparticles. For instance, the determination of equilibrium shape of small Pd nanoparticles dispersed on Al_2O_3 using high resolution transmission electron microscopy (HRTEM) has made it possible to calculate the interface energy as equal to 2.9 J m^{-2}.

The activity, selectivity and stability of a supported metal catalyst are also influenced by the physicochemical properties of the support. In general, three types of influence can be found: i) structural promotion; ii) electronic promotion; and iii) synergetic promotion. The structural promotion is related to the stabilization of the nanoparticles over the support surface. The electronic factor refers to the electron transfer between the metal and the support material influencing the energy barrier and resulting in a change of reaction rate for specific catalytic reactions. Synergetic promotion refers to energetic interaction between the support and the active metallic component, resulting in the formation of a new type of active entity in the interface region. The study of the effect of the support on catalytic performance of metal supported systems introduces the concept of *metal-support interaction*. The most common types of metal-support interactions are illustrated in *Figure 21*. When the metal-support interaction depends directly on interface energy, weak, medium and strong metal-support interaction can be found. The shape of the supported metal particle is determined by the surface energy of the contacting facet and by the facet/support surface interaction strength. If the adhesion energy between particle and support is small, the particle shape is not affected significantly by the substrate and the shape of the particle is described by the Wulff construction. On the other hand, if the metal particle interacts strongly with the support, particle dispersion can completely wet the support and a flattened-like shape can be observed. The strength of the interaction depends basically on the nature of the specific system components and pretreatment conditions.

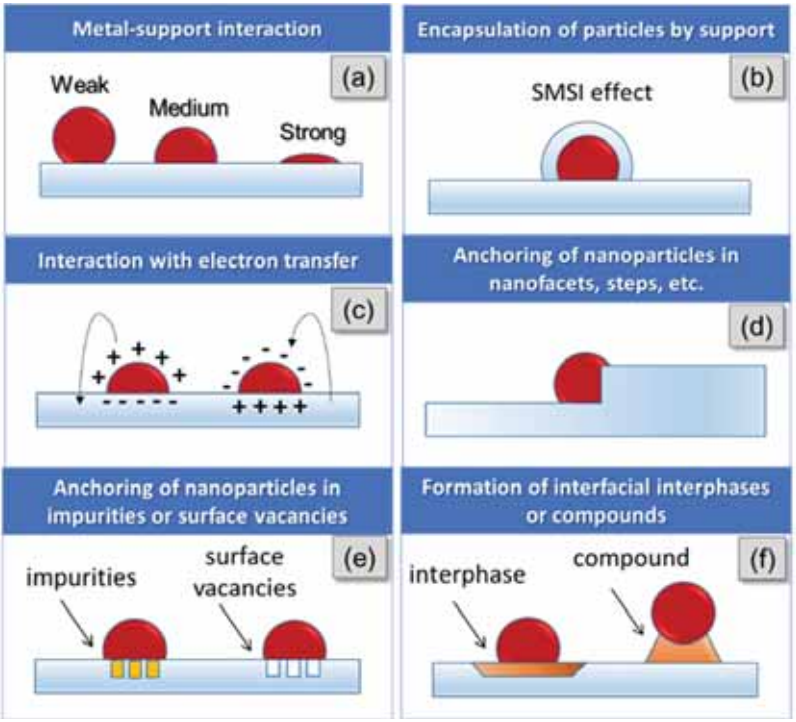

Figure 21. The most common types of metal-support interactions

When the nanoparticles are dispersed on reducible oxide supports such as TiO_2 or CeO_2, an enhancement of catalytic activity and selectivity is observed. This effect is commonly referred to as *strong metal-support interaction* (*SMSI*), a term introduced in 1978 by Tauster to describe the drastic changes observed in the chemisorption properties of group 8 metals supported on reducible oxides before and after a high-temperature reductive treatment in hydrogen. The definition of SMSI was later extended to all active metallic components and any support materials that present similar phenomena to that observed by Tauster. The explanation of this phenomenon is based on electronic effects and the electron transfer at the metal-support interface has been proposed as the origin of the SMSI effect. It was suspected that a Schottky-like barrier at the metal-support interface might be responsible for the formation of unique electronic interface structure. Early electron microscopy investigations of SMSI effect catalysts revealed the presence of new oxide species after reduction at elevated temperatures (*Figure 21 b*). An encapsulation model has been proposed to

explain the observed experimental data; the metallic component appears covered or encapsulated by the support material during the transition into the SMSI state.

The charge transfer between metal and support influences all elementary heterogeneous catalysis steps: adsorption, bond breaking and recombination, diffusion, and desorption (*Figure 21 c*). The role of the electronic transfer at the metal-oxide interface was first suggested by Schwab who introduced the donor-acceptor concept in heterogeneous catalysis. For instance, electron transfer to metal particles was used to explain the activity of Rh/TiO_2 catalysts in CO hydrogenation reaction, while electron transfer from Ru metal to the support was reported over many metal oxide support materials. The charge transfer between metal nanoparticles and support materials depends on the physicochemical properties of the support material.

Nanoparticles are thermodynamically unstable and tend to sinter when the diffusion barriers are overcome at high temperatures. As a consequence, one of the main causes of deactivation of supported metal catalysts is metal sintering. Avoidance of metal agglomeration makes it crucial to anchor the metal nanoparticles by using appropriate support materials or by altering their structure, morphology or composition. For instance, surface steps, kinks, nanoscale facets, or other types of surface modifications supply heterogeneous nucleation sites and hinder the movement of small nanoparticles (*Figure 21 c*), resulting in defect-free metal. Another mechanism for nanoparticle anchoring is the attraction provided by vacancies or impurity atoms on the surface (*Figure 21 d*). For example, oxygen vacancies in reducible metal oxide may provide sites for metal nanoparticle nucleation. Nanoparticles can be also anchored by other types of high-energy surface defects such as coordinatively unsaturated pentacoordinated Al^{3+} sites present on a γ-Al_2O_3 (100) surface, that attract and anchor Pt nanoparticles via special bonding mechanism. Other types of surface defects, such as colour centres (F-centres) can also anchor the deposited metal clusters. The strong anchoring effect of the F-centres is associated with the partial electron transfer from the F-centres to the adsorbed metal. Metals anchoring by surface defects may result in electron transfer that modifies the adsorption properties of the anchored metal, resulting in significant enhancement of their catalytic performances. For instance, charge transfer of MgO from F-centres to the supported gold nanoparticles was proposed as responsible for an important Co oxidation activity.

In the last case of metal-support interaction in *Figure 21 d* an interface reaction may take place and new phases may be formed as a consequence of chemical potential difference and intimate contact between the atoms of both metal and support. In practice, the migration of atoms depends on their kinetic behaviour. High temperature reduction, calcination or annealing are necessary to ensure interaction of metal particles with the support and formation of interface compounds. A typical example is found in Pt/CeO_2, where an intermetallic phase $PtCe_5$ is formed after reduction at 1073 K. The formation of Pt-Al alloys at the interface is also typical for Pt/Al_2O_3 catalysts when treated at high temperatures. In many cases, the formation of these compounds enhances the metal-support interaction, thus increasing sintering resistance; examples of this being the Ni/SiO_2, Fe/SiO_2 or Pd/Al_2O_3 systems.

Dynamic evolution of supported metal nanoparticles during catalytic reactions

One should be aware that surface energy depends on the presence of adsorbates and the morphology of the supported nanoparticles can be altered in a reaction environment. The dynamic behaviour of the supported metal nanoparticles is often related to the variations in surface energies caused by the reactive atmospheres at elevated temperatures, producing in turn variations in geometric shape and electronic properties.

Several review articles and book chapters comprehensively document and elegantly address the most important advances in characterization of heterogeneous catalysts under working conditions. In order to illustrate the dynamic behaviour of supported metal nanoparticles during catalytic reaction, we have selected an excellent piece of research reported in 2002 by the Haldor-Topsøe company in collaboration with Copenhagen University. This work proposes a study of the structural changes produced on Cu nanoparticles in model Cu/ZnO catalyst during activation pretreatment and in methanol synthesis reaction conditions. *In situ* transmission electron microscopy was used to obtain atom-resolved images of the dynamic behaviour of Cu nanoparticles (*Figure 22*). They found that the dynamic shape change of the Cu nanoparticles depends on the gas composition. In pure hydrogen (*Figure 22 A*), the majority of Cu particles appear in contact with the ZnO support through their (111) facet. The addition of water to the hydrogen gas results in more spherical Cu nanoparticles (*Figure 22 B*) with major (110) and (100) facets fraction. At the interface, however, the contact area between (111) planes of Cu and the

ZnO surface does not substantially alter, suggesting that the water adsorption on different Cu facets is the main driving force for gas-induced surface reconstructions and resulting reshaping of the Cu nanoparticles. In a reaction environment formed by H_2 and CO, the Cu nanoparticles are transformed into disc-like structures caused by the increase of the ZnO wetting. A high-resolution image (*Figure 22 C*) shows that Cu surface particles on ZnO are predominantly terminated by (111) and (100) facets with the Cu (111) facet parallel to the interface. In this case the interfacial area increases by about 50%, suggesting a large change in interface energy. This work clearly illustrates that the dynamic restructuring of the catalyst occurs under reaction conditions and the relevant active sites can be generated during the catalytic reaction.

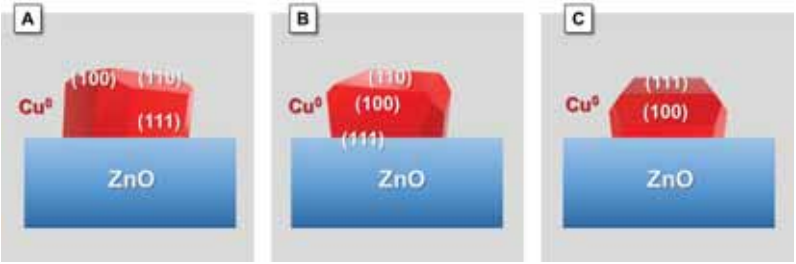

Figure 22. Wulff construction of the Cu nanocrystals on Cu/ZnO catalyst exposed in various gas environment. (**A**) At 220 ºC and pressure of 1.5 mbar of H_2. (**B**) At 220 ºC and total pressure of 1.5 mbar gas mixture of H_2 and water in H_2/H_2O = 3 molar ratio. (**C**) At 220 ºC and total pressure of 5 mbar in H_2 (95%) and CO (5%) in a gas mixture.

Used books and References

Beller M., Renken A. and van Santen R.A. *Catalysis – From Principles to Applications* (2012), Wiley-VCH

Chorkendorff, I. and Niemantsverdriet, J.W. *Concepts of Modern Catalysis and Kinetics* (2003), Wiley-VCH, 1st Edition

Ertl, G. *Reactions at solid surfaces* (2009), Wiley

Ertl, G., Knözinger, H., Schüth, F. and Weitkamp, J. *Handbook of Heterogeneous Catalysis* (2008), Wiley-VCH, 2nd Edition

Hagen, J. *Industrial Catalysis – A Practical Approach* (2006), Wiley-VCH, 2nd Edition

Henrich, V.E. and Cox, P.A. *The Surface Science of Metal Oxides* (1994), Cambridge University Press, Cambridge

Niemantsverdriet, J.W. *Spectroscopy in Catalysis – An introduction* (2007), Wiley-VCH 3rd Edition

Prims, R., Wang, A., and Li X. *Introduction to heterogeneous catalysis* (2016), Imperial College Press 1st Edition

Rothenberg, R. *Catalysis – Concepts and Green Applications* (2008), Wiley-VCH

Somorjai, G.A. and Li Y., *Introduction to surface chemistry and catalysis* (2010), John Wiley & Sons, 2nd Edition

van Santen, R.A. and Neurock, M. *Molecular Heterogeneous Catalysis – A Conceptual and Computational Approach* (2006), Wiley-VCH 1st Edition

K. Ann, G.A. Somorjai, *ChemCatChem* 4, 2012, 1512-1524

A. Baraldi, D. Giacomello, L. Rumiz, M. Moretuzzo, S. Lizzit, F. Buatier de Mongeot, G. Paolucci, G. Comelli, R. Rosei, B. E. Nieuwenhuys, U. Valbusa, M. P. Kiskinova, *J. Am. Chem. Soc.* 127, 2005, 5671-5674.

M. Cargnello,V. V. T. Doan-Nguyen, T. R. Gordon, R. E. Diaz, E. A. Stach, R. J. Gorte, P. Fornasiero, C.B. Murray, *Science* 341, 2013, 771-773.

A. S. Crampton, M. D. Rötzer, C. J. Ridge, F.F. Schweinberger, U. Heiz, B.Yoon, U. Landman *Nat. Commun.*7, 2015, 10389.

S. Chen, F. Xiong, W. Huang, *Surf. Sci. Rep.* 74, 2019, 100471.

Falicov, L. and Somorjai G.A. *Proc. Natl. Acad. Sci. USA* 82:2207 (1985)

H.J. Freund, H. Kuhlenbeck, T. Risse, *Chem. Phys. Solids Surf.* 9, 2001, 326-372.

P. Gai-Boyes, *Catal. Sci. Rev. Sci. Eng.* 34, 1992, 1-54.

W. Goodman, *Chem. Rev.* 95, 1996, 523-536.

P. L. Hansen, J. B. Wagner, S. Helveg, J. R. Rostrup-Nielsen, B. S. Clausen, H. Topsøe, *Science* 295, 2002, 2053-2055.

H. Knözinger, P. Ratnasamy *Catal. Sci. Rev. Sci. Eng.* 17, 1978, 31-70.

J. Lee, E.J. Jang, H.Y. Jeong, J.H. Kwak, *Appl. Catal. A Gen.* 556, 2018, 121-128.

J. Liu, *ChemCatChem* 3, 2011, 934-948.

H. Ohtani, C.T. Kao, M.A. van Hove, G.A. Somorjai, *Progr. Surf. Sci.* 23, 1986, 155-316.

T. Ressler, J. Wienold, R.E. Jentoft, T. Neisius , *J. Catal.* 210, 2002, 67-83.

S. Shauermann, H.J. Freund, *Acc. Chem. Res.* 48, 2015, 2775-2782.

G.A. Somorjai, J. Carrazza, *Ind. Eng. Chem. Fundam.* 25, 1986, 63-69.

G.A. Somorjai, *Surf. Sci.* 242, 1991, 481-488.

R.A. van Santen, *Acc. Chem. Res.* 42, 2009, 57-66.

L. Wang, W. Zhang, S. Wang, Z. Gao, Z. Luo, X. Wang, R. Zeng, A. Li, H. Li, M. Wang, X. Zheng, J. Zhu, W. Zhang, C. Ma, R. Si, J. Zeng *Nat. Commun.* 7, 2016, 14036.

J.M. White, C.T. Campbell, *J. Chem. Educ.* 57, 1980, 471-474.

R.C. Yeates, G.A. Somorjai *J. Catal.* 103, 1987, 208-212.

F. Zaera, *ACS Catal.* 7, 2017, 4947-4967.

Y. Zhou, C. Jin, Y. Li, W. Shen, *Nano Today* 20, 2018, 101-120.

APPENDIX I

Crystalline systems	Schönflies Symbols	International symbols			Inversion
		Full	Abbreviated	Directions	
Triclinic	C_1	1	1		none
	C_i	$\bar{1}$	$\bar{1}$		Centrosymmetric
Monoclinic	C_s	m	m		none
	C_2	2	2	[010] or [001]	none
	C_{2h}	2/m	2/m		Cent.
Orthorhombic	C_{2v}	2mm	2mm		none
	D_2	222	222	[100][010][001]	none
	D_{2h}	2/m 2/m 2/m	mmm		Cent.

Tetragonal	C_4	4	4		none.
	S_4	$\bar{4}$	4		none
	C_{4h}	4/m	4/m		Cent.
	D_{2d}	$\bar{4}$2m	$\bar{4}$2m	[001]{100}{110}	none
	C_{4v}	4mm	4mm		none
	D_4	422	422		none
	D_{4h}	4/m 2/m 2/m	4/mmm		Cent.
Trigonal	C3	3	3		none
	C3i				Cent.
	C3v	3m	3m	[001]{100}	none
	D3	32	32		none
	D3d				Cent.

Hexagonal	C6	6	6		none
	C3h				none
	C6h	6/m	6/m		Cent.
	D3h			[001]{100}[210]	none
	C6v	6mm	6mm		none
	D6	622	62		none
	D6h	6/m 2/m 2/m	6/mmm		none
Cubic	T	23	23		none
	Th	2/m 3	m3		Cent.
	Td			{100}{111}{110}	none
	O	432	432		none
	Oh	4/m 3 2/m	m3m		Cent.

APPENDIX II

METRIC TENSOR REDUCTION FOR SIX CRYSTALLINE SYSTEMS

$$\Gamma_{\mathbf{cubic}} = \begin{bmatrix} a^2 & 0 & 0 \\ 0 & a^2 & 0 \\ 0 & 0 & a^2 \end{bmatrix} \qquad \Gamma_{\mathbf{tetragonal}} = \begin{bmatrix} a^2 & 0 & 0 \\ 0 & a^2 & 0 \\ 0 & 0 & c^2 \end{bmatrix}$$

$$\Gamma_{\mathbf{orthorhombic}} = \begin{bmatrix} a^2 & 0 & 0 \\ 0 & b^2 & 0 \\ 0 & 0 & c^2 \end{bmatrix} \qquad \Gamma_{\mathbf{monoclinic}} = \begin{bmatrix} a^2 & 0 & abcos\beta \\ 0 & b^2 & 0 \\ cacos\beta & 0 & c^2 \end{bmatrix}$$

$$\Gamma_{\mathbf{rhombohedral}} = \begin{bmatrix} a^2 & a^2cos\alpha & a^2cos\alpha \\ a^2cos\alpha & a^2 & a^2cos\alpha \\ a^2cos\alpha & a^2cos\alpha & a^2 \end{bmatrix}$$

$$\Gamma_{\mathbf{hexagonal}} = \begin{bmatrix} a^2 & -\frac{a^2}{2} & 0 \\ -\frac{a^2}{2} & a^2 & 0 \\ 0 & 0 & c^2 \end{bmatrix}$$

APPENDIX III

COMMONLY USED X-RAY WAVELENGTHS, Å

Element	K_{α} (av.), Å	$K_{\alpha 1}$, Å	$K_{\alpha 2}$, Å	$K_{\beta 1}$, Å
Cr	2.29100	2.28970	2.29361	2.08487
Fe	1.93736	1.93604	1.93998	1.75661
Co	1.79026	1.78897	1.79285	1.62079
Cu	1.54184	1.54056	1.54439	1.39222
Mo	0.71073	0.70930	0.71359	0.63229

ADDITIONAL PROBLEMS AND QUESTIONS

1. Explain why tetragonal C lattice does not exist but monoclinic and orthorhombic C does.

2. What is the point group resulting from combination of:
   a) 3-fold and perpendicular 2-fold axis
   b) 4-fold axis and a mirror plane
   c) 6-fold and mirror plane perpendicular to it
   d) Two mirror planes oriented at 90º; 60º;45º;30º
   e) two 2-fold axis oriented at 60º

3. Specify the point group, Bravais lattice, crystal systems and translational elements, if any,

$Cmm2$ $P222_1$ $P4_12_12$ Pm $P6_3/mcm$ $P\bar{3}c1$ $P4_332$
$Ima2$ $P4$ $I4_1/amd$ $F\bar{4}3c$ $Im\bar{3}m$ $P4_2cm$ $Cccm$

4. Explain briefly to which crystalline system the point groups 4, 222, m3m and 6/mmm belong. Indicate the number of equivalent points for each group

5. AB_2X_4 compound crystalizes in *Pcc2* space group with lattice parameters a=6.17 Å b=13.87 Å and c=6.52 Å. Using its density 3.2 g/cm^3 and molecular weight 540 g/mol determine its crystal system and point group, elements of symmetry and coordinates of all general and special positions.

6. For a cubic crystal with lattice parameter of 4 Å and atoms A (1/2,1/2,1/2), B at (0,0,0), and O at (1/2,0,0), O; (0,1/2,0); (0,0,1/2) draw the cell projection (translations included) and determine compound unit cell and atom basis. Define number of coordination for A and B and calculate the A-O and B-O distance. If the A and B are different in size which of bigger? Determine the compound formula and atoms in (111), (200) and (110) plane.

7. The $ZnCl_2$ crystalizes in tetragonal **I** cell with lattice parameters a=5.39 Å and c=10.33 Å and atomic coordinates, Zn (0 0 0), (0 ½ ¼) and Cl (x, $^1/_4$ $^1/_8$), (-x, $^3/_4$ $^1/_8$), ($^3/_4$,x, $^7/_8$), ($^1/_4$, −x, $^7/_8$) with x=0.25. Draw the projection in *a-c* and *a-b* planes, determine the number of atoms, coordination number and calculate the Zn-Cl bond distance.

8. Cuprite presents a cubic cell (a=4.27 Å) with atomic coordinates Cu (¼¼¼), (¾¾¼), (¾¼¾), (¼¾¾); O (000), (½½½). Draw the projection in *a-b* plane, describe the structure and calculate the metal-oxygen bond distance and compound density (Cu-63.5 g/mol, O 16 g/mol).

9. Use the following table to identify the cubic structure and draw the cell projections, determine the number of coordination for each element and calculate the M-X metal bond

Formula	Atom	Atomic positions							
MX	M	½00	0½0	00½	½½½				
	X	000	½½0	½0½	0½½				
MX	M	¼¼¼	¾¾¼	¾¼¾	¼¾¾				
	X	000	½½0	½0½	0½½				
MX	M	½½½							
	X	000							
MX_2	M	000	½½0	½0½	0½½				
	X	¼¼¼	¼¼¾	¼¾¼	¼¾¾	¾¼¼	¾¼¾	¾¾¼	¾¾¾
MX_3	M	000							
	X	000	00½	0½0	½00				

10. Demonstrate that *c/a* ratio in ideal hexagonal close packed structure is 1.633 and calculate its packing factor.

11. In the cubic fluorite structure, Ca atoms occupy positions of the cubic F lattice and fluorine atoms are at the eight (±1/4,±1/4,±1/4) positions. Specify the lattice type and its basis. Identify the atoms in (002), (400) and 110) plane using sketches. Comment on maximum packing efficiency of the structure and compare it to the *fcc* and *bcc* metals?

12. Use the following table to draw the *a-b* and *a-c* projection of scheelite $CaWO_4$ structure. Determine Ca and W coordination and calculate M-O bonds. Are all W-O bonds of the same length?

Formula unit $CaWO_4$ scheelite	**Space group $I4_1/a$ (n.88)**
Cell dimensions	a=5.24 Å and c= 11.38 Å
Cell content	4 formula units
Atomic positions	Ca in (4b)
	(0,0, ½); (½, 0, ¼); +I
	W in (4a)
	(0,0, 0); (0, ½, ¼); +I
	O in (16f) (*x*,*y*,*z*); ($\bar{x}$,$\bar{y}$,*z*) (*x*, *y*+ ½, ¼ - *z*) ($\bar{x}$, ½-*y*, ¼-*z*) ($\bar{y}$, *x*, $\bar{z}$), (y, $\bar{x}$, $\bar{z}$), ($\bar{y}$, *x*+ ½, *z*+ ¼) (y, ½ -x, z+ ¼); +I *x= 0.25, y= 0.15, z=0.075*

13. Use the following table to draw the projection in *a-c* plane for $MoVO_4$ structure. Determine Mo and V coordination and calculate M-O bonds. Are all V-O bonds of the same length?

Formula unit $MoVO_4$	**Space group P*4/n* (n.85)**
Cell dimensions	a=6.608 Å and c= 4.265 Å
Cell content	2 formula units
Atomic positions	Mo in (2b)
	(¼,¾, ½); (¾,¼, ½)
	V in (2c)
	(¼,¼, *z*); (¾,¾,$\bar{z}$) *z*=0,84
	O in (16f) O (1) in (2c) (¼,¼,*z*); (¾,¾,$\bar{z}$) z=0.233 O (2) in (8g) (*x*,*y*,*z*) (½ -x, ½-*y* ,*z*) (½-*y*, *x*, *z*); ($\bar{x}$, $\bar{y}$, $\bar{z}$) (*x*+ ½, y+ ½, $\bar{z}$)), (y+ ½, $\bar{x}$, $\bar{z}$), ($\bar{y}$, *x*+ ½, $\bar{z}$) *x= 0.703, y= 0.462, z=0.26*

14. Au and Pt metals crystalize in *fcc* unit cells, a = 4.08 and 3.91 Å, respectively. Calculate metal atomic radius and density (Au 196.97 g/mol; Pt 195.08 g/mol).

15. What type of structure is expected for KBr and CsBr (ionic radii, K^+ 1.16 Å, Cs^+ 1.81 Å, Br^-1.95 Å). Calculate the packing factor of KBr.

16. At 20ºC, α-Fe crystalize in bcc unit cell, a = 2.866Å. At 950ºC, γ-Fe present the *fcc* structure, a = 3.656Å. At 1425ºC, δ-Fe is again *bcc*, a = 2.940 Å. For each temperature, calculate the density and atomic radius of Fe and comment on the results.

17. The ruby crystal presents corundum structure, $R\bar{3}c$ (Z=6) and lattice parameter a= 4.763 Å and c=13.09 Å. Using a cells volume $V = 0{,}966\ a^2c$ calculate ruby' density (Al 26.98 g/mol, Cr 52.00 g/mol and O 16 g/mol). Calculate the number of chromium atoms in 1 cm^3 of ruby crystal.

18. If the enthalpy for Schottky defects formation of a crystal with MX stoichiometry is ΔH=200 kJ/mol calculate the n_s/N relation and the number of defects/mol at 35º, 270º, 450º and 850ºC. Is it the same the number of defects for a solid with MX_2 stoichiometry with similar enthalpy of formation? and the vacancies number? (Boltzmann constant 1.38 10^{-23} J/K; Avogadro number: 6.022×10^{23}, universal gas constant 8.314 J/mol.K).

19. Using the table calculate the enthalpy of Schottky defect formation for CsI

T (K)	N_S/N
300	**$1.08\ 10^{-16}$**
400	**$1.06\ 10^{-12}$**
500	**$2.63\ 10^{-10}$**
600	**$1.04\ 10^{-8}$**
700	**$1.43\ 10^{-7}$**
900	**$4.76\ 10^{-6}$**

20. Using the Vegard's law and joined table determine the compositions of solid solutions A, B and C (all TiC_xN_{1-x})

SOLID SOLUTION	A, Å
TIC	**4.3274**
A	**4.3146**
B	**4.3006**
C	**4.2682**
TIN	**4.2471**

21. The oxides $MgGa_2O_4$ (a = 0.82780 nm) and $MgGaMnO_4$ (a = 0.83645 nm) form a solid solution according to the Vegard law. What is the expected composition for solid solution with a= 0.8300 nm.

22. The lattice parameter of zirconium sulphide $Fm\bar{3}m$ (Z=4) is 5.14 Å and its experimental density is 4.8 g/cm^3. Predict a defect structure for this compound and express its formula. (Zr 91.22 g/mol, S 32.07 g/mol).

23. What kind of defects are originated in the following cases; NaCl doped with $MnCl_2$, ZrO_2 doped with Y_2O_3, Si doped with As, partial reduction of WO_3. Assuming vacancies fraction at 750ºC of 10^{-5} for NaCl calculate the number of defects at 300ºC.

24. The experimental density of Ca stabilized zirconia (ZrO_2, $Fm\bar{3}m$, a=5.130 Å) is 5.270 g/cm^3. Assuming that oxygen vacancies are the principal point defect propose a formula for this compound. (Zr 91.22 g/mol, Ca 40.08 g/mol, O 16.00 g/mol)

25. For a tetragonal cell with parameters a=2 Å and c= 4 Å represent the reciprocal cell and calculate its volume.

26. Draw the (100), (110), (210), (310) and (410) planes in the cubic lattice and order them in increasing values of *d-spacing*.

27. Demonstrate that for a B-centered lattice the extinctions fulfil the condition *h+l=2n+1*

28. Determine the conditions of extinction (systematic absences) for the NaCl structure.

Na	(0 0 0), (½ ½ 0), (½ 0 ½), (0 ½ ½)
Cl	(½½½), (½ 0 0) (0 ½ 0) (0 0 ½)

29. The ammonium halides NH_4X present two polymorphs, one with NaCl type structure a=6.867 Å at 138ºC and another with CsCl type structure a=4.059 Å at room temperature. Identify the polymorph with density of 2.431 g/cm^3. Calculate the *d-spacings* for the first four diffraction lines for each polymorph. If you assume an effective radius of 1.5 Å and all cations and anions in close contact calculate anion radius. Are all anions in contact within the structures?

30. Rh crystalize in *fcc* structure. If the diffraction angle for the (311) plane is 36.12º (measured with λ=0,071 nm) calculate the interplanar distance d_{hkl} corresponding to that diffraction and Rh atomic radius.

31. W crystalize in *bcc* structure with X-ray diffraction (measured at λ= 0.1542 nm). Determine the Miller indexes (hkl) for every diffraction, the corresponding interplanar distance and lattice parameter.

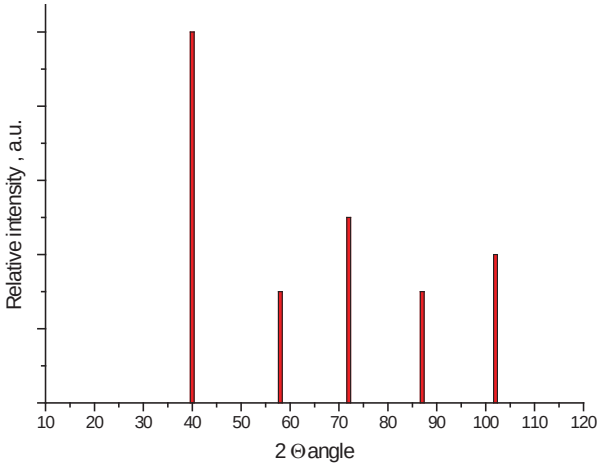

32. Au (atomic radius of 1.45 Å) crystalizes in *fcc* structure. Determine the first five diffraction lines in 2θ (measured with λ=1.544 nm) and corresponding d_{hkl}.

33. The energies of the MgO valence type orbitals are shown in joint table. Represent the simplified band structure for MgO on the base of the superposition of its orbitals.

Element	Valence orbitals	Energy (eV)
Mg	3s	-6.87
O	2s y 2p	-34.01 and -16.71

34. Considering that Cd occupies the ½ of the tetrahedral sites in CdO represent the simplified DOS of this structure and comment on its electric properties.

35. Consider the potassium tetrabromineaurate complex and describe its band structure. Describe the variation of the Bloch functions for k=0 and k=π/a, and justify the width of the observed bands. Represent the simplified DOS for the complex and deduce its electric properties.

36. Using the energy of the valence orbitals for TiO and considering that crystalizes in NaCl type structure, draw the simplified DOS

ELEMENT	ORBITALS	ENERGY (EV)
TI	3d	-5.58
	4s	-4.52
	4p	-3.47
O	2s	-34.01
	2p	-16.7

37. Explain with practical examples why solid catalysts are preferred in industrial processes.

38. Derive the Langmuir adsorption isotherm for (*i*) molecular adsorption of CO and (*ii*) dissociative adsorption of CO on platinum surface with equivalent adsorption sites.

39. Calculate metallic dispersion for 500 mg of 0.5 wt.% Pt/SiO_2 adsorbing 4 μmol of H_2.

40. Derive the rate equation for a bimolecular reaction following Eley-Rideal mechanism.

41. Nitrogen adsorption experiments estimate ZSM-5 zeolite specific surface area of 600 $m^2\ g^{-1}$ and pore volume of 0.45 $cm^3\ g^{-1}$. If we want to prepare 5 g of Fe/ZSM-5 catalyst with 2 Fe atoms loading per nm^2 what is the amount of $Fe(NO_3)_3 \cdot 9H_2O$ precursor that must be used to prepare the catalyst? If in one cycle of impregnation only 90% of the pore volume can be filled, how many impregnation cycles are necessary? The solubility in water at 20 ºC of the iron precursor is 870 g/L and its molecular weight is 404 g/mol.

42. Describe the Fischer-Tropsch synthesis for producing liquid fuels.

43. Estimate the *E*-factors for the following stoichiometric Ulmann reactions using metallic copper or alternative 5 wt.% Pt/SiO_2 solid catalyst and H_2. Compare the obtained *E*-factors and discuss the advantages of replacing the stoichiometric reactions with solid catalyst. Calculate TOF of Pt-based catalyst if 50 mg of catalyst achieves 80% of conversion in 30 min.

$$2C_6H_5I + Cu \rightarrow C_6H_5\text{-}C_6H_5 + CuI_2 \text{ (100\% yield)}$$
$$2C_6H_5Br + Cu \rightarrow C_6H_5\text{-}C_6H_5 + CuBr_2 \text{ (85\% yield)}$$
$$2C_6H_5Cl + Cu \rightarrow C_6H_5\text{-}C_6H_5 + CuCl_2 \text{ (80\% yield)}$$
$$2C_6H_5Br + H_2 \xrightarrow{Pt/SiO_2} C_6H_5\text{-}C_6H_5 + CuBr_2 \text{ (90\% yield)}$$

44. Fe_3O_4 catalyst for ammonia synthesis with 3wt.%Al_2O_3 as a binder is prepared by reduction of oxidized Fe (alumina remain unaltered) and present 29 m^2/g specific surface. When adsorbing N_2 dissociatively in standard conditions (1 bar and 273 K) a 2.2 cm^3 of N_2 is adsorbed per gram of catalyst. Considering that nitrogen atoms forms a (2x2) overlayer on the Fe (100) surface, estimate iron area per gram of catalyst using as lattice parameter 2.86 Å.

45. Draw the geometric structures of *fcc* Ni (110), (111) and (100) surfaces with (2x1) adsorbate monolayer.

46. Au atoms adsorbs preferentially on Ru (0001) defect sites. Give an explanation why the deposition of Au atoms on Ru surfaces decreases drastically N_2 dissociative chemisorption.

47. Estimate the number of metallic sites available on *bcc* W (100) surface using the values of metal density (19.6 g/cm^3) and atomic weight (183.8 g/mol).

48. Rh-based catalysts are typically used for automotive exhaust cleaning. Rh crystalizes in *fcc* structure with lattice parameter a = 3.8 Å and exposes mainly the (111) vs. (100) planes. Indicate which of these two surfaces is more reactive and give an explanation.

49. The reactivity of nickel surfaces can increase by growing Ni (111) overlayer on Ru (0001) surface. Calculate the turnover frequency for methane formation per exposed Ni atoms assuming that 1 gram of catalyst contains 15 m^2 of active Ni (111) on Ru surface. The weight of catalyst used for CO methanation reaction on stochiometric CO and H_2 mixture (50 ml/min) was 100 mg and the concentration of the produced methane 10%.

50. The reaction $2SO_2 + O_2 \rightarrow 2SO_3$ on V_2O_5 catalyst proceeds in two subsequent steps:

$$O_2 + 2* \rightarrow 2O*$$
$$SO_2 + O* \rightarrow SO_3 + *$$

Explain which mechanism is involved in the reaction and how we can verify it with isotopic labelling experiments.